Alma Mater Studiorum - Università di Bologna

DOTTORATO DI RICERCA IN

TECNOLOGIE INNOVATIVE E USO SOSTENIBILE DELLE RISORSE DI PESCA E BIOLOGICHE DEL MEDITERRANEO (FISHMED-PHD)

Ciclo 34

Settore Concorsuale: 03/B1 - FONDAMENTI DELLE SCIENZE CHIMICHE E SISTEMIINORGANICI

Settore Scientifico Disciplinare: CHIM/03 - CHIMICA GENERALE E INORGANICA

MULTISCALE COMPARATIVE ANALYSIS OF MARINE BIOMINERALS AND THEIR ECOLOGICAL IMPLICATIONS

Presentata da: Quinzia Palazzo

Coordinatore Dottorato

Stefano Goffredo

Supervisore

Giuseppe Falini

Co-supervisori

Jacobus Adrianus Kaandorp
Stefano Goffredo
Fabio Fiorentino
Beatriz Morales Nin

Esame finale anno 2022

"Biomineralization links soft organic tissues, which are compositionally akin to the atmosphere and oceans, with the hard materials of the solid Earth. It provides organisms with skeletons and shells while they are alive, and when they die these are deposited as sediment in environments from river plains to the deep ocean floor. It is also these hard, resistant products of life which are mainly responsible for the Earth's fossil record. Consequently, biomineralization involves biologists, chemists, and geologists in interdisciplinary studies at one of the interfaces between Earth and life."

(*Leadbeater and Riding 1986*)

ABSTRACT

Marine biomineralizing organisms provide a fundamental link between biology and environment. Calcified structure are important archives that can provide us main means of understanding organism adaptation, habits, environmental characteristics, and to look back in time and explore the past climate and their evolutionary history. In fact, biomineralized structures retain an unparalleled record of current and past ocean conditions through the investigation of their microchemistry and isotopes.

This thesis considers aspects of two different biomineralization systems: fish otolith and coral skeletons at macro-, micro- and nanoscale, with the aim to understand how their morphology, structural characteristics and compositions can provide information of their functionality, and the environmental, behavioural, and evolutionary context in which organisms are framed. To this end, I applied a multidisciplinary approach in the scope to investigate calcified structures as “information recorders” and as models to study the phenotypic plasticity.

INDEX

Chapter 1. General introduction

This chapter provides background information and the research objectives of this PhD project.

It firstly introduces the biomineralization in marine organisms, with a focus on fish otoliths and scleractinian corals. Then it gives an overview of the environmental and ecological influence on these calcified structures, providing some insights about the functional significance of morphological and structural differences.

Lastly, it presents the important role of calcified structure as (paleo)environmental archives, bioaccumulator of pollutants and bioindicator of marine contaminations.

Biomineralization in marine calcifying organisms

One of the amazing properties of biomineralization in organisms is that material, structure, and function are strongly correlated. Biominerals are highly controlled in structure, composition, shape, and organization, and can yield new multifunctional applications of bioinspired material synthesis in engineering (including mining) and medicine (Fig. 1) [1,2].

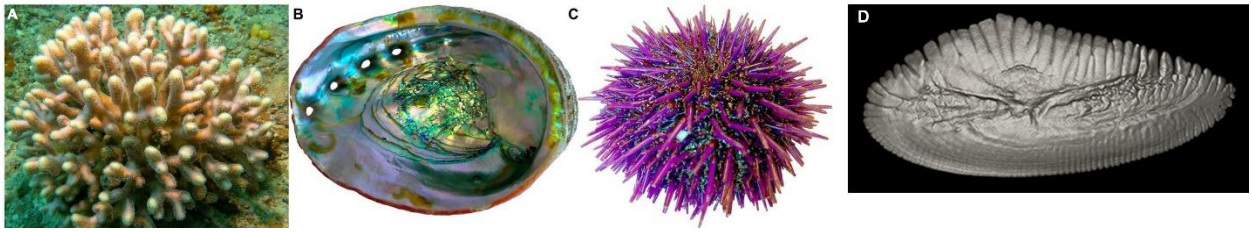

Figure 1. Biominerals across phyla: A) Cnidarians (*S. pistillata* coral in the Red Sea), B) mollusks (California red abalone *Haliotis rufescens*), C) echinoderms (California purple sea urchin *Strongylocentrotus purpuratus*) and D) teleosts (*Merluccius merluccius* otolith) (photos A-C from Gilbert et al., 2022).

It is currently held that most lineages with exoskeletons originally had a tough nonmineralized exoskeleton consisted of only biopolymers [3]. Only later in evolution, biomaterials became mineralized composite structures consisting of biopolymers (collagen, keratin and chitin), which provide toughness, and biominerals (hydroxyapatite, calcium carbonate and amorphous silica being the principal ones), which give the strength [4,5]. In fact, many arthropods and arthropod-like animals that appeared during the Cambrian explosion had hard skeletons of purely organic cuticles with no incorporated biominerals [6]. While the building blocks of these structures consist of two basic classes (biopolymers and biominerals) [4] they are combined in a significant level of complexity and result in a large variety of marine inorganic–organic composite materials possessing mechanical characteristics of stiffness, toughness, and strength that are superior to those of their constituent building blocks [7]. An advantage of mineralized exoskeletons over solely organic skeletons (e.g., the insect cuticle consists of a polysaccharide α-chitin) is that reinforcement by mineralization might be cheaper, in metabolic terms, than organic sclerotization [3,8]. In fact, it is assumed that the main metabolic cost of shell construction lies in the creation of the proteins and polysaccharides required for the shell's composite structure and not in the precipitation of the mineral components [6,9]. Thus, in order to stiffen the cuticle to a certain degree, it might be cheaper to use mineral reinforcement than enhancing sclerotization [3]. Therefore, combining the organic and inorganic material into a hybrid-

biocomposite material may has been an evolutionary solution to reduce the metabolic cost for the synthesis of biomaterials and to overcome the biominerals' disadvantage of being brittle structures [8].

The complex shapes of biominerals cannot be explained with simple mechanistic models of crystal growth (Fig. 2). The synthesis, as well as the size, morphology, composition, and location of these biogenic materials is genetically programmed and controlled by organisms [10]. Therefore, biomineralization describes the deposition of organized mineral structures through highly regulated cellular and molecular processes energetically costly which lead to the formation of functional structures [1,2]. In fact, biomineralization is characterized by chemical reactions in which the solubility is one the main protagonists of the process and involves proteins, the control of crystal growth and the inhibition depending on the crystallographic axis.

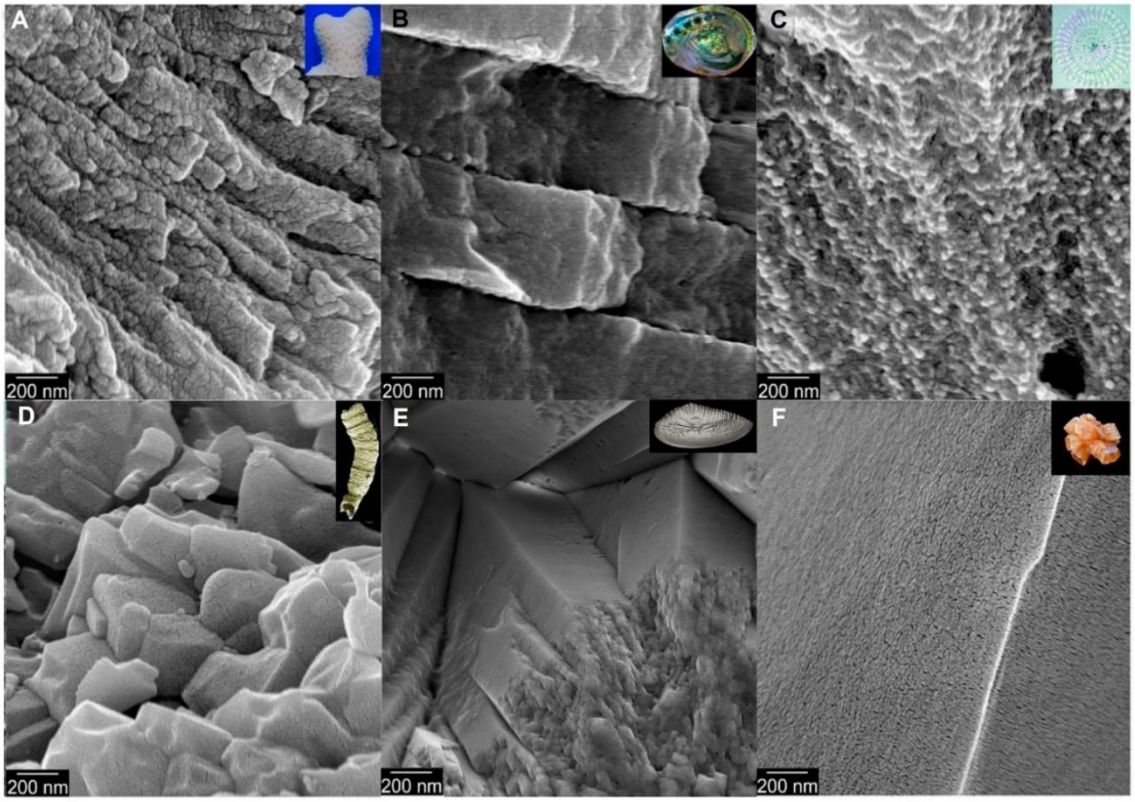

Figure 2. Scanning electron micrographs of modern and fossil marine biominerals showing nanoparticulate texture (A to E), whereas nonbiogenic minerals do not (F). (A and B) Modern aragonite biominerals: coral skeleton from *S. pistillata* (A) and nacre from *H. rufescens* (B). (C) Calcite sea urchin spine from *S. purpuratus*. (D) Phosphatized Ediacaran *Cloudina* (550 Ma before present) from Lijiagou, China. (E) Aragonite otolith from *Merluccius merluccius*. (F) Nonbiogenic aragonite from Sefrou, Morocco. arb. u., arbitrary units (Images A-D, F from Gilbert et al., 2022).

The outcome of the biomineralization is the synthesis of composite materials with interesting properties that cannot be produced by conventional chemical synthesis and having a high value within

bioinspired engineering research [1]. Some characteristics of materials produced by controlled biomineralization are: uniform particle sizes, well-defined structures and compositions, high levels of spatial organization, complex morphologies, controlled aggregation and texture, preferential crystallographic orientation, and higher-order assembly into hierarchical structures (Fig. 2) [2,11].

Crystal formation takes place in two steps: crystal nucleation (requires a high degree of saturation) and crystal growth (requires lower degree of saturation). The controlled crystal growth is mediated by an array of macromolecules (structural proteins, glycoproteins, and polysaccharides) which are incorporated in the biomineral, and are therefore termed "organic matrix" [2]. Several experiments have showed that the growing crystals can be shaped by organic molecules and have demonstrated polymorph selection influenced by different organic matrix mixture of macromolecules [10,12–14]. Therefore, the organic matrix acts as a meditator of mineralization and as crystal modifier. For this reason, Lowenstam proposed to define this kind of biostructures as "matrix-mediated minerals," characterized by formation very precisely controlled by the action of an organic component specifically produced by the organism [11]. Skeletal biomineralization requires energy and so imposes a metabolic cost on skeleton-forming organism [15]. For example, in corals, the formation of the skeleton and its organic matrix consumes about 30% of the coral's energy budget [16], energy that might otherwise go into reproduction. Therefore, for biomineralized skeletons to evolve, the benefits to the organisms must have outweighed their costs. Biomineralization has been around since the first Prokaryota appeared in the Archaean, the geological aeon from about 4 to 2.5 billion years ago [15]. Since the evolution of biomineralization in the Neoproterozoic (~ 742 ± 6 Mya), the employment of mineral structures by biology has become a near-ubiquitous part of life, and thousands of marine organisms (vertebrates, invertebrates, and plants) producing biominerals, with different structures, materials, processes, and functions have been identified so far (Fig. 3) [17]. Three minerals have prevailed in biological structures: carbonates ($CaCO_3$), phosphates ($Ca{-}PO_4$ variants) and silicates (SiO_2). Each mineral type is present across a wide range of organisms and is employed in a variety of functional roles. Among these, calcium carbonate ($CaCO_3$) biomineralizing organisms have played major roles in the history of life and the global carbon cycle during the past 541 Ma. In fact, calcium carbonate is the most abundant and widespread biogenic mineral [18], which has influenced the carbon cycle since its evolution during the Cambrian and Ordovician radiations marine animals and algae [19], affecting and being affected by the ambient environment on geologic time scales [20,21]. Whole mountain chains are formed from calcium carbonate in the form of chalk, limestone, marble, and dolomite. It constitutes more than 4% of the Earth's crust and almost every product in our daily lives either contains calcium carbonate or has some association with the mineral during its production.

The result of the evolutionary success of calcifying organisms is still reflected in their presence in multiple kingdoms, highlighting the many biological benefits that calcium carbonate mineralization provides such as: skeletons for protection, structural support, storage, optical and hearing detection, balance, and gravity sensing [12,19]. Biocalcification is performed by a variety of species in different environments that is manifested, for example, as the immense geologic reef structures built by corals and coralline algae as well as the formation of calcium carbonate structures in the inner ears of fishes [22].

(a) 	Cyanobacteria > 3 bya	Forming rock-like mounds called stromatolites classified as - laminated with microbial biofilm only - double layered with alternating biofilm and crystallized sediment layers
	Haptophytes ± 250 mya	Coccolithophores: ubiquitous bloom-forming planktonic microalgae. important component of marine food chains (extant) and of limestone deposits (fossil) throughout the world
	Calcareous algae ± 500 mya	Coralline red algae (Rhodophyta): crustose, geniculate, or as rhodoliths Calcifying green algae (Chlorophyta): lobate
	Foraminiferans ± 550 mya	Benthic or planktonic lifestyle
	Calcareous sponges ± 550 mya	Calcium carbonate (aragonite or calcite) spicules that may fuse to form massive, hollow, or honeycombed structures
	Protostostomian invertebrates 635 mya	Corals, crustaceans, marine worms
	Deuterostomian invertebrates ± 520 mya	Molluscs: shells, radula, cuttlefish bone Echinoderms: tests, plaques, spines, spicules, skeletal ossicles
	Teeth, scales, otoliths, bones ± 420 mya	Bony fish (Osteichthyes): teeth, scales, otoliths, and skeletal bones Cartilaginous fish (Chondrichthyes): teeth, skin dentin Marine turtles: teeth, scales, and skeletal bones Phosphated carbonates. Dentin
(b) 	Silicoflagellates 120 mya	Unicellular protists with relatively simple skeleton made of silica
	Radiolarians ± 500 mya	Unicellular protozoans with intricate skeletons Acantharea with skeleton made of silicate or of strontium sulfate Radiolarians are an essential component of the plankton
	Diatoms ± 150 mya	Pennate diatoms with bilateral symmetry Centric diatoms with radial symmetry Unicellular algae with siliceous frustules (exoskeletons) Unique urea cycle recently discovered
	Silica sponges ± 600 mya	Novel glass-like materials (cold synthesis using enzymes bioinspired from silicatein) from spicules made of silicon dioxide Skeleton scaffolds made of fused spicules have interesting mechanical properties

Figure 3. Major biogenic sources of marine biominerals, with age estimates of earliest fossil records. (a) carbonate-based marine biominerals; (b) silica-based marine biominerals (From: La Barre S. & Bates S., 2018).

Biomineralization evolved independently but convergently across phyla, suggesting a unity of mechanism transcending biological differences to respond to some broadly experienced selective pressure (Fig. 4) [2]. Changes in both the physical and biological environment have been proposed, but the observation that organisms evolved calcium carbonate, silica, phosphate, and agglutinated skeletons in the same time frame strongly implicates predation as a major driver [23].

Calcification is highly polyphyletic (there is no common, mineralizing ancestor), and it is believed to have evolved independently in eukaryotes at least 28 times (Fig. 4) [15]. The widespread utility of calcification by organisms and its independent evolution of mineralization throughout evolutionary history suggests that environmental conditions have consistently favored the evolution of calcification

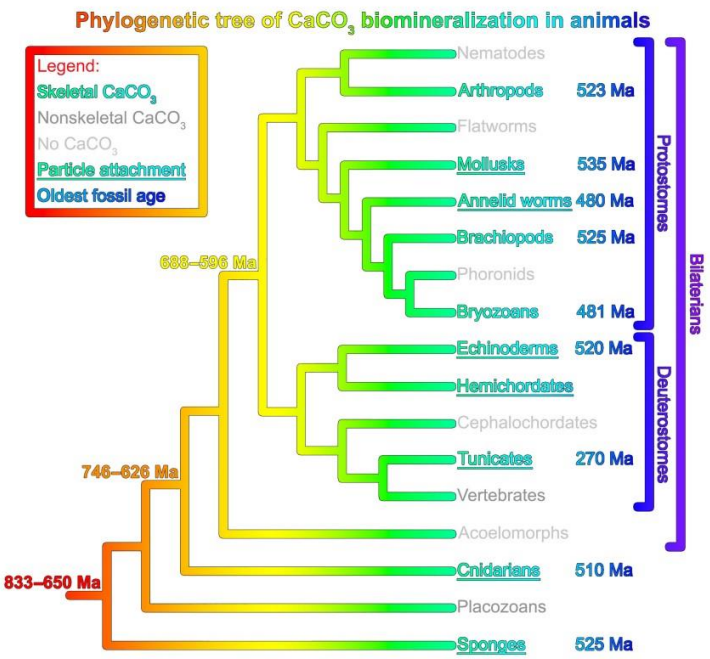

Figure 4. Phylogenetic distribution of $CaCO_3$ biomineralization in animals showing that biominerals appeared in the fossil record long after the different phyla had diverged from one another. Because the biomineralizing organisms in various phyla do not have a common ancestor that was itself biomineralizing, they must have evolved strategies to form carbonate biominerals independently. These strategies are remarkably similar in the building blocks and mechanisms across phyla; therefore, they evolved convergently (From Gilbert et al., 2022).

throughout geological time (even today, the majority of the ocean is supersaturated with respect to calcium carbonate), or that the cellular processes supporting biomineralization are similar to those employed in other life processes, or a combination of the two [15,24]. Both marine diversification and mass extinctions reflect physiological responses to environmental changes through time. Nevertheless, an integrated understanding of carbonate biomineralization is necessary to illuminate this evolutionary record and to understand how modern organisms will respond to 21st century global change [2].

Calcium carbonate occurs in three crystalline anhydrous polymorphs at ambient condition: calcite, aragonite (Fig. 4), and vaterite, two hydrated crystalline phases: monohydrocalcite ($CaCO_3 \cdot H_2O$) and ikaite ($CaCO_3 \cdot 6H_2O$), and various transient amorphous phases (ACC) with differences in short range order and degree of hydration that can act as a precursor to more stable crystalline forms [25]. Among the anhydrous polymorphs of $CaCO_3$, calcite is thermodynamically the most stable at ambient conditions. The order of thermodynamic stability is, from most to least, calcite, aragonite, and vaterite [26]. Despite lower stabilities from a thermodynamic point of view, aragonite and vaterite can be formed at ambient conditions owing to the kinetic constraints induced by synthesis factors such as temperature and impurities (e.g., Mg) [27], which can lead to crystallization of less stable aragonite or the least stable vaterite rather than forming calcite. A number of mechanistic studies have been conducted thus far to reveal the transformation mechanisms among the $CaCO_3$ polymorphs. Transformation and crystallization of ACC can follow an energetically downhill sequence: more metastable hydrated ACC → less metastable hydrated ACC⇒anhydrous ACC ~ biogenic anhydrous ACC⇒vaterite → aragonite → calcite. However, in a given reaction sequence, not all these phases need to occur. The transformations involve a series of ordering, dehydration, and crystallization processes, each lowering the enthalpy (and free energy) of the system, with crystallization of the dehydrated amorphous material lowering the enthalpy the most [28]. Organisms commonly deposit both calcite and aragonite mineral structures since they are more stable than the other polymorphs. Vaterite is rarely deposited as a primary biomineral phase, although there is evidence that it occurs as a transitory phase in inorganic precipitation [29], and is deposited during repair to damaged biomineral structures [30]. Aragonite and calcite have a similar crystal structure consisting of alternating layers of Ca^{2+} and CO_3^{2-} perpendicular c axis (in the ab plane). Calcium ions take up the same position in both polymorphs, unlike the carbonate ions. In the aragonite these are raised in the direction of the c axis and form two separate layers, in which the orientation of the ions is different (Fig. 5) [31].

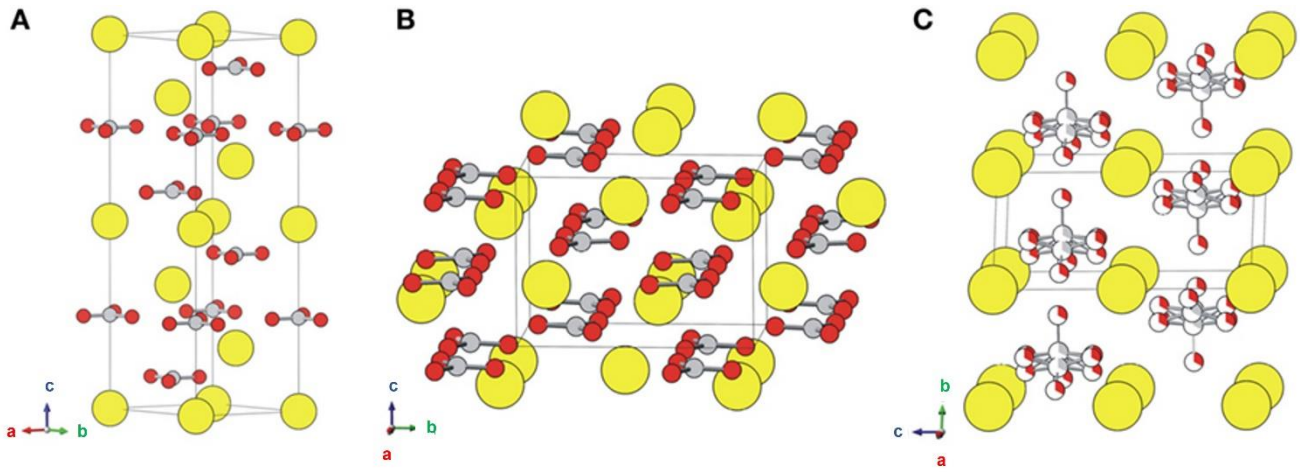

Figure 5. Crystal structures of (A) calcite, (B) aragonite, and (C) vaterite. Ca atoms are displayed as large yellow balls, and carbonate groups are illustrated with gray (carbon) and red (oxygen) balls (From Chang et al., 2017).

This structural difference gives different properties at the two forms. Aragonite is denser (2.95 g/mm^3) than calcite (2.71 g/mm^3) (Table 1) and its crystal systems are orthorhombic and growth more along c axes acquiring a needle-like shape (Fig. 6). Calcite is more stable, and its crystal systems is rhombohedral. In biological systems, both forms have a structural and defensive functions (i.e. shells, skeletons, etc.) [18] and the kind of polymorphs produced by organism is always under genetic control [32]. Aragonite usually set up spherulitic architecture with high superficial area and porosity, while calcite set up more large crystals but more brittle [32].

Polymorph	Crystal structure	Space group	Density (g cm^{-3})	Hardness (Mohs)	Solubility (-log K_{sp})	ΔG_f (KJ mol^{-1})
Calcite	Trigonal	*R3c*	2.710	3	8.30	-1128.8
Aragonite	Orthorhombic	*mmm*	2.947	3.5-4	8.12	-1127.8
Vaterite	Hexagonal	$P6_3/mmc$	2.645	3	7.73	-1125.5

Table 1. Properties of the anhydrous crystalline forms of calcium carbonates.

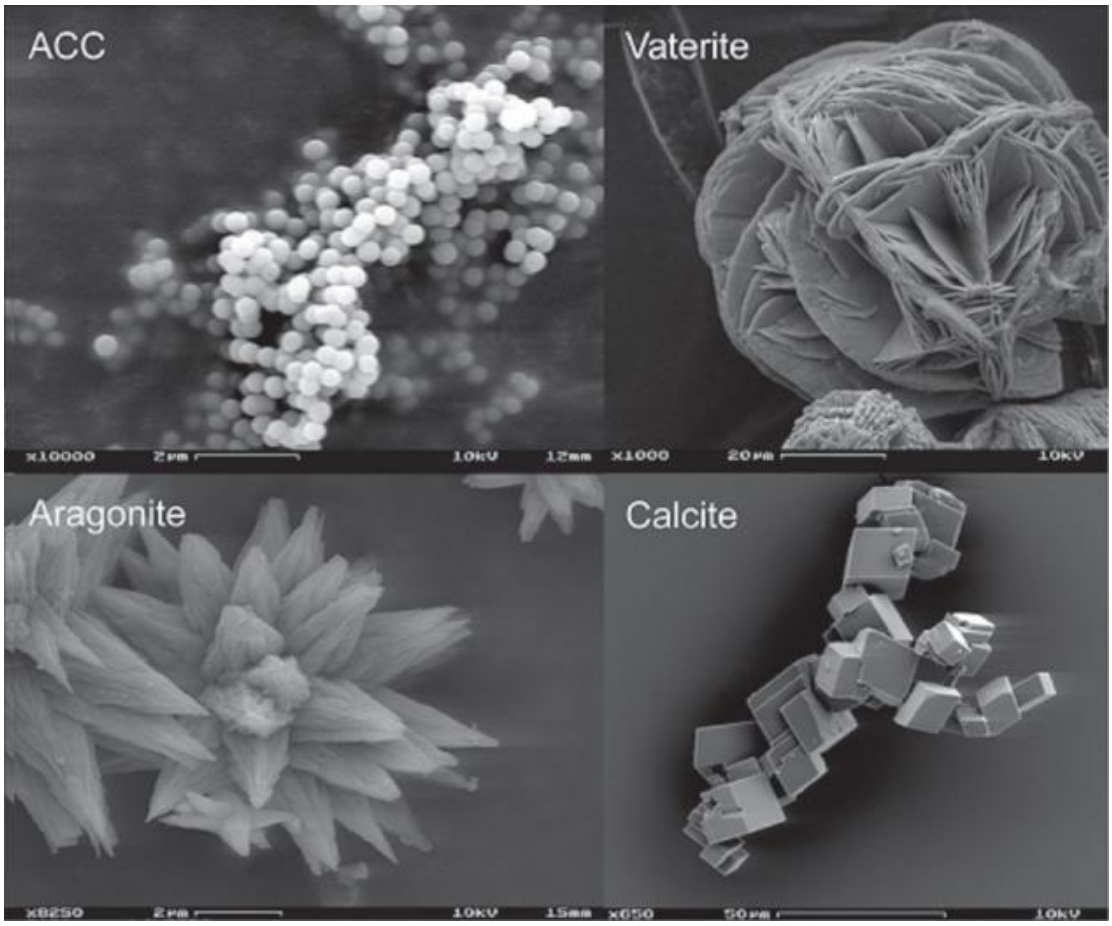

Figure 6. Conventional shape of calcium carbonate polymorphs. Anyway, the morphology of each crystalline polymorph can be changed due to the crystallization condition (From Dhami et al., 2013).

Beyond the variety of sizes, shapes, spatial organizations, and growth modes of the skeletal units of biomineralized structures, striking similarities have been revealed in these parameters when seen at submicrometer scales. Subunits with dimensions in the range of 10 nm can be recognized within Ca-carbonate structures, also among different taxa, highlighting similarity of growth mode and skeletogenesis at the micrometer scale (Fig. 7-8) [11]. Some vertebrates produce extremely interesting calcareous structures, such as otoliths, that present crystallization aspects (size of microstructural units and layered growth mode) (Fig. 7) that are comparable to those characteristic of invertebrates (Fig. 8) [33,34]. However, in contrast to the rather low mineralogical diversity of carbonates nanostructure, the calcification processes developed within major biological groups involve very different groups of genes [11].

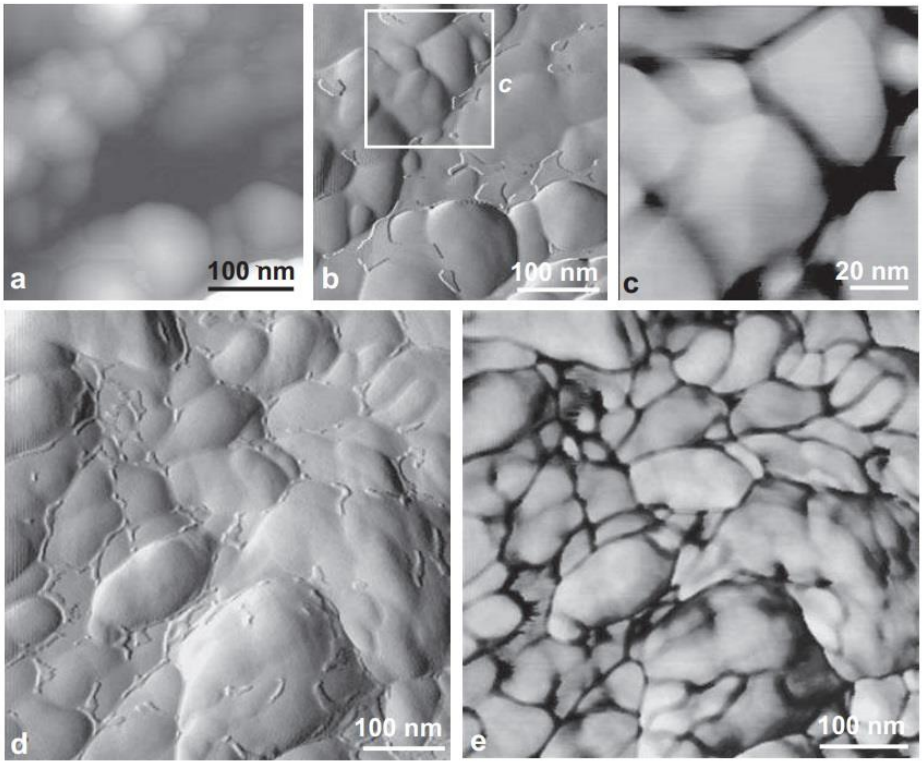

Figure 7. AFM images of aragonite in an otolith of *Gadus sp*. (a) Height image, here at low magnification, illustrates granules grouped in linear assemblages; (b–c) Amplitude image, demonstrating the interactive (= organic and/or amorphous) nature of the (c) envelopes; (d–e) Complementary images – amplitude (d) and phase (e) – summarizing the structural pattern of otolith calcification, and emphasizing similarities with invertebrate biological carbonates (From Dauphin and Dufour, 2008; Sorauf, 2010).

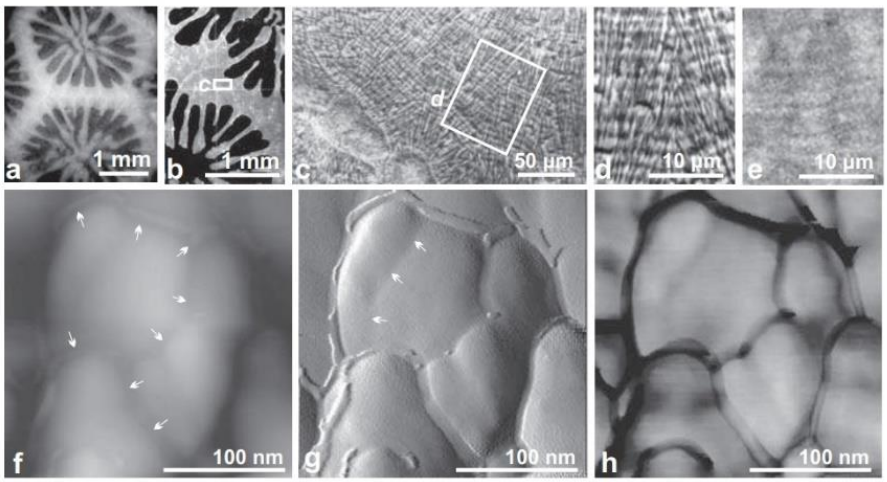

Figure 8. Growth layers and nanostructures in coral aragonite coral skeleton of the genus *Goniastrea*. **(a–c)** Section of corallites and layered microstructure of the fibrous material; **(d–e)** Correlation between growth layering (visible after etching) and distribution of sulfated polysaccharides mapped on the same polished surface; **(f)** Height image: topography of the sample surface at the nanometer scale; **(g)** Amplitude image; **(h)** Phase image (From Cuif et al., 2008).

1.2. Otolith as records of fishes' biological and ecological history: ecomorphological, behavioural and physiological patterns in otoliths

All vertebrates have small bioinorganic "ear stones" in their inner ear labyrinth that are essential for hearing and balance. Most non-mammalian vertebrates have three pairs of otolithic end organs (the saccule, utricle, and lagena) containing calcium carbonate crystals (Fig. 9) [35]. In most vertebrate species, the crystals are held together in the form of otoconial masses. In the teleost fishes, however, the calcium carbonate biomineralizes are solidified into a single mass in each otolithic end organ, the otoliths (Fig. 10-11) [36].

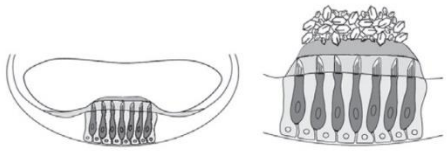

Figure 9. Drawing of the different types of biomineralizes (otoliths and/or otoconia) in the inner ear of different vertebrates (From Schulz-Mirbach et al., 2019).

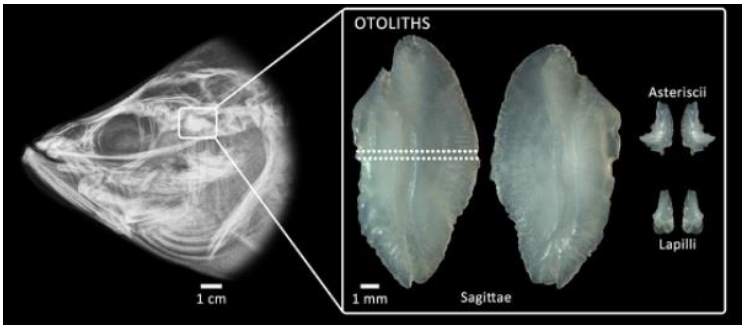

Figure 10. Detail of the fish's head showing the location of the three pairs of otoliths called sagittae, asteriscii, and lapilli.

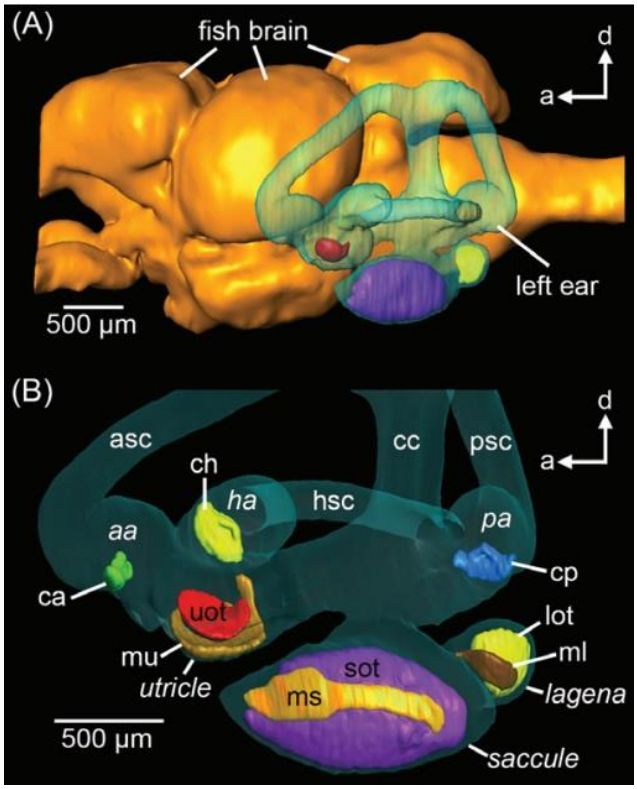

Figure 11. **(A)** The position of the teleost inner ear relative to the brain. **(B)** Detail of inner ear components in the cichlid *Steatocranus tinanti*. Three-dimensional (3D) reconstructions based on micro-computed tomography (microCT) imaging are shown in lateral (A) and medial (B) views illustrating the following inner ear components: (1) Semicircular canals: anterior (asc), horizontal (hsc), and posterior (psc) canals; ampulla of the anterior (aa), horizontal (ha), and posterior (pa) canals; cc, common canal (= crus commune); (2) otolith end organs: utricle, saccule, lagena; (3) sensory epithelia: cristae of the anterior (ca), horizontal (ch), posterior (cp) canals; maculae of the utricle (mu), saccule (ms), and lagena (ml); (4) otoliths: uot, utricular otolith (= lapillus), sot, saccular otolith (= sagitta), and lot, lagenar otolith (= asteriscus). a, anterior; d, dorsal (From Schulz-Mirbach et al., 2019).

The dense otoliths of teleost are of remarkable interest because they play a vital anatomical role in fish, acting as mechanoreceptors of the ear for sound perception and equilibrium [37,38]. These structure are metabolically inert, and therefore, do not undergo remodeling or resorption [39]. Thanks to this characteristic, otoliths are considered important tools in marine and fisheries research and are used to reconstruct the environmental histories by the analysis of stable isotopic compositions and the investigation of trace elements concentration, which give important information to infer about the natal origin, movement, habitat use, diet and the impacts of climate change [39–41]. Therefore, otolith can also reveal the time-keeping properties about the fish's life and the surrounding environments.

One of the three pairs of otoliths, the saccular one (named sagitta, Fig. 10) is the largest in most fishes, included the *Merluccius merluccius* (common name: European Hake), the species object of the studies presented in this thesis. Otoliths of the saccule (sagittae) are known to show species-specific (or even population-specific) contour differences, which have a significant genetic component, and thus, are regularly used in fisheries management for stock identification [42]. Therefore, for their peculiar characteristics, otolith are employed in a variety disciplines including systematics, auditory neuroscience, and fisheries [36].

Sound is a major sensory channel for fishes and plays a key role in their ecology and life-history strategies, since it is used for communication between conspecifics or heterospecifics, navigation, feeding, detection of predators, reproductive interactions, and habitat selection [43–45]. For its importance, fishes have evolved various physiological adaptations for sound reception and production [45,46]. The size and shape of otoliths likely influence the frequencies that can be detected and the sensitivity (auditory threshold) to those frequencies [47]. Thus, the wide variability in ear morphologies of fishes and particularly in otoliths is likely linked to the diversity in hearing mechanisms and capabilities among different species [48]. Otoliths first form in embryo and continue to grow throughout the life of an individual, with a double-banded increment composed of a calcium carbonate-rich region and an organic matrix-rich region being deposited daily, similarly to the growth bands observed in corals. Consequently, otolith structure can also vary substantially during fish growth in response to both physiological and ecological ontogenetic changes, and/or to differences in the acoustic environment related to a diverse habitat occupied by juveniles and adults [38,49]. Indeed, otoliths record the specifics of the physicochemical environment experienced by a fish at any given point in its life and also provide information about its physiology related to the ontogeny and feeding [38,50,51].

However, just few investigations have focused so far on the relation between the morphological and ultrastructural differences of otoliths and the eco-morphological adaptations of the auditory system to habitat features such as water depth, feeding modalities, spatial niches and mobility [36,52–54]. In addition to otolith' shape and its mass, other anatomical features within the otolith (including sulcus acusticus and protuberances) are thought to have functional significance but have generally received less attention so far [35,55].

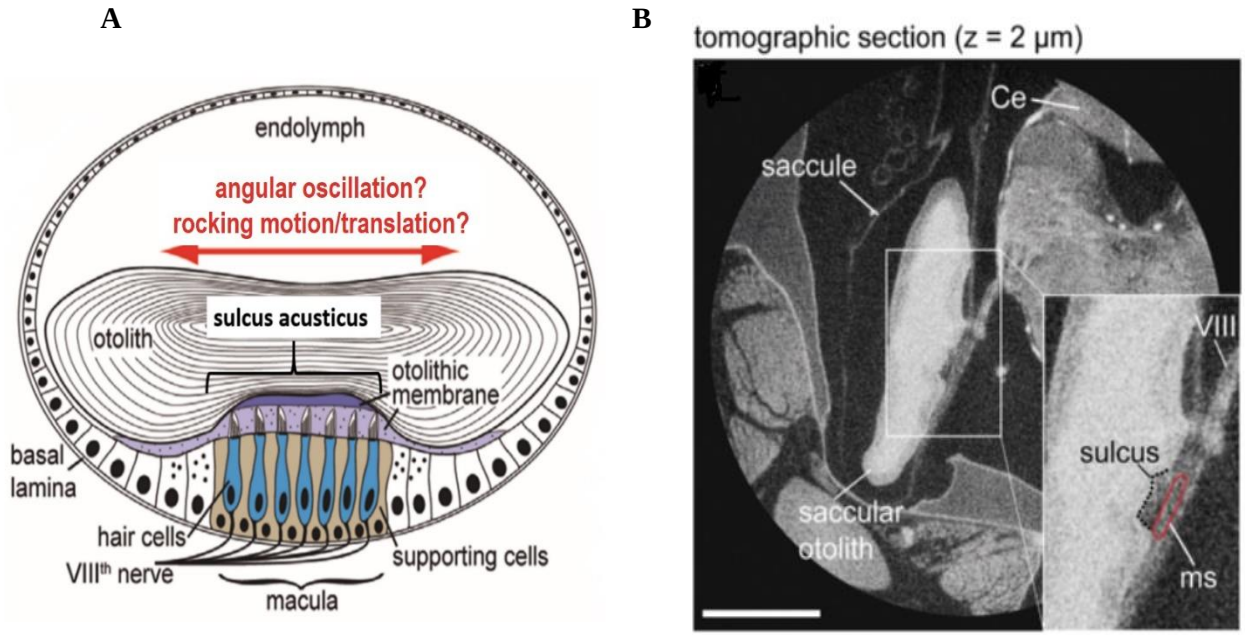

Figure 12. **(A)** Drawing of the otolith and the anatomical depressed structure (sulcus acusticus) which is in contact with the otolithic membrane that contains the sensory hair cells of the auditory systems (image modified from Schulz-Mirbach et al., 2019). **(B)** Higher resolution tomographic transverse section displaying the saccule, its otolith, the corresponding macula and the acustical nerve (VIII). The sulcus is the furrow on the medial face of the saccular otolith housing the macula sacculi. In the insert the sulcus is indicated by a dotted line and the macula is red labeled. Ce, cerebellum; ms, macula sacculi; VIII, part of the VIIIth cranial nerve innervating the macula sacculi. Scale bars, 500 µm (From Schulz-Mirbach et al., 2013).

The sulcus acusticus corresponds to a depressed portion of the proximal face of the otolith, which is in contact with the sensory epithelium (=macula) (Fig. 12). Therefore, the shape of the sulcus closely matches the shape of the respective macula that is overlain by the otolith [55]. Its characteristics may play an important role in determining the relative motion between the otolith and its respective sensory epithelium [56]. Difference in the 3D shape of sulcus acusticus may alter the mechanical resistance provoked by a different otolithic membrane, which consequently affect the stimulation pattern of the sensory hair cells [57]. Furthermore, the size of the sulcus acusticus relative to the size of saccular otolith is also assumed to alter the hearing abilities of the fish. Indeed, ecomorphological studies indicate that

the ratio of sulcus size (2D sulcus area, used as a proxy for macula size) to otolith size (area of the macula-oriented face of the otolith) seems to be correlated with habitat features such as water depth, food or spatial niches, and mobility, but may also vary during ontogeny [35,58]. However, one of the major difficulties concerning this issue that have been faced so far, is related to the reliably and reproducibility in the quantification of the dimensions (area and volume) of the sulcus acusticus and consequently, of the sensory epithelium [35].

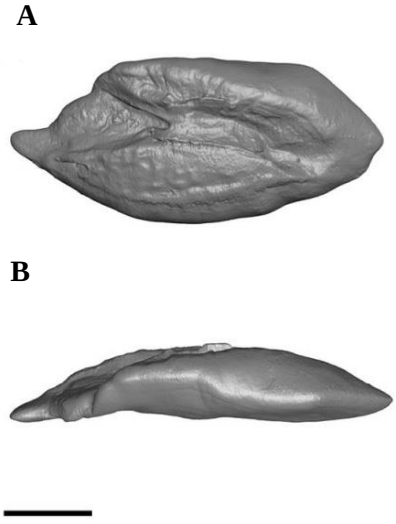

Figure 13. 3D reconstructions of *Steatocranus tinanti* otoliths. **A)** medial (sulcus) otolith face, **B)** dorsal (lateral) view. Scale bars, 500 µm (From Schulz-Mirbach et al., 2013).

A recent mathematical model of the motion of the otolith in acoustic fluids in response to progressive harmonic waves supported the assumption of shape-dependent otolith motion [59]. In this model the otolith has been considered as a rigid scatterer in acoustic fluid in response to progressive harmonic waves. The model predicts that the motion of irregular and asymmetrical shape scatterer, such as otolith, under harmonic wave excitation is not the simple two-dimensional back-and-forth accelerometer model proposed by de Vries but include both translational (rocking motion) and angular oscillation (Fig. 12). Indeed, the results suggested a frequency dependent pattern of otolith rotational movement as a result of linear horizontal translation, and this angular motion of the otoliths may be an additional acoustical cue that fish may use to process sounds [59,60]. The model suggest that the magnitude of the additional stimuli produced by the otolith rocking motion are expected to be much greater for more complex shapes that deviate from simple spherical shape [59] supporting the theoretical considerations of a shape-dependency of the movement [37,61–64]. Furthermore, first experimental evidence that otolith shape might influence its motion has been provided by a laser vibrometer study on perch saccular otoliths. In this study was observed that saccular otoliths in perch "vibrated" as the central and marginal portions of the otoliths displayed different motion patterns in terms of different relative velocities. At a stimulus frequency of 220Hz (horizontal sinusoidal vibration, 630 µm/s) the vertical movement at the otolith center amounted to ca. 50–60 µm/s which was within the range of the "background" movement of the skull (30–60 µm/s) whereas motion at the anterior and posterior margins was ca. 120–140 µm/s [65]. Interesting insights come from a recent experiment conducted using hard X-ray phase contrast imaging to visualize *in-situ* the motion of otoliths in response to directional wave sounds in two species of cichlid [64]. In this work, authors reported that the amount of maximum displacement of otolith seems depend on the position of the

otolith in the sound field or relative to the position of the sound source. In fact, a result of this study revealed that saccular otolith shows greater displacements when sound impinged on the dorsal otolith margin (Fig. 13A) than on the medial otolith face (Fig. 13B). It seems that when sound is impinging on the dorsal otolith margin, the otolith moves against less damping material (and consequently less resistance), with the narrow dorsal margin of the otolith pointing into the direction of the sound source. Therefore, more damping by surrounding tissue and attached tissue (otolithic membrane) may also account for the smaller displacements of otoliths *in-situ* [64].

In light of the above considerations, the use of conspecific in establishing the shape/structure–function relationships of otoliths, during their ontogenesis and between sex, can be a helpful tool in the prediction of fish auditory capabilities while avoiding phylogenetic bias [66–69].

1.3 Scleractinian coral skeleton as biomineralized ecological records of organism's adaptation, acclimatization, and bioaccumulation

Scleractinian corals (also referred as "hard corals" or "stony corals") represent a major source of biogenic carbonate, accordingly, they are principally known as the architects of coral reefs [70]. Their skeletons are composite structures, resulted from a biologically controlled biomineralization process, made of an organic fraction, typically referred to as the organic matrix (OM) (macromolecules consisting of proteins, carbohydrates, and lipids), embedded in calcium carbonate ($CaCO_3$) [71]. As the coral skeleton is made of calcium carbonate, the term calcification may be alternatively used to describe the process of coral skeletogenesis [72].

Coral calcification is a globally important biological and geochemical process as has allowed corals to build many thousands of square kilometers of biomineralized marine habitat (covering an area of about 284 300 km^2) in shallow tropical seas since their radiation in the Middle Triassic, developing one of the most ancient and dynamic ecosystems of the Earth [73]. The coral reefs not only provide extensive habitats for a myriad of marine life, but also act as a natural barrier by protecting the coastline from the open seas and preventing coastal erosion [74]. A lot of people living along long coastal depend on coral reefs for their livelihood since they provide benefits for humankind (e.g. reefs are an economic resource for tourism and fisheries) [75]. In addition, corals are also a source of chemical compounds of biomedical and biotechnological importance [76]. Furthermore, from their first appearance about 200 million years ago to present-day, corals provide an excellent natural archive of (paleo)environmental marine conditions. Indeed, it is possible to correlate the trace elements and isotopes (so-called geochemical "proxies") in the coral skeletons to ambient seawater because of the great ability of skeleton to contain a wealth of environmental information [77]. The evolutionary success of reef-building corals is often attributed to photosymbiosis, a mutualistic relationship scleractinian corals developed with unicellular photosynthetic dinoflagellates commonly called zooxanthellae (e.g. *Symbiodinium* sp.) [78]. Zooxanthellae photosynthesize within the coral tissue providing corals with most of their energy, while the coral hosts in turn live in shallow, clear waters where zooxanthellae have optimal exposure to sunlight for photosynthesis [79]. *Symbiodinium* photosynthesis significantly enhances coral calcification and growth [80] providing corals with photosymbiotic byproducts (e.g., oxygen and glucose), which allow the corals to calcify at an expedited rate, making zooxanthellate corals more efficient reef-builders than azooxanthellate corals in shallow and nutrient-depleted environment [72,81]. The success of scleractinian corals in oligotrophic tropical environments has been attributed to their extraordinary efficiency in collecting [82] and processing [83] light for carbon fixation. One of the enhancements for the light absorption

efficiency is closely related to a key functional role of the optical properties (multiple light scattering) of coral skeletons [78]. Indeed, has been documented that some coral skeletons properties have a direct impact on holobiont photosynthetic performance, and may play an important role in coral ecology and the diversification of modern symbiotic scleractinian [82]. Therefore, corals show morphological adaptations to maximize their light capture and energy acquisition and their zooxanthellate symbionts must continuously photoacclimate [84].

Different coral skeleton morphotypes and variations in their structural characteristics may be linked to differences in their functional traits, and consequently, on coral performance and sensitivity-robustness to natural perturbations [85,86] (Fig. 14). The trigger that leads to differentiation in the skeleton is often related to an adaptation or acclimatization to respond at environmental factors. In fact, plasticity in coral skeleton characteristic has been noted under different environmental conditions from the centimeter scale (colony) [87] to the millimeter scale (corallite, skeletal density and porosity) [88,89], while at the nanoscale, the coral skeleton's structural features hardly seem to vary. A wide variety of environmental parameters have been shown to affect skeleton morphogenesis: light, water chemistry and flow, sedimentation rate, food availability, competition for space, gravity [90]. Anyway, the mechanism supporting coral plasticity and how such process may be controlled is still unknown [72]. Probably, environmental parameters affect coral morphology by changing locally the rate of calcification. It can be hypothesized that environmental parameters alter the genetically-controlled pattern by increasing the supply of Ca^{2+} or inorganic carbon by ion-pumping mechanisms and/or increasing organic matrix synthesis and secretion toward the extracellular calcifying medium, either directly or by diffusion of hypothesized internal regulators such as the coral Bone Morphogenetic Protein (coral BMP2/4) in the calcifying epithelium [91].

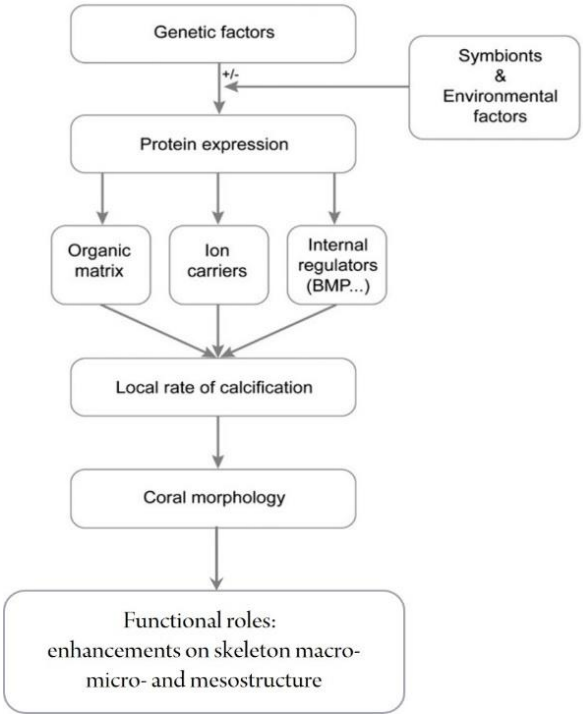

Figure 14. Schematic representation of the factors which can affect coral morphology (Modified from Tambutté et al. 2011)

The response of organisms to environmental change can occur through both genetic (i.e., adaptation) and nongenetic (i.e., acclimatization) processes (Fig. 15) [92]. Genetic adaptation is defined as a change in the phenotype from one generation to the next through natural selection and involves a genetic change in the form of allele frequency changes between generations. It is sometimes referred to as hard inheritance. Acclimatization is a phenotypic response to variation in the natural environment that alters performance and possibly enhances fitness but does not involve a genetic change. Until recently, acclimatization has been considered to occur only within the life span of an organism providing no trait evolution from one generation to the next. It is, however, becoming evident that some environmentally induced nongenetic changes are heritable. Indeed, this process, called trans-generational acclimatization or soft or non-genetic inheritance, occurs through epigenetic processes that cause a change in expression level of those genes without changing the actual gene sequence [93].

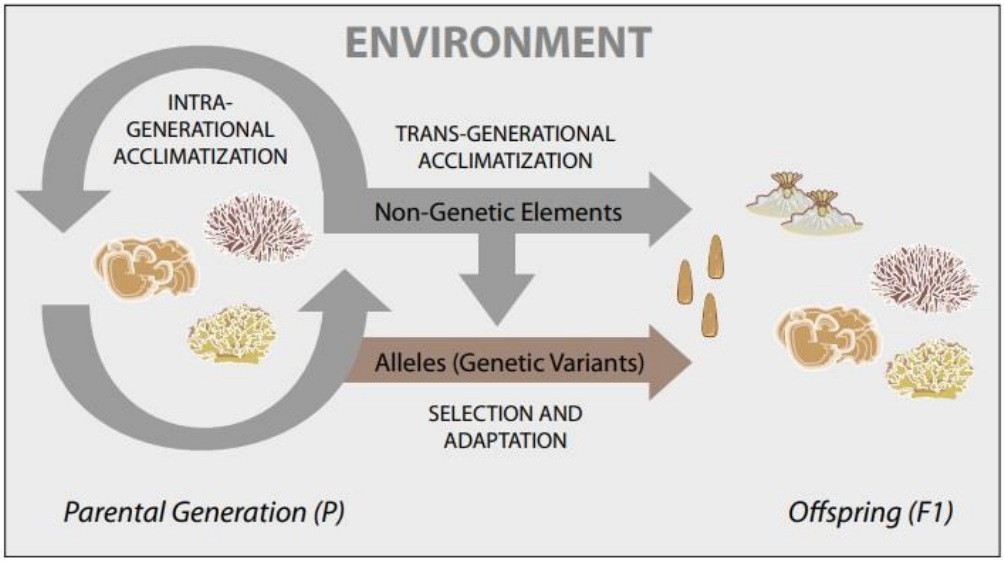

Figure 15. Diagram showing within-generation acclimatization through nongenetic processes, as well as transgenerational nongenetic and genetic inheritance (From Van Hoppen et al. 2014).

Identifying patterns and processes of how resilient coral species respond to environmental conditions has long been a goal in understanding community response to predicted climate change [94] and also to anthropogenic stressors such as increased sedimentation and terrestrial runoff [95].

Over the last century, humans have driven global climate change through industrialization and the release of increasing amounts of CO_2, resulting in shifts in ocean temperature, ocean chemistry, and sea level, as well as increasing frequency of storms, all of which can profoundly impact marine ecosystems. Ocean acidification (OA), from seawater uptake of anthropogenic CO_2, has a suite of negative effects on the ability of marine invertebrates to produce and maintain their skeletons. OA alters seawater carbonate chemistry, limiting the carbonate available to form the calcium carbonate ($CaCO_3$) minerals used to build skeletons. The reduced saturation state of $CaCO_3$ also causes corrosion of $CaCO_3$ structures. Global change is also accelerating coastal acidification driven by land-run off (e.g., acid soil leachates, tannic acid). Building and maintaining marine biomaterials in the face of changing climate will depend on the balance between calcification and dissolution. Therefore, and integrative morphology/structural-ecomechanics approach is key to understanding how marine biominerals will perform in the face of changing in the complexity of environmental factors.

The effects of ocean acidification (OA) on coral biomineralization have been identified in natural conditions emulating acidification scenarios predicted by the end of the 21st century (e.g., vent systems). Although some resilient corals are capable to adapt to changes in water pH, the combination of stressors may have significant negative effects on coral fitness [96].

Indeed, many interacting natural and anthropogenic stressors, including suspended sediments, nutrients, hypoxia, turbidity, temperature, and pollutants can impair the health and fitness of resident biota (Schulte, 2007). Many studies assessed the vulnerability of corals towards global warming and ocean acidification, while scarce attention until now was posed potential detrimental effects on corals from the exposure to legacy and emerging organic pollutants.

As bioaccumulators, corals can act as markers of human activities, since they can incorporate as particles diverse trace metals and organic pollutants into their skeleton [97]. Therefore, studies aimed to highlight the differences in pollutants accumulation among species, coral compartments, sites, and the effect of the relationship between environmental variables, are crucial to understand the distribution and origins of pollutants and the consequent impacts on coral health. For all the aspects considered above, scleractinian corals represent remarkable tools through which many phenomena of chemical, ecological, biomedical, geological, climatic, and paleontological interest can be investigated [98].

1.4 Research objectives

In effort to contribute to better understanding of similarities and divergences among calcified marine structures and their ecological implications, the studies of this PhD thesis were performed on two different models of calcified structure (otoliths and coral skeletons). The first comes from a vertebrate organism (*Merluccius merluccius*) and the second from invertebrate organisms (zooxanthellate and non-zooxantehllate scleractinian corals). The samples investigated in this thesis have been obtained from several different locations, spacing from Mediterranean Sea (*Merluccius merluccius*, *Balanophyllia europaea*, *Balanophyllia regia*) to Eastern (*Balanophyllia elegans*) and Western Pacific Ocean (*Galaxea fascicularis*, *Acropora millepora*, *Pocillopora damicornis*, massive *Porites*).

This PhD thesis has been divided into 3 sections to focus on:

Section 1. Structure-function relationship in otolith

Aim: investigate the morphology and structural properties of *Merluccius merluccius* otoliths during ontogenesis and between female and male individuals and discuss hypotheses on the possible factors influencing otolith shape, its motion, and thus, ear functioning.

This first section (containing Chapter 2 and 3) provides an integrated view of *Merluccius merluccius*'s saccular otolith characteristics according to fish size and sex, highlighting ontogenetic and sexual differences that can provide clues on different fish habits, physiology, or exposition to environmental factors. Furthermore, in this section new 3D analysis based on micro-CT scans are presented as innovative approaches to obtain from otolith, and from an important structure associated with it (sulcus acusticus), features not previously revealed and measured with the canonical methods based on 2D shape descriptors.

Section 2. Adaptation and acclimatation in coral skeletons

Aims: 1) assess the entity of evolutionary and adaptive driving forces in the skeleton of phylogenetically related coral species of the genus *Balanophyllia;* 2) investigate the response of environmental acidification on four different coral skeleton species in a volcanic CO_2 vent system used as natural laboratories.

The second section (including the Chapters 4-5) presents scleractinian corals as calcified organism model in which investigate coral skeleton plasticity. In the first work, a variety of skeleton parameters are compared in three phylogenetically related coral species of the genus *Balanophyllia* having different trophic strategies. The goal is to assess whether their skeletal features are more strongly influenced by their phylogenetic signals or by adaptative traits established during the long history of

this genus to cope with environmental changes. The second work presented in this session is a multi-species study conducted to document the combinate effects of local environmental conditions and long-term exposure to low pH values on skeletal parameter on four coral species (*Galaxea fascicularis, Acropora millepora, Pocillopora damicornis,* massive *Porites*) acclimatized to high pCO_2 occurring around two CO_2 vents in Papua New Guinea.

Section 3. Bioaccumulation of organic pollutants in corals

Aim: evaluate the sources, the accumulation and potentially effects of organic pollutants in scleractinian corals.

In the third section (Chapter 6), coral organisms are investigated as bioaccumulators and bioindicators of organic pollutants in costal marine ecosystems. The work presented is a study conducted on the zooxanthellate *Balanophyllia europaea* from the Mediterranean Sea, in which is reported 1) the bioaccumulation pattern of polycyclic aromatic hydrocarbons (PAHs) compounds within the three coral biological compartments (tissue, zooxanthellae, and skeleton); 2) the coral age effects on PAH concentration; 3) the capacity of coral skeleton to storage the PAHs in relation to the age structure in a population of *B. europaea*; 4) the use of QuEChERS extraction method as a methodological advancement protocol for quantifying PAHs in corals.

References

1. Gebeshuber IC. 2015 Biomineralization in marine organisms. In Springer Handbook of Marine Biotechnology, (doi:10.1007/978-3-642-53971-8_58)
2. Gilbert PUPA et al. 2022 Biomineralization: Integrating mechanism and evolutionary history. Sci. Adv. 8. (doi:10.1126/sciadv.abl9653)
3. Bentov S, Abehsera S, Sagi A. 2016 The Mineralized Exoskeletons of Crustaceans. In Extracellular Composite Matrices in Arthropods, pp. 137–163. Cham: Springer International Publishing. (doi:10.1007/978-3-319-40740-1_5)
4. Naleway SE, Taylor JRA, Porter MM, Meyers MA, McKittrick J. 2016 Structure and mechanical properties of selected protective systems in marine organisms. Mater. Sci. Eng. C 59, 1143–1167. (doi:10.1016/j.msec.2015.10.033)
5. Gilbert PUPA, Abrecht M, Frazer BH. 2018 The organic-mineral interface in biominerals. In Molecular Geomicrobiology, (doi:10.2138/rmg.2005.59.7)
6. Bengtson S. 2004 Early skeletal fossils. Paleontol. Soc. Pap. 10, 67–78. (doi:10.1017/S1089332600002345)
7. Nikolov S, Petrov M, Lymperakis L, Friák M, Sachs C, Fabritius H-O, Raabe D, Neugebauer J. 2010 Revealing the Design Principles of High-Performance Biological Composites Using Ab initio and Multiscale Simulations: The Example of Lobster Cuticle. Adv. Mater. 22, 519–

526. (doi:10.1002/adma.200902019)

8. Mann S. 2011 Principles and Concepts in Bioinorganic Materials Chemistry. Oxford Univ. Excess Demand

9. COHEN BL. 2005 Not armour, but biomechanics, ecological opportunity and increased fecundity as keys to the origin and expansion of the mineralized benthic metazoan fauna. Biol. J. Linn. Soc. 85, 483–490. (doi:10.1111/j.1095-8312.2005.00507.x)

10. De Yoreo JJ, Dove PM. 2004 Shaping crystals with biomolecules. Science (80-.). (doi:10.1126/science.1100889)

11. Sorauf JE. 2010 Biominerals and fossils through time. (doi:10.1017/CBO9780511781070)

12. Falini G, Albeck S, Weiner S, Addadi L. 1996 Control of aragonite or calcite polymorphism by mollusk shell macromolecules. Science (80-.). (doi:10.1126/science.271.5245.67)

13. Laipnik R, Bissi V, Sun CY, Falini G, Gilbert PUPA, Mass T. 2020 Coral acid rich protein selects vaterite polymorph in vitro. J. Struct. Biol. (doi:10.1016/j.jsb.2019.107431)

14. Belcher AM, Wu XH, Christensen RJ, Hansma PK, Stucky GD, Morse DE. 1996 Control of crystal phase switching and orientation by soluble mollusc-shell proteins. Nature (doi:10.1038/381056a0)

15. Knoll AH. 2003 Biomineralization and Evolutionary History. Rev. Mineral. Geochemistry (doi:10.2113/0540329)

16. Allemand D, Tambutté É, Zoccola D, Tambutté S. 2011 Coral calcification, cells to reefs. In Coral Reefs: An Ecosystem in Transition, (doi:10.1007/978-94-007-0114-4_9)

17. La Barre S, Bates SS. 2018 Marine Biominerals with a Biotechnological Future. In Blue Biotechnology, (doi:10.1002/9783527801718.ch27)

18. Lowenstam H, Weiner S. 1990 On Biomineralization . Heinz A. Lowenstam , Stephen Weiner. J. Geol. 98, 977–977. (doi:10.1086/629466)

19. Stigall AL, Freeman RL, Edwards CT, Rasmussen CMØ. 2020 A multidisciplinary perspective on the Great Ordovician Biodiversification Event and the development of the early Paleozoic world. Palaeogeogr. Palaeoclimatol. Palaeoecol. (doi:10.1016/j.palaeo.2019.109521)

20. Keith ML, Weber JN. 1965 Systematic relationships between carbon and oxygen isotopes in carbonates deposited by modern corals and algae. Science (80-.). (doi:10.1126/science.150.3695.498)

21. Ridgwell A, Zeebe RE. 2005 The role of the global carbonate cycle in the regulation and evolution of the Earth system. Earth Planet. Sci. Lett. (doi:10.1016/j.epsl.2005.03.006)

22. DeCarlo TM, Comeau S, Cornwall CE, Gajdzik L, Guagliardo P, Sadekov A, Thillainath EC, Trotter J, McCulloch MT. 2019 Investigating marine bio-calcification mechanisms in a changing ocean with in vivo and high-resolution ex vivo Raman spectroscopy. Glob. Chang. Biol. (doi:10.1111/gcb.14579)

23. Bengtson S, Morris SC, Cooper BJ, Jell PA, Runnegar BN. 1990 Early Cambrian fossils from South Australia. Mem. - Assoc. Australas. Palaeontol.

24. Pruss SB, Finnegan S, Fischer WW, Knoll AH. 2010 Carbonates in skeleton-poor seas: New

insights from Cambrian and Ordovician strata of Laurentia. Palaios 25, 73–84. (doi:10.2110/palo.2009.p09-101r)

25. Nývlt J. 1995 The Ostwald Rule of Stages. Cryst. Res. Technol. (doi:10.1002/crat.2170300402)

26. Declet A, Reyes E, Suárez OM. 2016 Calcium carbonate precipitation: A review of the carbonate crystallization process and applications in bioinspired composites. Rev. Adv. Mater. Sci.

27. Zhang Z, Xie Y, Xu X, Pan H, Tang R. 2012 Transformation of amorphous calcium carbonate into aragonite. J. Cryst. Growth (doi:10.1016/j.jcrysgro.2012.01.025)

28. Radha A V., Forbes TZ, Killian CE, Gilbert PUPA, Navrotsky A. 2010 Transformation and crystallization energetics of synthetic and biogenic amorphous calcium carbonate. Proc. Natl. Acad. Sci. U. S. A. (doi:10.1073/pnas.1009959107)

29. Pouget EM, Bomans PHH, Goos JACM, Frederik PM, De With G, Sommerdijk NAJM. 2009 The initial stages of template-controlled CaCO3 formation revealed by Cryo-TEM. Science (80-.). (doi:10.1126/science.1169434)

30. Kabalah-Amitai L, Mayzel B, Kauffmann Y, Fitch AN, Bloch L, Gilbert PUPA, Pokroy B. 2013 Vaterite crystals contain two interspersed crystal structures. Science (80-.). (doi:10.1126/science.1232139)

31. Falini G, Fermani S, Gazzano M, Ripamonti A. 2000 Polymorphism and architectural crystal assembly of calcium carbonate in biologically inspired polymeric matrices f. J. Chem. Soc. Dalt. Trans. (doi:10.1039/b003334k)

32. Weiner S, Addadi L. 1997 Design strategies in mineralized biological materials. J. Mater. Chem. (doi:10.1039/a604512j)

33. Dauphin Y, Dufour E. 2008 Nanostructures of the aragonitic otolith of cod (Gadus morhua). Micron (doi:10.1016/j.micron.2007.11.007)

34. Cuif JP, Dauphin Y, Farre B, Nehrke G, Nouet J, Salomé M. 2008 Distribution of sulphated polysaccharides within calcareous biominerals suggests a widely shared two-step crystallization process for the microstructural growth units. Mineral. Mag. (doi:10.1180/minmag.2008.072.1.233)

35. Schulz-Mirbach T, Ladich F, Plath M, Heß M. 2019 Enigmatic ear stones: what we know about the functional role and evolution of fish otoliths. Biol. Rev. 94, 457–482. (doi:10.1111/brv.12463)

36. Popper AN, Ramcharitar J, Campana SE. 2005 Why otoliths? Insights from inner ear physiology and fisheries biology. In Marine and Freshwater Research, (doi:10.1071/MF04267)

37. Popper AN, Platt C. 1983 Sensory surface of the saccule and lagena in the ears of ostariophysan fishes. J. Morphol. 176, 121–129. (doi:10.1002/jmor.1051760202)

38. Popper AN, Fay RR. 1993 Sound Detection and Processing by Fish: Critical Review and Major Research Questions (Part 1 of 2). Brain. Behav. Evol. 41, 14–25. (doi:10.1159/000113821)

39. Hüssy K, Limburg KE, de Pontual H, Thomas ORB, Cook PK, Heimbrand Y, Blass M,

Sturrock AM. 2021 Trace Element Patterns in Otoliths: The Role of Biomineralization. Rev. Fish. Sci. Aquac. 29, 445–477. (doi:10.1080/23308249.2020.1760204)

40. Campana SE, Neilson JD. 1985 Microstructure of Fish Otoliths. Can. J. Fish. Aquat. Sci. 42, 1014–1032. (doi:10.1139/f85-127)

41. Stevenson DK, Campana SE. 1993 Otolith microstructure examination and analysis. ICES J. Mar. Sci. (doi:10.1006/jmsc.1993.1053)

42. Schulz-Mirbach T, Plath M. 2012 All good things come in threes species delimitation through shape analysis of saccular, lagenar and utricular otoliths. Mar. Freshw. Res. (doi:10.1071/MF12132)

43. Popper AN, Hawkins AD. 2019 An overview of fish bioacoustics and the impacts of anthropogenic sounds on fishes. J. Fish Biol. 94, 692–713. (doi:10.1111/jfb.13948)

44. Fay RR, Simmons AM. 1999 The Sense of Hearing in Fishes and Amphibians. (doi:10.1007/978-1-4612-0533-3_7)

45. Putland RL, Montgomery JC, Radford CA. 2019 Ecology of fish hearing. J. Fish Biol. (doi:10.1111/jfb.13867)

46. Popper AN, Hawkins AD, Sand O, Sisneros JA. 2019 Examining the hearing abilities of fishes. J. Acoust. Soc. Am. 146, 948–955. (doi:10.1121/1.5120185)

47. Hawkins AD, Rasmussen KJ. 1978 The calls of gadoid fish. J. Mar. Biol. Assoc. United Kingdom (doi:10.1017/S0025315400056848)

48. Brawn VM. 1961 Sound Production By the Cod (Gadus Callarias L.). Behaviour (doi:10.1163/156853961X00150)

49. Campana SE. 1999 Chemistry and composition of fish otoliths: Pathways, mechanisms and applications. Mar. Ecol. Prog. Ser. (doi:10.3354/meps188263)

50. Popper AN, Hawkins AD. 2018 The importance of particle motion to fishes and invertebrates. J. Acoust. Soc. Am. 143, 470–488. (doi:10.1121/1.5021594)

51. Schulz-Mirbach T, Ladich F. 2016 Diversity of inner ears in fishes: Possible contribution towards hearing improvements and evolutionary considerations. In Advances in Experimental Medicine and Biology, (doi:10.1007/978-3-319-21059-9_16)

52. Gauldie R. 2002 An eco-morphological explanation of individual variability in the shape of the fish otolith: comparison of the otolith of Hoplostethus atlanticus with other species by depth. J. Fish Biol. 60, 1204–1221. (doi:10.1006/jfbi.2002.1938)

53. Capoccioni F, Costa C, Aguzzi J, Menesatti P, Lombarte A, Ciccotti E. 2011 Ontogenetic and environmental effects on otolith shape variability in three Mediterranean European eel (Anguilla anguilla, L.) local stocks. J. Exp. Mar. Bio. Ecol. (doi:10.1016/j.jembe.2010.11.011)

54. Deng X, Wagner HJ, Popper AN. 2013 Interspecific variations of inner ear structure in the deep-sea fish family melamphaidae. Anat. Rec. (doi:10.1002/ar.22703)

55. Schulz-Mirbach T, Heß M, Metscher BD. 2013 Sensory epithelia of the fish inner ear in 3D: Studied with high-resolution contrast enhanced microCT. Front. Zool. 10, 1. (doi:10.1186/1742-9994-10-63)

56. Tuset VM, Lombarte A, Assis CA. 2008 Otolith atlas for the western Mediterranean, north and central eastern Atlantic. Sci. Mar. 72, 7–198.

57. Ramcharitar J, Popper AN. 2004 Masked auditory thresholds in sciaenid fishes: A comparative study. J. Acoust. Soc. Am. 116, 1687–1691. (doi:10.1121/1.1771614)

58. Schulz-Mirbach T, Ladich F, Riesch R, Plath M. 2010 Otolith morphology and hearing abilities in cave- and surface-dwelling ecotypes of the Atlantic molly, Poecilia mexicana (Teleostei: Poeciliidae). Hear. Res. 267, 137–148. (doi:10.1016/j.heares.2010.04.001)

59. Krysl P, Hawkins AD, Schilt C, Cranford TW. 2012 Angular Oscillation of Solid Scatterers in Response to Progressive Planar Acoustic Waves: Do Fish Otoliths Rock? PLoS One 7, e42591. (doi:10.1371/journal.pone.0042591)

60. De Vries H. 1950 The mechanics of the labyrinth otoliths. Acta Otolaryngol. (doi:10.3109/00016485009118384)

61. Lychakov D V, Redbane YT. 1993 Effect of otolith shape on directional sound perception in fish. J. Evol. Biochem. Physiol. 28, 707–714. (doi:10.1016/j.heares.2006.03.019)

62. Lychakov DV, Rebane YT. 2005 Fish otolith mass asymmetry: morphometry and influence on acoustic functionality. Hear. Res. 201, 55–69. (doi:10.1016/j.heares.2004.08.017)

63. Lychakov DV, Rebane YT, Lombarte A, Fuiman LA, Takabayashi A. 2006 Fish otolith asymmetry: Morphometry and modeling. Hear. Res. 219, 1–11. (doi:10.1016/j.heares.2006.03.019)

64. Schulz-Mirbach T, Olbinado M, Rack A, Mittone A, Bravin A, Melzer RR, Ladich F, Heß M. 2018 In-situ visualization of sound-induced otolith motion using hard X-ray phase contrast imaging. Sci. Rep. 8, 1–12. (doi:10.1038/s41598-018-21367-0)

65. Sand O, Michelsen A. 1978 Vibration measurements of the perch saccular otolith. J. Comp. Physiol. ? A 123, 85–89. (doi:10.1007/BF00657346)

66. Lombarte A, Olaso I, Bozzano A. 2003 Ecomorphological trends in the Artedidraconidae (Pisces: Perciformes: Notothenioidei) of the Weddell Sea. Antarct. Sci. 15, 211–218. (doi:10.1017/S0954102003001196)

67. Lombarte A, Palmer M, Matallanas J, Gómez-Zurita J, Morales-Nin B. 2010 Ecomorphological trends and phylogenetic inertia of otolith sagittae in Nototheniidae. Environ. Biol. Fishes 89, 607–618. (doi:10.1007/s10641-010-9673-2)

68. Tuset VM et al. 2016 Otolith shape lends support to the sensory drive hypothesis in rockfishes. J. Evol. Biol. (doi:10.1111/jeb.12932)

69. Taylor MD, Fowler AM, Suthers IM. 2020 Insights into fish auditory structure–function relationships from morphological and behavioural ontogeny in a maturing sciaenid. Mar. Biol. 167, 21. (doi:10.1007/s00227-019-3619-9)

70. Drake JL, Mass T, Stolarski J, Von Euw S, Schootbrugge B, Falkowski PG. 2020 How corals made rocks through the ages. Glob. Chang. Biol. 26, 31–53. (doi:10.1111/gcb.14912)

71. Coronado I, Fine M, Bosellini FR, Stolarski J. 2019 Impact of ocean acidification on crystallographic vital effect of the coral skeleton. Nat. Commun. (doi:10.1038/s41467-019-10833-6)

72. Tambutté S, Holcomb M, Ferrier-Pagès C, Reynaud S, Tambutté É, Zoccola D, Allemand D.

2011 Coral biomineralization: From the gene to the environment. J. Exp. Mar. Bio. Ecol. 408, 58–78. (doi:10.1016/j.jembe.2011.07.026)

73. Veron JEN. 1995 Corals in Space and Time: The Biogeography and Evolution of the Scleractinia. Ed. Cornell Univ. Press

74. Connell JH. 1978 Diversity in tropical rain forests and coral reefs. Science (80-.). (doi:10.1126/science.199.4335.1302)

75. Wafar M, Venkataraman K, Ingole B, Ajmal Khan S, LokaBharathi P. 2011 State of Knowledge of Coastal and Marine Biodiversity of Indian Ocean Countries. PLoS One 6, e14613. (doi:10.1371/journal.pone.0014613)

76. Cooper EL, Hirabayashi K, Strychar KB, Sammarco PW. 2014 Corals and their potential applications to integrative medicine. Evidence-based Complement. Altern. Med. (doi:10.1155/2014/184959)

77. Robinson LF, Adkins JF, Frank N, Gagnon AC, Prouty NG, Brendan Roark E, de Flierdt T van. 2014 The geochemistry of deep-sea coral skeletons: A review of vital effects and applications for palaeoceanography. Deep. Res. Part II Top. Stud. Oceanogr. (doi:10.1016/j.dsr2.2013.06.005)

78. Tornabene C, Martindale RC, Wang XT, Schaller MF. 2017 Detecting Photosymbiosis in Fossil Scleractinian Corals. Sci. Rep. (doi:10.1038/s41598-017-09008-4)

79. Stanley G, van de Schootbrugge B. 2018 The Evolution of the Coral–Algal Symbiosis and Coral Bleaching in the Geologic Past. pp. 9–26. (doi:10.1007/978-3-319-75393-5_2)

80. Muscatine L, Weis V. 1992 Productivity of Zooxanthellae and Biogeochemical Cycles. In Primary Productivity and Biogeochemical Cycles in the Sea, (doi:10.1007/978-1-4899-0762-2_14)

81. Allemand D, Ferrier-Pagès C, Furla P, Houlbrèque F, Puverel S, Reynaud S, Tambutté É, Tambutté S, Zoccola D. 2004 Biomineralisation in reef-building corals: From molecular mechanisms to environmental control. Comptes Rendus - Palevol (doi:10.1016/j.crpv.2004.07.011)

82. Enríquez S, Méndez ER, Iglesias-Prieto R. 2005 Multiple scattering on coral skeletons enhances light absorption by symbiotic algae. Limnol. Oceanogr. (doi:10.4319/lo.2005.50.4.1025)

83. Rodríguez-Román A, Hernández-Pech X, Thomé PE, Enríquez S, Iglesias-Prieto R. 2006 Photosynthesis and light utilization in the Caribbean coral Montastraea faveolata recovering from a bleaching event. Limnol. Oceanogr. (doi:10.4319/lo.2006.51.6.2702)

84. Hennige S, Smith D, Perkins R, Consalvey M, Paterson D, Suggett D. 2008 Photoacclimation, growth and distribution of massive coral species in clear and turbid waters. Mar. Ecol. Prog. Ser. 369, 77–88. (doi:10.3354/meps07612)

85. Ow YX, Todd PA. 2010 Light-induced morphological plasticity in the scleractinian coral Goniastrea pectinata and its functional significance. Coral Reefs (doi:10.1007/s00338-010-0631-4)

86. Loya Y, Sakai K, Yamazato K, Nakano Y, Sambali H, Van Woesik R. 2001 Coral bleaching: The winners and the losers. Ecol. Lett. (doi:10.1046/j.1461-0248.2001.00203.x)

87. Anthony KRN, Hoogenboom MO, Connolly SR. 2005 Adaptive variation in coral geometry and the optimization of internal colony light climates. Funct. Ecol. (doi:10.1111/j.0269-8463.2005.00925.x)

88. Klaus JS, Budd AF, Heikoop JM, Fouke BW. 2007 Environmental controls on corallite morphology in the reef coral Montastraea annularis. Bull. Mar. Sci.

89. Fantazzini P et al. 2015 Gains and losses of coral skeletal porosity changes with ocean acidification acclimation. Nat. Commun. 6, 7785. (doi:10.1038/ncomms8785)

90. Todd PA. 2008 Morphological plasticity in scleractinian corals. Biol. Rev. 83, 315–337. (doi:10.1111/j.1469-185X.2008.00045.x)

91. Zoccola D, Moya A, Béranger GE, Tambutté E, Allemand D, Carle GF, Tambutté S. 2009 Specific expression of BMP2/4 ortholog in biomineralizing tissues of corals and action on mouse BMP receptor. Mar. Biotechnol. (doi:10.1007/s10126-008-9141-6)

92. Van Oppen MJH, Oliver JK, Putnam HM, Gates RD. 2015 Building coral reef resilience through assisted evolution. Proc. Natl. Acad. Sci. U. S. A. (doi:10.1073/pnas.1422301112)

93. Boyko A, Kovalchuk I. 2011 Genetic and epigenetic effects of plant-pathogen interactions: An evolutionary perspective. Mol. Plant. (doi:10.1093/mp/ssr022)

94. Guinotte JM, Buddemeier RW, Kleypas JA. 2003 Future coral reef habitat marginality: Temporal and spatial effects of climate change in the Pacific basin. In Coral Reefs, (doi:10.1007/s00338-003-0331-4)

95. Fabricius KE. 2005 Effects of terrestrial runoff on the ecology of corals and coral reefs: Review and synthesis. Mar. Pollut. Bull. (doi:10.1016/j.marpolbul.2004.11.028)

96. Prada F et al. 2017 Ocean warming and acidification synergistically increase coral mortality. Sci. Rep. (doi:10.1038/srep40842)

97. Ranjbar Jafarabadi A, Riyahi Bakhtiari A, Aliabadian M, Laetitia H, Shadmehri Toosi A, Yap CK. 2018 First report of bioaccumulation and bioconcentration of aliphatic hydrocarbons (AHs) and persistent organic pollutants (PAHs, PCBs and PCNs) and their effects on alcyonacea and scleractinian corals and their endosymbiotic algae from the Persian Gulf, Iran. Sci. Total Environ. (doi:10.1016/j.scitotenv.2018.01.185)

98. Cohen AL. 2003 Geochemical Perspectives on Coral Mineralization. Rev. Mineral. Geochemistry (doi:10.2113/0540151)

Section 1. Structure-function relationship in otolith

− The fate and behaviour of an organism are directly linked to its perception of the environment. −

This section investigates the morphology and structural properties of *Merluccius merluccius* otoliths and discuss hypotheses on the possible factors influencing otolith shape, its motion, and thus ear functioning.

Chapter 2. Multi-scale analysis on otolith structural features reveals differences in ontogenesis and sex in the *Merluccius merluccius* in the western Adriatic Sea

(Published in Royal Society Open Science)

Multiscale analysis on otolith structural features reveals differences in ontogenesis and sex in *Merluccius merluccius* in the western Adriatic

Quinzia Palazzo[1,7], Marco Stagioni[2], Steven Raaijmakers[3], Robert G. Belleman[3], Fiorella Prada[4,7], Jörg U. Hammel[5], Simona Fermani[1,6], Jaap Kaandorp[3,*], Stefano Goffredo[4,7,*], Giuseppe Falini[1,7,*]

[1] Department of Chemistry "Giacomo Ciamician", University of Bologna, Via Selmi 2, 40126 Bologna, Italy

[2] Laboratory of Fisheries and Marine Biology at Fano, Department of Biological, Geological and Environmental Sciences, University of Bologna, Viale Adriatico 1/N, 61032, Fano, Italy

[3] Computational Science Lab, University of Amsterdam, Science Park 904, 1098XH, Amsterdam, the Netherlands

[4] Marine Science Group, Department of Biological, Geological and Environmental Sciences, University of Bologna, Via Selmi 3, 40126 Bologna, Italy

[5] Institute of Materials Physics, Helmholtz-Zentrum Hereon, Max-Planck-Straße 1, Geesthacht, D-21502, Germany

[6] CIRI Health Sciences & Technologies (HST), University of Bologna, I-40064 Bologna, Italy

[7] Fano Marine Center, The Inter-Institute Center for Research on Marine Biodiversity, Resources and Biotechnologies, Viale Adriatico 1/N 61032 Fano, Italy

* corresponding authors: Jaap Kaandorp, J.A.Kaandorp@uva.nl;
Stefano Goffredo, s.goffredo@unibo.it; Giuseppe Falini, giuseppe.falini@unibo.it

ABSTRACT

Otolith biomineralization results from biochemical processes regulated by the interaction of internal (physiological) and external (environmental) factors which lead to morphological and ultrastructural variability at intra- and inter-specific levels. The aim of this study was to conduct a multi-scale analysis of the sagittal otoliths of the *Merlucius merlucius* (European Hake) from the wester Adriatic Sea in order to correlate otolith features with fish ontogeny and sex. We show that otoliths of sexually undifferentiated (non-sexed) individuals having a fish body total length (TL) < 15 cm had faster growth in length, width, area, perimeter, volume, and weight and a higher amount of organic matrix compared to otoliths of sexually differentiated individuals (females and males) having a fish size range of 15-50 cm. Most importantly, with increasing fish TL, female saccular otoliths contained higher number of protuberances and rougher surface compared to male specimens which showed more uniform mean curvature density. The differences between females and males discovered in this study could be associated with fish hearing adaptation to reproductive behavioral strategies during the spawning season. The outcomes of this research provide insights on how size and sex related variations in otolith features may be affected by fish ecological and behavioral patterns.

Keywords: *Merluccius merluccius*, Adriatic Sea, ecomorphology, micro-CT scanning, functional morphology, sagitta

INTRODUCTION

Otoliths, or ear stones, are three dense paired calcium carbonate (CaCO3) structures within a proteinaceous matrix, contained in three chambers associated with the inner ear of teleosts [1]. Otoliths act as mechanoreceptors involved in hearing through the detection of particle motion [2,3]. The size and shape of otoliths likely influence the frequencies that can be detected and the sensitivity (auditory threshold) to those frequencies [4]. Thus, the wide variability in ear morphologies and otoliths of fishes is likely linked to the diversity in hearing mechanisms and capabilities among different species [2]. Otoliths form during embryo development and continue to grow in incremental layers of CaCO3 in an organic matrix [5]. Consequently, otolith structure can also vary substantially during fish growth [6] in response to both physiological and ecological ontogenetic changes, and/or to differences in the acoustic environment related to diverse habitats occupied by juveniles and adults. Indeed, otoliths record the specifics of the physicochemical environment experienced by a fish at any given point in its life and also provide information about its physiology related to ontogeny and feeding [7,8]. However, to date only few investigations have focused on the relation between the morphological and ultrastructural differences of otoliths and the ecomorphological adaptations of the auditory system to habitat features such as water depth, feeding modalities, spatial niches and mobility [5,9–11].

The European hake (*Merluccius merluccius*) is a major component of the demersal fish assemblages and is distributed over a wide depth range (20 −1000 m) throughout the Mediterranean Sea and the northeast Atlantic region [12]. The hake is an important predator of deeper shelf-upper slope Mediterranean communities. Previous studies, which were also conducted by experimental trawl surveys carried out in the Mediterranean [13], have observed a different bathymetric distribution during the ontogenesis of this species, while no differences were highlighted between females and males [14–16]. Juveniles' hakes are mostly found around 170 –220 m depth, intermediate hakes reach the highest abundance mainly on the continental shelf with a preference for shallower depths (70 –100 m), especially when they reach 18 – 20 cm length [14,15,17]. Large hakes (>36 cm) are found in a wide depth range but concentrate on the shelf break during the spawning period. Migration of juvenile hake from nursery areas on the shelf break and upper slope to the mid-shelf [17] is induced by a change in trophic requirements [18]. During its early life, the hake feeds on small crustaceans (Euphausiacea), where shrimp are among the most common preys in the muddy bottom communities of the Mediterranean Sea [15]. Subsequently, juvenile hakes mi-grate from the nursery areas to the parental stock, and when they reach a total length between 18 and 32 cm, they gradually change their diet towards pelagic and necto-benthic fish such as *Sardina*

pilchardus and *Engraulis encrasicolus* [15,16]. These preys inhabit the coastal continental shelf and form schools usually deeper than 25 m [12]. Moreover, such trophic shifts coincide with an increase in the area of the inner ear of hake responsible for the detection and localization of objects, which takes place approximately at the critical size of 14 –15 cm and could be important in detecting mobile prey such as fish [19]. Indeed, although hakes are demersal fishes, they feed typically upon fast moving pelagic prey caught in mid-water or near the surface at night, undertaking daily vertical migrations [20,21]. Growth induces a continuous qualitative and quantitative change in diet that is reflected in the increasing mean weight of prey [15]. The shift towards large fish prey usually occurs slightly before maturity, the life history stage with much higher energetic demands due to gonadal development [22]. Thus, increased energy demands related to sexual requirements, gonadal development, and breeding activity appear to be the critical factors driving the changes in feeding strategy of *Merluccius merluccius*. Furthermore, in large hakes (> 36 cm), also cannibalism has been observed, likely in response to a great accessibility of conspecifics in the same area [23]. Nevertheless, most of the literature reports no difference in feeding habits be-tween females and males [15,24].

The hake *M. merluccius* should be capable of vocalizing, as highlighted by the presence of paired drumming muscles for sound production located at the anterior wall of the swim bladder, similar to those found in known vocalists [25]. The same study also observed a sexual dimorphism in the drumming muscles during the spawning period of this species. In fact, only the drumming muscles from males are hypertrophied, while in females this effect is not observed, suggesting that adult males may increase the vocalizations in the context of spawning, like the males of other previous-ly studied gadoids [25].

This multi-scale study investigated the sagittal otoliths characteristics of the *M. merluccius* from the central western Adriatic Sea. The first hypothesis is that different habitat distribution and feeding habits during the ontogenesis can leave a fingerprint in otolith characteristics that might provide clues related to hearing eco-functional adaptations to different environments and/or ecology during hake growth. To provide knowledge that could help in unravelling the challenging is-sue of "how sagitta morphology and structure varies regarding fish's ecological features and life-style (e.g., bathymetric distribution, habitat, feeding strategy and mobility pattern)?" we per-formed an integrated comparison analysis of the morphometry, morphology and structure of otolith of sexually undifferentiated individuals (having gonads not macroscopically distinguishable and fish total length (fish TL) below the critical size of 15 cm) with data of sexually differentiated fishes (female or male with a size > 15 cm).

The second hypothesis concerns the sex-specific developmental pattern of the drumming muscles during

the spawning season of hake previously seen in another study, which probably reflect different sound production associated to the calls in the reproductive behavior of male respect female [25]. Consequently, it is reasonable to think that females exhibit auditory features capable of detecting the advertisement calls of males, since acoustic communication may play a crucial role in reproductive interactions [26]. Furthermore, the otolith features have an important role in fish hearing capabilities and in particular, the morphology of otoliths is known to bring a functional significance. Although recent studies have focused in understanding the relationship between otolith features (e.g., biometry, morphology, density) and fish response to acoustic signals, [27–31], little is still known about the shape/structure-dependent otolith motion in response to harmonic waves. Therefore, it is interesting to compare otolith characteristics between conspecific which share the same ecological context in order to exclude the otolith shape heterogeneity that can be determined by environmental, or/and ecological difference. In the context of the species investigated in this study, we performed an accurate description of the sagittae for sexually differentiated individuals (females vs males) to assess whether exist differences in otolith characteristics which could be related to hearing adaptation associated with acoustic communication in context of spawning.

The aims of this study were to: i) correlate the morphometry (using 2D image scanning pro-grams), morphologic (by 2D image scanning programs shape descriptors and micro-CT scans analysis), structural (through porosimetry technique) and compositional (X ray diffraction, thermogravimetric analysis and spectroscopy) otolith features with fish ontogeny and sex, ii) verify whether there are any differences among undifferentiated, female and male otoliths which could be related to hearing adaptations to different habitats or behavioural contexts, iii) provide a new micro-CT scan based approach developed using Python in combination with Visualization Toolkit libraries to investigate otolith shape curvature and perimetral irregularities (protuberances) dis-playing features not revealed with the canonical methods based on 2D images.

MATERIALS AND METHODS

Otolith biometry, 2D contour, 3D shapes, density, and porosity, mineralogic composition, organic matrix content and incorporated elements were assessed. Furthermore, a new approach was developed to investigate the overall curvature of otolith surface and to detect and count the protuberances of the contours based on micro-CT scans, providing a methodological advancement towards the establishment

of a reproducible, accurate, and manual error-free measurement of 3D otolith shapes. *M. merluccius* was selected for the study for the following reasons: i) it is a widely distributed, commercially important species in Mediterranean Sea; ii) otolith extraction is easier compared to other species, iii) otolith data from other geographic areas in the Mediterranean Sea are available, and iv) it is a target species in which different methodologies have been applied, v) ecological and behavioural characteristics during ontogenesis and sexes make this species suitable to test adaptation to different habitat.

Sample collection

A total of 210 *M. merluccius* (61 non-sexed and 149 sexed) were collected from commercial catch, by benthic trawlers, longlines and gillnets, on May 2018 in the western Adriatic Sea, off the San Benedetto del Tronto coast (N 42° 52' 6.056" E 14° 33' 43.29", fig. S1). In the Mediterranean Sea, *M. merluccius* has three genetic clusters corresponding to the western, central and eastern Mediterranean populations [20,32,33]. Previous genetic studies based on molecular markers have not consistently defined a subdivision within western Adriatic hake stocks [34,35], therefore the samples used in this study were considered as belonging to the same fishing stocks.

For each specimen, fish total length (TL ± 1 cm) and weight (TW ± 1 g) were measured, and a macroscopic inspection of gonads was conducted to sex the fish. Sex categories were based on the sex maturity codes used by MEDITS-Handbook (2017) [36]. Undifferentiated or non-sexed fish showed inactive gonads. These fish are commonly referred to as juveniles [37] with less than 15 cm TL. Differentiated or sexed fish were 66 males (M) and 83 females (F) showing developed gonads and a body length greater than 15 cm TL.

Both sagittal otoliths were manually removed making a transverse cut with knife from the dorsal side of the fish head deep enough to reach the otic capsule. Then the head was flexed as if hinged near the snout, exposing the otic capsule and the otoliths which were then removed using forceps, cleaned from tissue with 3% H2O2 for 15 min and then washed with Milli-Q water, dried and stored inside Eppendorf microtubes. For the following analysis, the right otoliths were arbitrarily chosen since no scientific evidence suggests a side dimorphism in otoliths in this species [38].

Otolith biometry, morphology, and structural parameters

Fish of a body range length of 6.9 to 45. 5 cm TL were included in the 210 otolith analyses based on digital images. These images were taken from a DCM 500 usb 2.0 5 MP linked to a Wild Heerbrugg

M5A Microscope. However, only 148 images of otoliths (40 non-sexed fish, 61 females and 47 males) were used to calculate structural parameters by buoyant weight. The relationships of otolith parameters with fish TL were determined for undifferentiated, females, males and for all the individuals combined (tables S1-S2). Details on biometry, morphology, and structural parameters are provided in the supporting information.

Otolith composition

For the mineral characterization of the samples analyses were conducted by X-ray powder Diffraction (XRD) and Fourier Transform Infrared Spectroscopy (FTIR). The otolith organic matrix and water content was assessed by thermogravimetric analysis (TGA) performed on powdered samples.

For the XRD analyses the air-dried samples were ground in a mortar to obtain a fine and homogeneous powder (grains smaller than 100 µm) that was then loaded on a low background silica holder. XRD analyses were performed on 34 otoliths (8 undifferentiated, 13 females and 13 males) using a PANanalytical X'Pert Pro powder diffractometer equipped with X'Celerator detector (fig. S3).

Fourier transform infrared spectroscopic (FTIR) analyses were conducted on samples previously used for the diffractometric analysis, by using a Nicolet FTIR 380 spectrometer working in the range of wavenumbers 4000-400 cm-1 at a resolution of 2 cm-1. This technique was used to confirm the X-ray powder diffraction data.

An estimation of the organic matter content for 35 powered samples (9 undifferentiated, 14 females and 12 males) was performed by thermogravimetric analysis (TGA) on a SDT Q600 simultaneous thermal analysis instrument (TA Instruments, fig. S4) Details on the XRD, FTIR and TGA procedures are provided in the supporting information.

Analysis of otolith microchemistry

Elemental analyses were conducted on powdered samples of 6 undifferentiated, 9 females and 9 males using induced coupling plasma optical emission spectroscopy (ICP OES). The analyses were performed on otoliths previously treated to remove surface contamination. Details are provided in the supporting material.

Morphological analysis on 3D reconstruction of otoliths based on microcomputed tomography imaging

To investigate the 3D shape of a subset of 24 otolith samples, high resolution microcomputed tomography (Micro-CT) scans were acquired with a GE phoenix X-ray Nanotom S (fig. S5). The dataset consisted of 6 immature individuals and 18 adult samples, split in 9 females and 9 males having the same fish TL, in order to remove the impact of the different fish body size units and avoiding the standardization step. The isotropic voxel sizes in the scans varied from 2.024 to 8.333 µm depending on the actual size of the investigated otolith sample. Details on the procedure are extensively reported in the supporting material.

Statistical analysis

The relationships between otolith parameters (length, OL; width, OW; perimeter, OP; area, OA; circularity, OC; aspect ratio, OAR; roundness, OR; solidity, OS; volume, OV; weight, Oweight; micro-density, Omicro; bulk density, Obulk; porosity, Oporo; organic matrix, OM%) and TL were determined for undifferentiated, females, males and for all the individuals combined [39]. The best fits with the data to describe the relationships between otolith variables and fish somatic growth was first evaluated by curve estimation regression for 3 different curve models (linear, power and exponential, table S3). When the best fitting was defined with non-linear functions (power or exponential models) $y = ax^b$ or $y = ae^{bx}$, "y" is the otolith parameter, "x" is fish length, "a" is the factor, and "b" is the exponent. The parameters "a" and "b" were estimated through the linear regression analysis on log-transformed data: $\log(y) = \log(a) + b \log(x)$ (for power models) and $\log(y) = \log(a) + bx$ (for exponential model). The relationships between otolith parameters and fish size were determined first for the entire group of individuals and then separately for undifferentiated, females and males, so that four growth curves were derived for each parameter (tables 1, S4). The significance of the correlation was verified using Pearson's correlation coefficient. The statistical differences in regression slopes among groups were examined using a double approach to strengthen the analyses: comparing the confidence intervals of regression coefficients and checking the slopes of regression relationships through the analysis of covariance (ANCOVA). Post hoc tests after ANCOVA provided specific information on which regression lines were significantly different from each other in slope (table 1). Finally, principal component analysis (PCA) based on correlation matrix between groups were used to identify which otolithic biometric (length, width, perimeter), morphologic (circularity, aspect ratio, roundness, solidity, area) and structural (micro-density, porosity, bulk density, organic matrix content and initial temperature of degradation of $CaCO_3$) parameters among the three otolith groups (undifferentiated, female, and male) were more related to each other (fig. S11).

Statistical analyses were performed using SPSS 20.0 and PAST 3 software.

RESULTS

Otolith biometry, morphology, and structural parameters

Curve regression analyses (linear, power and exponential) were performed for testing the best fitting model for describing the general relationship for each dependent variable (parameters) with fish TL (table S3 and S4).

The results of the relationships between otolith length, width, area with fish TL among the three fish's groups showed differences (ANCOVA) between non-sexed and differentiated fishes, while no differences were highlighted between the females and males (table 1). The regression coefficients of undifferentiated fishes were significantly higher compared to males and females' ones. There was significant difference in otolith perimeter-fish TL relationship among the three groups with a higher value of the regression coefficient in undifferentiated, followed by females and lastly the males one.

Furthermore, the relation between otolith area and otolith perimeter showed a higher value of the regression coefficients in females samples respect males (table 1). For the circularity index, the correlation analysis with TL was significant only for undifferentiated and females and didn't show differences in the regression coefficient between these two groups. The correlation analyses of the aspect ratio and roundness with fish TL were significant only in female. Concerning the solidity shape index, the correlation analysis was significant in females and males and the Post Hoc didn't show differences in the regression slopes between the two sex categories. The relationships between otolith volume with fish TL showed that the regression coefficients of undifferentiated fishes were significantly higher compared to males and females' ones, while no differences were highlighted between the sexes (table 1).

Concerning the otolith structural parameters (micro-density, bulk density, and porosity), otolith micro-density increased with increasing fish TL, from 2.64 g cm^{-3} at fish TL of 13.5 cm to 2.82 g cm^{-3} in individuals of 44.6 cm (tables 2, S4, fig. S6). Also, bulk density correlated positively with fish size, while porosity showed an opposite trend (tables S4, fig. S6). The bulk density correlated negatively with porosity while micro-density was positively correlated with bulk density (fig. S7).

The content of organic matrix (OM wt%) decreased as fish TL increased (fig. S8; tables 2, S4). Furthermore, a negative correlation between organic matrix content and both bulk density and micro

density was observed (fig. S9). The TGA profiles of most of the otolith samples contained two or three events with weight loss in the temperature range 130°C to 460°C (fig. S4). The initial temperature of decarbonation of $CaCO_3$ is also reported (fig. S8; table 2) and there was a shift toward lower initial decarboxylation temperatures with increasing fish TL. No differences in otolith composition (100% aragonite) were found in undifferentiated, females and males (fig. S3). However, the measure of FWHM values from the diffraction patterns showed a change in crystallite size with fish TL, with the presence of smaller crystallites in undifferentiated than in differentiated fishes (fig. S10).

Biplots of the principal component analysis (PCA) on the correlation matrix between the three groups representing the undifferentiated, female, and male otolith categories of the *M. merluccius* individuals are given in fig. S11. The first two axes (PC1 and PC2) of the PCA plots (fig. S11) showed a partial separation of otolith between the three groups representing the undifferentiated, female, and male otolith categories of the *M. merluccius* individuals investigated. In particular, PC1 (fig. S11 a: ~ 84%, b: 79%, c: ~78%) separated the undifferentiated from differentiated through the otolith variables of length, width, area, perimeter, solidity, porosity, organic matrix content (OM%) and T° of CaCO3 decarbonation. Whereas PC2 slightly separated undifferentiated and males (which showed a wider overlapping area) otolith circularity, aspect ratio, bulk-density parameters from females (a:16%, b: ~21%, c: ~22%).

Analysis of otolith microchemistry

In four over six undifferentiated samples the concentration of trace elements resulted under the detection limits of the instrument not allowing the statistical analysis (table S5). For 9 females and 9 males otoliths the concentration of twelve trace elements (Ba, Ca, Co, K, Li, Mg, Mn, Na, P, S, Sr and Zn) are reported in absolute concentrations (µg/g, table S6) and normalised to Ca (µmol/mol, table S7). Statistical analyses were conducted for each element but didn't reveal any differences in the quantitative analysis (ANOVA, $p > 0.05$, table S6). Differently, the metal:Ca molar ratio values showed a significant difference in K/Ca and Na/Ca between sex (ANOVA, $p < 0.05$, table S7). Moreover, a unique pool of individuals was then taken in account in this analysis (females + males; fig. S12). For all the elements, except K/Ca, Mn/Ca and Na/Ca, a negative correlation between the element and fish TL was observed, with a higher concentration of these elements in smaller adult sizes (fig. S12).

Morphological analysis on 3D reconstruction of otoliths based on microcomputed tomography imaging

The otolith 3D reconstructions based on micro-CT imaging (fig. 1, S5) of non-sexed fishes showed fewer perimetric irregularities, no prominent branching-like protuberances, and a flat shape from the lateral view (fig. 1, S5). Instead, otoliths of sexed fishes showed a more elaborate structure, with a high number of irregularities on both the internal and external surfaces (fig. 1, S5). The curvature of the internal face tended to become more pronounced as the length of the fish increased, assuming an evident convex shape for the older samples (fig. S5). The number of otolith protuberances increased as fish grew (fig. 2) and between females and males of equal fish TL the number of detected otolith protuberances was consistently higher for females. Peaks in the distribution H (mean curvature) - acquired via kernel density estimations (KDE) - for male otoliths were higher than those in females (fig. 2). The peakedness (third moment of the density curve) decreased from top to bottom (less peaked shape) in female otoliths as fish grew (fig. S13).

DISCUSSION

The study of eco-functional modifications in relation to changes in otolith features during fish growth is still at its infancy. In this study, we provided regression models describing the ontogenetic variation in otolith biometry, morphology, structural parameters (i.e., micro-density, bulk density, porosity, organic matrix content, crystallite size) and elemental composition of representative otolith samples from non-sexed and differentiated fishes of size range between 6.9 - 45.5 cm fish TL.

Under a same increase in fish TL, undifferentiated individuals (6.9 cm < TL <15.0 cm) had a more pronounced increase in otolith length, width, and perimeter compared to differentiated ones. We observed a higher concentration of organic matrix in otoliths of undifferentiated fishes compared to differentiated ones, which could explain the higher growth rates observed in the former compared to the latter. Indeed, the organic matrix contains various organic compounds (e.g., proteins, amino acids, collagens, proteoglycans) which are known to guide temporally and spatially the biomineralization process controlling and promoting the crystallites nucleation, orientation and growth [40–42]. Furthermore, the number of touching branch-like structures (referred to as protuberances) increased with fish TL. These differences suggest a heterogeneous distribution of the organic matrix, which can reflect a non-homogeneous deposition of $CaCO_3$ along the surface of the otolith during fish growth [43]. Previous investigations performed on other species showed a decrease in otolith organic matrix content during fish ontogenesis and reported that the decrease in organic matrix content could be related to the

change in trophic strategies [44,45]. Accordingly, the reduction in organic matrix content with fish growth, could be related to 1) changes in feeding strategies and diet that occur during the life cycle of *M. merluccius* [8], 2) reduction in feeding rates associated with energy demanding processes (e.g., sexual maturation and spawning) which could affect the biosynthesis of organic matrix macromolecules and their entrapment within the growing biomineral [46]. Since the mineralogic investigations have revealed uniform compositions ($CaCO_3$ in aragonite form) regardless of fish TL, the decrease in otolith organic matrix with fish size could also explain the increase in micro-density from undifferentiated to differentiated fishes as the organic matrix has a lower density compared to aragonite [47]. Bulk density also increased with fish size, likely as the combination of increased micro-density and decreased apparent porosity. The ontogenetic variations in otolith biometric, morphological, structural, and compositional parameters were also confirmed by the PCA analysis on the correlation matrix among the three otolith categories. Variations in otolith shape and structure during the ontogenesis can be associated with differences in terms of sound detections (structure-function relationship). The micromechanics of the tensors associated masses (excrescences, roughness, furrows) of otolith shape and the otolith density may influence the acoustic stimulation and consequently, modify the hearing capabilities in relation to fish size [27,30,48]. Otolith crystalline features also changed with fish size. Earlier studies have shown that the time-dependent distribution of a protein involved in the formation of otoliths (Starmaker-like protein) can have a significant effect on the crystallite size of growing crystals [42]. Therefore, the increment in aragonite crystallite size during otolith growth observed in *M. merluccius* could depend on variations in organic matrix composition [42]. Concerning otolith microchemistry, most of the investigated trace elements (element:Ca molar ratio) showed a negative correlation with fish size (Ba, Co, Li, Mg, P, S, Sr, Zn) which could depend on: 1) different water chemistry associated with water depth (Sr and Ba) [49], probably related to fish migration, and consequently 2) shift in dietary sources (S) [50], and 3) ontogenetic changes of the organic matrix content (P and Zn) [51]. Although most of the ontogenetic changes in otolith morphology and structure highlighted in *M. merluccius* could be the result of ecological adaptations to different habitats and/or trophic strategies, further acoustic and ecological studies must be carried out to assess the relations of structure-functionality associated with our observations.

Micro-CT imaging analysis resulted as a valuable approach to detect otolith protuberances and to quantify the amount of overall surface curvatures (ripples) of *M. merluccius* otoliths. The integration of the use of regression analysis of 2D shape descriptors with a new method designated to analyse the otolith

3D curvature from micro-CT images revealed for the first time a sexual dimorphism in the shape of sagittal otoliths in *M. merluccius*. Under a same increase in otolith area, females showed a higher increase in perimeter than males. The indices of circularity, roundness and aspect ratio with fish TL showed a higher amount of irregularities (dentate protuberances) in the contour and a more elliptical shape in otoliths from females compared to males. The morphological results obtained by the canonical 2D image scanning programs were also corroborated by computational analyses based on micro-CT scans which highlighted the presence of a higher number of protuberances in the otolith of females in comparison to males of equal fish TL. In addition, the comparison of distribution plots by kernel density estimation (KDE) for H (mean curvature) on the otoliths surface of males and females of equal fish length showed that the peaks of male otoliths were consistently higher than its female counterparts. Consequently, the H values on otoliths were more uniform for males indicating smoother surfaces respect female, which instead were characterized by more wrinkled surfaces. Since no evidence of a spatial segregation between sexes has been reported so far [14–16], female and male fishes likely cohabit the same environment and are subject to the same exogenous factors. Therefore, the otolith shape dimorphism is probably less related to environmental factors and likely more influenced by genetically and physiologically controlled factors [6,52]. The differences highlighted between male and female otolith shapes may have a functional meaning linked to the sexual dimorphism of sound-generating muscles (drumming muscles) previously observed in this species [25]. Nonetheless, further studies aiming to establish the shape/structure–function relationships in otoliths are needed to confirm the hypothesis of an adaptive role in female's otolith related to the perception of male calls in the spawning context.

CONCLUSIONS

This study reports variations in otolith shape, morphology, structure, and composition during hake (*M. merluccius*) ontogenesis. We revealed for the first time a sexual dimorphism in the otolith shape of hakes from the same geographical area by using a computational method developed to analyse otolith 3D shape based on micro-CT scans.

The economic importance of hakes for European fishery makes this species subject of population studies in which establishing the sex of the specimens is a common practice. In such context, our study provides the basis for a new methodology for sex identification in hake specimens unrelated to gonadal inspection. This approach based on otolith sex dimorphism can be useful when fish gonadal tissues are unavailable

due to damage or degradation (e.g., freezing), or to evaluate sex of preys from otoliths recovered from stomach of predators.

ACKNOWLEDGMENTS

The research leading to these results has been conceived under the International PhD Program "Innovative Technologies and Sustainable Use of Mediterranean Sea Fishery and Biological Resources(http://www.fishmed-phd.org/). This study represents partial fulfilment of the requirements for the Ph.D. thesis of Quinzia Palazzo".

REFERENCES

1. Campana SE. 1999 Chemistry and composition of fish otoliths: Pathways, mechanisms and applications. Mar. Ecol. Prog. Ser. 188, 263–297. (doi:10.3354/meps188263)

2. Popper AN, Fay RR. 1993 Sound Detection and Processing by Fish: Critical Review and Major Research Questions (Part 1 of 2). Brain. Behav. Evol. 41, 14–25. (doi:10.1159/000113821)

3. Popper AN, Hawkins AD. 2018 The importance of particle motion to fishes and invertebrates. J. Acoust. Soc. Am. 143, 470–488. (doi:10.1121/1.5021594)

4. Gauldie R. 1988 Function, form and time-keeping properties of fish otoliths. Comp. Biochem. Physiol. Part A Physiol. 91, 395–402. (doi:10.1016/0300-9629(88)90436-7)

5. Taylor MD, Fowler AM, Suthers IM. 2020 Insights into fish auditory structure–function relationships from morphological and behavioural ontogeny in a maturing sciaenid. Mar. Biol. 167, 21. (doi:10.1007/s00227-019-3619-9)

6. Tuset VM et al. 2016 Otolith shape lends support to the sensory drive hypothesis in rockfishes. J. Evol. Biol. 29, 2083–2097. (doi:10.1111/jeb.12932)

7. Campana SE, Neilson JD. 1985 Microstructure of Fish Otoliths. Can. J. Fish. Aquat. Sci. 42, 1014–1032. (doi:10.1139/f85-127)

8. Hüssy K, Limburg KE, de Pontual H, Thomas ORB, Cook PK, Heimbrand Y, Blass M, Sturrock AM. 2021 Trace Element Patterns in Otoliths: The Role of Biomineralization. Rev. Fish. Sci. Aquac. 29, 445–477. (doi:10.1080/23308249.2020.1760204)

9. Gauldie R. 2002 An eco-morphological explanation of individual variability in the shape of the fish otolith: comparison of the otolith of Hoplostethus atlanticus with other species by depth. J. Fish

Biol. 60, 1204–1221. (doi:10.1006/jfbi.2002.1938)

10. Assis IO, da Silva VEL, Souto-Vieira D, Lozano AP, Volpedo A V., Fabré NN. 2020 Ecomorphological patterns in otoliths of tropical fishes: assessing trophic groups and depth strata preference by shape. Environ. Biol. Fishes (doi:10.1007/s10641-020-00961-0)

11. Jaramilo AM, Tombari AD, Benedito Dura V, Eugeni Rodrigo M, Volpedo A V. 2014 Otolith eco-morphological patterns of benthic fishes from the coast of Valencia (Spain). Thalass. Rev. Ciencias Del Mar 30, 57–66.

12. Lloret-Lloret E, Navarro J, Giménez J, López N, Albo-Puigserver M, Pennino MG, Coll M. 2020 The Seasonal Distribution of a Highly Commercial Fish Is Related to Ontogenetic Changes in Its Feeding Strategy. Front. Mar. Sci. 7, 1–17. (doi:10.3389/fmars.2020.566686)

13. Abella A, Fiorentino F, Mannini A, Orsi Relini L. 2008 Exploring relationships between recruitment of European hake (Merluccius merluccius L. 1758) and environmental factors in the Ligurian Sea and the Strait of Sicily (Central Mediterranean). J. Mar. Syst. 71, 279–293. (doi:10.1016/j.jmarsys.2007.05.010)

14. Bartolino V, Ottavi A, Colloca F, Ardizzone GD, Stefánsson G. 2008 Bathymetric preferences of juvenile European hake (Merluccius merluccius). ICES J. Mar. Sci. 65, 963–969. (doi:10.1093/icesjms/fsn079)

15. Stagioni M, Montanini S, Vallisneri M. 2011 Feeding Habits of European Hake, Merluccius Merluccius (Actinopterygii: Gadiformes: Merlucciidae), from the Northeastern Mediterranean Sea. Acta Ichthyol. Piscat. 41, 277–284. (doi:10.3750/AIP2011.41.4.03)

16. Sion L et al. 2019 Spatial distribution pattern of european hake, merluccius merluccius (Pisces: Merlucciidae), in the mediterranean sea. Sci. Mar. 83, 21–32. (doi:10.3989/scimar.04988.12A)

17. Carpentieri P, Colloca F, Cardinale M, Belluscio A, Ardizzone GD. 2005 Feeding habits of European hake (Merluccius merluccius) in the central Mediterranean Sea. Fish. Bull. 103, 411–416.

18. Tamario C, Sunde J, Petersson E, Tibblin P, Forsman A. 2019 Ecological and Evolutionary Consequences of Environmental Change and Management Actions for Migrating Fish. Front. Ecol. Evol. 7, 1–24. (doi:10.3389/fevo.2019.00271)

19. Lombarte A, Popper AN. 1994 Quantitative analyses of postembryonic hair cell addition in the otolithic endorgans of the inner ear of the european hake,merluccius merluccius (gadiformes, teleostei). J. Comp. Neurol. 345, 419–428. (doi:10.1002/cne.903450308)

20. Orsi Relini L, Papaconstantinou C, Jukic-Peladic S, Souplet A, Gil de Sola L, Piccinetti C, Kavadas S, Rossi M. 2002 Distribution of the Mediterranean hake populations (Merluccius merluccius smiridus Rafinesque, 1810) (Ostheichthyes: Gadiformes) based on six years monitoring by trawl-surveys: some implications for management. Sci. Mar. 66, 21. (doi:10.3989/scimar.2002.66s221)

21. Cartes JE, Hidalgo M, Papiol V, Massutí E, Moranta J. 2009 Changes in the diet and feeding of the hake Merluccius merluccius at the shelf-break of the Balearic Islands: Influence of the mesopelagic-boundary community. Deep Sea Res. Part I Oceanogr. Res. Pap. 56, 344–365. (doi:10.1016/j.dsr.2008.09.009)

22. Ross ST. 1978 Trophic ontogeny of the Leopard Searobin, Prionotus scitulus (Pisces: Triglidae). Fish. Bull. 76, 225–234.

23. Preciado I, Punzón A, Velasco F. 2015 Spatio-temporal variability in the cannibalistic behaviour of European hake Merluccius merluccius : the influence of recruit abundance and prey availability. J. Fish Biol. 86, 1319–1334. (doi:10.1111/jfb.12642)

24. Bozzano A, Sardà F, Ríos J. 2005 Vertical distribution and feeding patterns of the juvenile European hake, Merluccius merluccius in the NW Mediterranean. Fish. Res. 73, 29–36. (doi:10.1016/j.fishres.2005.01.006)

25. Groison AL, Kjesbu OS, Suquet M. 2011 Sexual dimorphism of drumming muscles in European hake (Merluccius merluccius). Environ. Biol. Fishes 91, 7–13. (doi:10.1007/s10641-010-9753-3)

26. de Jong K, Amorim MCP, Fonseca PJ, Fox CJ, Heubel KU. 2018 Noise can affect acoustic communication and subsequent spawning success in fish. Environ. Pollut. 237, 814–823. (doi:10.1016/j.envpol.2017.11.003)

27. Krysl P, Hawkins AD, Schilt C, Cranford TW. 2012 Angular Oscillation of Solid Scatterers in Response to Progressive Planar Acoustic Waves: Do Fish Otoliths Rock? PLoS One 7, e42591. (doi:10.1371/journal.pone.0042591)

28. Schulz-Mirbach T, Olbinado M, Rack A, Mittone A, Bravin A, Melzer RR, Ladich F, Heß M. 2018 In-situ visualization of sound-induced otolith motion using hard X-ray phase contrast imaging. Sci. Rep. 8, 1–12. (doi:10.1038/s41598-018-21367-0)

29. Schulz-Mirbach T, Ladich F, Mittone A, Olbinado M, Bravin A, Maiditsch IP, Melzer RR, Krysl P, Heß M. 2020 Auditory chain reaction: Effects of sound pressure and particle motion on auditory structures in fishes. PLoS One 15, 1–30. (doi:10.1371/journal.pone.0230578)

30. Hawkins AD, Popper AN. 2018 Directional hearing and sound source localization by fishes. J. Acoust. Soc. Am. 144, 3329–3350. (doi:10.1121/1.5082306)

31. Zhang X, Tao Y, Zhou Y, Tang L, Liu M, Xu X. 2021 Acoustic Properties of the Otolith of the Large Yellow Croaker Larimichthys crocea (Perciformes : Sciaenidae). 64, 1–11. (doi:10.6620/ZS.2021.60-64)

32. Mattiucci S, Abaunza P, Ramadori L, Nascetti G. 2004 Genetic identification of Anisakis larvae in European hake from Atlantic and Mediterranean waters for stock recognition. J. Fish Biol. 65, 495–510. (doi:10.1111/j.0022-1112.2004.00465.x)

33. Castillo AGF, Alvarez P, Garcia-Vazquez E. 2005 Population structure of Merluccius merluccius along the Iberian Peninsula coast. ICES J. Mar. Sci. 62, 1699–1704. (doi:10.1016/j.icesjms.2005.06.001)

34. Milano I et al. 2014 Outlier SNP markers reveal fine-scale genetic structuring across European hake populations (Merluccius merluccius). Mol. Ecol. 23, 118–135. (doi:10.1111/mec.12568)

35. Lundy CJ, Moran P, Rico C, Milner RS, Hewitt GM. 1999 Macrogeographical population differentiation in oceanic environments: A case study of European hake (Merluccius merluccius), a commercially important fish. Mol. Ecol. 8, 1889–1898. (doi:10.1046/j.1365-294X.1999.00789.x)

36. Medits-Handbook. 2017 MEDITS Working Group. Version n., 106.

37. D'Iglio C et al. 2021 Intra- and interspecific variability among congeneric Pagellus otoliths. Sci. Rep. 11, 16315. (doi:10.1038/s41598-021-95814-w)

38. Otxotorena U, Díez G, de Abechuco EL, Santurtún M, Lucio P. 2010 Estimation of age and growth of juvenile hakes (Merluccius merluccius Linneaus, 1758) of the Bay of Biscay and Great Sole by means of the analysis of macro and microstructure of the otoliths. Fish. Res. 106, 337–343. (doi:10.1016/j.fishres.2010.09.001)

39. Pattoura P, Lefkaditou E, Megalofonou P. 2015 Age estimation of juvenile European hake Merluccius merluccius based on otolith microstructure analysis: a slow or fast growth pattern? J. Fish Biol. 86, 907–923. (doi:10.1111/jfb.12598)

40. Lowenstam H, Weiner S. 1990 On Biomineralization . Heinz A. Lowenstam , Stephen Weiner. J. Geol. 98, 977–977. (doi:10.1086/629466)

41. Payan P, De Pontual H, Bœuf G, Mayer-Gostan N. 2004 Endolymph chemistry and otolith growth in fish. Comptes Rendus - Palevol 3, 535–547. (doi:10.1016/j.crpv.2004.07.013)

42. Różycka M et al. 2019 Lattice Shrinkage by Incorporation of Recombinant Starmaker-Like Protein within Bioinspired Calcium Carbonate Crystals. Chem. – A Eur. J. 25, 12740–12750. (doi:10.1002/chem.201902157)

43. Wu D, Freund JB, Fraser SE, Vermot J. 2011 Mechanistic Basis of Otolith Formation during Teleost Inner Ear Development. Dev. Cell 20, 271–278. (doi:10.1016/j.devcel.2010.12.006)

44. Stefano M, Eleonora B, Francesca B, Maria V. 2015 Fish otolith biomineralization process: first investigations about organic matrix and growth of Triglidae (Scorpaeniformes) otoliths. Front. Mar. Sci. 2, 3. (doi:10.3389/conf.fmars.2015.03.00142)

45. Hüssy K, Mosegaard H, Jessen F. 2004 Effect of age and temperature on amino acid composition and the content of different protein types of juvenile Atlantic cod (Gadus morhua) otoliths. Can. J. Fish. Aquat. Sci. 61, 1012–1020. (doi:10.1139/f04-037)

46. Sturrock AM, Hunter E, Milton JA, Johnson RC, Waring CP, Trueman CN, EIMF. 2015 Quantifying physiological influences on otolith microchemistry. Methods Ecol. Evol. 6, 806–816. (doi:10.1111/2041-210X.12381)

47. Keil RG, Mayer LM. 2014 Mineral Matrices and Organic Matter. In Treatise on Geochemistry, pp. 337–359. Elsevier. (doi:10.1016/B978-0-08-095975-7.01024-X)

48. Lychakov DV, Rebane YT, Lombarte A, Fuiman LA, Takabayashi A. 2006 Fish otolith asymmetry: Morphometry and modeling. Hear. Res. 219, 1–11. (doi:10.1016/j.heares.2006.03.019)

49. Marini M, Maselli V, Campanelli A, Foglini F, Grilli F. 2016 Role of the Mid-Adriatic deep in dense water interception and modification. Mar. Geol. 375, 5–14. (doi:10.1016/j.margeo.2015.08.015)

50. Weber PK, Hutcheon ID, McKeegan KD, Ingram BL. 2002 Otolith sulfur isotope method to reconstruct salmon (*Oncorhynchus tshawytscha*) life history. Can. J. Fish. Aquat. Sci. 59, 587–591. (doi:10.1139/f02-038)

51. Hüssy K, Gröger J, Heidemann F, Hinrichsen H-H, Marohn L. 2016 Slave to the rhythm: seasonal signals in otolith microchemistry reveal age of eastern Baltic cod (Gadus morhua). ICES J. Mar. Sci. 73, 1019–1032. (doi:10.1093/icesjms/fsv247)

52. Tuset VM, Imondi R, Aguado G, Otero-Ferrer JL, Santschi L, Lombarte A, Love M. 2015 Otolith patterns of rockfishes from the northeastern pacific. J. Morphol. 276, 458–469. (doi:10.1002/jmor.20353)

Figures

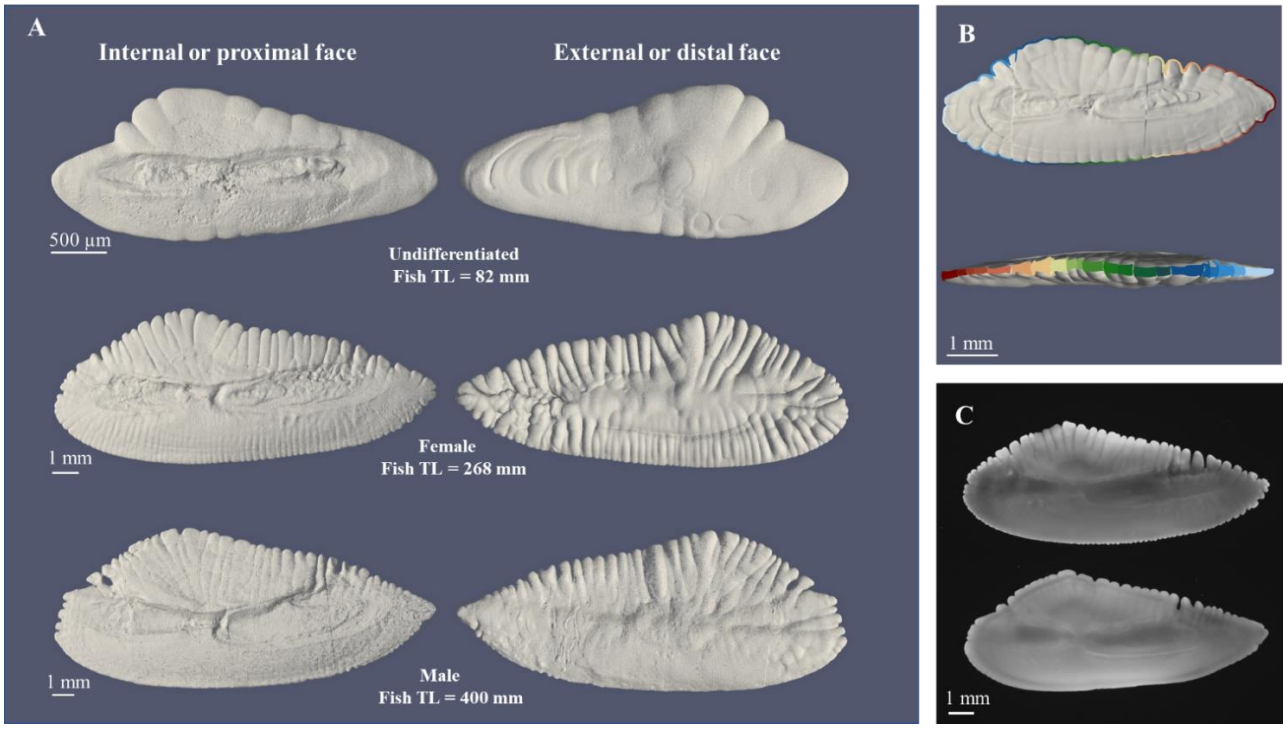

Figure 1. A) Representative surface reconstruction of otolith's internal and external face by Marching Cubes algorithm visualized with ParaView. Fish TL means fish total length. **B)** Representative images of detected protuberances (separated by colour) on proximal face (at the top) and sagittal plane (at the bottom) of a reconstructed otolith. **C)** Otolith's sample of female (at the top) and male (at the bottom) of *M. merluccius.* The fish TL for both specimens is 300 mm. Otolith length is 14.6 mm and 14.4 mm in female and male, respectively. Note the difference in the shape and in the dentate protuberances along the perimeter (more pronounced in female). Otolith perimeter is 45.0 mm and 38.1 mm in female and male, respectively, while otolith area is almost the same between female (59 mm^2) and male (60 mm^2).

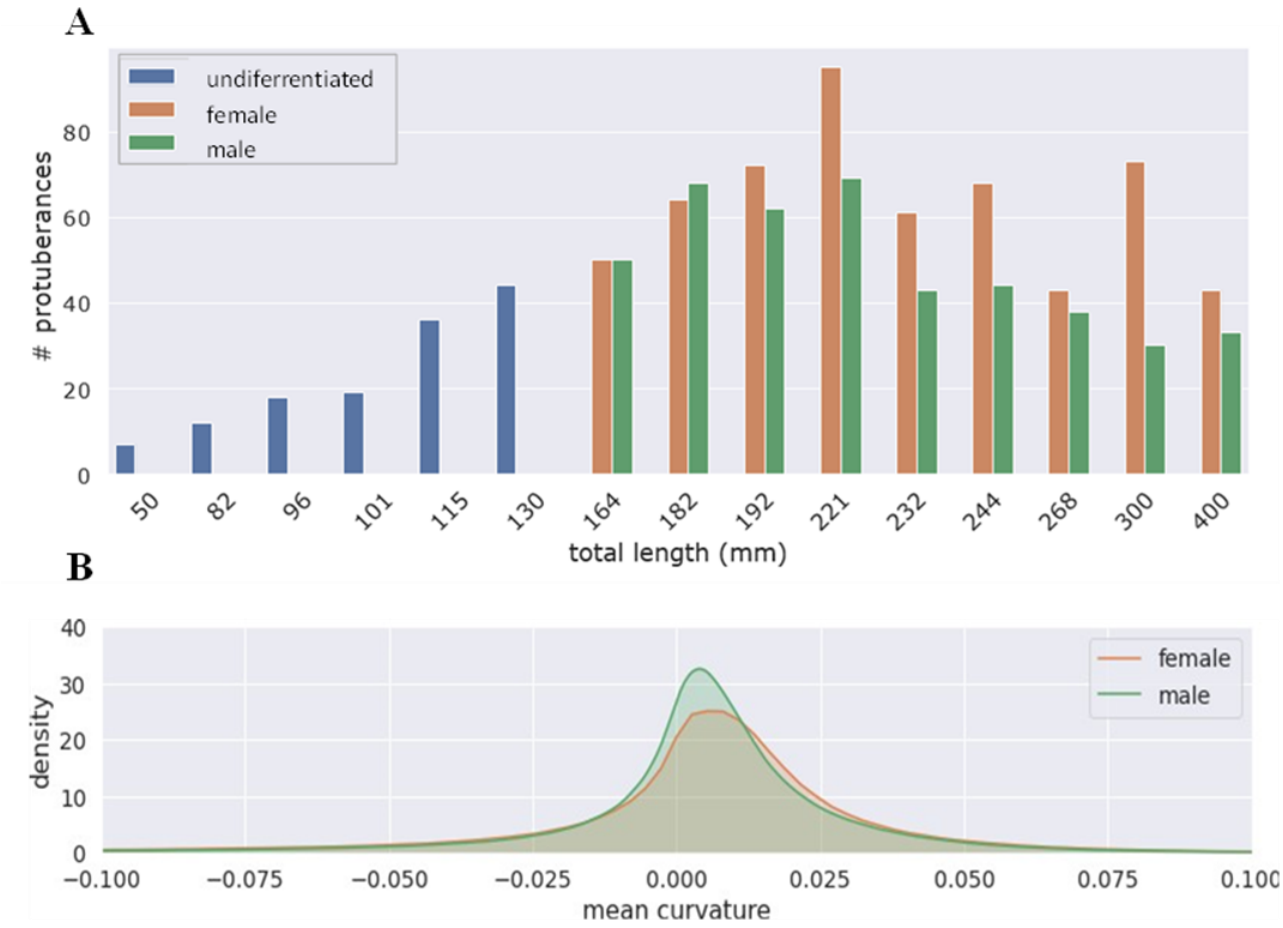

Figure 2. A) Number of detected protuberances per fish total length for 24 samples. For females and males, a pairwise comparison of equal fish TL was performed. **B)** Comparison of distribution plots by kernel density estimation (KDE) for *H* (mean curvature) on the surface for all female and male otoliths. The distribution for females contains considerably more positive *H* values in comparison to males (the female curve is shifted to the right). A comparison between distribution plots of H for males and females of equal fish length (see supplementary) shows the peaks of male otoliths to be consistently higher than its female counterparts. Consequently, the *H* values on male otoliths are more uniform which indicates a smoother surface. This is also reflected by the difference in the number of detected protuberances.

Supplementary Material for

Multiscale analysis on otolith structural features reveals differences in ontogenesis and sex in *Merluccius merluccius* in the western Adriatic

Quinzia Palazzo, Marco Stagioni, Steven Raaijmakers, Robert G. Belleman, Fiorella Prada, Jörg U. Hammel, Simona Fermani, Jaap Kaandorp*, Stefano Goffredo*, Giuseppe Falini*

*Corresponding authors: J.A.Kaandorp@uva.nl; s.goffredo@unibo.it; giuseppe.falini@unibo.it

Additional methods

Otolith biometry, morphology, and structural parameters

Otolith orientation for digital images was standardized by positioning all samples along the longest sulcus acusticus axis, from the anterior ostium to the posterior cauda (left). These images were processed by ImageJ software [1] and used to measure otolith length (maximum feret - the longest distance between any two points along the selection boundary), width (minimum feret - the shortest distance perpendicular to the maximum feret), perimeter, area and four shape descriptors (circularity, roundness, aspect ratio and solidity) (figure S2, tables S1-S2). Circularity and roundness provide information on the similarity of various features regarding a perfect circle. In detail, circularity is a shape descriptor that can mathematically indicate the degree of similarity to a perfect circle but essentially captures perimeter smoothness. A circularity value of 1.0 designates a perfectly smooth circle; as the circularity value approaches 0 the perimeter is increasingly more irregular. Roundness is similar to circularity but is insensitive to irregular borders along the perimeter of the otolith, thus, it provides information of the overall structural shape. This shape factor also takes into consideration the major axis of the best fit ellipse, giving a value directly relative to the aspect ratio. A roundness value of 1.0 indicates a perfect circle and larger values indicate oblong objects. Solidity describes the extent to which a shape is convex or concave. The solidity of a completely convex shape is 1.0, the farther the solidity deviates from 1.0, the greater the extent of concavity in the structure. Thus, this latter parameter is a way to estimate irregularity along the perimeter. Aspect ratio specifies whether the changes in the axes are proportional. An aspect ratio value equal to 1.0 represents a case of maximum symmetry and as the value approaches 0 the shape results more elongated (Table S2) [2,3].

Otolith dry mass was measured with Ohaus Explorer Pro balance (± 0.0001 g). The buoyant weight technique using the density determination kit of the Ohaus Explorer Pro balance [4,5] was used to obtain the structural parameters: otolith bulk-density (total density, including pores), micro-density (density of the material, excluding pores), and porosity (percentage of pores connected with the external surface).

Otolith composition

XRD analysis

A diffractogram was obtained for each sample using the following settings: tension = 40 kV; current = 40 mA; Cu k-alpha radiation (k) = 1.540 Å; divergence slit = $^1/_2$; anti-scatter slit = $^1/_2$; counting time =59.690 s; step size = 0.0167 °; start angle °2Theta = 20.0000; end angle °2Theta = 40.0034. The XRD patterns were analyzed using the X'Pert HighScore Plus software (PANalytical) (figure S3). The average crystallite sizes (D) were calculated by Scherrer's equation $D = K\lambda / (B\cos\theta)$, where B represents the half width of the (111) X-ray diffraction peaks (FWHM)

K is the shape factor or Scherrer Constant (K = 1 was applied)

λ is the wavelength of Cu K-alpha laser (1.540 Å)

θ is the angular XRD peak position.

FTIR analysis

Disk was obtained by mixing little amount (< 1 mg) of powder sample with 20 mg of potassium bromide (KBr, Sigma Aldrich, FTIR grade, P99%) and applying a pressure of 48.6 psi (670.2 MPa) to the mixture using a hydraulic press. Obtained qualitative data were analyzed with the software EZ OMNIC (Thermo Electron Corporation).

TGA analysis

The analysis was conducted on otolith powders having a weight of about 10 mg in nitrogen flow from 30° to 120 °C with a heating rate of 10 °C min^{-1}, an isothermal at 120 °C for 5 min (to remove the non-structural water absorbed) was performed, and another cycle from 120 to 600 °C with a heating rate of 10°C/min to evaluate the structural water and the organic matrix from the weight lost between 135°C and 450° (figure S4).

Analysis of otolith microchemistry

24 otoliths were soaked in sodium hypochlorite (5 wt.%) for 24 h, then rinsed with distilled water and dried in a desiccator. The powdered samples were then dissolved in HCl and HNO_3 in a 1: 3 volume ratios, adjusting the volume with milliQ water until 5 mL. Solvents and reagents with trace analysis grade of purity were used. Two blank solutions have been also taken though the sample preparation process to check the adequacy of the decontamination procedure. Each sample was measured three times, 12 s each, with 60 s of pre-running, using an ICP-OES, Spectro Arcos-Ametek, Inductive Coupled Plasma Optical Emission Spectroscopy with an axial torch and high

salinity kit. The Ba signal was measured at 455 nm, the Ca at 183 nm, the Co signal at 229 nm, the Cu at 325 nm, the K at 767 nm, the Li at 671 nm, the Mg at 279 nm, the Mn at 258 nm, the Na at 590 nm, the P at 178 nm, the S at 182 nm, the Sr at 408 nm, and the Zn at 214 nm. Certified standards in the experimental buffer were used to prepare the calibrating curves.

Morphological analysis on 3D reconstruction of otoliths based on microcomputed tomography imaging

All image processing steps and the developing method to 1) detect and measure the protuberances and 2) describe the 3D curvature of the shape were performed with Python3, in combination with Visualization Toolkit (VTK) [7], OpenCV [8] and NumPy [9] open-source libraries. The 3D rendering visualization of the objects were obtained with ParaView freeware (figure 1). In order to measure the curvature of the shape we followed the approach of the mean curvature H, which is an extrinsic measure of curvature describing the local curvature of a surface. In point p, $H(p)$ can be derived by taking the average of its principal curvatures k_1 and k_2, which are the minimum and maximum curvature in p respectively. The sign of $H(p)$ is positive if the surface in p is convex. Alternatively, $H(p)$ is negative when the surface is concave. The derivation of H allows to assess the extent of the curvature distribution for the otolith scans. Additionally, through H we can localize the tops of the protuberances as the tops consist of multiple vertices where $H(p) > 0$ (figure 1). Moreover, the tops are separated by valleys which are characterized by vertices where $H(p) < 0$. After the derivation of H and successful detection of the protuberances, several experiments were conducted to examine the otolith curvature. In the first experiment, the number of detected protuberances per otolith were counted. Subsequently, the total fish lengths (TL) were plotted against the number of detected protuberances to examine a potential relationship. During this experiment, the total length only serves as an age indication. Additionally, the otoliths were separated per gender to emphasize potential gender dimorphism. In the second experiment concerning the mean curvature of the entire shape, the distributions of H for a female and male otolith of equal total length were juxtaposed to examine a potential sex dimorphism for the otolith curvature. This concerns the distribution of H on the entire otolith surface, including the internal and external faces of the otolith. The distributions of H were then related to the number of detected protuberances to find a potential correlation between the overall H and protuberances.

Figures

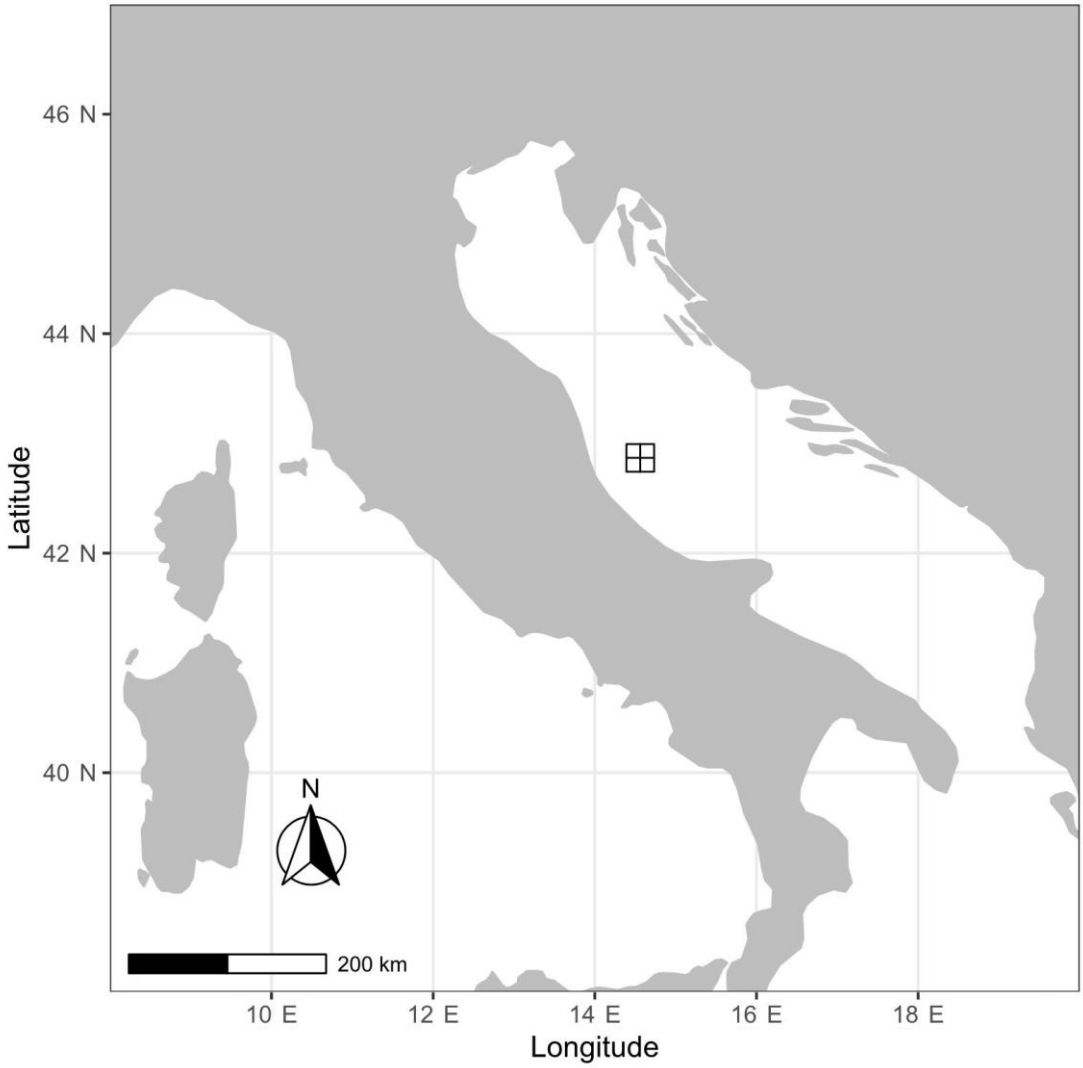

Figure S1: Map of the site where fish samples were collected, off the San Benedetto del Tronto coast in the western Adriatic Sea (N 42° 52' 6.056" E 14° 33' 43.29").

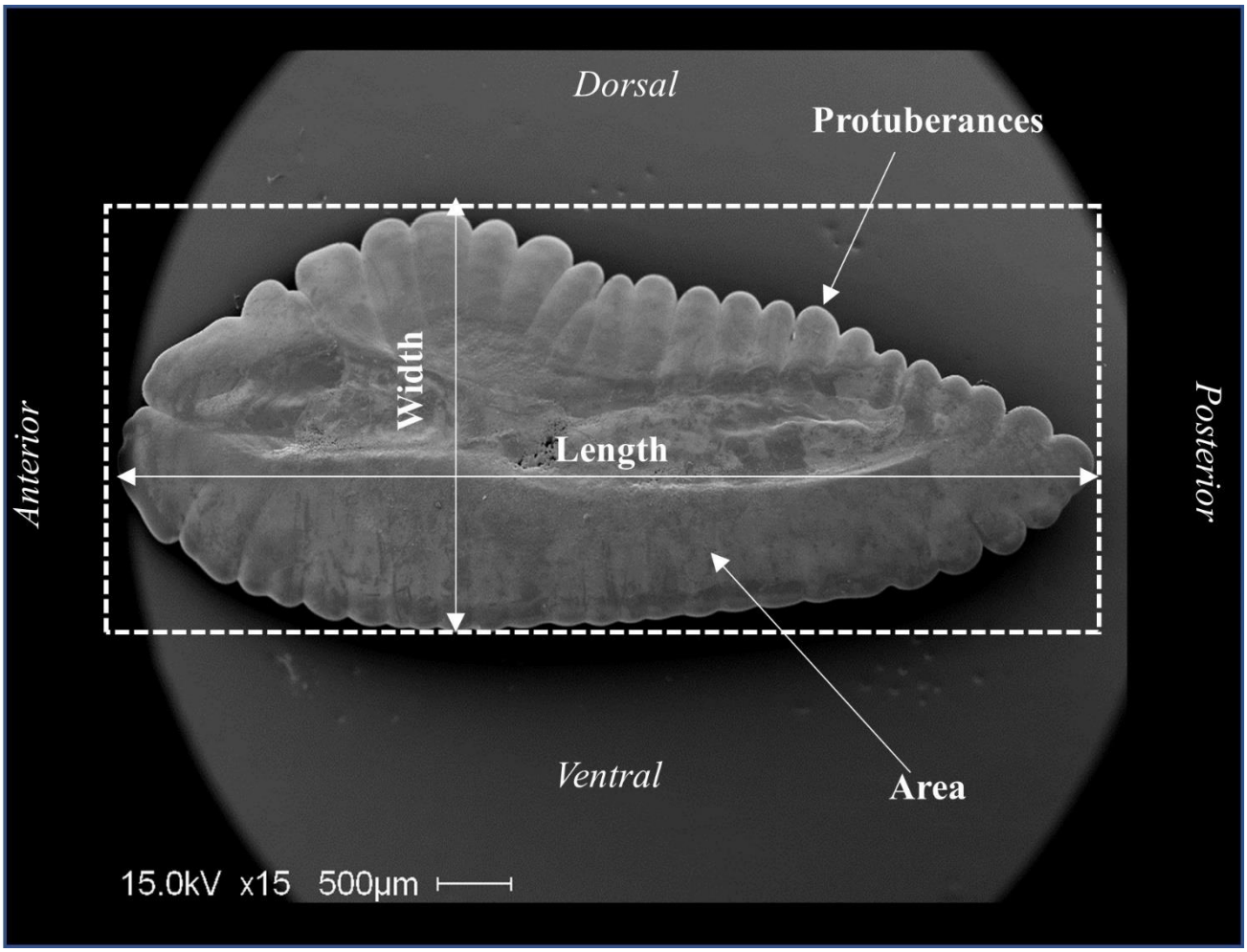

Figure S2: Otolith morphometrics viewed on a SEM micrograph of proximal (inner) face of sagittal otolith of *Merluccius merluccius*.

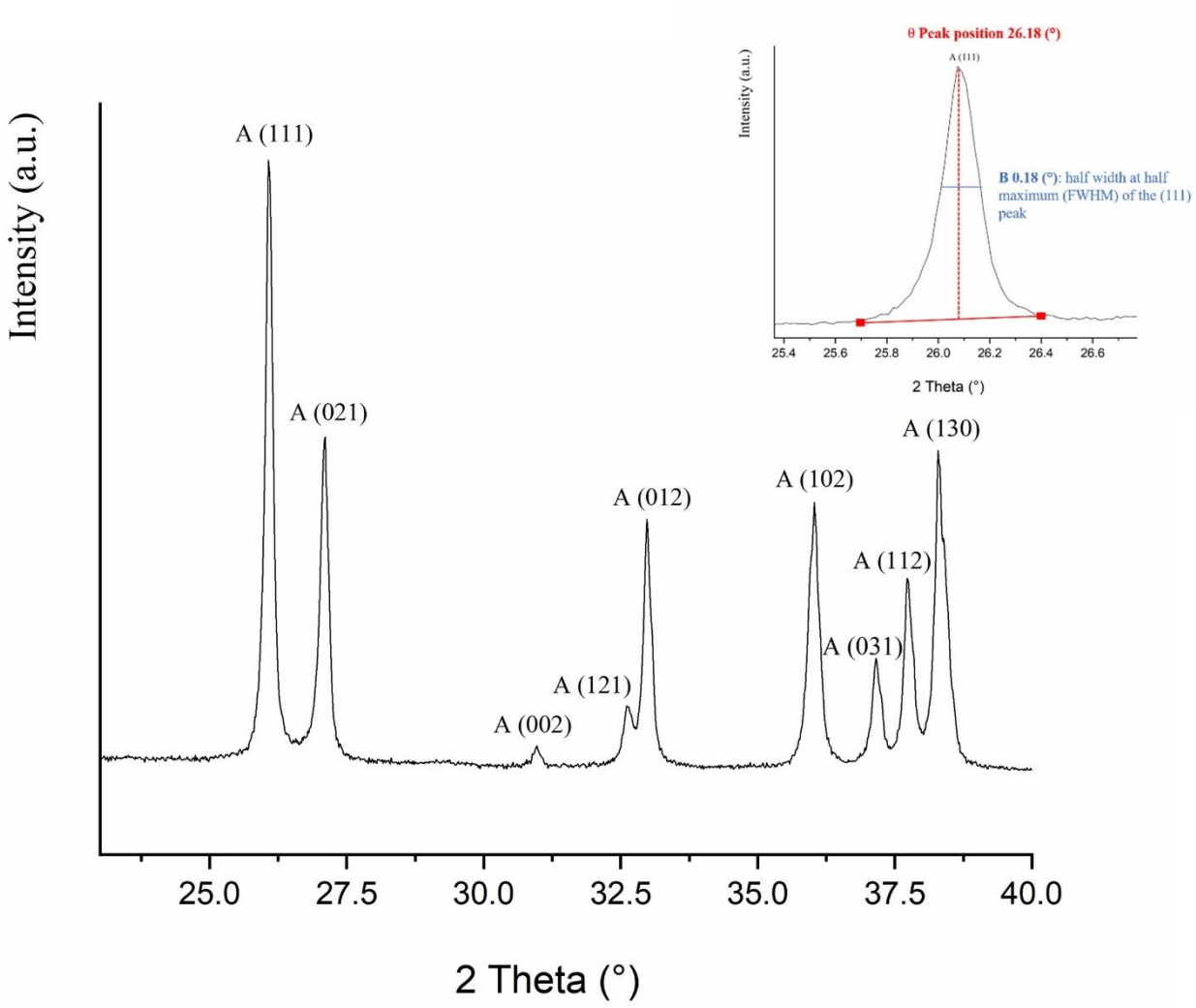

Figure S3: Representative X-ray powder diffraction pattern of otoliths.

The characteristic diffraction peaks from aragonite (A). The main diffraction peaks of the Miller index are indicated according to the following reference patterns of aragonite PDF 01–075–2230 [10]. The inserted graph is a zoom of 25.4°-26.6° diffractogram where the full width at half maximum (FWHM) measurements were performed on the main (111) peak of otoliths.

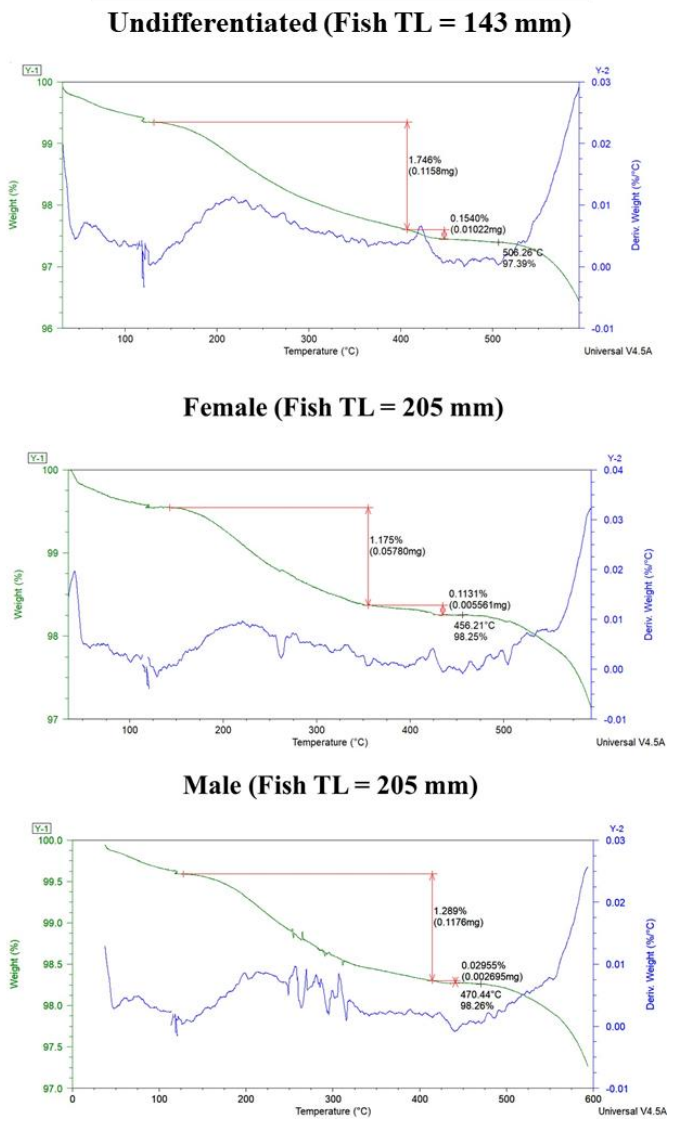

Figure S4: Representative Thermo-Gravimetric (TGA) profiles of undifferentiated, female and male otoliths.

The two lines show the percentage weight loss of the samples with increasing temperature (thermo-gravimetric profiles, green curves) and the first derivate of change weight (blue curves). The weight loss profiles of each samples showed significant mass loss events occurring between 135-440°C, which are associated with pyrolysis of the organic matrix and the structured water loss. The initial temperature of the decomposition process of calcium carbonate is also reported. Notice that the corresponding initial temperature of the thermal decomposition of calcium carbonate decrease by 30–50 C° between undifferentiated and adults, which may be due to the incorporation of organic acids [11].

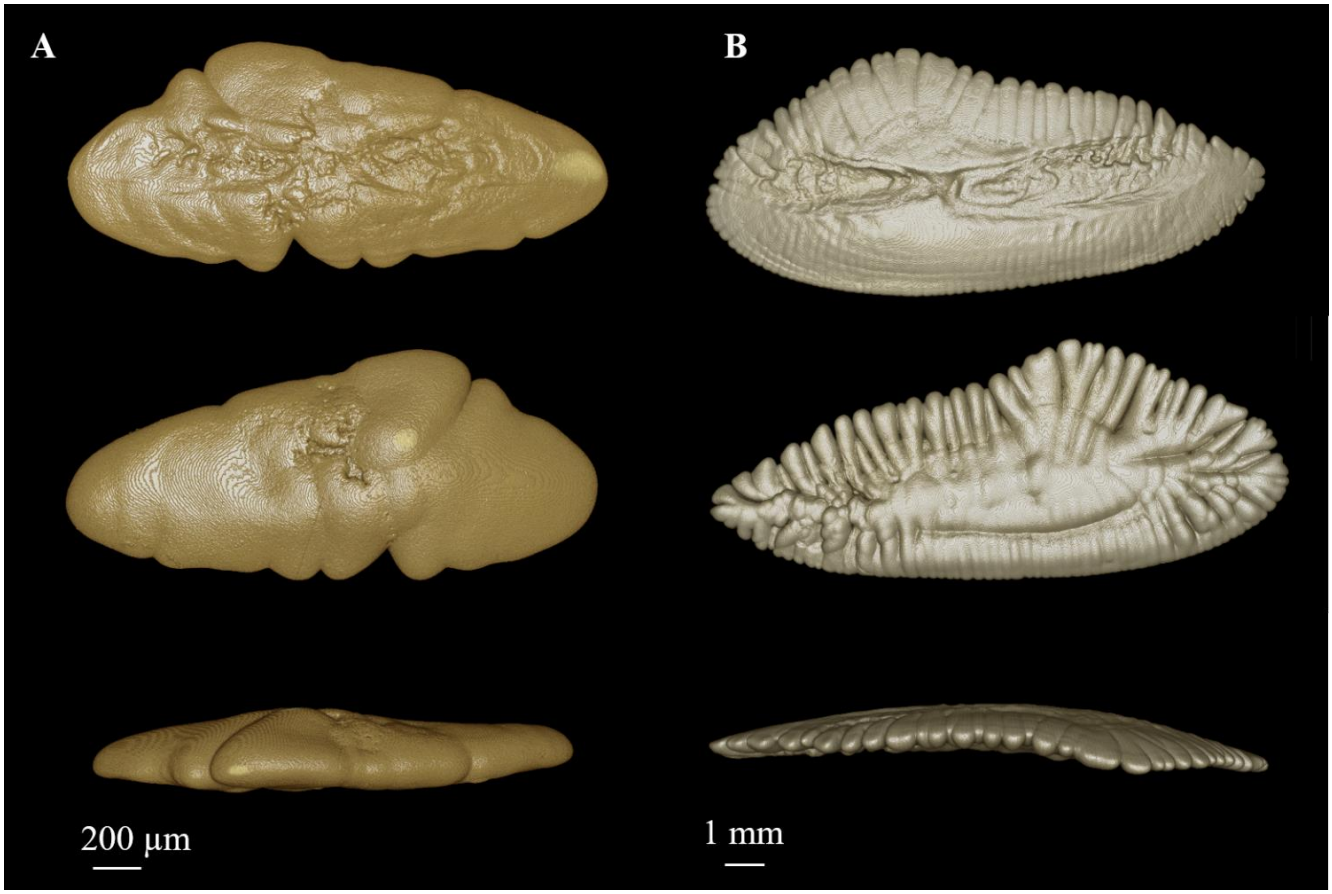

Figure S5: Representative renderings of otoliths.

A) Undifferentiated individual with fish length of 50 mm (micro CT scan resolution 2.024 µm, otolith length 2.06 mm). **B)** Female sample of fish length of 268 mm (micro CT scan resolution 8.333 µm, otolith length 12.55 mm). From top to bottom: inner or proximal face, external or distal face and lateral or sagittal vie

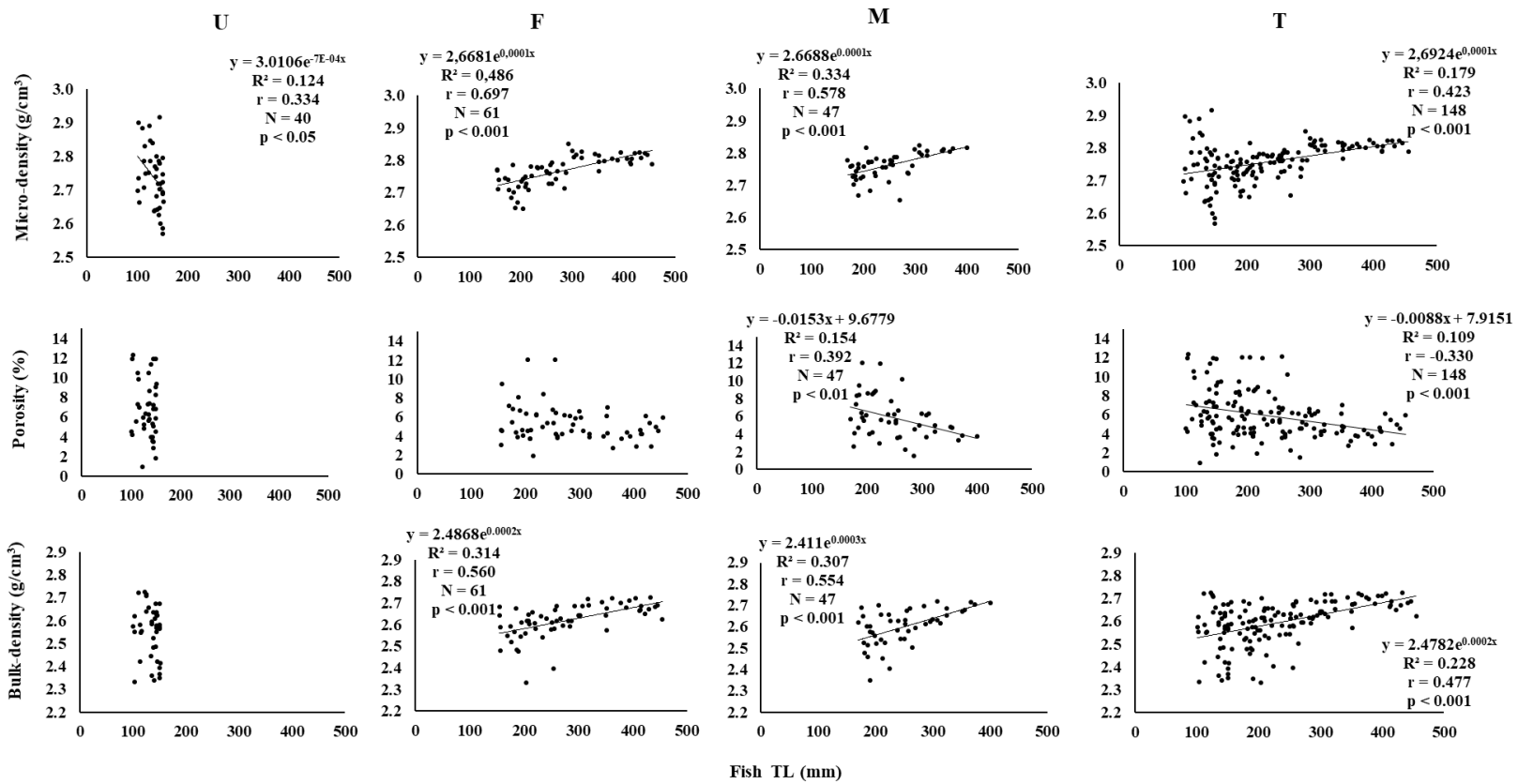

Figure S6: Relationships between otolith structural parameters with fish length (TL). Curves and their respectively equations of undifferentiated (U), females (F), males (M) and general (T = all the data pooled). Curves are not reported when the relations were not significant. N, number of samples; R^2, Pearson's coefficient of determination; R, Pearson's correlation coefficient

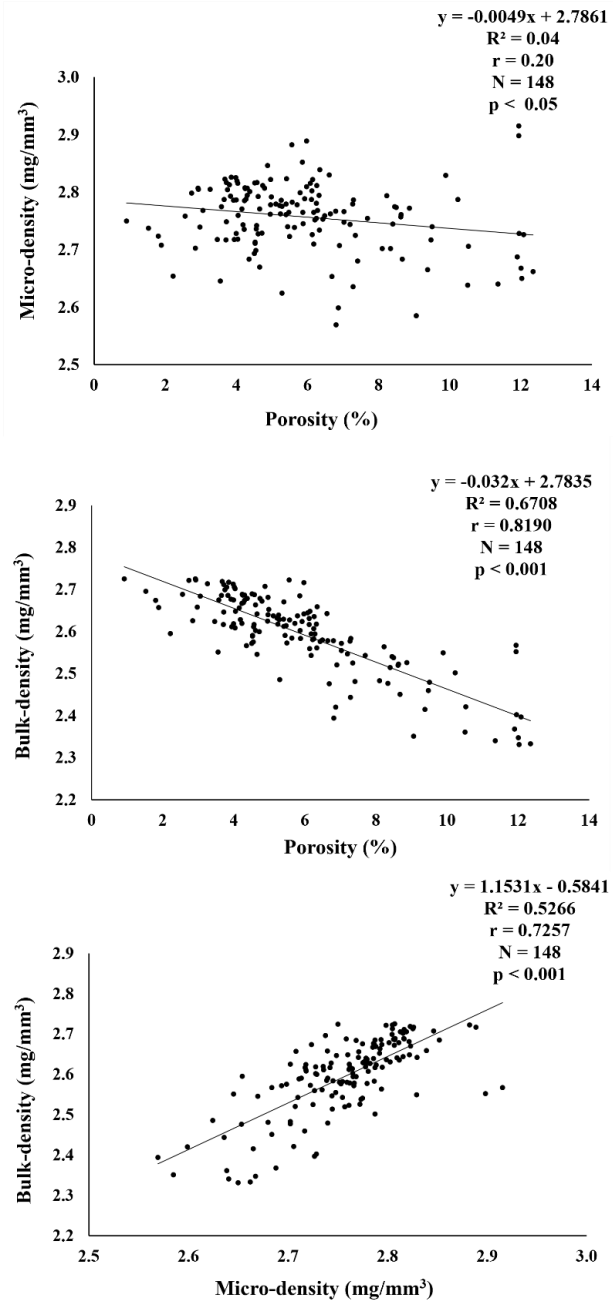

Figure S7: Correlation analyses between skeletal parameters of otoliths.

N, number of samples; R^2, Pearson's coefficient of determination; R, Pearson's correlation coefficient

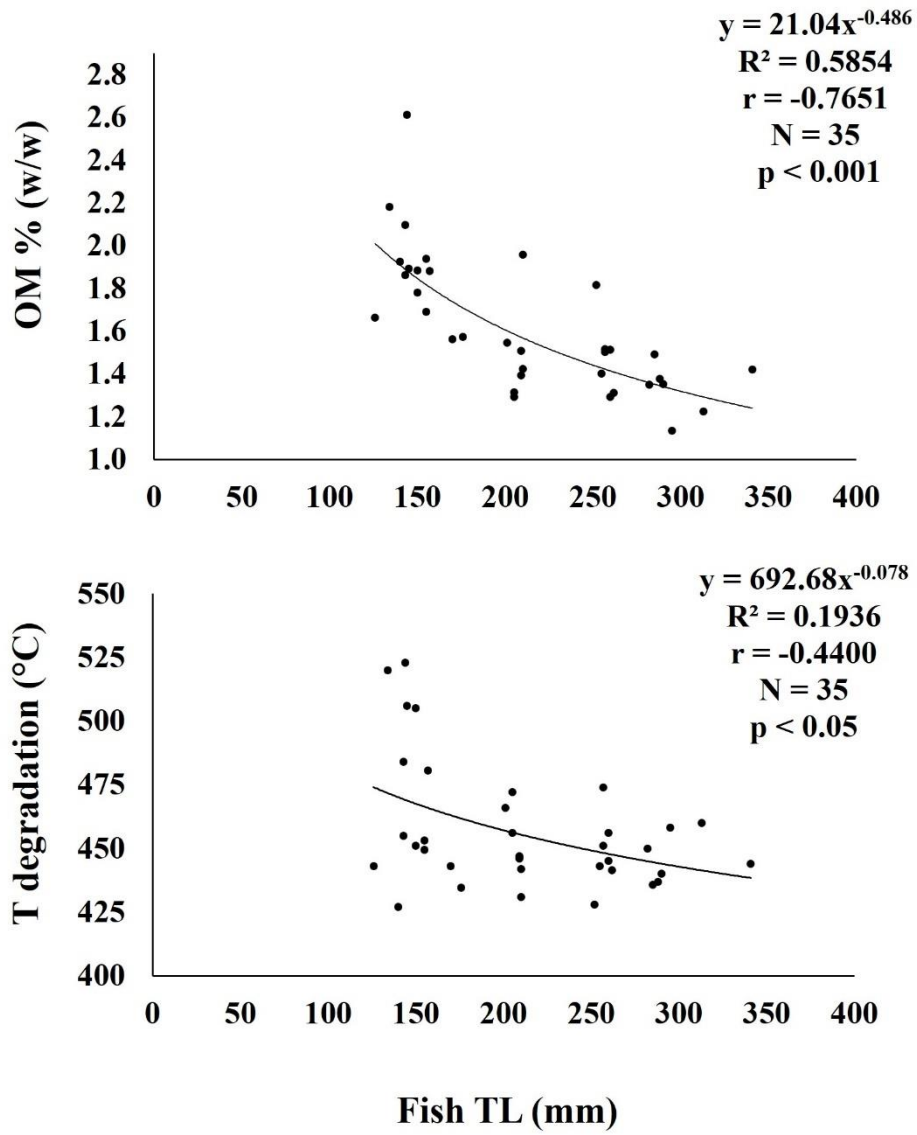

Figure S8: Relationships between the weight percentage values of the organic matrix (OM%). OM% is expressed in terms of weight loss (water + OM), and the initial temperature peak of the thermal calcium carbonate decarboxylation with fish total length (TL) of total individuals (data of undifferentiated, females and males pooled). N, number of samples; R^2, Pearson's coefficient of determination; R, Pearson's correlation coefficient

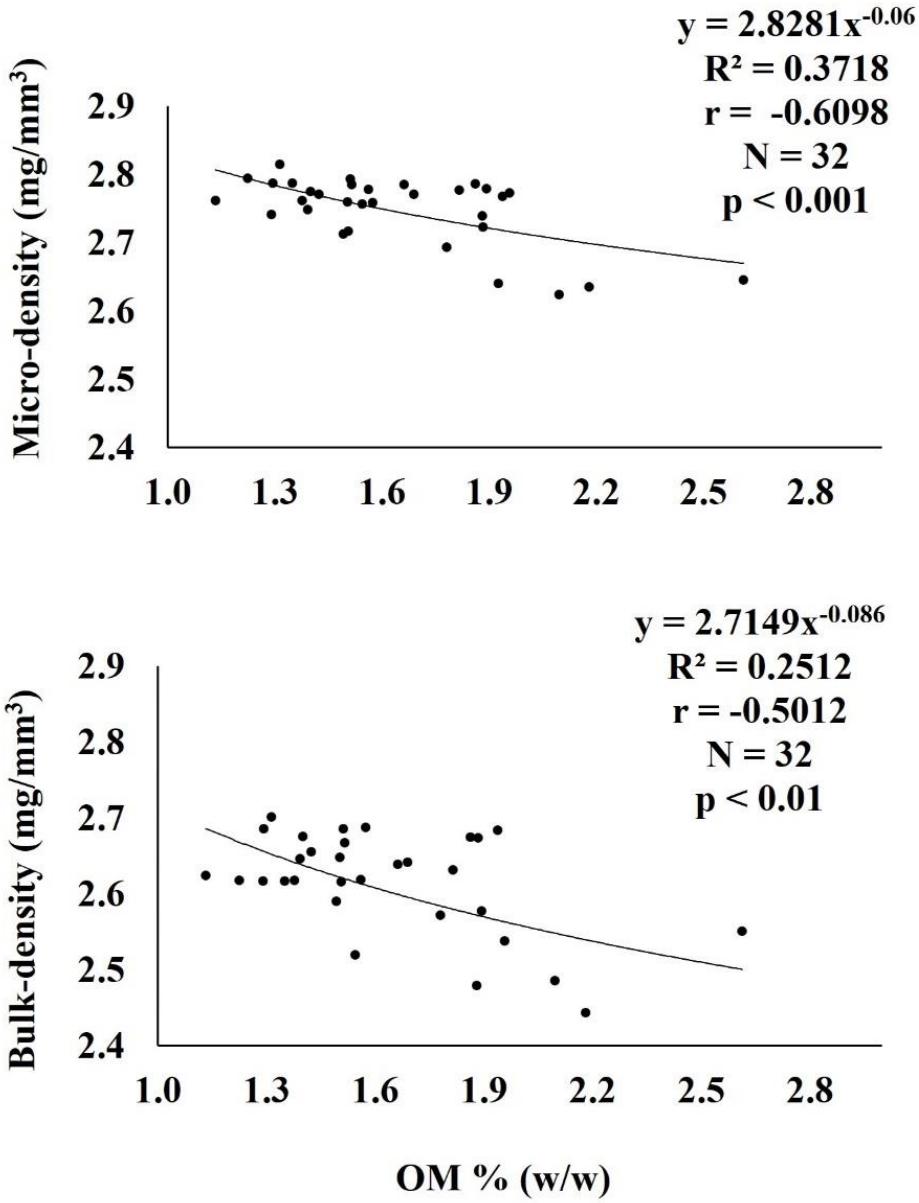

Figure S9: Relationships between the weight percentage values of the organic matrix (OM%) with the otolith's structural parameters.

Relationships are based on the total of individuals (data of undifferentiated, females and males pooled). N, number of samples; R^2, Pearson's coefficient of determination; R, Pearson's correlation coefficient

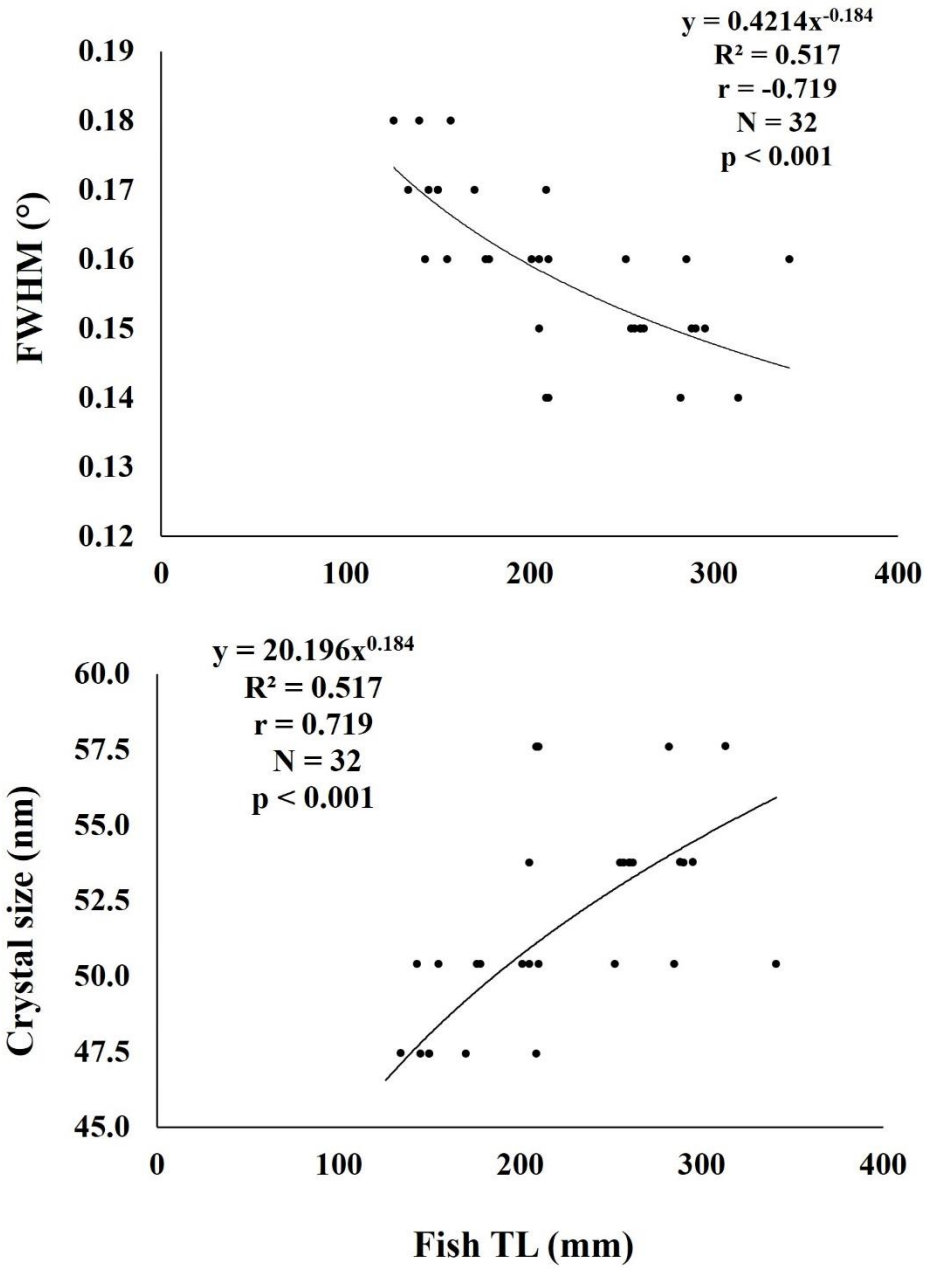

Figure S10: Relationships between FWHM with fish TL.

Fullwidth at half-maximum (FWHM) of the greatest aragonite peak (111) obtained by analysis of XRD peak profiles and the crystallite size (nm) with fish length (TL). Based on the Scherrer equation FWHM is indicative of crystallite size: the smaller the size the greater the value of FWHM. N, number of samples; R^2, Pearson's coefficient of determination; R, Pearson's correlation coefficient

a)

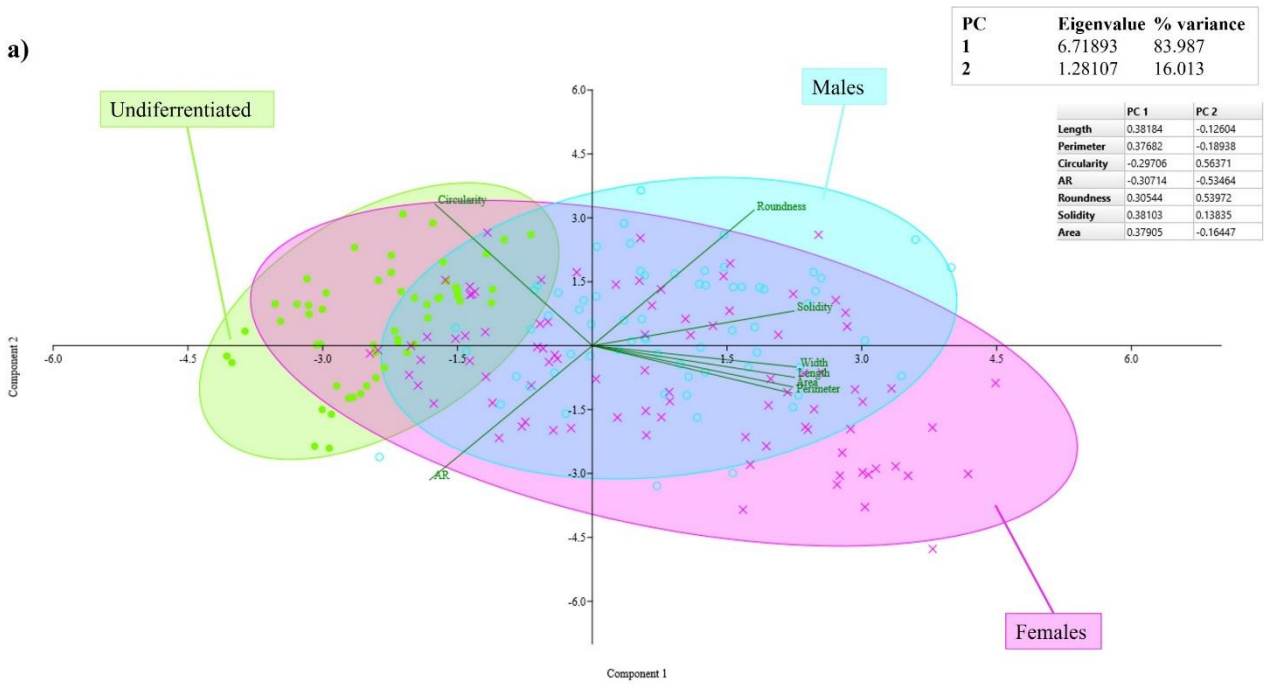

PC	Eigenvalue	% variance
1	6.71893	83.987
2	1.28107	16.013

	PC 1	PC 2
Length	0.38184	-0.12604
Perimeter	0.37682	-0.18938
Circularity	-0.29706	0.56371
AR	-0.30714	-0.53464
Roundness	0.30544	0.53972
Solidity	0.38103	0.13835
Area	0.37905	-0.16447

b)

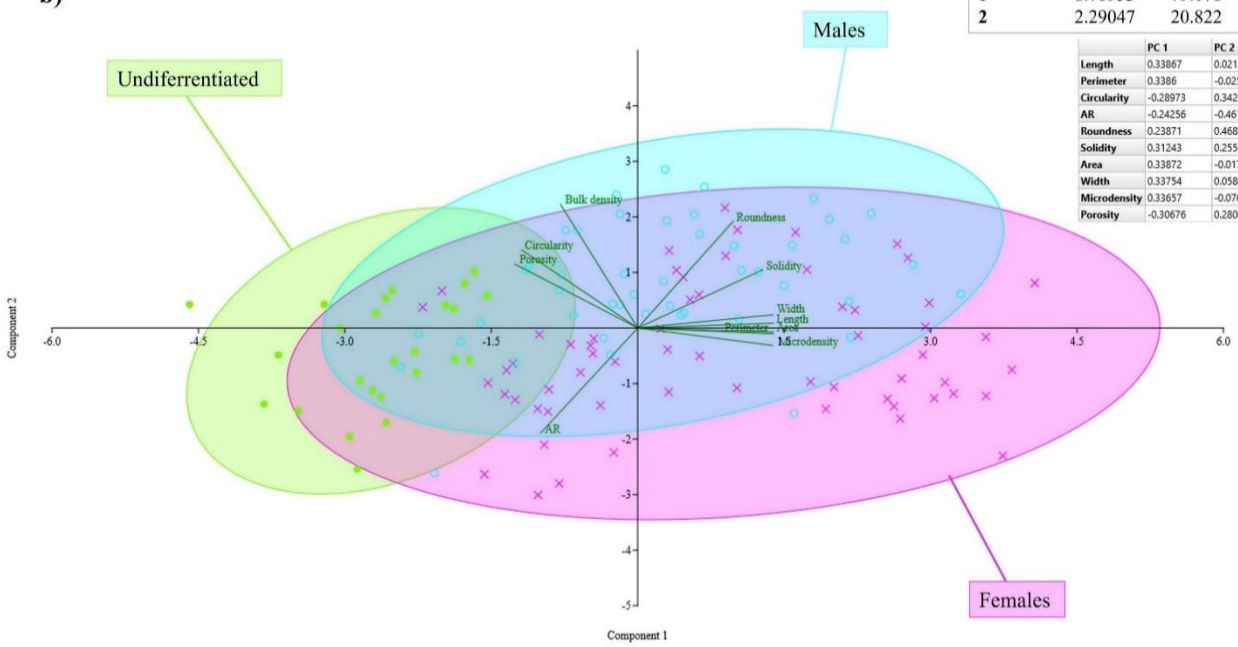

PC	Eigenvalue	% variance
1	8.70953	79.178
2	2.29047	20.822

	PC 1	PC 2
Length	0.33867	0.021298
Perimeter	0.3386	-0.025401
Circularity	-0.28973	0.34263
AR	-0.24256	-0.46137
Roundness	0.23871	0.46895
Solidity	0.31243	0.25579
Area	0.33872	-0.017835
Width	0.33754	0.058009
Microdensity	0.33657	-0.076483
Porosity	-0.30676	0.28067

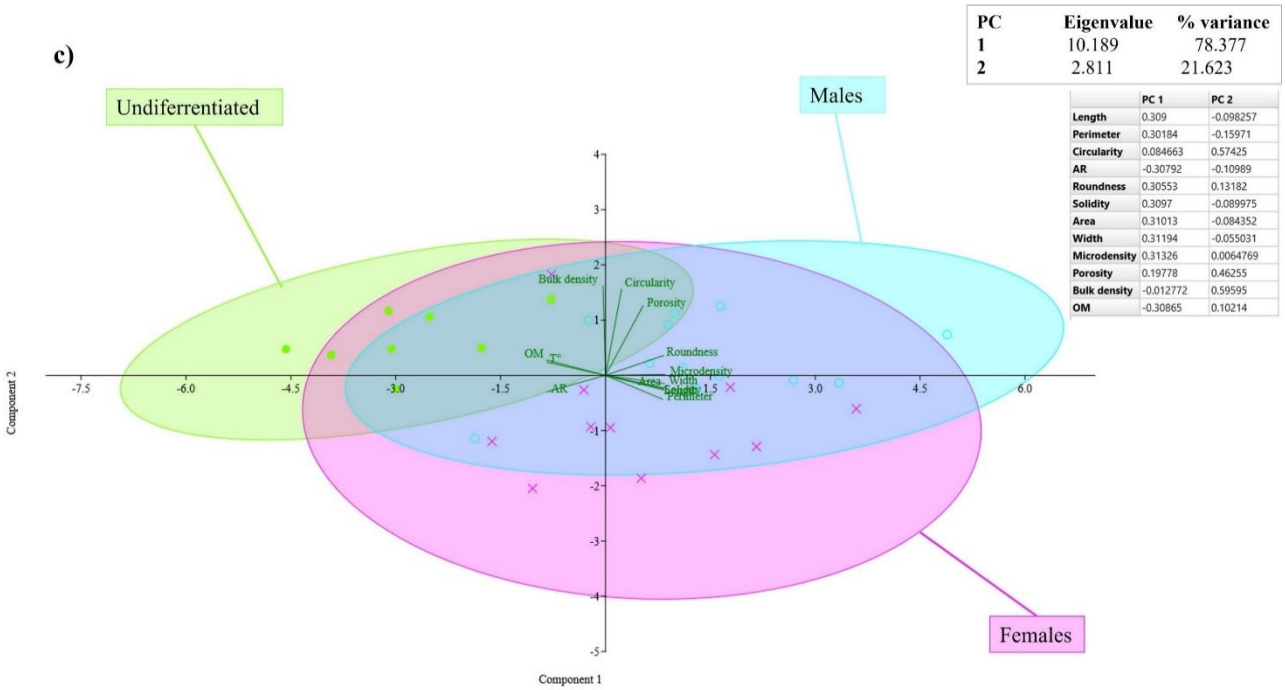

PC	Eigenvalue	% variance
1	10.189	78.377
2	2.811	21.623

	PC 1	PC 2
Length	0.309	-0.098257
Perimeter	0.30184	-0.15971
Circularity	0.084663	0.57425
AR	-0.30792	-0.10989
Roundness	0.30553	0.13182
Solidity	0.3097	-0.089975
Area	0.31013	-0.084352
Width	0.31194	-0.055031
Microdensity	0.31326	0.0064769
Porosity	0.19778	0.46255
Bulk density	-0.012772	0.59595
OM	-0.30865	0.10214

Figure S11: Biplots of the principal component analysis (PCA) on the correlation matrix between the three groups representing the undifferentiated, female, and male otolith categories of the *M. merluccius* individuals investigated. Each symbol represents one otolith sample. Undifferentiated in green dots; females in pink crosses; males in blue cercles. Green arrows indicate the correlation of the different parameters with PC1 and PC2. Eigenvalue's plot shows the percentage of explained variance for the two components. **a)** PCA plot of the distribution of the values in the space related to the bi-dimensional otolithic biometric and morphologic parameters (length, width, perimeter, circularity, aspect ratio, roundness, solidity, area) for a sample number of 210, interpreted by PC1 and PC2 (PC1= 83.987 %, PC2= 16.013 %). **b)** PCA plot of the distribution of the values in the space related to the bi-dimensional otolithic biometric, morphologic and density parameters (length, width, perimeter, circularity, aspect ratio, roundness, solidity, area, microdensity, porosity, bulk-density) for a sample number of 148, interpreted by PC1 and PC2 (PC1= 79.178 %, PC2= 20.822%). **c)** PCA plot of the distribution of the values in the space related to the bi-dimensional otolithic biometric, morphologic, density and structural parameters (length, width, perimeter, circularity, aspect ratio, roundness, solidity, area, microdensity, porosity, bulk-density, organic matrix content and initial temperature of degradation of $CaCO_3$) for a sample number of 35, interpreted by PC1 and PC2 (PC1= 78.377%, PC2= 21.623%).

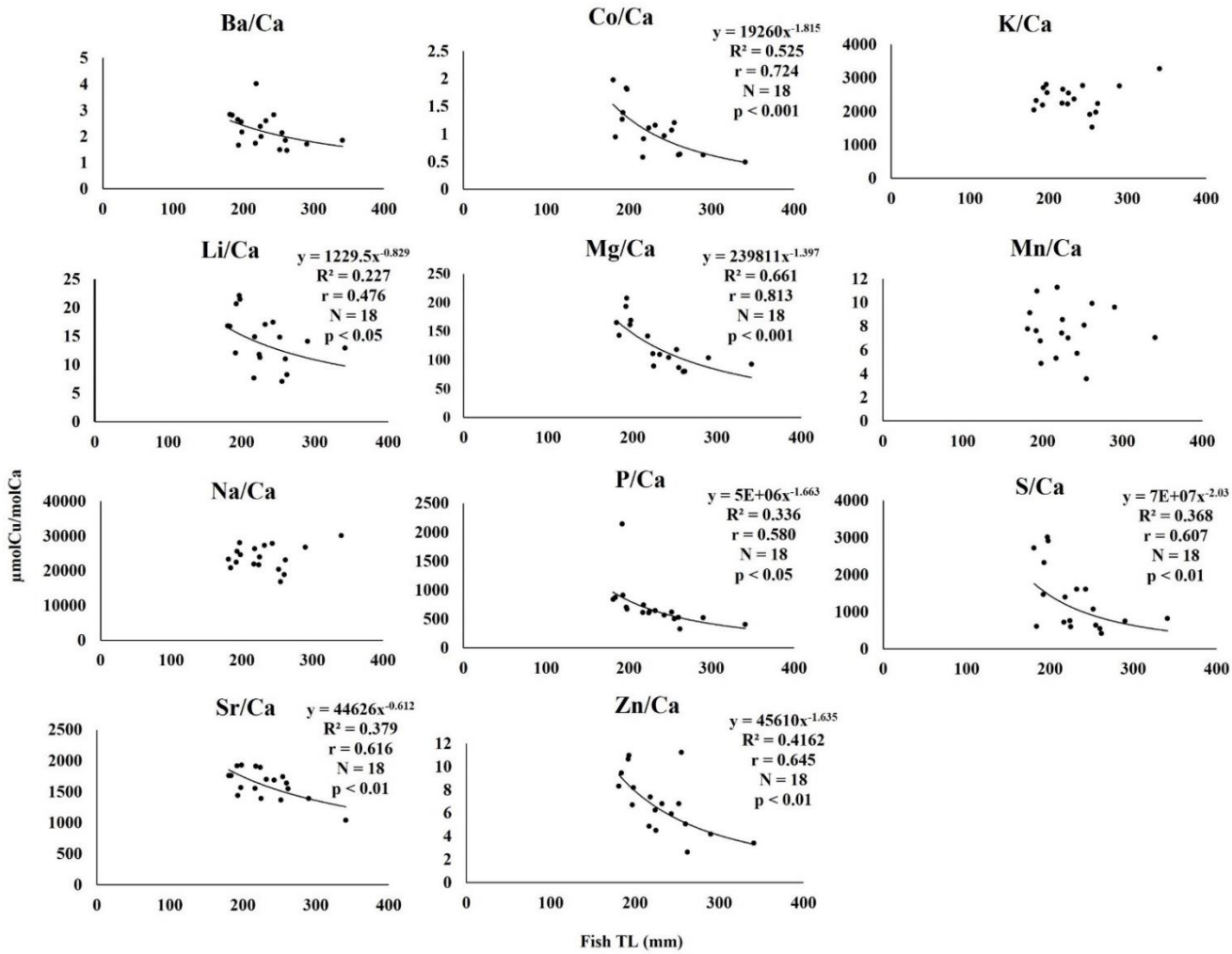

Figure S12: Relationships between otoliths trace elements with fish total length (TL).

In order to increase the sample size, a unique pool of individuals (females + males) was then taken in account in this analysis. Therefore, a unique curve is reported for each element. Equations are not reported when the relations were not significant. N, number of samples; R^2, Pearson's coefficient of determination; R, Pearson's correlation coefficient

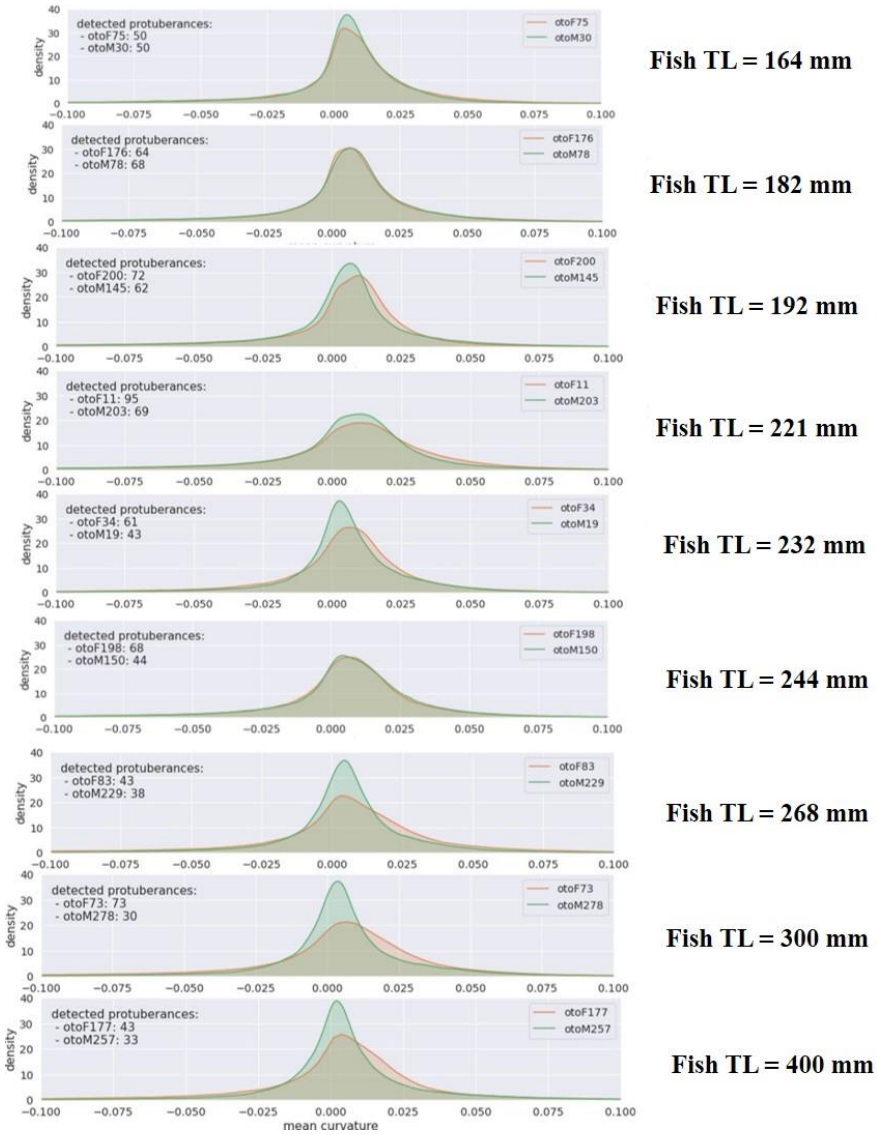

Figure S13: Distribution plot by kernel density estimation (KDE) for *H* (mean curvature) obtained from the surface of nine female and nine male otoliths compared in pairs of the same fish length.

Tables

Table S1: Biometric, density, 2D-3D morphological and compositional parameters investigated in relation to fish length.

The analyses were performed for all individuals pooled and for undifferentiated, females and males separately.

Biometric parameters	Structural parameters
FishTL vs OtoLength FishTL vs OtoWidth FishTL vs OtoPerimeter FishTL vs OtoArea Oto Perimeter vs OtoArea	FishTL vs OtoVolume FishTL vs OtoWeight FishTL vs OtoMicrodensity FishTL vs OtoBulkdensity FishTL vs OtoPorosity
2D-3D Morphological parameters	**Compositional parameters**
FishTL vs OtoCircularity FishTL vs OtoAspectRatio FishTL vs OtoRoundness FishTL vs OtoSolidity FishTL vs OtoMeanCurvature FishTL vs OtoNumberProtuberances	FishTL vs OM % FishTL vs Initial T° Degradation $CaCO_3$ FishTL vs Crystallite size FishTL vs Trace elements

Table S2: Otolith shape indices with the relative formula and the biometric parameters. Units are mm^2 for OA, and mm for OP, OL and OW.

Biometric parameters *	**Shape descriptors**
Area (A)	Circularity = $4 \pi * (A/P^2)$
Perimeter (P)	Roundness = $4 \pi * (A) / (OL)^2$
Ferret Length (OL)	Aspect ratio = (OL) / (OW)
Ferret Width (OW)	Solidity = (A) / (Convex area)

Table S3: Curve estimation regression for 3 different curve models (linear, power and exponential) for each dependent variable investigated for the total of individuals.

Biometric (OL = otolith length; OW = otolith width; OP = otolith perimeter; OA = otolith area), morphologic (OC = otolith circularity; OAR = otolith aspect ratio; OR = otolith roundness; OS = otolith solidity;) and structural parameters (OV = otolith volume, Oweight = otolith weight, Omicro = otolith microdensity; Obulk = otolith bulk density; Oporo = otolith porosity; OM% = otolith intraskeletal matter; T° degradation) and fish size (TL = total length) of European Hake for the total of individuals. The lines highlighted in grey represent the best fit for each curve data. N = sample size; R^2 = coefficient of determination; R = Pearson's correlation coefficient; F = ratio of the mean regression sum of squares divided by the mean error sum of squares; Sign. (*p*) = *p*-value; a = constant; b = slope.

Curves estimation	Total							
	N		R^2	R	F	Sig. (*p*)	a	b
TL vs OL	210	Linear	0.988	0.994	16725.040	< 0.001	0.676	0.044
		Power	0.989	0.994	18110.142	< 0.001	0.062	0.952
		Exponential	0.938	0.968	3143.243	< 0.001	3.911	0.004
TL vs OW	210	Linear	0.975	0.987	8092.317	< 0.001	0.484	0.017
		Power	0.980	0.990	9986.917	< 0.001	0.030	0.920
		Exponential	0.917	0.958	2298.967	< 0.001	1.646	0.004
TL vs OP	210	Linear	0.976	0.988	8378.403	< 0.001	0.075	0.131
		Power	0.981	0.990	10551.701	< 0.001	0.116	1.022
		Exponential	0.924	0.961	2539.182	< 0.001	10.026	0.004
TL vs OA	210	Linear	0.974	0.987	7727.436	< 0.001	-27.712	0.284
		Power	0.987	0.993	16138.421	< 0.001	0.001	1.882
		Exponential	0.929	0.964	2738.319	< 0.001	4.472	0.008
OA vs OP	210	Linear	0.956	0.978	4539.834	< 0.001	13.185	0.448
		Power	0.985	0.992	13848.54	< 0.001	4.480	0.541
		Exponential	0.860	0.927	1282.408	< 0.001	15.864	0.015
TL vs OC	210	Linear	0.291	0.539	85.220	< 0.001	0.554	0.000
		Power	0.303	0.550	90.579	< 0.001	1.135	-0.163
		Exponential	0.290	0.539	84.926	< 0.001	0.559	-0.001
TL vs OAR	210	Linear	0.001	0.032	0.154	> 0.005	2.548	0.000
		Power	0.001	0.032	0.296	> 0.005	2.605	-0.004
		Exponential	0.001	0.032	0.132	> 0.005	2.547	0.000
TL vs OR	210	Linear	0.001	0.032	0.114	> 0.005	0.393	0.000
		Power	0.001	0.032	0.293	> 0.005	0.384	0.004
		Exponential	0.001	0.032	0.135	> 0.005	0.393	0.000
TL vs OS	210	Linear	0.395	0.628	135.794	< 0.001	0.957	0.000

		Power	0.413	0.643	146.124	< 0.001	0.912	0.011
		Exponential	0.394	0.628	135.501	< 0.001	0.957	0.000
TL vs OV	148	Linear	0.938	0.969	2191.945	< 0,001	-32.274	0.252
		Power	0.981	0.990	7626.685	< 0,001	0.000	2.418
		Exponential	0.927	0.963	1863.604	< 0,001	1.690	0.010
TL vs Oweight	148	Linear	0.933	0.966	2036.6	< 0,001	-0.088	0.001
		Power	0.983	0.991	8217.769	< 0,001	0.000	2.468
		Exponential	0.931	0.965	1982.846	< 0,001	0.004	0.010
TL vs Omicro	148	Linear	0.175	0.418	30.929	< 0,001	2.694	0.000
		Power	0.142	0.377	24.102	< 0,001	2.461	0.021
		Exponential	0.176	0.420	31.278	< 0,001	2.693	0.000
TL vs Obulk	148	Linear	0.232	0.482	44.153	< 0,001	2.479	0.001
		Power	0.207	0.455	38.020	< 0,001	2.051	0.044
		Exponential	0.228	0.477	43.036	< 0,001	2.478	0.000
TL vs Oporo	148	Linear	0.109	0.330	17.775	< 0,001	7.915	-0.009
		Power	0.071	0.266	11.134	< 0,01	25.972	-0.293
		Exponential	0.073	0.270	11.554	< 0,01	7.250	-0.001
TL vs OM%	35	Linear	0.521	0.722	35.884	< 0,001	2.412	-0.004
		Power	0.585	0.765	46.575	< 0,001	21.04	-0.486
		Exponential	0.555	0.745	41.223	< 0,001	2.572	-0.002
TL vs T°	35	Linear	0.180	0.424	7.223	< 0.05	493.334	-0.171
		Power	0.195	0.442	7.991	< 0.01	693.750	-0.079
		Exponential	0.176	0.420	7.029	< 0.05	492.472	0.000

Table S4: Regression parameters of the relationships between the otolith parameters and fish length for the total of individuals**.** Biometric (OL = otolith length; OW = otolith width; OP = otolith perimeter; OA = otolith area), morphologic (OC = otolith circularity; OAR = otolith aspect ratio; OR = otolith roundness; OS = otolith solidity;) and structural parameters (OV = otolith volume, Oweight = otolith weight, Omicro = otolith microdensity; Obulk = otolith bulk density; Oporo = otolith porosity; OM% = otolith intraskeletal matter) and fish size (TL = total length) of European Hake for the total of individuals. n = sample size; a = constant; b = slope, CI (b) = 95% confidence interval; R^2 = coefficient of determination. Empty space indicates that the correlation was not significant.

Relationship		Total					
		n	a	b	CI (b)	R^2	P
TL vs OL	Power	210	0.062	0.952	0.938-0.966	0.989	< 0.001
TL vs OW	Power	210	0.030	0.920	0.902-0.939	0.980	< 0.001
TL vs OP	Power	210	0.116	1.022	1.002-1.042	0.981	< 0.001
TL vs OA	Power	210	0.001	1.882	1.852-1.911	0.987	< 0.001
OP vs OA	Power	210	4.480	0.541	0.532-0.550	0.985	< 0.001
TL vs OC	Power	210	1.135	-0.163	(-0.196)-(-0.129)	0.303	< 0.001
TL vs OAR	Power	210				0.001	> 0.05
TL vs OR	Power	210				0.002	> 0.05
TL vs OS	Power	210	0.912	0.011	0.009-0.013	0.413	< 0.001
TL vs OV	Power	148	0.000	2.418	2.363-2.472	0.981	< 0.001
TL vs Oweight	Power	148	0.000	2.468	2.412-2.523	0.983	< 0.001
TL vs Omicro	Exponential	148	2.626	0.000	0,000-0,000	0.179	< 0,001
TL vs Obulk	Exponential	148	2.478	0.000	0,000-0,000	0.228	< 0.001
TL vs Oporo	Linear	148	-0.009	7.915	(-0.013)-(-0.0,005)	0.109	< 0.001
TL vs OM%	Power	35	21.040	-0.486	(-0.630)-(-0.341)	0.585	<0.001

Table S5: Raw dataset including the microchemistry measurements initially conducted on 6 undifferentiated, 9 females and 9 males otoliths by ICP-OES. Undifferentiated' samples were excluded from the statistical analysis since their values resulted under the detection limits of the instrument or outliers' data points (*). Data are represented as µg/g and approximate. U =undifferentiated, F = females, M = males. LOD = limit of detection.

Sample	Gender	Fish length (mm)	Weight of the powder for ICP (g)	Ba (ppm)	Ca (ppm)	Co (ppb)	Cu (ppm)	K (ppm)	Li (ppm)	Mg (ppm)	Mn (ppm)	Na (ppm)	P (ppm)	S (ppm)	Sr (ppm)	Zn (ppm)
MMOtoDX201*	U	136	0.00273	0.001	60.10	1.54	0.003	0.079	0	under LOD	0.002	0.85	under LOD	under LOD	0.296	0.062
MMOtoDX267*	U	145	0.00030	0.004	7.61	under LOD	0.004	under LOD	under LOD	under LOD	0.001	4.23	under LOD	under LOD	0.153	0.033
MMOtoDX177*	U	148	0.00157	0.009	21.90	5.02	0.017	under LOD	0.002	1.42	0.003	1.81	under LOD	2.84	0.145	0.128
MMOtoDX212*	U	148	0.00703	0.005	410.00	2.27	0.003	0.804	0.002	0.031	0.005	4.40	0.166	0.621	1.790	0.010
MMOtoDX244*	U	149	0.00423	0.005	259.00	1.92	0.003	0.421	0.001	0.030	0.003	2.62	0.136	0.289	1.110	0.006
MMOtoDX211*	U	150	0.00792	0.002	112.00	1.23	0.002	0.144	0	under LOD	0.002	6.94	0.08	under LOD	0.633	0.008
MMOtoDX140	M	181	0.01648	0.010	1028.00	3	0.004	2.06	0.003	0.103	0.011	13.80	0.670	2.240	3.970	0.014
MMOtoDX108	F	184	0.01716	0.010	1035.00	1.45	0.004	2.36	0.003	0.090	0.013	12.40	0.698	0.502	4.000	0.016
MMOtoDX109	F	192	0.02422	0.013	1433.00	2.68	0.017	3.07	0.003	0.168	0.015	18.50	2.380	1.680	6.020	0.025
MMOtoDX312	M	193	0.02443	0.008	1394.00	2.86	0.005	3.69	0.005	0.176	0.021	20.50	0.983	2.600	4.410	0.025
MMOtoDX117	F	197	0.03451	0.016	1825.00	4.92	0.004	5.01	0.007	0.179	0.017	29.40	0.992	4.400	6.280	0.020
MMOtoDX194	M	198	0.02264	0.010	1341.00	3.58	0.006	3.36	0.005	0.138	0.009	19.00	0.696	3.130	5.680	0.018
MMOtoDX41	M	217	0.03487	0.009	1507.00	1.3	0.002	3.32	0.002	0.098	0.011	19.00	0.718	0.869	5.140	0.012
MMOtoDX34	M	218	0.03969	0.016	1161.00	1.56	0.002	3.02	0.003	0.100	0.018	17.60	0.665	1.300	4.860	0.014
MMOtoDX36	M	224	0.02811	0.008	979.00	1.6	0.002	2.13	0.002	0.066	0.010	12.20	0.461	0.597	4.070	0.010

MMOtoDX33	F	225	0.03868	0.014	2040.00	under LOD	0.003	5.08	0.004	0.111	0.024	28.10	1.000	0.970	6.220	0.015
MMOtoDX71	F	232	0.03935	0.012	1349.00	2.31	0.002	3.13	0.004	0.090	0.013	21.20	0.675	1.740	5.020	0.015
MMOtoDX26	F	243	0.04420	0.016	1650.00	2.35	0.002	4.48	0.005	0.105	0.013	26.40	0.726	2.130	6.100	0.016
MMOtoDX78	M	252	0.01770	0.006	1168.00	1.84	0.003	2.18	0.003	0.084	0.013	13.70	0.561	1.000	3.500	0.013
MMOtoDX57	M	255	0.01185	0.006	816.00	1.45	0.014	1.22	0.001	0.043	0.004	7.91	0.317	0.417	3.120	0.015
MMOtoDX79	M	260	0.02569	0.01	1572.00	1.44	0.003	3.04	0.003	0.076	0.012	17.10	0.646	0.694	5.650	0.013
MMOtoDX15	F	262	0.02988	0.007	1393.00	1.3	0.002	3.05	0.002	0.068	0.019	18.50	0.350	0.460	4.730	0.006
MMOtoDX18	F	290	0.04211	0.012	2042.00	1.88	0.003	5.51	0.005	0.129	0.027	31.40	0.825	1.220	6.230	0.014
MMOtoDX16	F	341	0.06731	0.017	2683.00	1.95	0.004	8.6	0.006	0.151	0.026	46.50	0.844	1.760	6.130	0.015

Table S6: Mean values for twelve trace elements expressed in µg/g.

Measurements were initially conducted on 6 undifferentiated, 9 females and 9 males otoliths by ICP OES. Juveniles' samples were then excluded from the statistical analysis since their values resulted under the detection limits of the instrument or outliers' data points. Data are represented as µg/g and approximate. F = females, M = males. Statistical analysis was conducted between females and males for each element but didn't reveal any differences (ANOVA, $p > 0.05$).

Sex	**Ba**		**Ca**		**Co**		**K**		**Li**		**Mg**		**Mn**		**Na**		**P**		**S**		**Sr**		**Zn**	
	Mean	**s.d.**	**Mean**	**s.d.**	**Mean**	**s.d.**	**Mean**	**s.d.**	**Mean**	**s.d.**	**Mean**	**s.d.**	**Mean**	**s.d.**	**Mean**	**s.d.**	**Mean**	**s.d.**	**Mean**	**s.d.**	**Mean**	**s.d.**	**Mean**	**s.d.**
F	1.88	0.63	239827	46538	0.35	0.19	106	35	0.61	0.21	18.0	8.7	2.65	0.81	3476	479	151	136	0.32	0.24	826	249	2.46	1.50
M	1.98	0.55	267782	71102	0.49	0.26	139	46	0.66	0.32	22.3	9.4	2.55	0.98	3358	827	138	45	0.17	0.11	982	255	3.46	1.64

Table S7: Mean values of for eleven element:Ca ratio expressed in µmolMe/molCa.

Measurements were initially conducted on 6 undifferentiated, 9 females and 9 males otoliths by ICP-OES. Undifferentiated samples were then excluded from the statistical analysis since their values resulted under the detection limits of the instrument or outliers' data points. F = females, M = males. Data are represented as µmolMe/molCa and approximate. Statistical analysis was conducted between females and males for each ratio. When difference was significative (K/Ca and Na/Ca) also *p*-value was reported (ANOVA, $p < 0.05$).

Sex	**Ba/Ca**		**Co/Ca**		**K/Ca**			**Li/Ca**		**Mg/Ca**		**Mn/Ca**		**Na/Ca**			**P/Ca**		**S/Ca**		**Sr/Ca**		**Zn/Ca**	
	Mean	**s.d.**	**Mean**	**s.d.**	**Mean**	**s.d.**	***p***	**Mean**	**s.d.**	**Mean**	**s.d.**	**Mean**	**s.d.**	**Mean**	**s.d.**	***p***	**Mean**	**s.d.**	**Mean**	**s.d.**	**Mean**	**s.d.**	**Mean**	**s.d.**
F	2.28	0.52	0.99	0.43	2590	351	**0.04**	14.7	1.4	120	37.78	7.94	1.44	25611	3110	**0.03**	758	544	1207	819	1557	257	6.04	2.70
M	2.26	0.78	1.19	0.48	2209	389		14.0	5.2	135	44.211	7.21	1.44	22199	3142		671	137	1455	945	1696	207	7.68	2.29

References

1. Rasband WS. 2014 ImageJ, U.S. National Institutes of Health, Bethesda, Maryland, USA. http://imagej.nih.gov/ij/.

2. Medalia AI. 1971 Dynamic shape factors of particles. Powder Technol. 4, 117–138. (doi:10.1016/0032-5910(71)80021-9)

3. Tuset VM, Lozano IJ, GonzÍez JA, Pertusa JF, García-Díaz MM. 2003 Shape indices to identify regional differences in otolith morphology of comber, Serranus cabrilla (L., 1758). J. Appl. Ichthyol. 19, 88–93. (doi:10.1046/j.1439-0426.2003.00344.x)

4. Caroselli E, Prada F, Pasquini L, Marzano FN, Zaccanti F, Falini G, Levy O, Dubinsky Z, Goffredo S. 2011 Environmental implications of skeletal micro-density and porosity variation in two scleractinian corals. Zoology 114, 255–264. (doi:10.1016/j.zool.2011.04.003)

5. Fantazzini P et al. 2015 Gains and losses of coral skeletal porosity changes with ocean acidification acclimation. Nat. Commun. 6, 7785. (doi:10.1038/ncomms8785)

6. Pattoura P, Lefkaditou E, Megalofonou P. 2015 Age estimation of juvenile European hake Merluccius merluccius based on otolith microstructure analysis: a slow or fast growth pattern? J. Fish Biol. 86, 907–923. (doi:10.1111/jfb.12598)

7. Kitware~Inc. 2014 The Visualization Toolkit (VTK). Open Source

8. Bradski G. 2000 References. Lang. Learn. 50, 439–461. (doi:10.1111/0023-8333.50.s1.10)

9. Harris CR et al. 2020 Array programming with NumPy. Nature 585, 357–362. (doi:10.1038/s41586-020-2649-2)

10.J arosch D, Heger G. 1986 Neutron diffraction refinement of the crystal structure of aragonite. TMPM Tschermaks Mineral. und Petrogr. Mitteilungen 35, 127–131. (doi:10.1007/BF01140844)

11. Li XG, Lv Y, Ma BG, Wang WQ, Jian SW. 2017 Decomposition kinetic characteristics of calcium carbonate containing organic acids by TGA. Arab. J. Chem. 10, S2534–S2538. (doi:10.1016/j.arabjc.2013.09.026)

Chapter 3. Characterization of fish otolith sulcus acusticus by electron microscopy and micro-CT imaging

(Manuscript in preparation)

Characterization of fish otolith sulcus acusticus by electron microscopy and micro-CT imaging

Manuscript in preparation

Quinzia Palazzo[1,7], Steven Raaijmakers[2], Robert G. Belleman[2], Fiorella Prada[3,7], Jörg U. Hammel[4], Marco Stagioni[5], Simona Fermani[1,6], Jaap Kaandorp[2*], Stefano Goffredo[3,7*], Giuseppe Falini[1,7]*

[1] Department of Chemistry <<Giacomo Ciamician>>, University of Bologna, Via Selmi 2, 40126 Bologna, Italy

[2] Computational Science Lab, University of Amsterdam, Science Park 904, 1098XH, Amsterdam, the Netherlands

[3] Marine Science Group, Department of Biological, Geological and Environmental Sciences, University of Bologna, Via Selmi 3, 40126 Bologna, Italy

[4] Institute of Materials Physics, Helmholtz-Zentrum Geesthacht, Max-Planck-Straße 1, Geesthacht, D-21502, Germany

[5] Laboratory of Fisheries and Marine Biology at Fano, Department of Biological, Geological and Environmental Sciences, University of Bologna, Viale Adriatico 1/N, 61032, Fano, Italy

[6] CIRI Health Sciences & Technologies (HST), University of Bologna, I-40064 Bologna, Italy

[7] Fano Marine Center, The Inter-Institute Center for Research on Marine Biodiversity, Resources and Biotechnologies, Viale Adriatico 1/N 61032 Fano, Italy

* corresponding authors: Jaap Kaandorp, J.A.Kaandorp@uva.nl;
Stefano Goffredo, s.goffredo@unibo.it; Giuseppe Falini, giuseppe.falini@unibo.it

ABSTRACT

Fishes are able to use auditory cues to discriminate between sounds of different amplitude and frequency between calls that differ in their temporal characteristics and to seek out the location of a sound source. For its importance, fishes have evolved various physiological adaptations for sound reception and production. The size, the shape of otoliths and their sub-anatomical characteristics (i.e., sulcus acusticus), likely influence the frequencies that can be detected and the sensitivity (auditory threshold) to those frequencies. Hence, some otolith's traits are thought to have functional significance but have generally received less attention so far. Thus, the wide variability in otoliths morphologies is likely linked to the diversity in hearing mechanisms and capabilities among different species. Therefore, exploring the relationships between the features of otoliths and their ecological-behavioral function (i.e., structure–function relationships) within the same species, using different size class that exhibit different habits and ecological changes during the ontogenesis, can provide clues about fish's hearing mechanisms and capabilities while avoiding phylogenetic bias. In this work, the sulcus acusticus and its sub-regions (ostial colliculum, caudal colliculum and collum) were extensively characterized and the corresponding area and volume were measured in three sex groups (undifferentiated, females and males) of *Merluccius Merluccius* individuals from western Adriatic Sea. Furthermore, an investigation of the ultrastructure of the proximal surface was conducted by scanning electron microscopy (SEM). We showed that undifferentiated otoliths had a higher value of sulcus volume:otolith ratio (SV:OV) compared to differentiated' otoliths. Through the SEM investigation it was observed that the morphology and size of crystals changed depending on the otolith area. In addition, developmental changes in the ultrastructure of the collum region were observed during the ontogenesis. Indeed, undifferentiated samples showed irregular pits of variable size in this region which tended to be filled up during the growth and disappearing in larger size samples. Future virtual experiments of vibroacoustic will be addressed in order to establish the shape/structure–function relationships in otoliths during fish ontogenesis and between sex and, consequently, investigate if there are any differences in the otolith response to sound waves which could enhance auditory abilities in a certain habitat or improve fish communication in specific contexts.

Keywords: *Merluccius merluccius*, Adriatic Sea, micro-CT scanning, computational biology

INTRODUCTION

Sound is a major sensory channel for fishes and plays a key role in their ecology and life-history strategies, since it is used for communication between conspecifics or heterospecifics, navigation, feeding, detection of predators, reproductive interactions, and habitat selection [1–3]. For its importance, fishes have evolved various physiological adaptations for sound reception and production [2,3]. The size and shape of otoliths likely influence the frequencies that can be detected and the sensitivity (auditory threshold) to those frequencies [4]. Thus, the wide variability in ear morphologies of fishes and particularly in otoliths is likely linked to the diversity in hearing mechanisms and capabilities among different species [5].

Fishes obtain substantial information about the surrounding environment by analyzing the "acoustic scene" or soundscape, which is the ensemble of ambient sounds associated with a specific location at a particular time [6]. Because sound propagates more efficiently and over large distances underwater compared with air, it provides fishes with directional information from far greater distances than do other sensory stimuli [3]. However, sound signal changes in relation to the environment (e.g., deep ocean vs shallow coastal waters, temperate vs tropical environments) because the speed and the medium density upon which sound propagates are dependent on the pressure, temperature, and salinity of the water [7]. Pressure increases with depth, so the speed of sound does too. Furthermore, an increase in temperature or in salinity produce an increase in sound speed [7]. Consequently, many of the most important aspects of hearing are likely to have evolved to enhance analysis of the soundscape [8] and therefore, also the acoustic environment should be taken into account when investigating the hearing capabilities of fishes.

Otoliths first form in embryo and continue to grow throughout the life of an individual, with a double-banded increment composed of a calcium carbonate-rich region and an organic matrix-rich region being deposited daily, similarly to the growth bands observed in corals. Consequently, otolith structures can also vary substantially during fish growth in response to both physiological and ecological ontogenetic changes, and/or to differences in the acoustic environment related to a diverse habitat occupied by juveniles and adults [9,10]. The otolithic organs act as mechanoreceptor involved in hearing through the detection of particle motion [9,11,12]. However, determining hearing capabilities of fishes is a complex problem that requires dealing not only with the animal, but the acoustic environment, and the experimental techniques and approach used in making the determinations [3]. Furthermore, understanding the way the auditory organs analyze sound quality and the mechanisms that enable fish to discriminate between sounds from different directions pose more difficulties [13]. Nevertheless, the investigation of the features of the auditory parts of the fish

ear (the otolith organs) can be used in support of the hearing data.

There is very substantial variation in the morphology of the ears of fishes and particularly in the regions associated with hearing [14–16], leading to suggest that there is very substantial diversity in hearing mechanisms (and potentially capabilities) in different species [9]. Indeed, otolith shape's morphology is species-specific and undergoes ontogenetic changes that are linked to hearing potential [17]. Furthermore, the size and shape of otoliths are likely to influence 1) the frequencies that can be detected and 2) the sensitivity (auditory threshold) to those frequencies [18]. Therefore, they can be used to explore the relationships between the morphology of auditory structures and their ecological-behavioral function (i.e., structure–function relationships) using species that differ in their ecology [19–21] or to predict behavioral patterns through otolith morphological examination [17]. However, just few investigations have focused so far on the relation between the morphological and ultrastructural differences of otoliths and the eco-morphological adaptations of the auditory system to habitat features such as water depth, feeding modalities, spatial niches, and mobility [22–25]. In addition to otolith' shape and its mass, another anatomical feature within the otolith, the sulcus acuustics, is thought to have functional significance but have generally received less attention so far [26,27]. The internal face of the saccular otolith (sagitta) houses the sulcus acusticus, characterized by a groove [28]. The sulcus acusticus corresponds to a depressed portion of the proximal face of the otolith, which is in contact with the sensory epithelium (i.e., macula) which is composed of numerous hair cells [29]. Therefore, the shape of the sulcus closely matches the shape of the respective macula that is overlain by the otolith [27]. Its characteristics may play an important role in determining the relative motion between the otolith and its respective sensory epithelium [28]. Difference in the 3D shape of sulcus acusticus may alter the mechanical resistance provoked by a different otolithic membrane, which consequently affect the stimulation pattern of the sensory hair cells [30]. The size of the sulcus acusticus relative to the size of saccular otolith is also assumed to alter the hearing abilities of the fish. Indeed, ecomorphological studies indicate that the ratio of sulcus size (2D sulcus area, used as a proxy for macula size) to otolith size (area of the macula-oriented face of the otolith) seems to be correlated with habitat features such as water depth, food or spatial niches, and mobility, but may also vary during ontogeny [26,31]. However, one of the major difficulties concerning this issue that have been faced so far, is related to the reliably and reproducibility in the quantification of the dimensions (area and volume) of the sulcus acusticus and consequently, of the sensory epithelium [26].

The traditional view for the transduction mechanism of the sound proposes that fish tissue has similar acoustic properties (in terms of density and elasticity) to the surrounding water [12]. When the fish is reached by a sound, the denser otoliths respect the surrounding medium, move in relation to receptors

with a lag because of their inertia, thereby creating the deformation of the directional polarized sensory hair cells in response to mechanical stimulation [13,32]. The geometrical characteristics of the sulcus acusticus may influence/change the dynamics of the relative motion between the otolith and sensory epithelium due to differences in mechanical resistance provoked by a different otolithic membrane, which consequently affect the stimulation pattern of the sensory hair cells [33,34].

The European hake is a teleost fish of the genus Merluccius. This species is a major component of the demersal fish assemblages and is distributed over a wide depth range (20−1000 m) throughout the Mediterranean Sea and the northeast Atlantic region [35,36]. The European hake is an important predator of deeper shelf-upper slope Mediterranean communities. It has always been an important food resource for the population of western Europe throughout history. Previous studies, which were also conducted by experimental trawl surveys carried out in the Mediterranean [37,38] have observed a different spatial (bathymetric) distribution during the ontogenesis of this species, while no differences were highlighted in the spatial distribution between female and male [39–43]. They have shown that small European hakes have the greatest preference for depths of 170–220 m, while larger hakes persist on the continental shelf with a preference for water 70–100 m deep, especially when they reach 18–20 cm long [39–41,44]. It has been verified that such migration is induced by a change in trophic requirements [45]. Indeed, the bathymetric changes are also attended by a variation of the diet that would coincide with the migration of juvenile hake from nursery areas on the shelf break and upper slope to the mid-shelf [44,46]. The behavioral and ecological changes related to the ontogenesis of *Merluccius merluccius* in the central Adriatic Sea led to hypothesize that they may also have an impact on the macro- and micro-scale characteristics of the otolith.

Here, for the first time, we characterize the sulcus acusticus and its subregions (ostial colliculum, caudal colliculum and collum) and measure the corresponding area and volume in juveniles, females, and males *Merluccius Merluccius* individuals. We present a method to characterize the anatomical information of the sulcus acusticus from scans obtained by micro-CT imaging of sagittal otoliths.

The changes observed in the otolith features and sulcus acusticus regions during the growth could be linked to an eco-morphological adaptation to different biological, behavioral, and environmental characteristics between juveniles and adults, which could have a functional meaning in terms of otolith response to sound waves (shape/structure–function relationships). Based on the outcomes of this first investigation, the use of innovative approaches is promising in highlighting differences in otoliths that could bring functional significance in specific ecological and behavioral contexts. Furthermore, the results obtained from this study can also provide inputs for further investigations aiming to understand otolith growth process according to fish size and gender and to explore the sources of otolith morphological variability during ontogenesis.

Future virtual experiments of vibroacoustic will be addressed to establish the shape/structure–function relationships in otoliths during fish ontogenesis and between sex and, consequently, investigate if there are any differences in the otolith response to sound waves which could enhance auditory abilities in a certain habitat or improve fish communication in specific contexts.

MATERIALS AND METHODS

Sample collection

A total of 52 individuals, 18 juveniles (J) and 34 adults (A), consisting of 17 females (F) and 17 males (M), of European hake (*Merluccius merluccius*) were collected in the western Adriatic Sea by local fishermen through commercial benthic trawlers, longlines and gillnets. The Mediterranean hake stocks are attributable to three main genetic clusters corresponding to the western, central, and eastern Mediterranean populations [37,47,48]. Previous genetic studies based on molecular markers have not consistently defined a subdivision within western Adriatic hake stocks [49,50]. Therefore, the samples used in this study were considered as belonging to the same fishing stocks.

Each individual was processed measuring the total length (± 1 cm) and weight (± 1 g). The macroscopic inspection of the gonads was performed to differentiate among juvenile, female, and male samples. In order to define these three sex categories, the codes of sex maturity for bony fish reported in the MEDITS-Handbook were applied [51]. The juvenile size class included individuals which do not have yet reached the macroscopic development of the gonads (undetermined and immature samples) and a total body length <15 cm. The adult size class included 17 males (M) and 17 females (F) having gonads macroscopically developed (sex distinguished by naked eye) and total body length 15-50 cm.

Both sagittal otoliths were removed, cleaned, air-dried, and stored. For the following analysis, the right otoliths were arbitrarily chosen since no scientific evidence suggests a side dimorphism in otoliths in this species.

Ultrastructure of otolith proximal surface

Images of otolith proximal surface of 12 juvenile individuals and 16 adult samples (8 females and 8 males) were collected by SEM using a Philips SEM 515 with a tension of 15 kV. The samples were glued on carbon tape, dried in a desiccator, and coated with 20 nm of gold prior image them.

Morphological analysis of otoliths and their sub-anatomical characteristics based on microcomputed tomography

To investigate the 3D shape of a subset of 24 otolith samples, high resolution microcomputed tomography (Micro-CT) scans were acquired with a GE phoenix X-ray Nanotom S. The isotropic voxel sizes in the scans varied from 2.024 to 8.333 μm depending on the actual size of the investigated otolith sample. The dataset consisted of 6 juvenile individuals and 18 adult samples, spitted in 9 females and 9 males having the same fish length to remove the impact of the different fish body size units and avoiding the standardization step.

All image processing steps (Fig. S1, S2) and the developing method to measure the sulcus acusticus (S3) and its portioned three sub anatomical regions (ostial colliculum, caudal colliculum and callum) were performed with Python3, in combination with Visualization Toolkit (VTK) [52], OpenCV [53] and NumPy [54] open-source libraries. The 3D rendering visualization of the objects were obtained with ParaView freeware.

Analysis of the curvature angles

The angles of curvature of the extremes of the longitudinal section of the otoliths were calculated using the Grasshopper plugin supported by the Rhinoceros modelling program. The procedure applied are summarized in the following three points (Fig. S4): (1) first, the mesh was divided with a vertical plane orthogonal to the otolith, obtaining a flat section containing the silhouette of the object. Then it was projected for convenience at the origin of the xy plane; (2) after mapping the contour polyline of the section, the reference points for calculating the angle of curvature (i.e., the vertical extremes of the section), the vertical centerline point, and the horizontal end of the section were easily obtained; (3) as a last step, the vertical lines passing through the center point and the horizontal end of the section were drawn. Then, the lines joining the two points just mentioned and the vertical ends of the section were also drawn. Once the reference lines have been obtained, the angle between them was calculated.

The use of Grasshopper and a single algorithm for calculating the angles of curvature resulted as an advantageous method to obtain automated and rapid measurements applicable to multiple heterogeneous meshes containing the 3D models of the otoliths.

Statistical analysis

The relationships of otolith parameters with fish length were determined for juveniles, females, males and for all the individuals combined. The best fit with the data to describe the relationships between otolith variables and fish somatic growth was defined with a non-linear function (power model) y = axb, where “y” is the otolith parameter, “x” is fish length, “a” is the factor, and “b” is the exponent. The parameters “a” and “b” were estimated through the linear regression analysis on log-transformed

data: log (y) = log (a) + b log (x). The relationships between otolith parameters and fish size were determined first for the entire group of individuals and then separately for juveniles, females, and males, so that four growth curves were derived for each parameter. The significance of the correlation was verified using Pearson's correlation coefficient. The statistical differences in regression slopes between sexes were examined comparing the confidence intervals of regression coefficients. Statistical analyses were performed using SPSS 20.0.

RESULTS

Ultrastructure of otolith proximal surface

The external crystalline morphology of the proximal surface (internal or sulcal side) of saccular otoliths (sagitta) of juveniles, females, and males' individuals of *Merluccius merluccius* were investigated by scanning electron microscopy (SEM, Fig. 1, S5).

At higher magnifications, the surface of the otoliths resolves as small aragonitic crystals (Fig. S5). The morphology and size of crystals depend on the otolith area. All the samples showed a specific trait: the presence of rounded spots of crystals at the boundary between the ostial colliculum and the anteriorly outer area (Fig. S5). These spots are presented in all the individuals and seem to show the same crystal texture (small and thinner acicular crystals) observed inside the sulcus acusticus. Here, the microcrystalline texture is composed by massive groups of acicular crystals. Outside the sulcus and the isolated spots, flat crystals characterize the crystalline texture (Fig. S5).

Developmental changes in the ultrastructure of the collum region, the bridge that join the ostium and the cauda of the sulcus acusticus, are observed. Indeed, juveniles' samples show irregular pits of variable size in this region (Fig. 1 A-B) which tend to be filled up during the growth, disappearing in the adult samples (Fig. 1 C-F).

Morphological analysis of otoliths and their sub-anatomical characteristics based on microcomputed tomography

Otolith volume (OV), otolith area (OA), sulcus volume (SV), sulcus area (SA), the area and volume of the three sulcus acusticus sub regions (ostial colliculum, caudal colliculum and collum) and their percentage with respect to the entire sulcus acusticus were measured and reported in Table 1.

Relationships between fish size vs otolith and sulcus measures for juveniles, females, males and all the data together were described using power regression model between measures (Tables 1,2; Fig.3-7; S6-S14). The fitted power equation for the fish TL (total length) vs SA showed a positive allometric

growth, while the relationship between the OA vs SA showed a negative allometric growth. The relationship between SV vs TL and SV vs OV revealed a positive allometric growth for both the curves (Fig. 3,4). Sulcus area to otolith area ratio (SA:OA) decreased during the ontogenesis (Fig. 5, Table 2). The mean SA:OA ratio for juveniles was 0.285, for females 0.239, and for males 0.248 (Table 1). This showed that mature hakes have a considerably lower value than the juveniles. Anyway, the average SA:OA ratio for males is not statistically different from females. The box plot of Figure 8 demonstrates the distribution of the SA:OA and SV:OV ratio per gender. Differently, no difference in the ratio between the sulcus volume and otolith volume (SV:OV) was revealed (Fig. 5,8).

In order to remove the effect size in the comparison of the ratios of the sulcus vs otolith measurements between juveniles and adults, the sulcus and otolith measures were normalized to a sphere-like objects (SAs, SVs, OAs; OVs; Table 1). Then, the following relations were obtained (Fig. S9, S10): a) the ratios of sulcus area normalized to a sphere-like objects (SAs) and the normalized otolith volume (OVs) with fish length were significant just for females and showed a positive allometric relationship through ontogenetic development; b) the ratios of SAs and the volume of sulcus normalized to a sphere-like objects (SVs) with fish length resulted significant only for male and negatively correlated; c) the ratios of SVs and the area of otolith normalized to a sphere-like objects (OAs) with fish length were significant only for the general curves (all the data pollen) and showed a negative relations; d) the ratios of OAs and OVs with fish length were significant only for the general curve and showed a positive allometric regression.

The percentage of the sulcus acusticus surface and volume occupied by the area and volume of ostial colliculum, caudal colliculum and the collum were also measured (Table 1; Fig. 9, S14) and revealed a change in the relative ratio of area and volume of the sulcus acusticus three sub-regions during the ontogenesis. In detail, the percentage of the sulcus acusticus surface and volume occupied by the area and volume of ostial colliculum and collum decrease during the growth (Table 1) showing an inverse allometric relationship with fish length (Fig. 6). Differently, the relationship between the percentage of the sulcus acusticus surface and volume occupied by the area and volume of caudal colliculum increased during the growth and showed a negative allometric growth (Fig. 6, 9; Table 1). This shows an asymmetric development of these three sulcus acusticus regions during otolith growth.

Analysis of the curvature angles

A stronger three-dimensional curvature of both otolith and sulcus acusticus is observed in adults respect juveniles (Fig. 2,7). The juveniles' samples are flatter than the adult ones which tend to curve during the growth. The process of curvature is more accentuated for the ostial side respect the caudal one for both otolith silhouette and the reconstructed shape of the macula which correspond to the

positive mould of the sulcus area.

DISCUSSION

The otolith's changes observed during the growth could be related to a mixture of effects reflecting endogenous processes such as development, and external conditions associated with changes in habitat, behavior, and diet.

The internal face of the saccular otolith houses the sulcus acusticus characterized by a groove. The sulcus is an important anatomical structure since it is in contact with the sensory epithelium, or macula. For most teleost fishes, including the hake, there exists a morpho-anatomical relation between the sulcus and the macula [10]. The sulcus size is therefore often used as a proxy for the size of the macula.

Although the overall shape of the otolith and sulcus are the result of its ultrastructure patterns (checks, microincrements), few studies have considered the discontinuities and crystal shape within the otoliths as part of otolith morphology (Lombarte 1995). The investigations of the otolith proximal surface performed by SEM revealed ontogenetic differences in the narrowing part of the sulcus called collum (Fig. 1). This region presented several pores in small individuals that disappeared in the adults. This observation may indicate a genetic regulation in the growth of the sulcus. Some sculpturing was found inside the sulcus and the region within the sulcus acusticus shows a more complex structure than the external ones.

The relative sensory area of the sagittal otolith, approximated by the area of the sulcus acusticus, relative to the total area of the sagitta (S:O), has been a focus of investigations of auditory structure–function to date, owing to the relationships between sensory area and hearing frequency and sensitivity (Gauldie 1988; Popper and Lu 2000; Schulz-Mirbach et al. 2019). The ratio between the sulcus size and the total otolith size (S:O ratio) is correlated to habitat features (such as water depth, diet, and mobility) and has been found to vary among species [10]. Moreover, the S:O ratio influences the hearing abilities, where larger S:O ratios are linked to better hearing abilities [11]. However, the effects of the ratio have not been researched extensively since it is difficult to reliably quantify the dimensions of the sulcus [15]. In Lombarte [16], the S:O relation is examined for the *Merluccius capensis* and *Merluccius paradoxus*. To ascertain whether their findings may be applied also to *Merluccius merluccius*, we examined the micro-CT scans containing 24 right saccular otoliths of hakes to answer to the following research questions: How does the saccular sulcus area and volume relate to the saccular otolith size for the European hake? The ratios between sulcus and otolith

measures remain constant or vary during the ontogenesis? Are there any differences in the ratios between females and males?

The relationship between the sulcus area (SA) and the saccular otolith area (OA) is linear for the European hake. The SA growth with respect to the total length is negative allometric. This also applies to the OA growth with respect to the total length. The average SA : OA ratio for mature hakes is significantly lower in comparison to juveniles. This is following our assumption that the SA : OA ratio is higher for juvenile hakes which typically inhabit the sea at deeper levels and therefore are more dependent on their hearing. However, a higher presence of protuberances, as observed for mature hakes, presumably contributes to a lower SA : OA ratio. Since the proximal surface barely contains any protuberances, it would be more appropriate to examine the proximal surface area of the sulcus and the otolith to reduce the influence of the protuberances on the ratio. The relationship between the sulcus volume (SV) and the saccular otolith volume (OV) is linear. The SV growth relative to the total length is negative allometric. Likewise, the OV growth with respect to the total length is positively allometric. The difference between the slopes for both relationships is less significant in comparison to the surface area alternatives. Consequently, the SV : OV ratios per gender are more evenly distributed in comparison to the SA : OA ratio. This implies that the effect of the protuberances on the SV : OV ratio is less significant compared to the SA : OA ratio.

In this study we also applied a method to segmentate the sulcus acoustics into its three parts: ostial colliculum, caudal colliculum and the collum (the central narrowing of the sulcus) and we observed that these three parts tend to growth differently during the ontogenesis.

This study provided a new 3D approach to investigate the otolith and the sulcus acustics that emphasizes features not revealed with the canonical methods based on 2D descriptors. In detail, we presented a method to characterize some anatomical and sub-anatomical information from scans obtained by micro-CT imaging of sagittal otoliths of European hake specimens of different sizes and sex.

ACKNOWLEDGMENTS

The research leading to these results has been conceived under the International PhD Program "Innovative Technologies and Sustainable Use of Mediterranean Sea Fishery and Biological Resources (http://www.fishmed-phd.org/). This study represents partial fulfilment of the requirements for the Ph.D. thesis of Quinzia Palazzo".

REFERENCES

1. Fay RR, Simmons AM. 1999 The Sense of Hearing in Fishes and Amphibians. (doi:10.1007/978-1-4612-0533-3_7)
2. Putland RL, Montgomery JC, Radford CA. 2019 Ecology of fish hearing. J. Fish Biol. (doi:10.1111/jfb.13867)
3. Popper AN, Hawkins AD, Sand O, Sisneros JA. 2019 Examining the hearing abilities of fishes. J. Acoust. Soc. Am. 146, 948–955. (doi:10.1121/1.5120185)
4. Hawkins AD, Rasmussen KJ. 1978 The calls of gadoid fish. J. Mar. Biol. Assoc. United Kingdom (doi:10.1017/S0025315400056848)
5. Brawn VM. 1961 Sound Production By the Cod (Gadus Callarias L.). Behaviour (doi:10.1163/156853961X00150)
6. Popper AN, Fay RR. 2011 Rethinking sound detection by fishes. Hear. Res. 273, 25–36. (doi:10.1016/j.heares.2009.12.023)
7. Putland RL, Montgomery JC, Radford CA. 2019 Ecology of fish hearing. J. Fish Biol. 95, 39–52. (doi:10.1111/jfb.13867)
8. Popper AN, Hawkins AD. 2019 An overview of fish bioacoustics and the impacts of anthropogenic sounds on fishes. J. Fish Biol. 94, 692–713. (doi:10.1111/jfb.13948)
9. Popper AN, Fay RR. 1993 Sound Detection and Processing by Fish: Critical Review and Major Research Questions (Part 1 of 2). Brain. Behav. Evol. 41, 14–25. (doi:10.1159/000113821)
10. Campana SE. 1999 Chemistry and composition of fish otoliths: Pathways, mechanisms and applications. Mar. Ecol. Prog. Ser. 188, 263–297. (doi:10.3354/meps188263)
11. Popper AN, Platt C. 1983 Sensory surface of the saccule and lagena in the ears of ostariophysan fishes. J. Morphol. 176, 121–129. (doi:10.1002/jmor.1051760202)
12. Popper AN, Hawkins AD. 2018 The importance of particle motion to fishes and invertebrates. J. Acoust. Soc. Am. 143, 470–488. (doi:10.1121/1.5021594)
13. Krysl P, Hawkins AD, Schilt C, Cranford TW. 2012 Angular Oscillation of Solid Scatterers in Response to Progressive Planar Acoustic Waves: Do Fish Otoliths Rock? PLoS One 7, e42591. (doi:10.1371/journal.pone.0042591)
14. Schulz-Mirbach T, Ladich F. 2016 Diversity of inner ears in fishes: Possible contribution towards hearing improvements and evolutionary considerations. In Advances in Experimental Medicine and Biology, (doi:10.1007/978-3-319-21059-9_16)
15. Ladich F, Schulz-Mirbach T. 2016 Diversity in fish auditory systems: One of the riddles of sensory biology. Front. Ecol. Evol. 4. (doi:10.3389/fevo.2016.00028)
16. Schulz-Mirbach T, Ladich F, Plath M, Heß M. 2019 Enigmatic ear stones: what we know about the functional role and evolution of fish otoliths. Biol. Rev. (doi:10.1111/brv.12463)

17. Taylor MD, Fowler AM, Suthers IM. 2020 Insights into fish auditory structure–function relationships from morphological and behavioural ontogeny in a maturing sciaenid. Mar. Biol. 167, 21. (doi:10.1007/s00227-019-3619-9)

18. Gauldie R. 1988 Function, form and time-keeping properties of fish otoliths. Comp. Biochem. Physiol. Part A Physiol. 91, 395–402. (doi:10.1016/0300-9629(88)90436-7)

19. Norton SF, Luczkovich JJ, Motta PJ. 1995 The role of ecomorphological studies in the comparative biology of fishes. Environ. Biol. Fishes (doi:10.1007/BF00005921)

20. Aguirre H, Lombarte A. 1999 Ecomorphological comparisons of sagittae in Mullus barbatus and M. surmuletus. J. Fish Biol. (doi:10.1006/jfbi.1999.0974)

21. Lombarte A, Popper AN. 2004 Quantitative changes in the otolithic organs of the inner ear during the settlement period in European hake Merluccius merluccius. Mar. Ecol. Prog. Ser. (doi:10.3354/meps267233)

22. Popper AN, Ramcharitar J, Campana SE. 2005 Why otoliths? Insights from inner ear physiology and fisheries biology. In Marine and Freshwater Research, (doi:10.1071/MF04267)

23. Gauldie R. 2002 An eco-morphological explanation of individual variability in the shape of the fish otolith: comparison of the otolith of Hoplostethus atlanticus with other species by depth. J. Fish Biol. 60, 1204–1221. (doi:10.1006/jfbi.2002.1938)

24. Capoccioni F, Costa C, Aguzzi J, Menesatti P, Lombarte A, Ciccotti E. 2011 Ontogenetic and environmental effects on otolith shape variability in three Mediterranean European eel (Anguilla anguilla, L.) local stocks. J. Exp. Mar. Bio. Ecol. (doi:10.1016/j.jembe.2010.11.011)

25. Deng X, Wagner HJ, Popper AN. 2013 Interspecific variations of inner ear structure in the deep-sea fish family melamphaidae. Anat. Rec. (doi:10.1002/ar.22703)

26. Schulz-Mirbach T, Ladich F, Plath M, Heß M. 2019 Enigmatic ear stones: what we know about the functional role and evolution of fish otoliths. Biol. Rev. 94, 457–482. (doi:10.1111/brv.12463)

27. Schulz-Mirbach T, Heß M, Metscher BD. 2013 Sensory epithelia of the fish inner ear in 3D: Studied with high-resolution contrast enhanced microCT. Front. Zool. 10, 1. (doi:10.1186/1742-9994-10-63)

28. Tuset VM, Lombarte A, Assis CA. 2008 Otolith atlas for the western Mediterranean, north and central eastern Atlantic. Sci. Mar. 72, 7–198.

29. Fay RR, Popper AN. 1978 Structure and function in teleost auditory systems. J. Acoust. Soc. Am. (doi:10.1121/1.2004089)

30. Ramcharitar J, Popper AN. 2004 Masked auditory thresholds in sciaenid fishes: A comparative study. J. Acoust. Soc. Am. 116, 1687–1691. (doi:10.1121/1.1771614)

31. Schulz-Mirbach T, Ladich F, Riesch R, Plath M. 2010 Otolith morphology and hearing abilities in cave- and surface-dwelling ecotypes of the Atlantic molly, Poecilia mexicana (Teleostei: Poeciliidae). Hear. Res. 267, 137–148. (doi:10.1016/j.heares.2010.04.001)
32. Radford CA, Montgomery JC, Caiger P, Higgs DM. 2012 Pressure and particle motion detection thresholds in fish: A re-examination of salient auditory cues in teleosts. J. Exp. Biol. (doi:10.1242/jeb.073320)
33. Schulz-Mirbach T, Heß M, Metscher BD. 2013 Sensory epithelia of the fish inner ear in 3D: Studied with high-resolution contrast enhanced microCT. Front. Zool. 10, 1–11. (doi:10.1186/1742-9994-10-63)
34. Ramcharitar JU, Deng X, Ketten D, Popper AN. 2004 Form and function in the unique inner ear of a teleost: The silver perch (Bairdiella chrysoura). J. Comp. Neurol. (doi:10.1002/cne.20192)
35. Fischer W, Schneider M, Bauchot M-L. 1987 Fiches FAO d'identification des espèces pour les besoins de la pêche : Mediterranée et Mer Noir / Volume II / Vertèbrés : Rajidae. In Fiches FAO d'identification des espèces pour les besoins de la pêche : Mediterranée et Mer Noir / Volume II / Vertèbrés,
36. Lloret-Lloret E, Navarro J, Giménez J, López N, Albo-Puigserver M, Pennino MG, Coll M. 2020 The Seasonal Distribution of a Highly Commercial Fish Is Related to Ontogenetic Changes in Its Feeding Strategy. Front. Mar. Sci. 7, 1–17. (doi:10.3389/fmars.2020.566686)
37. Orsi Relini L, Papaconstantinou C, Jukic-Peladic S, Souplet A, Gil de Sola L, Piccinetti C, Kavadas S, Rossi M. 2002 Distribution of the Mediterranean hake populations (Merluccius merluccius smiridus Rafinesque, 1810) (Ostheichthyes: Gadiformes) based on six years monitoring by trawl-surveys: some implications for management. Sci. Mar. 66, 21. (doi:10.3989/scimar.2002.66s221)
38. Abella A, Fiorentino F, Mannini A, Orsi Relini L. 2008 Exploring relationships between recruitment of European hake (Merluccius merluccius L. 1758) and environmental factors in the Ligurian Sea and the Strait of Sicily (Central Mediterranean). J. Mar. Syst. 71, 279–293. (doi:10.1016/j.jmarsys.2007.05.010)
39. Bartolino V, Ottavi A, Colloca F, Ardizzone GD, Stefánsson G. 2008 Bathymetric preferences of juvenile European hake (Merluccius merluccius). ICES J. Mar. Sci. 65, 963–969. (doi:10.1093/icesjms/fsn079)
40. Riccioni G, Stagioni M, Piccinetti C, Libralato S. 2018 A metabarcoding approach for the feeding habits of European hake in the Adriatic Sea. Ecol. Evol. 8, 10435–10447. (doi:10.1002/ece3.4500)
41. Stagioni M, Montanini S, Vallisneri M. 2011 Feeding Habits of European Hake, Merluccius

Merluccius (Actinopterygii: Gadiformes: Merlucciidae), from the Northeastern Mediterranean Sea. Acta Ichthyol. Piscat. 41, 277–284. (doi:10.3750/AIP2011.41.4.03)

42. Philips AE, Ragheb E. 2013 Reproductive Biology of European Hake Merlucciusmerluccius (Linnaeus , 1758) in the Egyptian Mediterranean Waters. Egypt. J. Aquat. Biol. Fish. (doi:10.12816/0011051)

43. Sion L et al. 2019 Spatial distribution pattern of european hake, merluccius merluccius (Pisces: Merlucciidae), in the mediterranean sea. Sci. Mar. 83, 21–32. (doi:10.3989/scimar.04988.12A)

44. Stagioni M, Montanini S, Vallisneri M. 2011 Feeding Habits of European Hake, Merluccius Merluccius (Actinopterygii: Gadiformes: Merlucciidae), from the Northeastern Mediterranean Sea. Acta Ichthyol. Piscat. 41, 277–284. (doi:10.3750/AIP2011.41.4.03)

45. Tamario C, Sunde J, Petersson E, Tibblin P, Forsman A. 2019 Ecological and Evolutionary Consequences of Environmental Change and Management Actions for Migrating Fish. Front. Ecol. Evol. 7, 1–24. (doi:10.3389/fevo.2019.00271)

46. Andaloro F, Arena P, Prestipino Giarritta S. 1985 Contribution to the knowledge of the age, growth and feeding of hake Merluccius merluccius (L., 1758) in the Sicilian Channel. FAO Rapp. Pech. Fish. Rep.

47. Mattiucci S, Abaunza P, Ramadori L, Nascetti G. 2004 Genetic identification of Anisakis larvae in European hake from Atlantic and Mediterranean waters for stock recognition. J. Fish Biol. 65, 495–510. (doi:10.1111/j.0022-1112.2004.00465.x)

48. Castillo AGF, Alvarez P, Garcia-Vazquez E. 2005 Population structure of Merluccius merluccius along the Iberian Peninsula coast. ICES J. Mar. Sci. 62, 1699–1704. (doi:10.1016/j.icesjms.2005.06.001)

49. Milano I et al. 2014 Outlier SNP markers reveal fine-scale genetic structuring across European hake populations (Merluccius merluccius). Mol. Ecol. 23, 118–135. (doi:10.1111/mec.12568)

50. Lundy CJ, Moran P, Rico C, Milner RS, Hewitt GM. 1999 Macrogeographical population differentiation in oceanic environments: A case study of European hake (Merluccius merluccius), a commercially important fish. Mol. Ecol. 8, 1889–1898. (doi:10.1046/j.1365-294X.1999.00789.x)

51. Medits-Handbook. 2017 MEDITS Working Group. Version n., 106.

52. Kitware~Inc. 2014 The Visualization Toolkit (VTK). Open Source

53. Bradski G. 2000 References. Lang. Learn. 50, 439–461. (doi:10.1111/0023-8333.50.s1.10)

54. Harris CR et al. 2020 Array programming with NumPy. Nature 585, 357–362. (doi:10.1038/s41586-020-2649-2)

55. De Vries H. 1950 The mechanics of the labyrinth otoliths. Acta Otolaryngol.

(doi:10.3109/00016485009118384)
56. Lychakov D V, Redbane YT. 1993 Effect of otolith shape on directional sound perception in fish. J. Evol. Biochem. Physiol. 28, 707–714. (doi:10.1016/j.heares.2006.03.019)
57. Lychakov DV, Rebane YT. 2005 Fish otolith mass asymmetry: morphometry and influence on acoustic functionality. Hear. Res. 201, 55–69. (doi:10.1016/j.heares.2004.08.017)
58. Lychakov DV, Rebane YT, Lombarte A, Fuiman LA, Takabayashi A. 2006 Fish otolith asymmetry: Morphometry and modeling. Hear. Res. 219, 1–11. (doi:10.1016/j.heares.2006.03.019)
59. Schulz-Mirbach T, Olbinado M, Rack A, Mittone A, Bravin A, Melzer RR, Ladich F, Heß M. 2018 In-situ visualization of sound-induced otolith motion using hard X-ray phase contrast imaging. Sci. Rep. 8, 1–12. (doi:10.1038/s41598-018-21367-0)
60. Sand O, Michelsen A. 1978 Vibration measurements of the perch saccular otolith. J. Comp. Physiol. ? A 123, 85–89. (doi:10.1007/BF00657346)
61. Söllner C, Burghammer M, Busch-Nentwich E, Berger J, Schwarz H, Riekel C, Nicolson T. 2003 Control of crystal size and lattice formation by starmaker in otolith biomineratization. Science (80-.). (doi:10.1126/science.1088443)
62. Berg F, Almeland OW, Skadal J, Slotte A, Andersson L, Folkvord A. 2018 Genetic factors have a major effect on growth, number of vertebrae and otolith shape in Atlantic herring (Clupea harengus). PLoS One (doi:10.1371/journal.pone.0190995)
63. Campana SE. 1999 Chemistry and composition of fish otoliths: Pathways, mechanisms and applications. Mar. Ecol. Prog. Ser. (doi:10.3354/meps188263)
64. Vignon M, Morat F. 2010 Environmental and genetic determinant of otolith shape revealed by a non-indigenous tropical fish. Mar. Ecol. Prog. Ser. (doi:10.3354/meps08651)
65. Mille T, Mahé K, Cachera M, Villanueva MC, De Pontual H, Ernande B. 2016 Diet is correlated with otolith shape in marine fish. Mar. Ecol. Prog. Ser. (doi:10.3354/meps11784)
66. Torres GJ, Lombarte A, Morales-Nin B. 2000 Variability of the sulcus acusticus in the sagittal otolith of the genus Merluccius (Merlucciidae). Fish. Res. 46, 5–13. (doi:10.1016/S0165-7836(00)00128-4)
67. Popper AN, Ramcharitar J, Campana SE. 2005 Why otoliths? Insights from inner ear physiology and fisheries biology. Mar. Freshw. Res. 56, 497–504. (doi:10.1071/MF04267)
68. Deng X. 2010 Comparative studies on the structure of the ears of deep-sea fishes.
69. Tuset VM, Farré M, Otero-Ferrer JL, Vilar A, Morales-Nin B, Lombarte A. 2016 Testing otolith morphology for measuring marine fish biodiversity. Mar. Freshw. Res. (doi:10.1071/MF15052)
70. Avigliano E, Martínez G, Stoessel L, Méndez A, Bordel N, Pisonero J, Volpedo A. 2020

Otoliths as indicators for fish behaviour and procurement strategies of hunter-gatherers in North Patagonia. Heliyon 6. (doi:10.1016/j.heliyon.2020.e03438)

71. Parmentier E, Vandewalle P, Lagardère F. 2001 Morpho-anatomy of the otic region in carapid fishes: Eco-morphological study of their otoliths. J. Fish Biol. (doi:10.1006/jfbi.2000.1511)

72. Gaemers PAM. 1984 Fish otoliths from the Bassevelde Sand (Late Tongrian) of Ruisbroek, Belgium, and the stratigraphy of the Early Oligocene of Belgium. Meded. - Werkgr. voor Tert. en Kwartaire Geol.

73. Nolf D. 1985 Otolithi Piscium. In in Handbook of Paleoichthyology,

74. Lychakov DV, Rebane YT. 2000 Otolith regularities. Hear. Res. 143, 83–102. (doi:10.1016/S0378-5955(00)00026-5)

75. Paxton JR. 2000 Fish otoliths: Do sizes correlate with taxonomic group, habitat and/or luminescence? Philos. Trans. R. Soc. B Biol. Sci. 355, 1299–1303. (doi:10.1098/rstb.2000.0688)

76. Parmentier E, Marucco Fuentes E, Millot M, Raick X, Thiry M. 2020 Sound production, hearing sensitivity, and in-depth study of the sound-producing muscles in the cowfish (Lactoria cornuta). J. Anat. (doi:10.1111/joa.13353)

77. Lombarte A, Olaso I, Bozzano A. 2003 Ecomorphological trends in the Artedidraconidae (Pisces: Perciformes: Notothenioidei) of the Weddell Sea. Antarct. Sci. 15, 211–218. (doi:10.1017/S0954102003001196)

78. Lombarte A, Palmer M, Matallanas J, Gómez-Zurita J, Morales-Nin B. 2010 Ecomorphological trends and phylogenetic inertia of otolith sagittae in Nototheniidae. Environ. Biol. Fishes 89, 607–618. (doi:10.1007/s10641-010-9673-2)

79. Tuset VM et al. 2016 Otolith shape lends support to the sensory drive hypothesis in rockfishes. J. Evol. Biol. (doi:10.1111/jeb.12932)

Figures

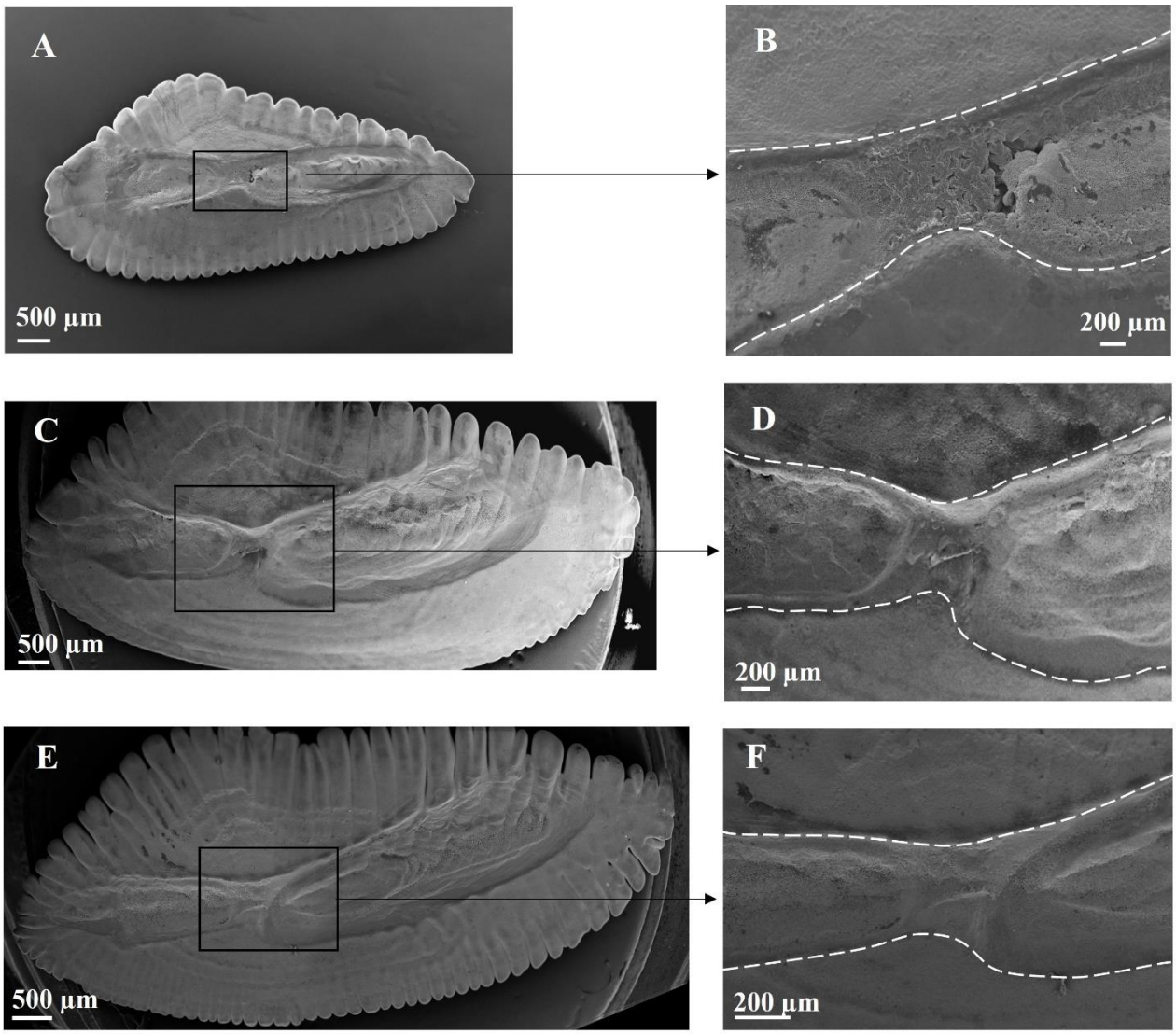

Figure 1. Representative otolith's scanning electron microscopy images. In (A-B) images from an undifferentiated individual (fish length = 148 mm) at increasing magnifications of a cross section of the collum, the bridge that join the ostium and the cauda of the sulcus acusticus. Notice the presence of porosity in this region. In (C-D) images at increasing magnifications of a male individual (fish length = 285 mm). In (E-F) images at increasing magnifications of a female individual (fish length = 293 mm). Notice that the pits first observed in the collum region of undifferentiated individuals (A-B) are no longer present in the differentiated individuals (C-F).

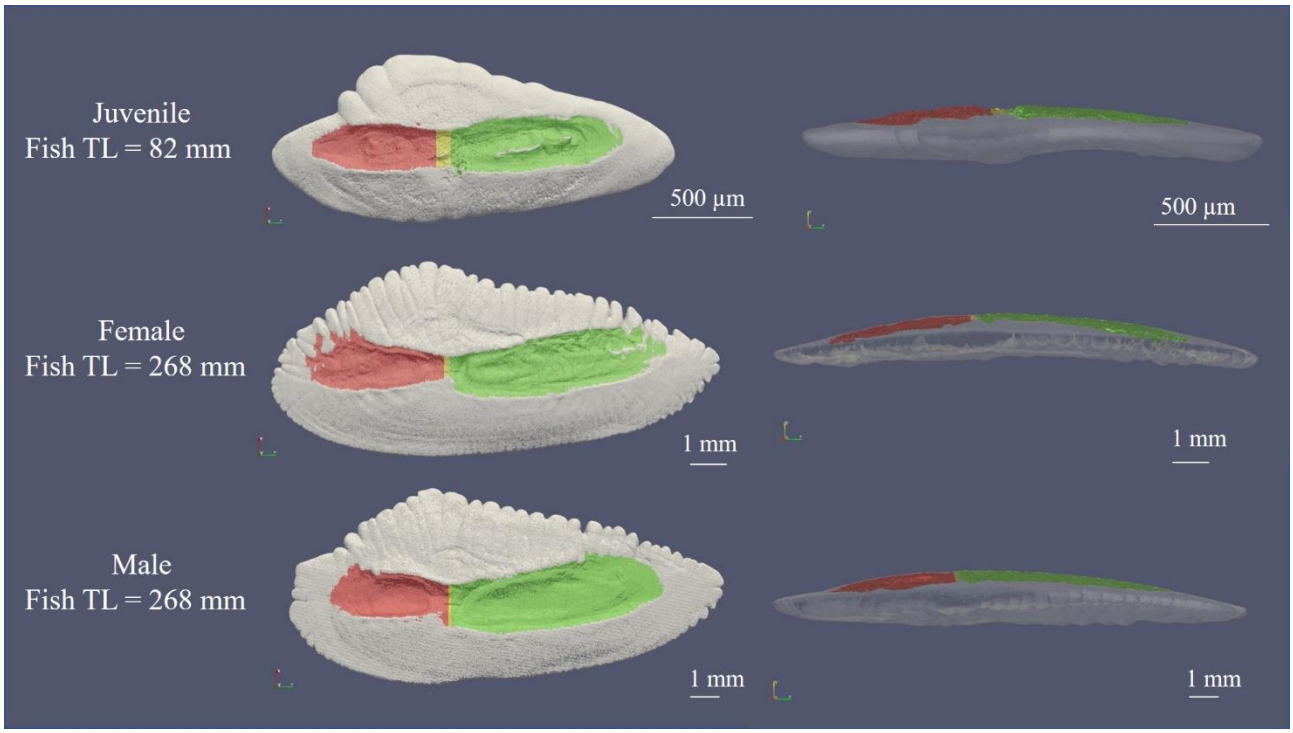

Figure 2. Representative surface reconstructions of juvenile, female and male otolith and sulcus acusticus parts in *xz*-plane alignment (left) and *yz*-plane one (right) visualized with ParaView. The red part represents the ostial colliculum, the yellow region represents the collum (the central narrowing of the sulcus) and the green one is the caudal colliculum.

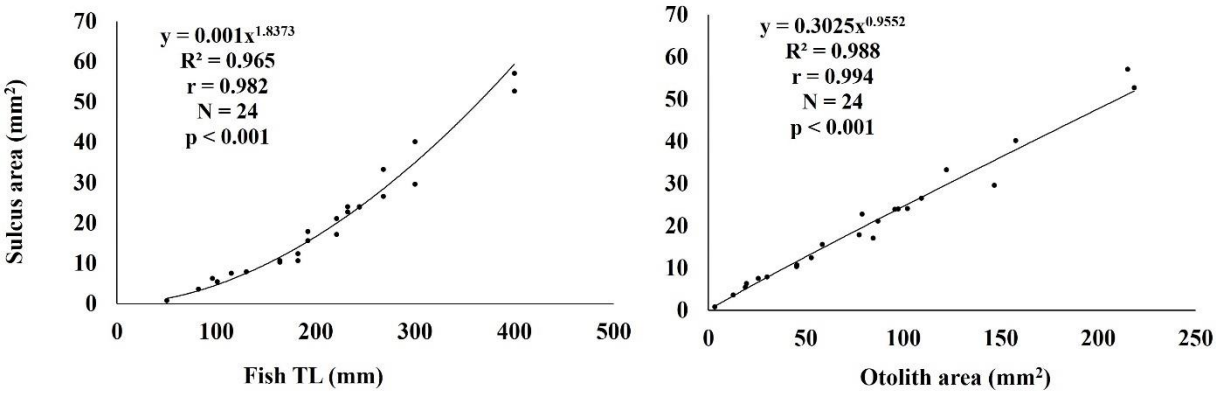

Figure 3. Relationship between **a)** sulcus area and fish length, **b)** sulcus area and otolith area. The curves and their respectively equations represent the general curves for all the individuals polled together (immatures+females+males). N, number of samples; R^2, Pearson's coefficient of determination; R, Pearson's correlation coefficient.

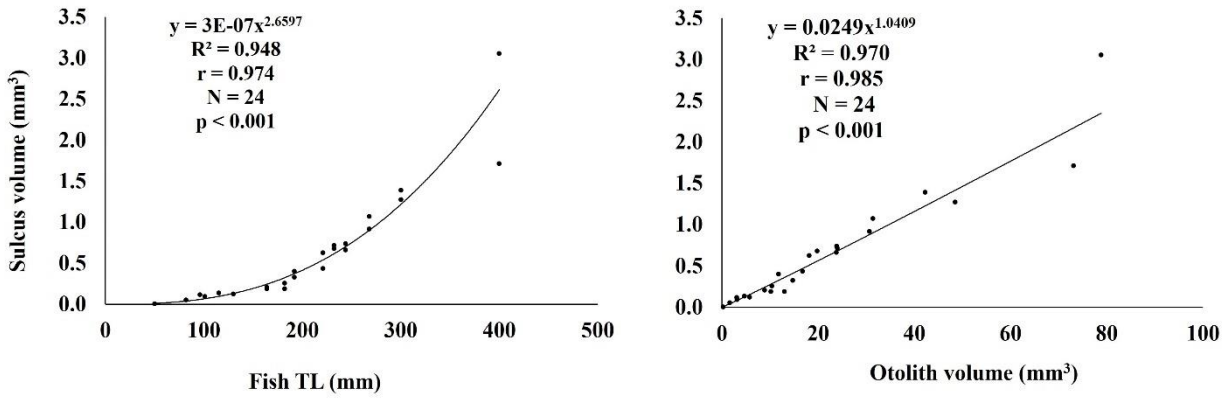

Figure 4. Relationship between a) sulcus volume and fish length, b) sulcus volume and otolith volume. The curves and their respectively equations represent the general curves for all the individuals polled together (immatures+females+males). N, number of samples; R2, Pearson's coefficient of determination; R, Pearson's correlation coefficient.

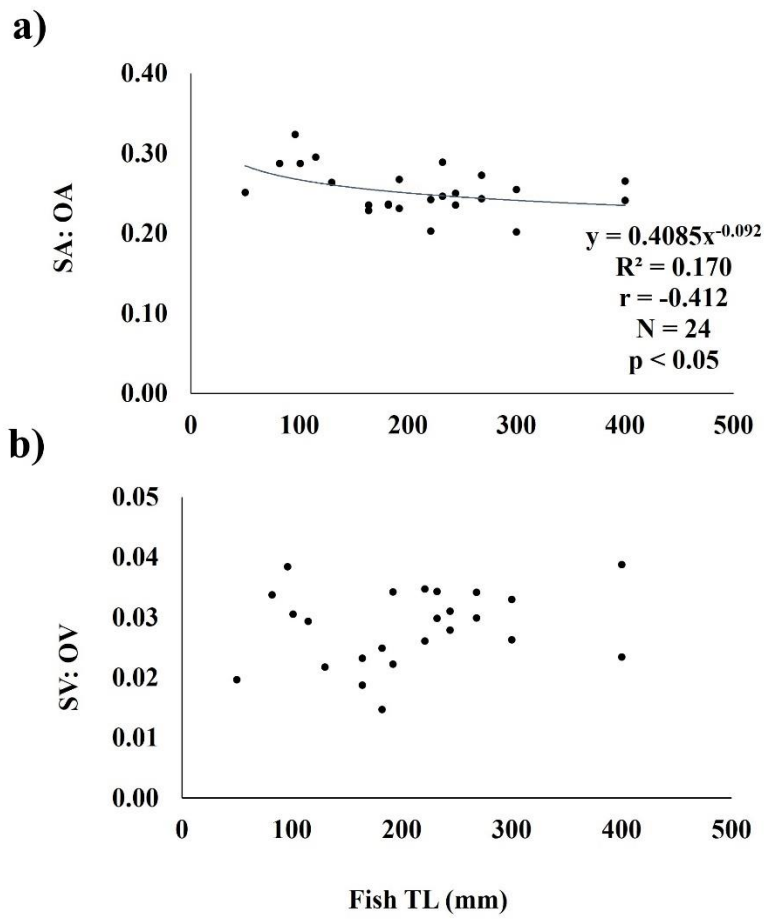

Figure 5. Relationship between **a)** the ratios of computed surface area of sulcus (SA) and otolith area (OA) with fish length; **b)** the ratios of sulcus volume (SV) and otolith volume (OV) with fish length for all the data pooled (general curve). Curve and its respectively equation is no reported when the relation was no significant. N, number of samples; R^2, Pearson's coefficient of determination; R, Pearson's correlation coefficient.

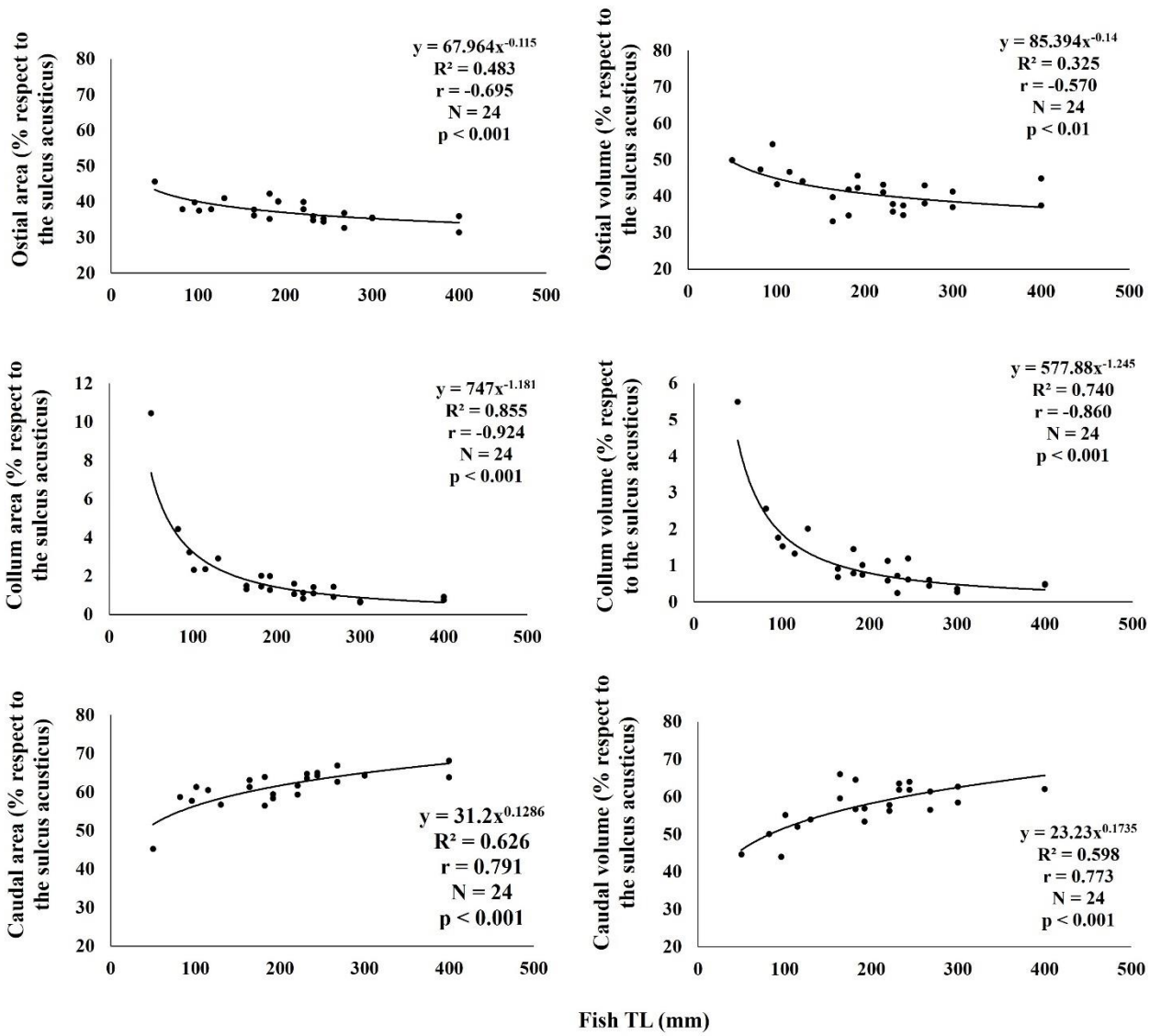

Figure 6. Relationship between the ostial, collum and caudal area and volume, expressed as the percentage of the area and volume with respect to the entire sulcus acusticus, with fish length for all the data pooled (general curves). N, number of samples; R^2, Pearson's coefficient of determination; R, Pearson's correlation coefficient.

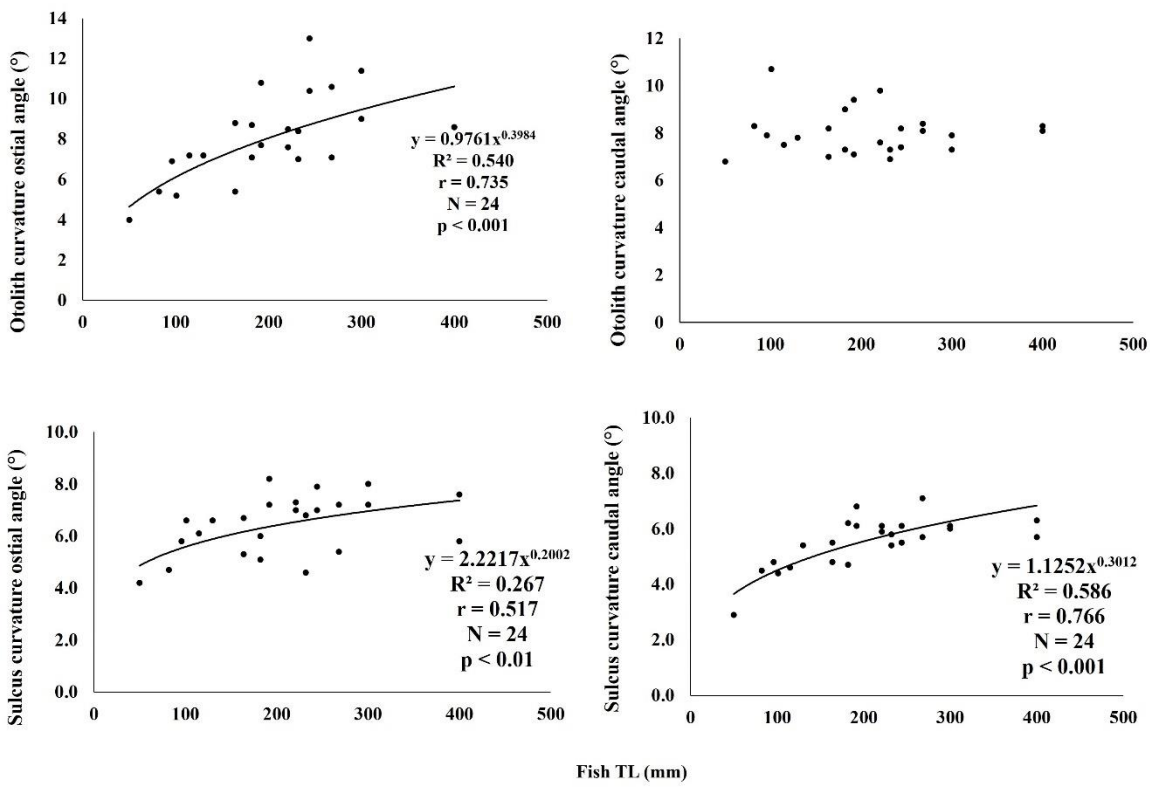

Figure 7. Relationship between the otolith and sulcus curvature with fish length for all the data pooled (general curves). N, number of samples; R^2, Pearson's coefficient of determination; R, Pearson's correlation coefficient.

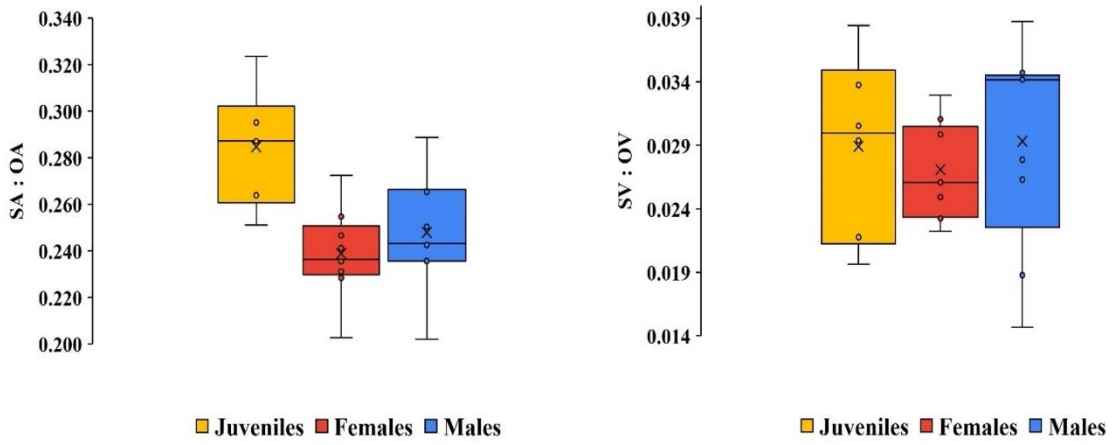

Figure 8. Boxplots of the ratios in immature individuals (on the left), in female (in the middle), and males (on the right). The box indicates the 25th and 75th percentiles and the line within the box marks the median. Whisker length is equal to 1.5 × interquartile range (IQR). Circles represent outliers. N = 6 for immature; N = 9 for females; N = 9 for males.

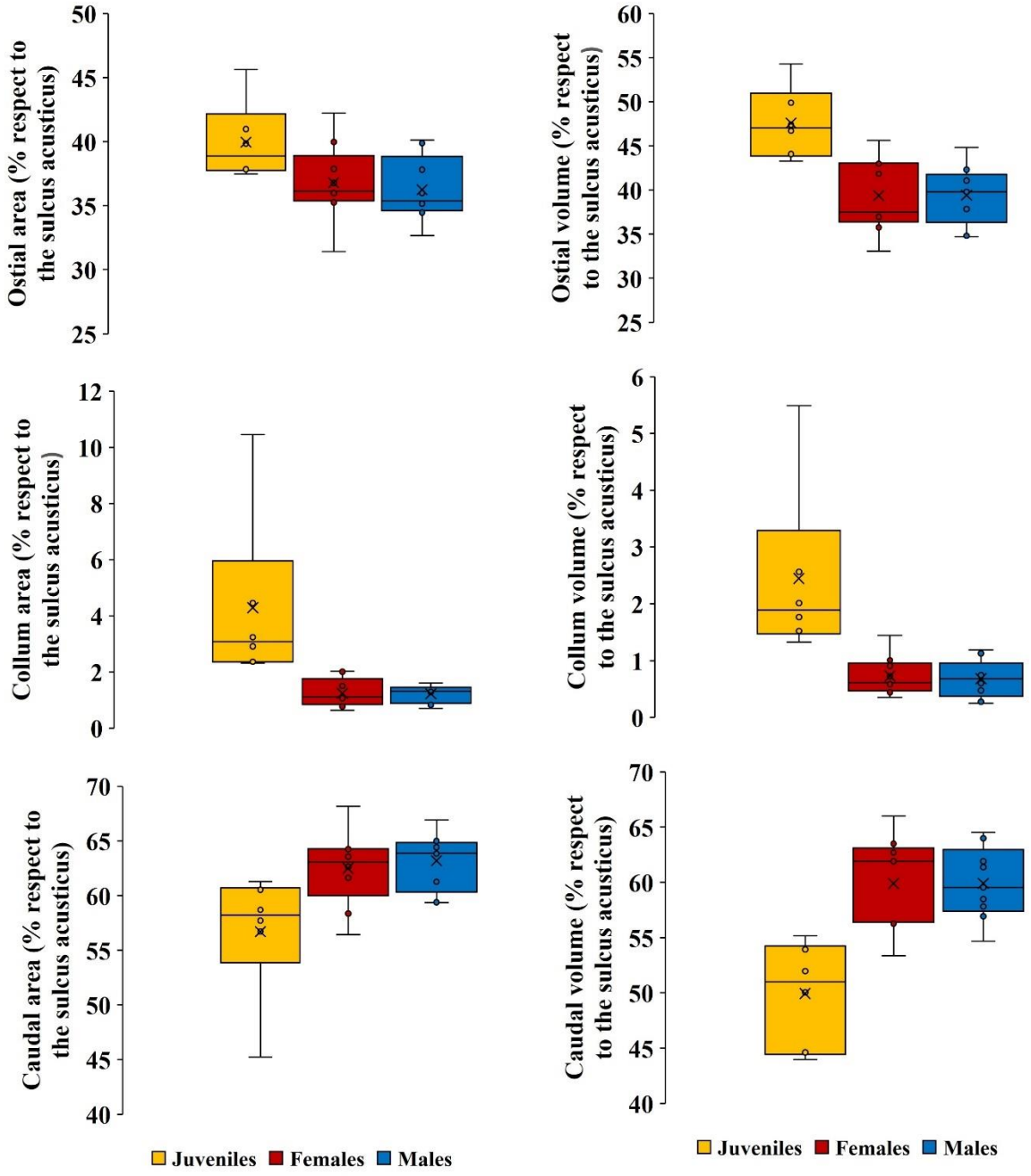

Figure 9. Boxplots of the ratios in immature individuals (on the left), in female (in the middle), and males (on the right) of the three sulcus parts (ostial, collum, caudal) expressed as the percentage of the area and volume with respect to the entire sulcus acusticus. The box indicates the 25th and 75th percentiles and the line within the box marks the median. Whisker length is equal to 1.5 × interquartile range (IQR). Circles represent outliers. N = 6 for immature; N = 9 for females; N = 9 for males.

Tables

Table 1. Computed surface area and volume estimates of the sulci and otoliths and their respective ratios. Data are presented as mean ± Standard Deviation (SD). Pairwise comparisons between species were performed with ANOVA or Mann-Whitney U test. Significant *p*-values are in bold. J = Juvenile, F = Female, M = Male. * $p < 0.01$, ** $p < 0.01$, *** $p < 0.001$.

	Gender			**Pairwise comparison**	
	Juvenile (mean ± SD)	**Female (mean ± SD)**	**Male (mean ± SD)**	**Gender compared**	***p*- value**
OV (mm^3)	3.06 ± (1.98)	27.17 ± (20.15)	28.36 ± (22.35)	J x F J x M F x M	*** *** NS
OA (mm^2)	18.36 ± (9.52)	106.42 ± (54.17)	98.00 ± (54.58)	J x F J x M F x M	*** *** NS
SV (mm^3)	0.089 ± (0.050)	0.745 ± (0.522)	0.906 ± (0.883)	J x F J x M F x M	*** *** NS
SA (mm^2)	5.290 ± (2.686)	25.79 ± (13.91)	24.24 ± (14.00)	J x F J x M F x M	*** *** NS
SV:OV	0.029 ± (0.007)	0.027 ± (0.004)	0.029 ± (0.008)	**J x F** **J x M** **F x M**	**NS** **NS** **NS**
SA:OA	0.285 ± (0.025)	0.239 ± (0.019)	0.248 ± (0.024)	**J x F** **J x M** **F x M**	*** *** **NS**
SA*s*:OV*s*	0.731 ± (0.043)	0.774 ± (0.043)	0.745 ± (0.063)	J x F J x M F x M	NS NS NS
SA*s*:SV*s*	2.400 ± (0.101)	2.585 ± (0.131)	2.445 ± (0.115)	J x F J x M F x M	** NS *
SV*s*:OA*s*	0.223 ± (0.017)	0.189 ± (0.010)	0.204 ± (0.012)	J x F J x M F x M	*** * *
OA*s*:OV*s*	1.370 ± (0.027)	1.585± (0.057)	1.497 ± (0.090)	J x F J x M F x M	*** ** *

OstialA (mm^2)	2.07 ± (1.06)	9.20 ± (4.29)	8.71 ± (4.96)	J x F J x M F x M	** ** NS
CollumA (mm^2)	0.16 ± (0.05)	0.27 ± (0.08)	0.28 ± (0.13)	J x F J x M F x M	* * NS
CaudalA (mm^2)	3.10 ± (1.61)	16.43 ± (9.66)	15.43 ± (9.09)	J x F J x M F x M	*** *** NS
OstialV (mm^3)	0.04 ± (0.02)	0.29 ± (0.19)	0.37 ± (0.40)	J x F J x M F x M	** ** NS
CollumV (mm^3)	0.002 ± (0.001)	0.004 ± (0.002)	0.005 ± (0.004)	J x F J x M F x M	** ** NS
CaudalV (mm^3)	0.045 ± (0.026)	0.452 ± (0.329)	0.527± (0.480)	J x F J x M F x M	** ** NS
OstialA (% of the sulcus)	39.95 ± (3.10)	36.79 ± (3.06)	36.25 ± (2.53)	J x F J x M F x M	* * NS
CollumA (% of the sulcus)	4.29 ± (3.12)	1.24 ± (0.50)	1.22 ± (0.32)	J x F J x M F x M	** ** NS
CaudalA (% of the sulcus)	56.69 ± (5.86)	62.48 ± (3.44)	63.19 ± (2.62)	J x F J x M F x M	* * NS
OstialV (% of the sulcus)	47.59 ± (4.04)	39.37 ± (4.15)	39.40 ± (3.39)	J x F J x M F x M	** ** NS
CollumV (% of the sulcus)	2.45 ± (1.55)	0.73 ± (0.34)	0.68 ± (0.33)	J x F J x M F x M	** ** NS
CaudalV (% of the sulcus)	49.95 ± (4.72)	59.90 ± (4.24)	59.92 ± (3.29)	J x F J x M F x M	*** *** NS

Table 2. Regression parameters of the relationships between otolith parameters (OA= otolith surface area; OV= otolith volume) and sulcus acusticus parameters (SA= sulcus surface area; SV= sulcus volume; OstialA= ostial surface area; CollumA= collum surface area; CaudalA= caudal surface area; OstialV= ostial volume; CollumV= collum volume; CaudalV= caudal volume) with respect to fish size (TL = total length) of European Hake for females, males and juveniles. n = sample size; a = constant; b = slope, CI (b) = 95% confidence interval; R^2 = coefficient of determination. Bold characters indicate that the differences in the slope (b) between the curves of juveniles and females and juveniles and males are significant.

Relationship	Juveniles						Females						Males					
	n	a	b	CI (b)	R^2	P	n	a	b	CI (b)	R^2	P	n	a	b	CI (b)	R^2	P
TL vs SA	6	0.000	2.496	1.719-3.274	0.953	<0.001	9	0.001	1.899	1.472-2.315	0.942	< 0.001	9	0.001	1.878	1.535-2.220	0.961	<0.001
TL vs SV	6	0.000	3.661	2.050-5.272	0.953	<0.01	9	0.000	2.608	1.987-3.229	0.934	<0.001	9	0.000	3.177	2.574-3.778	0.957	<0.001
TL vs OA	6	0.000	2.385	1.943-2.821	0.983	<0.001	9	0.006	1.778	1.471-2.087	0.964	<0.001	9	0.003	1.874	1.583-2.150	0.972	<0.001
TL vs OV	**6**	**0.000**	**3.413**	**2.809-4.016**	**0.984**	**<0.001**	**9**	**0.000**	**2.431**	**2.134-2.728**	**0.982**	**<0.001**	**9**	**0.000**	**2.452**	**2.120-2.783**	**0.978**	**<0.001**
OA vs SA	6	0.242	1.060	0.926-1.194	0.992	<0.001	9	0.173	1.071	0.931-1.202	0.980	<0.001	9	0.261	0.987	0.816-1.170	0.963	<0.001
OV vs SV	6	0.035	1.098	0.819-1.377	0.968	<0.001	9	0.021	1.082	0.904-1.260	0.967	<0.001	9	0.013	1.242	0.871-1.613	0.899	<0.001
TL vs OstialA	6	0.0E+00	2.350	1.696-3.002	0.96	<0.001	9	0.001	1.665	1.167-2.163	0.899	<0.001	9	0.0005	1.776	1.310-2.242	0.921	<0.001
TL vs CollumA	6	0.0024	0.927	0.148-1.706	0.732	<0.05	9						9	0.0002	1.286	0.362-2.210	0.607	<0.05
TL vs CaudalA	6	9.0E-06	2.774	1.799-3.750	0.94	<0.01	9	0.000	2.052	1.635-2.469	0.951	<0.001	9	0.0003	1.946	1.638-2.253	0.97	<0.001
TL vs OstialV	6	3.0E-09	3.551	1.748-5.354	0.882	<0.01	9	2E-07	2.576	1.924-3.227	0.926	<0.001	9	3E-09	3.316	2.565-4.066	0.94	<0.01
TL vs CollumV	6	4.0E-08	2.310	1.213-3.407	0.895	<0.01	9	3E-06	1.339	0.598-2.081	0.723	<0.01	9	8E-09	2.386	0.625-4.148	0.595	<0.05
TL vs CaudalV	6	8.0E-10	3.852	2.342-5.362	0.926	<0.01	9	2E-07	2.657	1.948-3.365	0.918	<0.001	9	2E-08	3.088	2.535-3.642	0.961	<0.001

Supplementary Material for

Characterization of fish otolith sulcus acusticus by electron microscopy and micro-CT imaging

Manuscript in preparation

Quinzia Palazzo[1,7], Steven Raaijmakers[2], Robert G. Belleman[2], Fiorella Prada[3,7], Jörg U. Hammel[4], Marco Stagioni[5], Simona Fermani[1,6], Jaap Kaandorp[2*], Stefano Goffredo[3,7*], Giuseppe Falini[1,7]*

Figures

a)

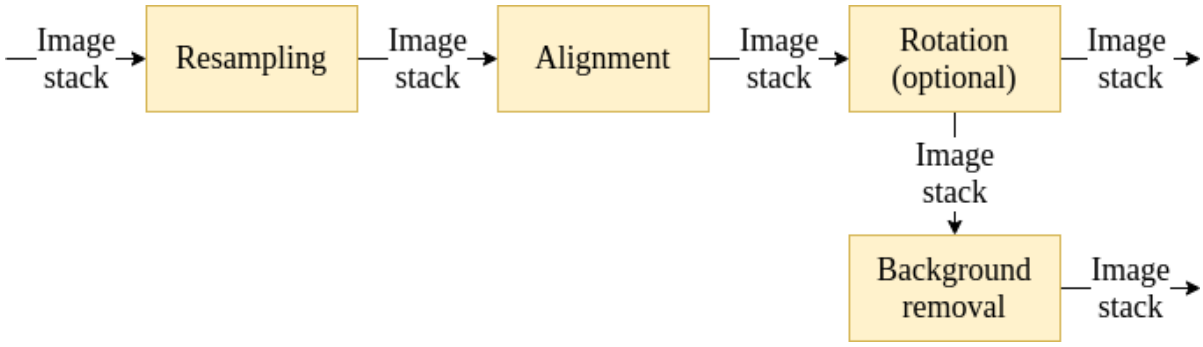

b)

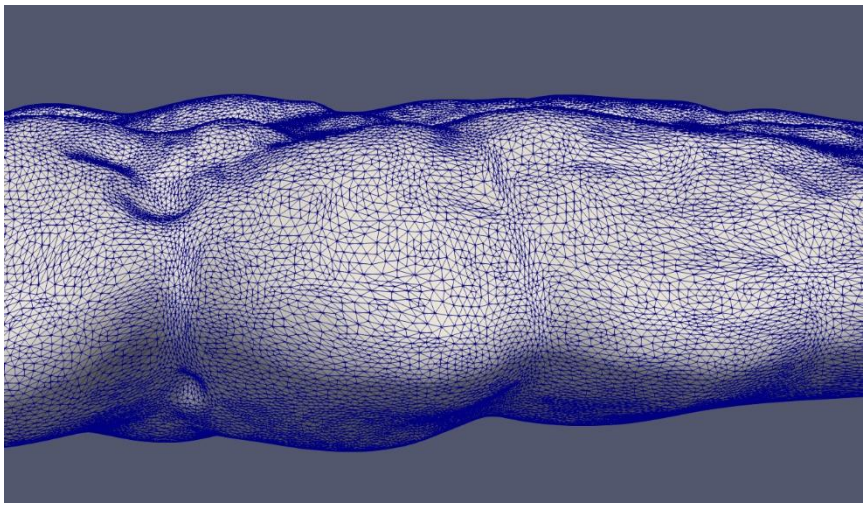

Figure S1. a) Applied image stack transformations of micro-CT scans. **b)** Transformed image stack into triangular mesh (Marching Cubes).

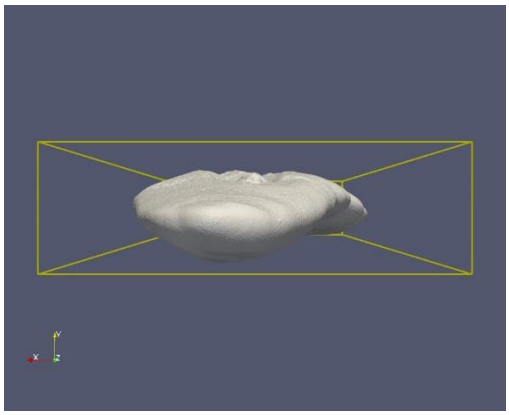

(a) Front of *xy*-plane

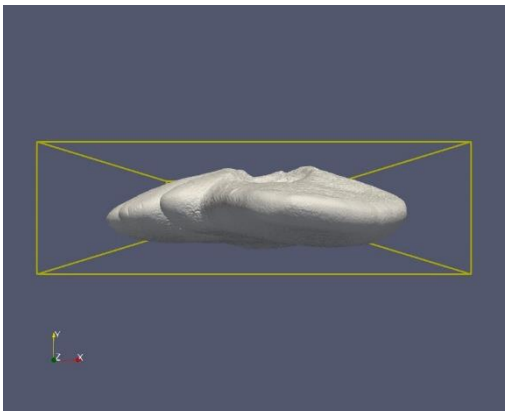

(b) Back of *xy*-plane

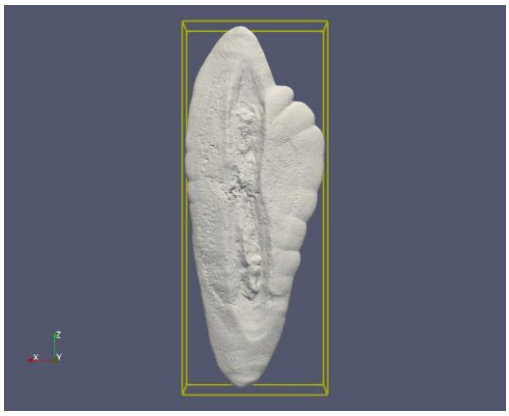

(c) Front of *xz*-plane

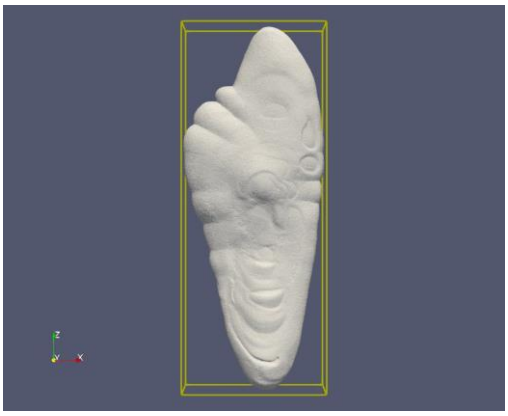

(d) Back of *xz*-plane

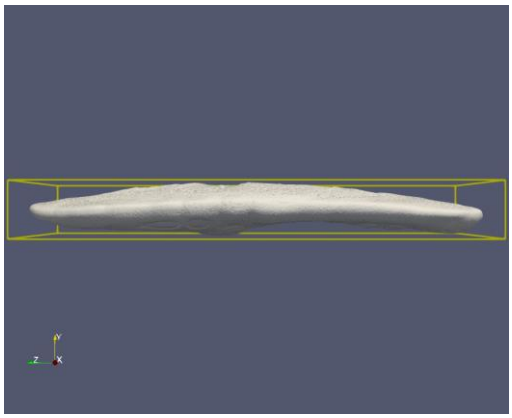

(e) Front of *yz*-plane

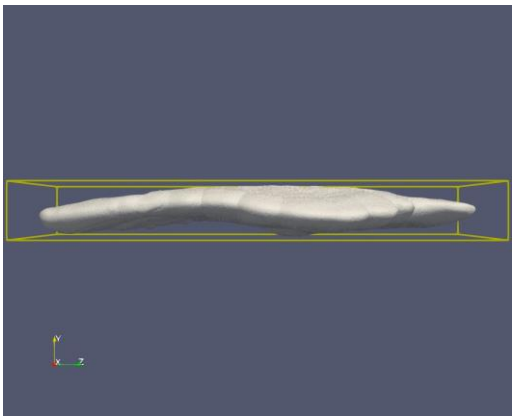

(f) Back of *zy*-plane

Figure S2. Orientation of otolith sample after alignment and rotation performed algorithmically through the transformation matrix which improves consistency. The yellow rectangle represents the bounding box (OBB): the smallest box that completely encloses the otolith volume.

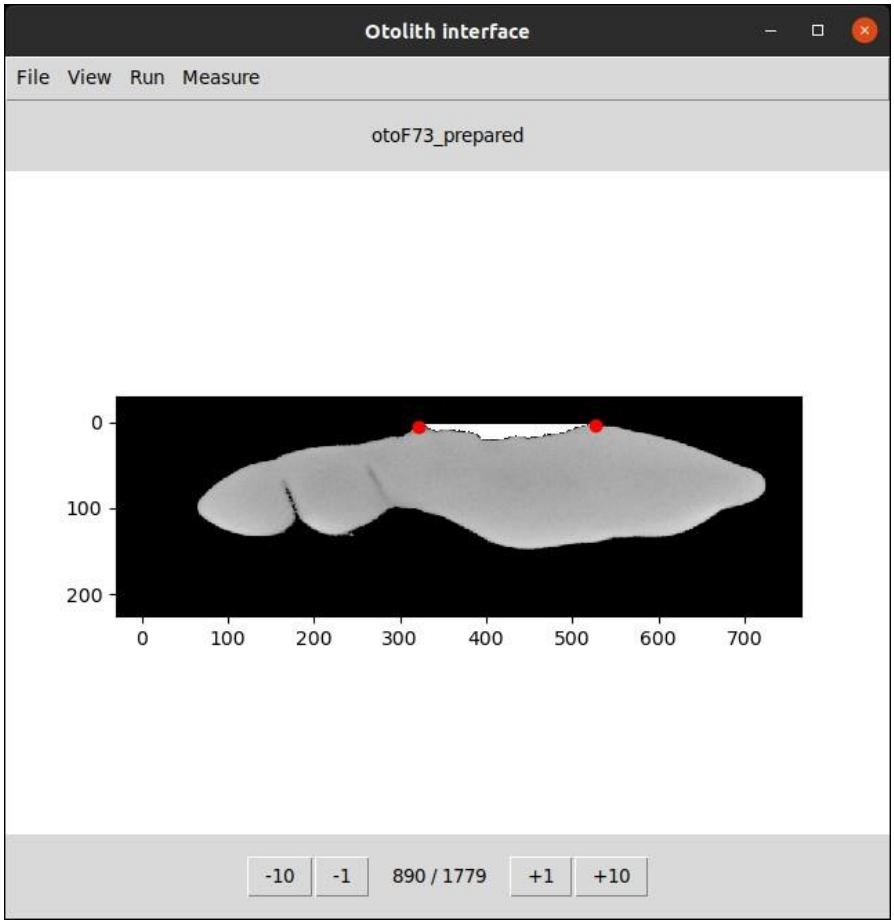

Figure S3. Interface on Ubuntu 20.04.

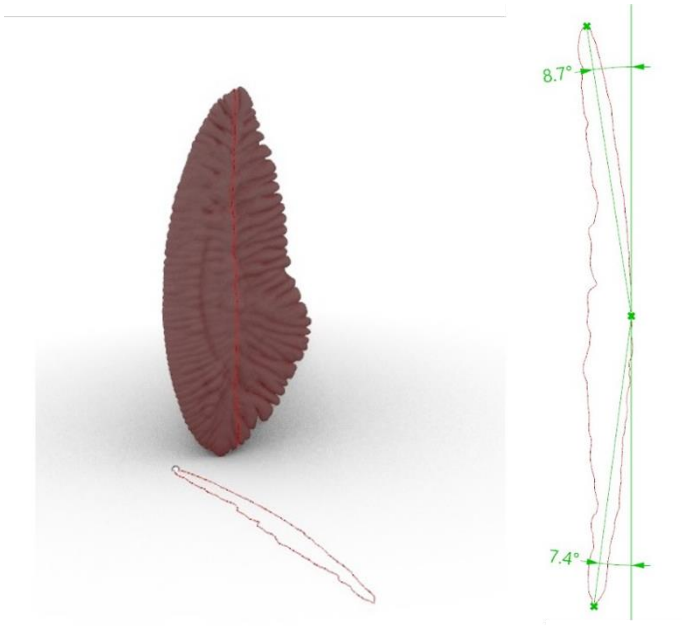

Figure S4. Procedure for measuring the angles of curvature of the otolith and of the cast of the reconstructed sulcus acusticus on Rhinoceros.

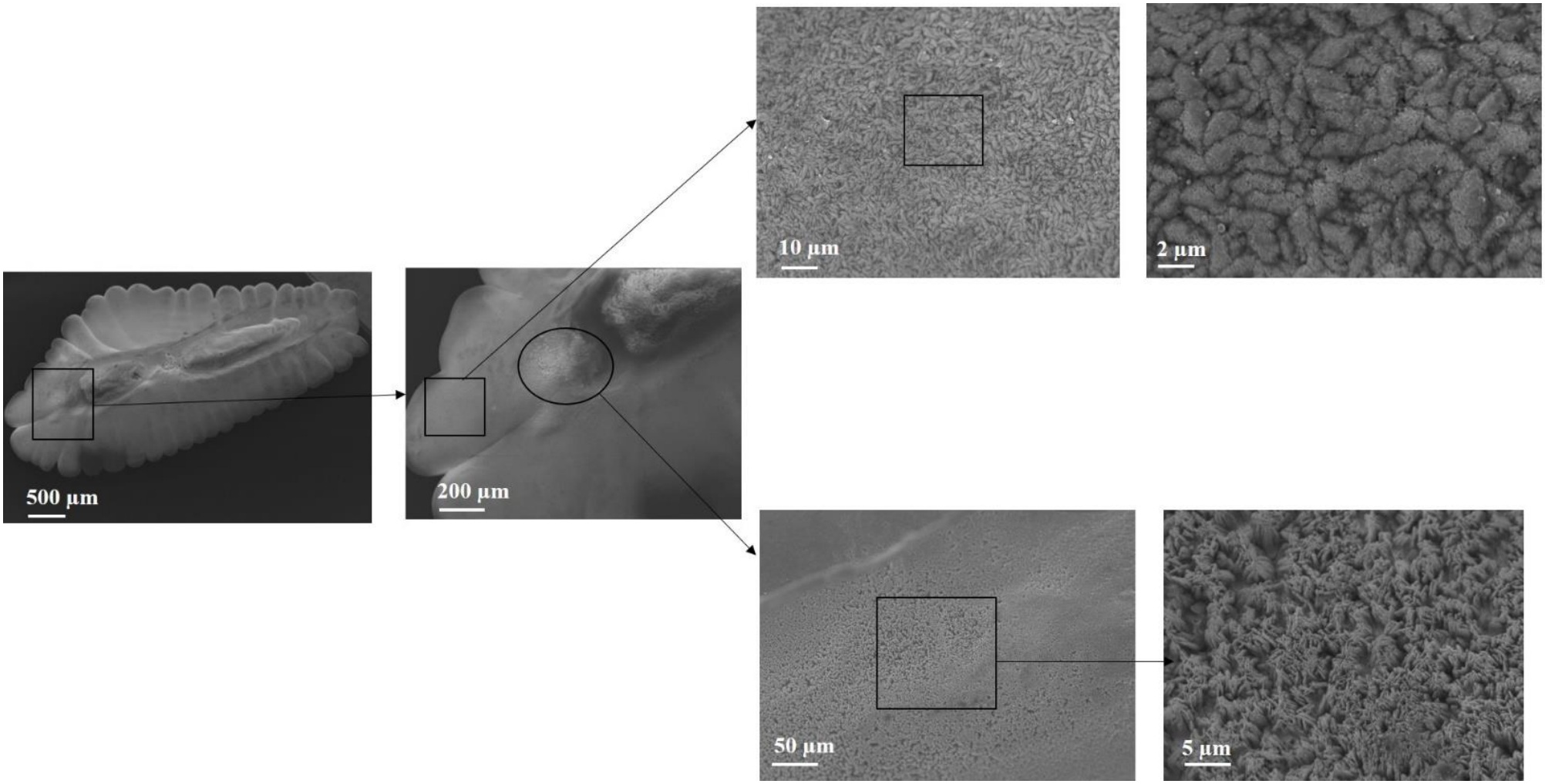

Figure S5. Representative otolith's scanning electron microscopy images. At higher magnification is reported a detail of the external part of the sulcus acusticus (top) and an island of crystals spot (bottom) on the left side of the ostial colliculum having a different texture respect the external side of the sulcus acusticus. These spots are presented in all the individuals and seem to show the same crystal texture observed inside the sulcus acusticus.

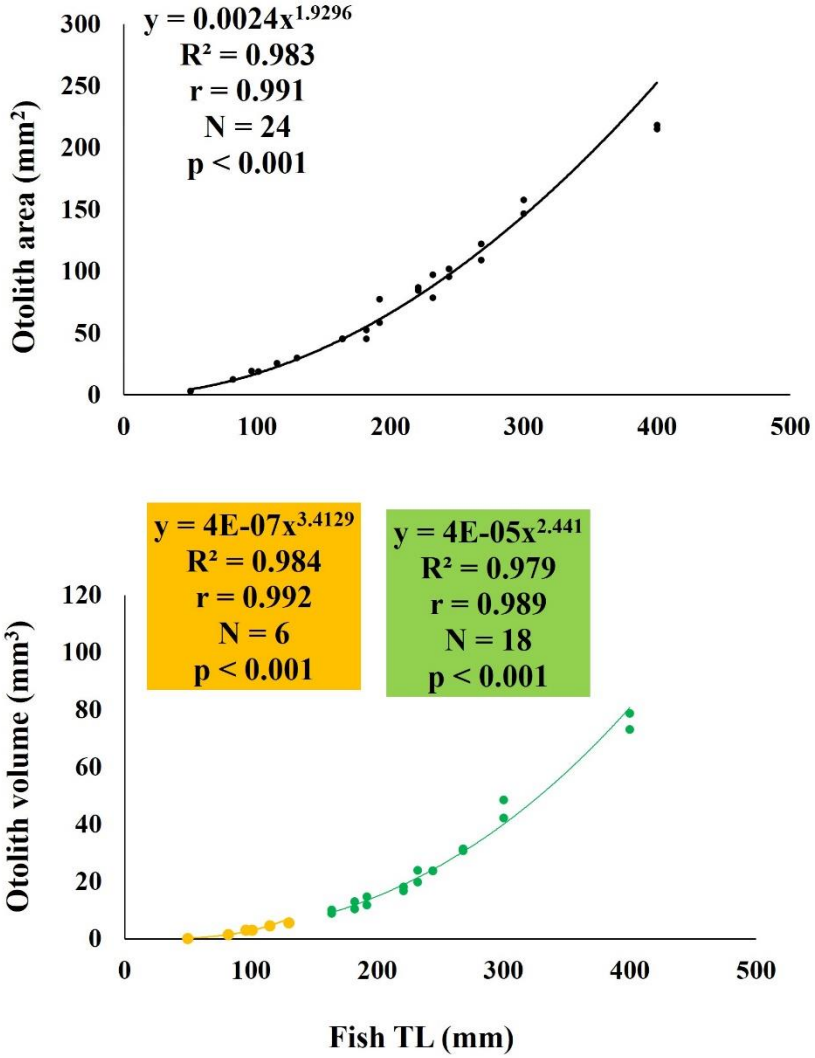

Figure S6. Relationship between **a)** otolith area and fish length, **b)** otolith volume and fish length. The colours of the dots, the curves and their respectively equations represent in black the general curves (immatures+females+males), in yellow the immature individuals, in green the adult (females+males), N, number of samples; R^2, Pearson's coefficient of determination; R, Pearson's correlation coefficient.

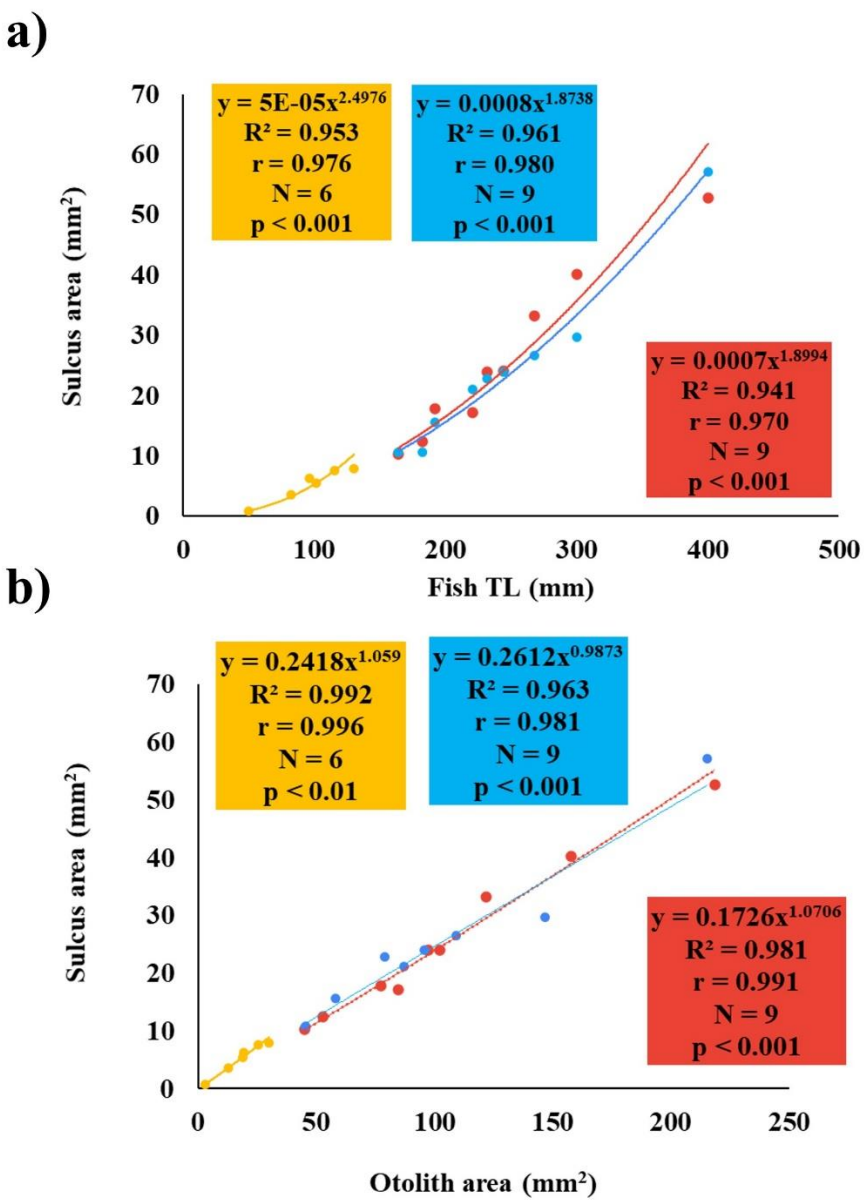

Figure S7. Relationship between **a)** sulcus area and otolith area, **b)** sulcus area and fish length for immatures, females and males' individuals. The colours of the dots, the curves and their respectively equations represent in yellow the immature individuals, in red the females. N, number of samples; R^2, Pearson's coefficient of determination; R, Pearson's correlation coefficient.

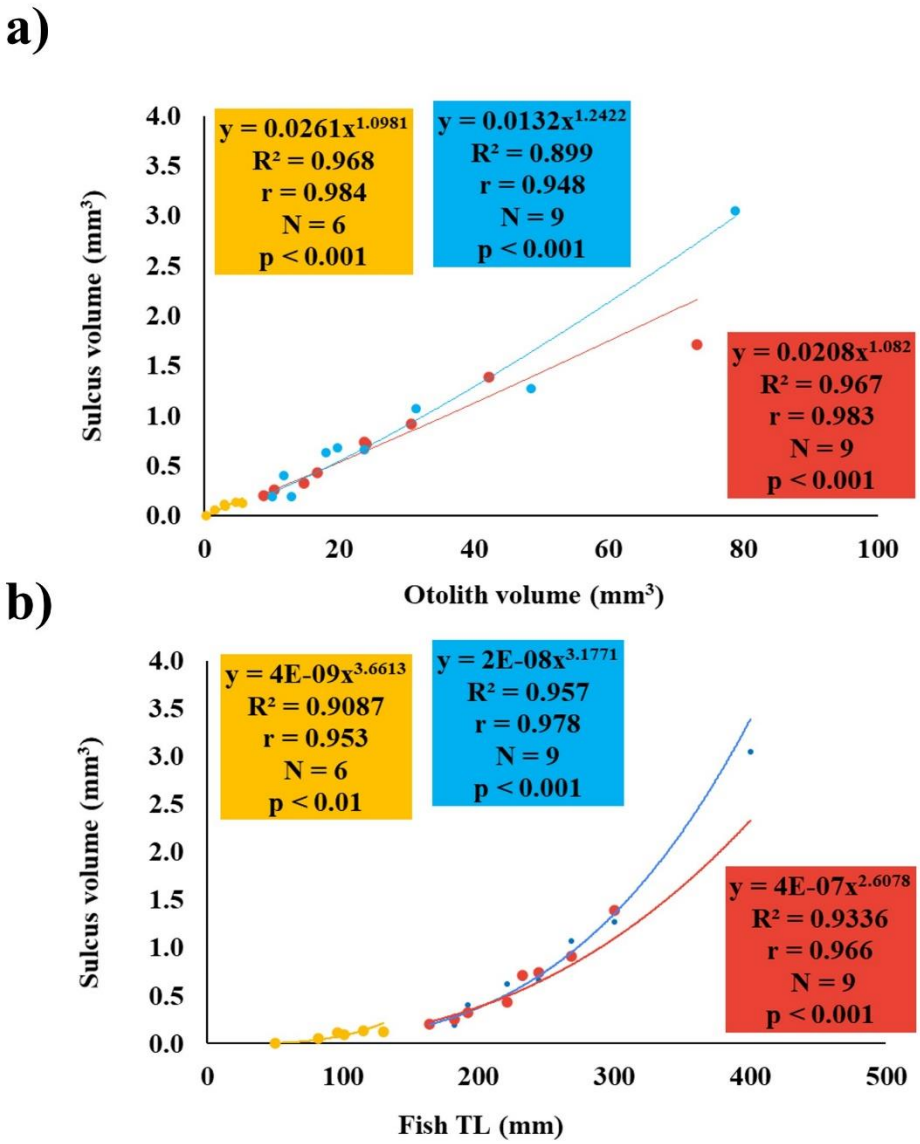

Figure S8. Relationship between **a)** sulcus volume and otolith volume, **b)** sulcus volume and fish length for immatures, females and males' individuals. The colours of the dots, the curves and their respectively equations represent in yellow the immature individuals, in red the females. N, number of samples; R^2, Pearson's coefficient of determination; R, Pearson's correlation coefficient.

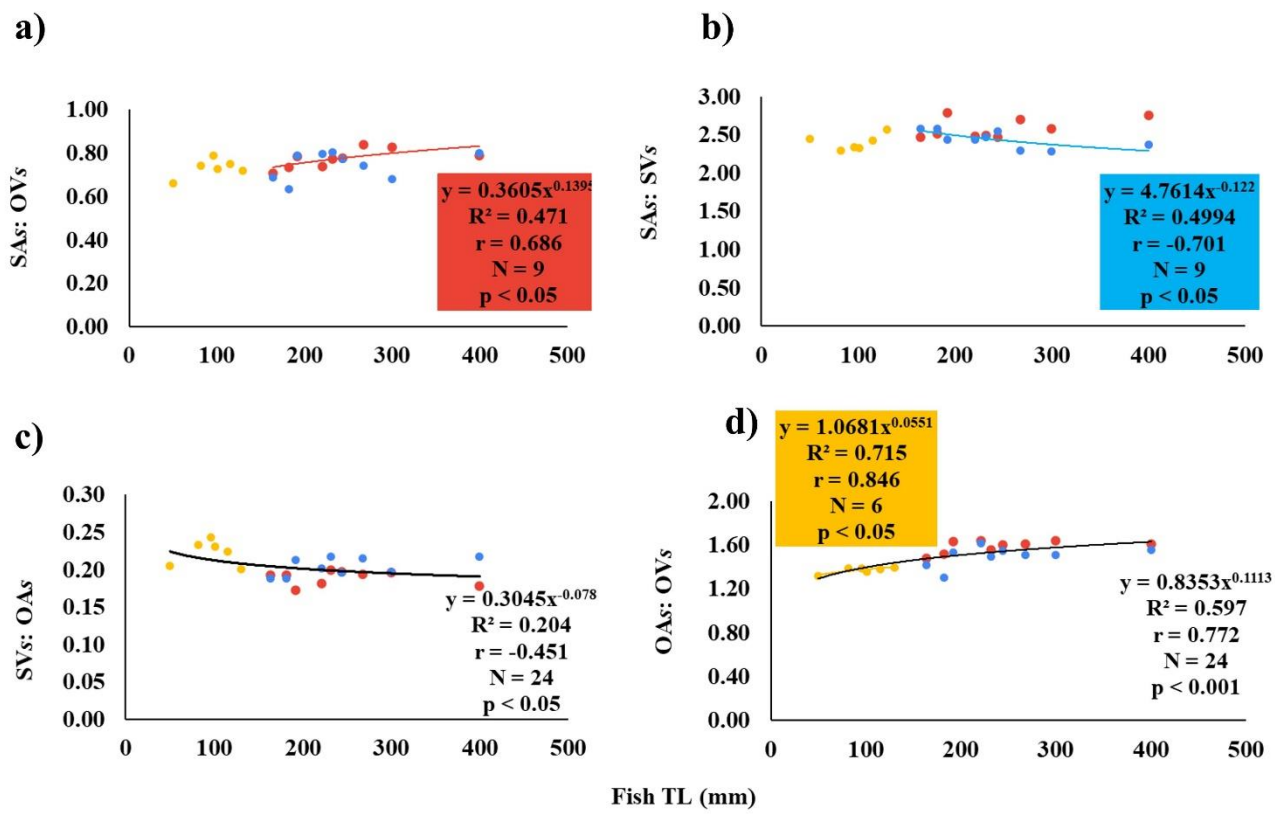

Figure S9. Relationship between **a)** the ratios of surface area of sulcus normalized to a sphere-like objects (SA*s*) and the normalized otolith volume (OV*s*) with fish length; **b)** the ratios of SA*s* and the volume of sulcus normalized to a sphere-like objects (SV*s*) with fish length; **c)** the ratios of SV*s* and the surface area of otolith normalized to a sphere-like objects (OA*s*) with fish length; **d)** the ratios of OA*s* and OV*s* with fish length. The colours of the dots, the curves and their respectively equations represent in yellow the immature individuals, in red the females, in blue the males and in black the general curves (all the data pooled). Curves and their respectively equations are no reported when the relations were no significant. N, number of samples; R^2, Pearson's coefficient of determination; R, Pearson's correlation coefficient.

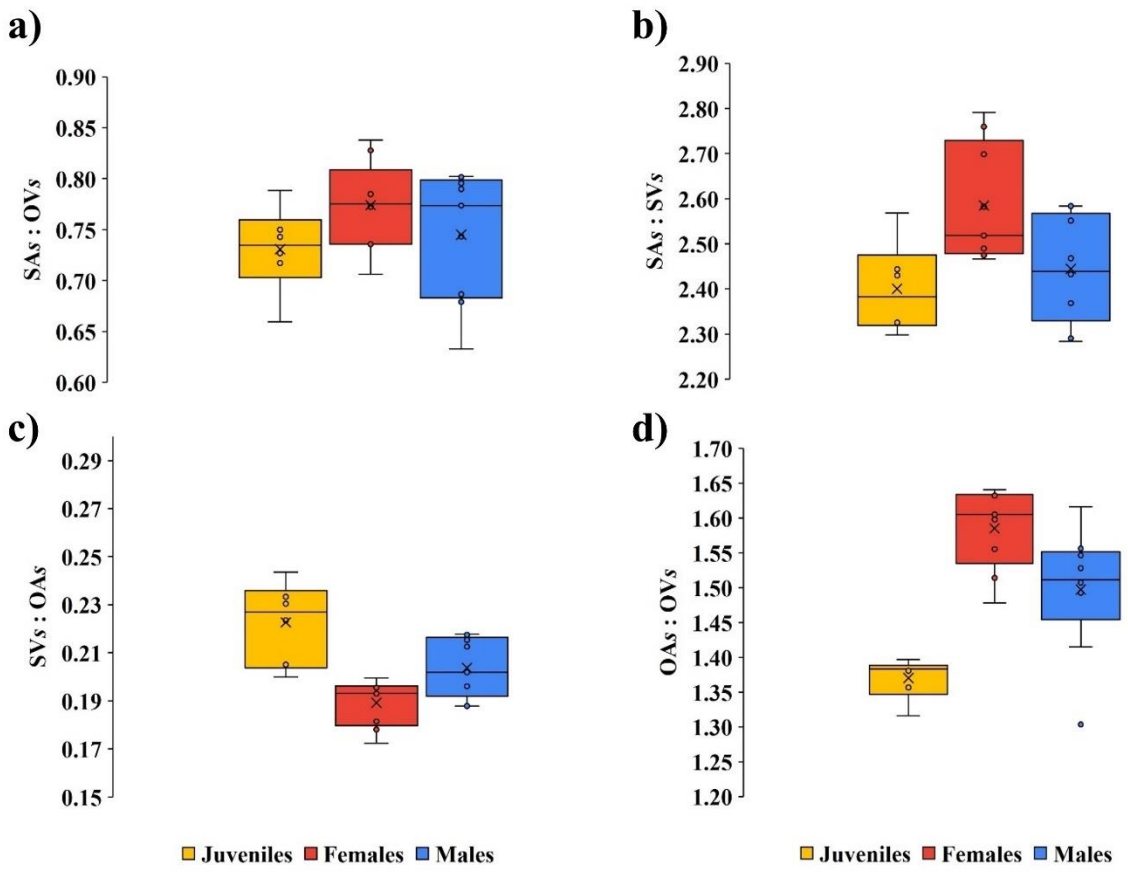

Figure S10. Boxplots of **a)** the ratios between the surface area of sulcus normalized to a sphere-like objects (SA*s*) and the normalized otolith volume (OV*s*); **b)** the ratios between the SA*s* and the volume of sulcus normalized to a sphere-like objects (SV*s*); **c)** the ratios of SV*s* and the surface area of otolith normalized to a sphere-like objects (OA*s*); **d)** the ratios of OA*s* and OV*s* with fish length, in immature individuals (on the left), in female (in the middle), and males (on the right). The box indicates the 25th and 75th percentiles and the line within the box marks the median. Whisker length is equal to 1.5 × interquartile range (IQR). Circles represent outliers. N = 6 for immature; N = 9 for females; N = 9 for males.

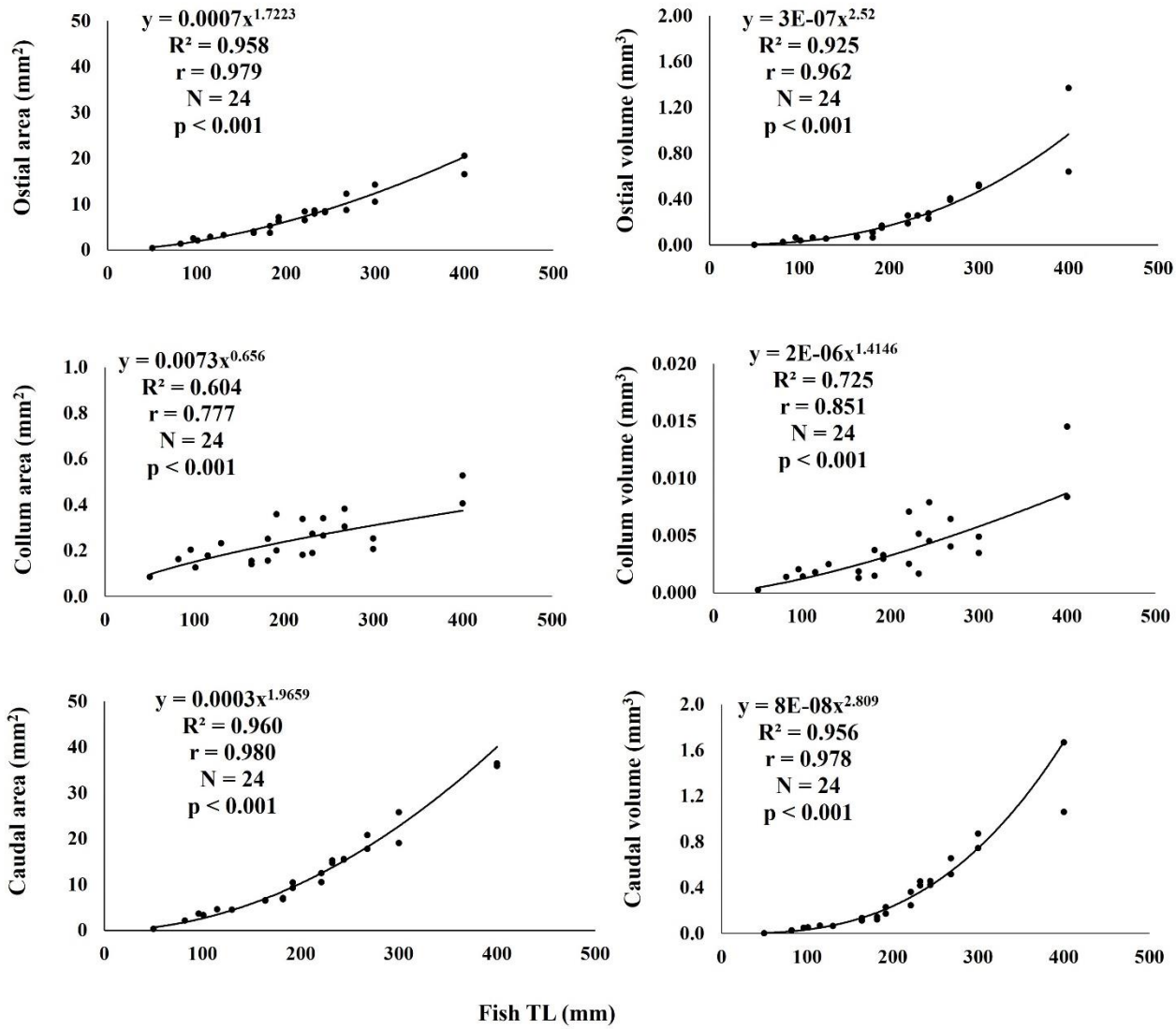

Figure S11. Relationship between the ostial, collum and caudal area and volume with fish length for all the data pooled (general curves). N, number of samples; R^2, Pearson's coefficient of determination; R, Pearson's correlation coefficient.

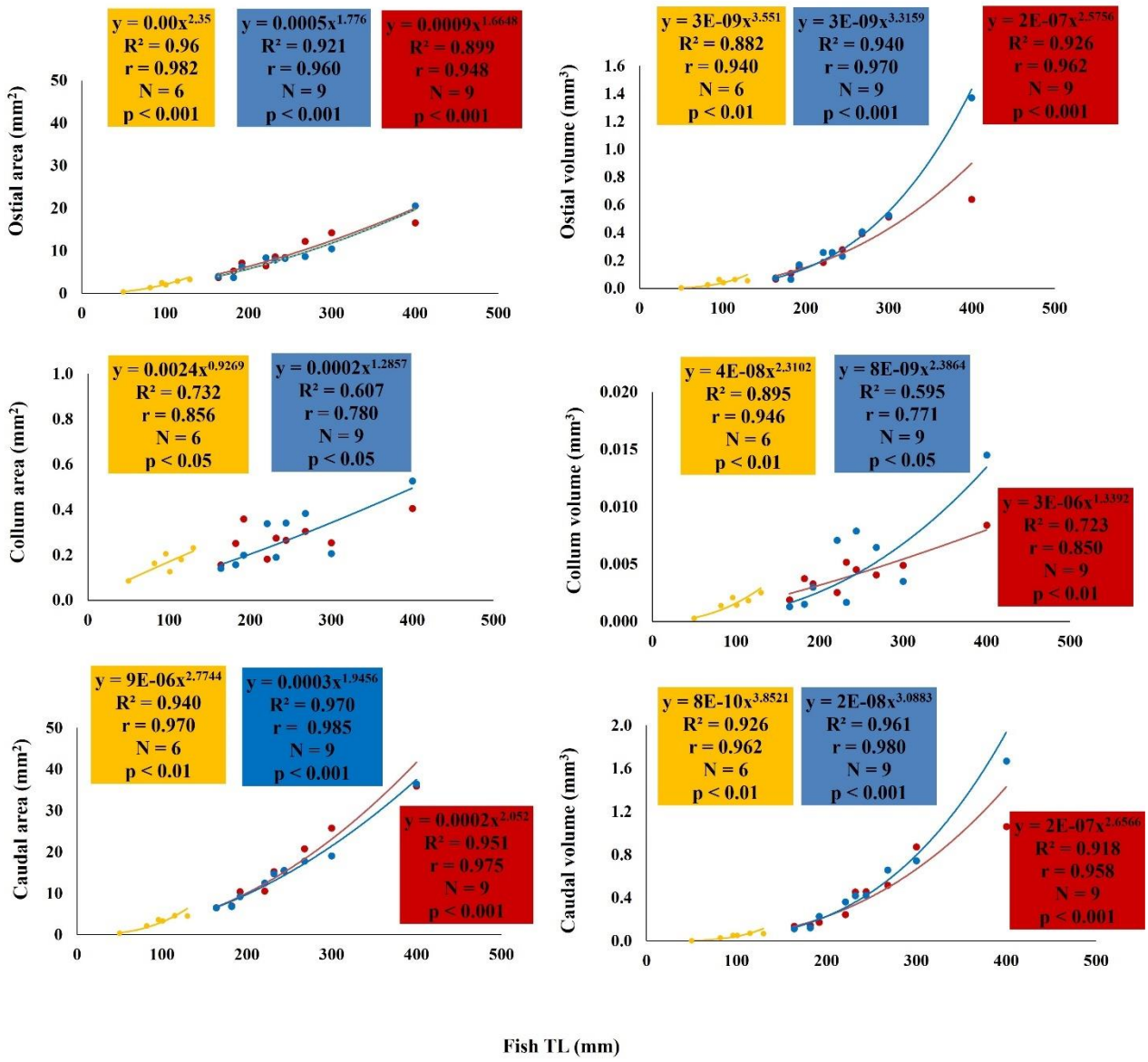

Figure S12. Relationship between the ostial, collum and caudal area and volume with fish length. The colours of the dots, the curves and their respectively equations represent in yellow the immature individuals, in red the females, in blue the males and in black the general curves (all the data pooled). Curves and their respectively equations are no reported when the relations were no significant. N, number of samples; R^2, Pearson's coefficient of determination; R, Pearson's correlation coefficient.

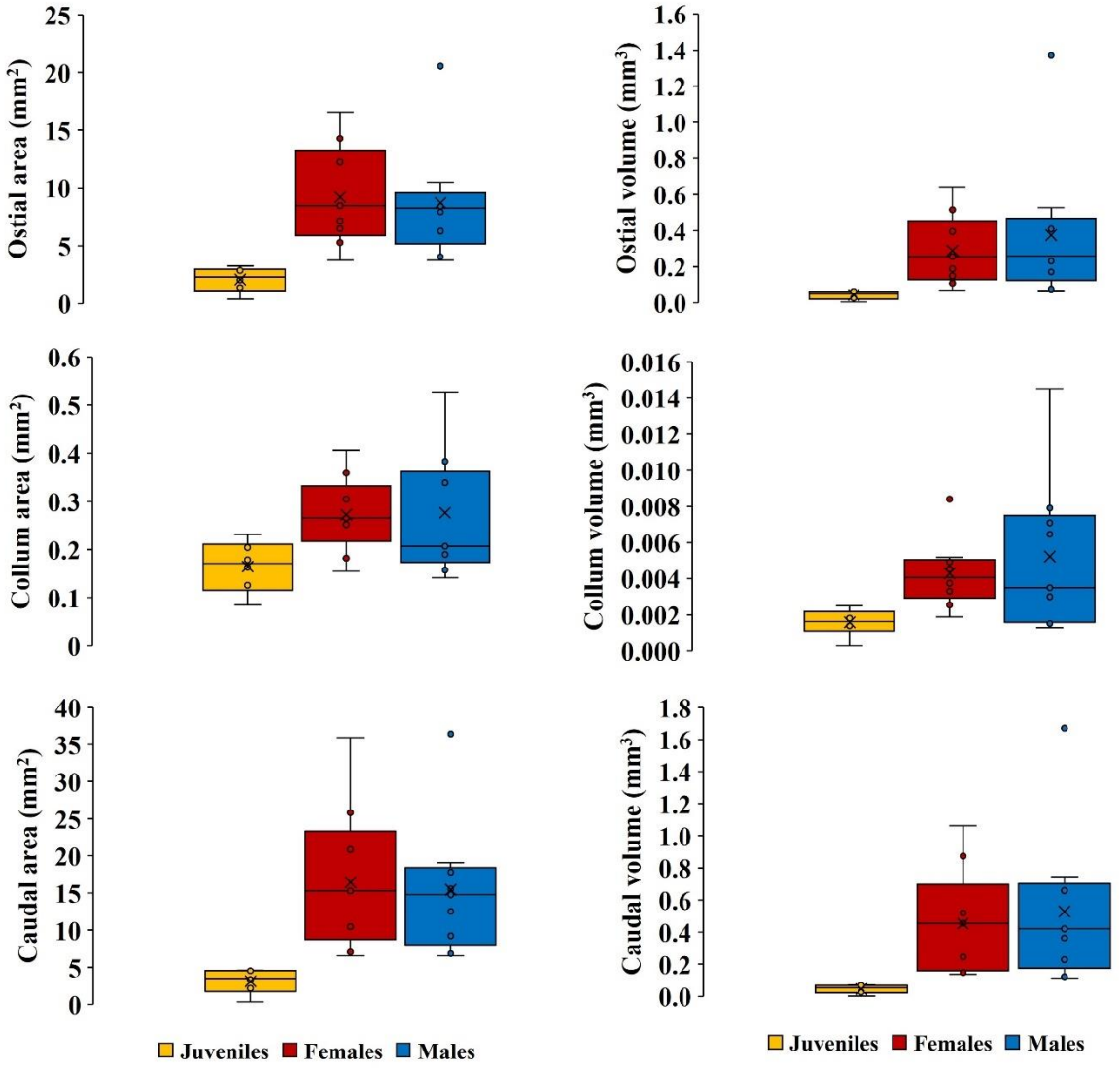

Figure S13. Boxplots of the ratios in immature individuals (on the left), in female (in the middle), and males (on the right) of the three sulcus parts (ostial, collum and caudal). The box indicates the 25th and 75th percentiles and the line within the box marks the median. Whisker length is equal to 1.5 × interquartile range (IQR). Circles represent outliers. N = 6 for immature; N = 9 for females; N = 9 for males.

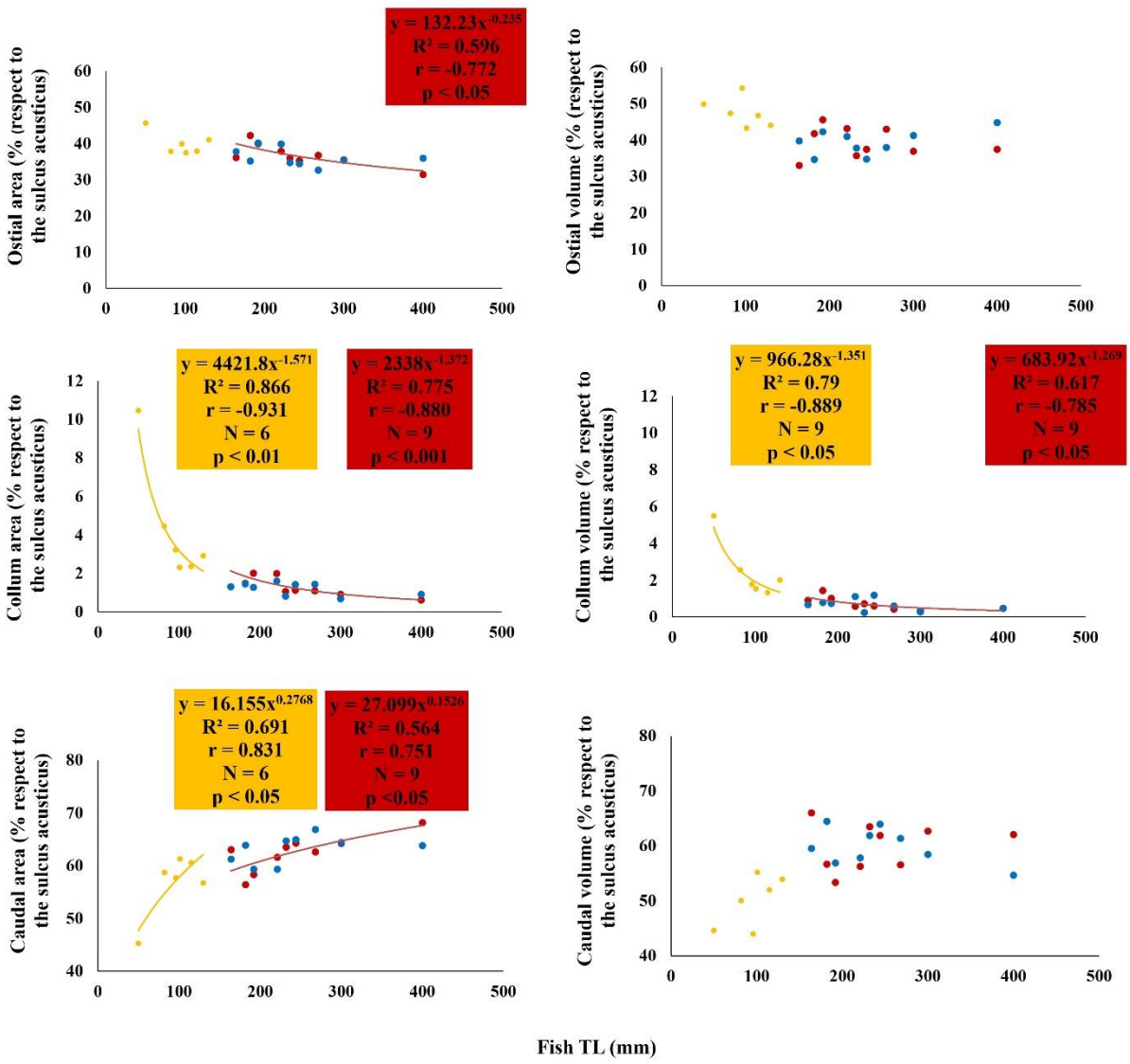

Figure S14. Relationship between the ostial, collum and caudal area and volume, expressed as the percentage of the area and volume with respect to the entire sulcus acusticus, with fish length. The colours of the dots, the curves and their respectively equations represent in yellow the immature individuals, in red the females, in blue the males and in black the general curves (all the data pooled). Curves and their respectively equations are no reported when the relations were no significant. N, number of samples; R^2, Pearson's coefficient of determination; R, Pearson's correlation coefficient.

Section 2. Adaptation and acclimatation in coral skeletons

− One of the extraordinary things about nature is that it offers solutions to most of our problems. −

This session highlights the remarkable plasticity of coral skeletons which repeatedly allowed Scleractinia group to adapt to a range of changing environments throughout its geological history.

Using a multiscale approach, a variety of coral skeleton parameters are compared in order to assess the evolutionary and adaptive driving forces in phylogenetically related coral species of the genus *Balanophyllia*.

Furthermore, this section also considers the response of environmental acidification of several coral skeletons in a volcanic CO_2 vent system used as natural laboratories to investigate the impacts of near and far future ocean acidification.

Chapter 4. The skeleton of phylogenetically related coral species suggests adaptive traits linked to the onset of mixotrophy

(Published in Science of the Total Environment)

Science of the Total Environment 795 (2021) 148778

Contents lists available at ScienceDirect

Science of the Total Environment

journal homepage: www.elsevier.com/locate/scitotenv

The skeleton of *Balanophyllia* coral species suggests adaptive traits linked to the onset of mixotrophy

Quinzia Palazzo [a,g,1], Fiorella Prada [b,g,1], Tim Steffens [c], Simona Fermani [a,h], Chiara Samorì [a], Giacomo Bernardi [d], Alexis Terrón-Sigler [e,i], Francesca Sparla [f,*], Giuseppe Falini [a,g,j,**], Stefano Goffredo [b,g,**]

[a] Department of Chemistry <<Giacomo Ciamician>>, University of Bologna, Via Selmi 2, 40126 Bologna, Italy
[b] Marine Science Group, Department of Biological, Geological and Environmental Sciences, University of Bologna, Via Selmi 3, 40126 Bologna, Italy
[c] Xell AG, Waldweg 21, 33758 Schloss Holte-Stukenbrock, Germany
[d] Department of Ecology and Evolutionary Biology, University of California Santa Cruz, 115 McAllister Way, Santa Cruz, CA 95060, USA
[e] Departamento de Zoología, Facultad de Biología, Universidad de Sevilla, Avda. Reina Mercedes 6, 41012 Sevilla, Spain
[f] Department of Pharmacy and Biotechnology, University of Bologna, Via Irnerio 42, 40126 Bologna, Italy
[g] Fano Marine Center, The Inter-Institute Center for Research on Marine Biodiversity, Resources and Biotechnologies, Viale Adriatico 1/N, 61032 Fano, Italy
[h] CIRI Health Sciences & Technologies (HST), University of Bologna, I-40064 Bologna, Italy
[i] Asociacion Hombre y Territorio, C/Betania no. 13, CP. 41007 Sevilla, Spain
[j] Consiglio Nazionale delle Ricerche, Istituto per lo Studio dei Materiali Nanostrutturati (CNR-ISMN), Via P. Gobetti 101, 40129 Bologna, Italy

HIGHLIGHTS

- Preserved skeletal structural features in *Balanophyllia* azooxanthellate species.
- The onset of mixotrophy led to larger, denser and less porous coral skeletons.
- Higher amount of intra-skeletal organic matrix found in zooxanthellate species.
- Skeletal protein migration differs between azooxanthellate and zooxanthellate species.
- Crystallographic features preserved regardless of trophic strategy.

GRAPHICAL ABSTRACT

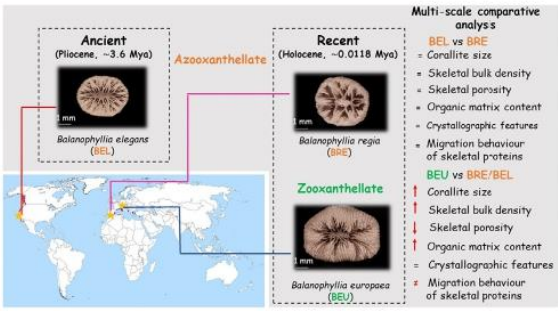

ARTICLE INFO

Article history:
Received 26 April 2021
Received in revised form 26 June 2021
Accepted 27 June 2021
Available online 1 July 2021

Editor: Henner Hollert

Keywords:
Balanophyllia
Skeletal features
Intra-skeletal organic matrix

ABSTRACT

The diversity in the skeletal features of coral species is an outcome of their evolution, distribution and habitat. Here, we explored, from macro- to nano-scale, the skeletal structural and compositional characteristics of three coral species belonging to the genus *Balanophyllia* having different trophic strategies. The goal is to address whether the onset of mixotrophy influenced the skeletal features of *B. elegans*, *B. regia*, and *B. europaea*. The macroscale data suggest that the presence of symbiotic algae in *B. europaea* can lead to a surplus of energy input that increases its growth rate and skeletal bulk density, leading to larger and denser corals compared to the azooxanthellate ones, *B. regia* and *B. elegans*. The symbiosis would also explain the higher intra-skeletal organic matrix (OM) content, which is constituted by macromolecules promoting the calcification, in *B. europaea* compared to the azooxanthellate species. The characterization of the soluble OM also revealed differences between *B. europaea* and the azooxanthellate species, which may be linked to diverse macromolecular machineries responsible for skeletal biosynthesis and final morphology. Differently, the crystallographic features were homogenous among species, suggesting that the basic building blocks of skeletons remained a conserved trait

* Corresponding author.
** Corresponding authors at: Fano Marine Center, The Inter-Institute Center for Research on Marine Biodiversity, Resources and Biotechnologies, Viale Adriatico 1/N, 61032 Fano, Italy.
E-mail addresses: francesca.sparla@unibo.it (F. Sparla), giuseppe.falini@unibo.it (G. Falini), s.goffredo@unibo.it (S. Goffredo).
[1] Equally contributing authors.

https://doi.org/10.1016/j.scitotenv.2021.148778
0048-9697/© 2021 Elsevier B.V. All rights reserved.

Biomineralization
Trophic strategy

in these related species, regardless of the trophic strategy. These results show changes in skeletal phenotype that could be triggered by the onset of mixotrophy, as a consequence of the symbiotic association, displaying remarkable plasticity of coral skeletons which repeatedly allowed this coral group to adapt to a range of changing environments throughout its geological history.

© 2021 Elsevier B.V. All rights reserved.

1. Introduction

Scleractinian corals are an important group of organisms responsible for creating the framework of reefs and exerting important controls on global climate and the marine environment (Dishon et al., 2020). The evolutionary history of Scleractinia has long been tackled through: 1) traditional systematics based on an analysis of the macro scale skeletal characters (Cairns, 2001) and 2) molecular phylogenetics (Arrigoni et al., 2014). The incongruence between traditional and molecular systematics has stimulated the search for new fine-scale micromorphological and microstructural characters, both in the skeleton and soft tissue (Arrigoni et al., 2014; Terrón-Sigler and López-González, 2005).

Among Scleractinia, the genus *Balanophyllia* has ~50 species and a world-wide distribution (Vaughan and Wells, 1943). The distribution of these species is the result of several factors (e.g., larval dispersal ability, environmental conditions) which had important consequences for biogeography and species evolution, which include intrinsic larval dispersal ability (Gerrodette, 1981). The genus *Balanophyllia* has colonized the Mediterranean Sea since the Miocene or at least the early Pliocene (Vertino et al., 2014). During the Late Miocene (~ 7.2 to 5.3 Mya) the Mediterranean Sea underwent one of its most dramatic changes causing the extinction of many species and the shallow-water coral-reef province (Vertino et al., 2014). The causes that led to the regression of the Mediterranean coral fauna diversity are supposed to be: 1) the Messinian Salinity Crisis, 2) the closure of the open marine seaway through the Middle East (Bosellini and Perrin, 2008), and 3) the decreasing seawater surface temperature (Martín et al., 2012). Therefore, the environmental conditions of the Mediterranean varied enormously during the late Miocene, and these modifications may have acted as driving forces for the acquisition of the symbiosis in the *Balanophyllia* genus, resulting in an evolutionary advantage in the highly oligotrophic Mediterranean Sea (Stanley, 2003) which led to the appearance of *Balanophyllia europaea* in the Pleistocene (~2.5–0.0117 Mya) (Vertino et al., 2014).

Subtle differences in growth form, algal symbiosis, sexual system and life history traits confer advantages to growth under certain environmental conditions among species of the same genus (Pandolfi and Jackson, 2001) and these differences are generally established over millions of years. The genus *Balanophyllia* offers a unique opportunity to perform a comparative study among phylogenetically related species characterized by different energy intake strategies, namely zooxanthellate and azooxanthellate species. In particular, the current study was performed on two azooxanthellate corals, namely *B. elegans and B. regia,* and the zooxanthellate *B. europaea*. The first appearance in the fossil record of the species *B. elegans* dates back to the middle Pliocene (~ 5.3 to 2.6 Mya) on the Pacific Coast of North America (Gerrodette, 1981). The Pacific Ocean during the Paleogene (between 65 and 23 Ma) was connected to the other oceans (Lyle et al., 2008) until the closure of the Panama Gateway around 3 Ma (Coates and Obando, 1996). *B. elegans* has been detected only in the Eastern Pacific, from Alaska, USA, to Baja California, Mexico. To the best of our knowledge, no *Balanophyllia* species has been found to inhabit simultaneously the American Pacific and Atlantic coast and no amphi-Atlantic species have been reported so far. The lack of ecological and genetic information of this genus makes difficult the reconstruction of an exhaustive framework of the evolution and genetic connectivity.

Balanophyllia europaea's recent history compared to *B. elegans* and *B. regia* is supported by the fact that the former is zooxanthellate and that it is the only species in the genus *Balanophyllia* that exhibits hermaphroditism (Goffredo et al., 2000; Goffredo et al., 2004). In fact, strong evidence suggests that once the symbiosis is acquired, reverting to an azooxanthellate mode is highly unlikely, if not impossible (Campoy et al., 2020). The symbiosis provides zooxanthellate corals with additional energy compared to the azooxanthellate species, which is reflected in fast metabolism and generally higher calcification rates in the former (Stanley and van de Schootbrugge, 2009). Thus, losing the symbiotic association and adapting to an entirely heterotrophic feeding strategy would be disadvantageous in evolutionary terms. In light of the above considerations, it is reasonable to hypothesize that the zooxanthellate *B. europaea,* evolved from the azooxanthellate *B. regia*, which survived the Messinian salinity crisis in the Late Miocene. Another supporting evidence that *B. europaea* is the most recent species among those investigated in this study, is related to the mating system. In fact, studies have shown that gonochorism is over 100 times more likely to be lost than gained, since it may represent an adaptation to a sessile lifestyle by increasing the probability of finding each sex in a given area (Kerr et al., 2011). Therefore, the sexual modes might have been a trait under selection during the Mediterranean Late Miocene scenario, showing a switch from gonochorism to hermaphrodism, as a consequence of environmental change.

B. elegans (Verrill, 1864) is an aragonitic scleractinian solitary azooxanthellate coral typically found in the subtidal down to ~300 m in depth. *B. elegans* reproduces only sexually, is gonochoric, and broods its embryos (Fadlallah and Pearse, 1982). It generally occurs on the top, middle, and near the base of vertical surfaces of rocks (Foster et al., 2013). Its average linear extension rates are 0.64 ± 0.56 mm yr^{-1} (average ± SD), measured off the coast of Southern California (USA), where abundance at 7–13 m depth averaged more than 500 individuals per m^2 (Fadlallah, 1983a). Growth in *B. elegans* slows asymptotically with increase in size.

B. regia (Gosse, 1860) is an aragonitic scleractinian solitary azooxanthellate coral, rarely fused forming pseudocolonies (Zibrowius, 1980). The reproductive mode is brooding while the sexual condition is assumed to be gonochoric since *Balanophyllia europaea* is considered the only hermaphrodite species of the genus (Goffredo et al., 2000; Fadlallah, 1983b). However, further studies are needed to verify this assumption. It lives on rocky shores from very shallow water down to 25 m depth and occurs in the Mediterranean Sea and northeastern Atlantic from southeast Ireland and England to Morocco and the Canary Islands (Zibrowius, 1980). Its average linear extension rate, measured off the coast of South Finistère (Northern France), is 1.09 ± 0.47 mm yr^{-1} and decreases with size/age (Brahmi et al., 2010).

B. europaea (Risso, 1826) is an aragonitic scleractinian solitary coral and it is the only zooxanthellate species of the genus *Balanophyllia*. Because of its symbiosis with zooxanthellae it colonizes rocky shores exposed to light from near the surface to 50 m depth (Zibrowius, 1980), with abundances of more than 100 individuals m^2 (Goffredo et al., 2004). In the well-characterized populations of the northwestern Mediterranean Sea, the oral disc of *B. europaea* becomes more oval as it grows older (Goffredo et al., 2007) skeletal growth decreases with age (Goffredo et al., 2008). Its average linear extension rate, measured in the Genoa population (Northern Italy), where it was collected for the current study, is 1.17 ± 0.04 mm yr^{-1} (Goffredo et al., 2009).

B. europaea is endemic to the Mediterranean Sea and is a hermaphroditic brooding species.

Coral species descriptions were traditionally based solely on skeletal morphology. However, coral skeletal features are known to exhibit variations unrelated to evolutionary divergence and linked to other factors (e.g., different environments and ecological niches), which may explain why coral species are notoriously difficult to identify, hindering our ability to understand their ecology, evolution, and biodiversity (Todd, 2008). This multi-scale comparative analysis of the skeletal structural and compositional features of three related coral species belonging to the genus *Balanophyllia* and characterized by different trophic strategies aimed to assess whether the investigated skeletal features were more influenced by the onset of mixotrophy.

2. Materials and methods

Coral skeletal features were investigated using experimental techniques that allow multi-scale analysis (Fig. S1).

2.1. Coral collection and treatment

B. elegans specimens ($n = 65$) were randomly collected by SCUBA diving on May 10th 2017 at ~25 m depth off the California coast at Pacific Grove (36° 37′ 18″ N 121° 53′ 53″ W; Fig. S2). The samples were retrieved on exposed large rocks fixed to the sea bottom (not small boulders), where also the cup coral *Astrangia* is also present. *B. regia* specimens ($n = 67$) were randomly collected on February 7th 2017 at 8 m depth along the Granada coast, southern Iberian Peninsula, on Marina del Este beach, specifically in the Punta de la Mona (36° 43′ 08″ N 3° 43′ 38″ W; Fig. S2), where hydrodynamism is generally low (Terrón-Sigler et al., 2016). *B. europaea* specimens ($n = 116$) were randomly collected was collected on March 11th 2017 at 8–9 m depth in a rocky shore site (Punta Chiappa), east of Genoa, Italy (44° 21′ 44.54" N, 9° 07′ 49.17″ E; Ligurian Sea, North-Western Mediterranean Sea; Fig. S2), near the Marine Protected Area of Portofino, characterized by strong hydrodynamism (Misic et al., 2011). Details on coral treatments and preparation of the coral skeleton for destructive analysis are provided in the additional methods section of Appendix A Supplementary data.

2.2. Biometric parameters

Skeletal length (L: maximum axis of the oral disc), width (W: minor axis of the oral disc) and height (h: oral-aboral axis) were measured using a caliper (Goffredo et al., 2007). For each species, samples were divided in three length classes (small, medium, large) by dividing the maximum length value by three. This allowed us to account for possible differences related to the life stage of the corals, as previous studies conducted on one of the three investigated, as well as in other scleractinian corals, have shown a strong relationship between length and age. species (Goffredo et al., 2004; Goffredo et al., 2008). Dry corallite mass (M) was determined with an Ohaus Explorer Pro analytical balance (±0.0001 g) (Caroselli et al., 2011). Surface/volume (S/V) ratio was obtained by dividing S by V, where V is the total volume of the skeleton including its opened pores (obtained by buoyant weight), and S is the surface of the coral, obtained as a sum of the surface of the oral disc $\pi \times (L/2) \times (W/2)$ and the lateral surface of the coral obtained with the formula $\pi\times [3\times (\frac{L}{2}+\frac{W}{2})-\sqrt{(3\times\frac{L}{2}+\frac{W}{2})\times(L/2+3\times W/2}]\times h$ (Caroselli et al., 2015), excluding the base in contact with the substratum.

2.3. Skeletal parameters

Skeletal parameters (i.e., micro-density, bulk density and porosity) were obtained by buoyant weight using a hydrostatic balance (±0.0001 g, Ohaus Corp., Pine Brook, NJ, USA) following a standard non-destructive protocol (Caroselli et al., 2011). A subsample of specimens of each species were randomly selected and used for the destructive analyses.

2.4. Scanning electron microscopy (SEM) observations

One entire skeleton for each species was blued on a stub with carbon tape. The skeleton was then gold sputter (about 20 nm thick). The observations were performed using a Leica Cambridge Stereoscan 360 scanning electron microscope equipped with an Everhart&Thornley SE detector. The images were collected using a tension of 20 kV.

2.5. X-ray and high resolution X-ray powder diffraction (XRD and HR-XRD) analyses

X-ray powder diffraction (XRD) analyses were performed on 19 powdered samples of *B. europaea*, 20 of *B. regia* and 20 of *B. elegans*. High resolution X-ray powder diffraction (HR-XRD) analyses were performed on 3 powdered samples of each species. The diffractograms were collected using a PANanalytical X'Pert Pro equipped with X'Celerator detector diffractometer for a qualitative and quantitative analysis of calcium carbonate polymorphism. A quantitative analysis of the crystalline phases was performed using the software "Quanto" which is based on the Rietveld method (Marchegiani et al., 2009). Details on the XRD and HR-XRD procedures are provided in Appendix A Supplementary data. The structural parameters were refined by Rietveld analysis using the software Quanto and a Pseudo-Voigt peak shape function by CMPR software (Toby, 2005). The estimation of the crystallite size and microstrain fluctuations of aragonite crystals of the skeletons were performed using line profile analysis of the two most intense peaks of aragonite, (111) and (021), from the calculus of FWHM after a multipeak PseudoVoigt peak shape function fitting. The crystallite size for each reflection was calculated using Scherrer equation (Langford and Wilson, 1978) and the microstrain fluctuation on the diffraction peak broadening was derived by line profile analysis (Zolotoyabko, 2014).

2.6. Spectroscopic measurements

Fourier transform infrared spectroscopic (FTIR) analyses were conducted on a subset of random samples previously used for the diffractometric analysis, by using a Nicolet FTIR 380 spectrometer working in the range of wavenumbers 4000–400 cm^{-1} at a resolution of 2 cm^{-1}. Obtained qualitative data were analysed with the software EZ OMNIC (Thermo Electron Corporation). This technique was used to confirm the X-ray powder diffraction data. Details on the FTIR procedure is provided in Appendix A Supplementary data.

2.7. Thermogravimetric analysis (TGA)

Thermogravimetric analysis (TGA) was performed to estimate the Organic Matrix (OM) content, as weight percentage, of the powdered skeletons, using an SDT Q600 simultaneous thermal analysis instrument (TA instrument). From each powdered sample previously investigated through XRD, 5 to 10 mg of powder has been heated under a linear gradient from ambient (30 °C) up to 600 °C. The analyses were performed in N_2 flow from 30° to 120 °C with a heating rate of 10 °C/min, an isothermal at 120 °C for 5 min to remove the non-structural water absorbed moister, and another cycle from 120 to 600 °C with a heating rate of 10 °C/min to evaluate the structural water and the organic matrix from the weight lost between 150 °C and 450 °C.

2.8. Extraction of the intra-skeletal organic components

For each species, 2.5 g of a mix of the powdered skeletons previously investigated, has been used for the extraction of the organic components. Each powdered skeleton mixture was dispersed in 5 ml of milli-Q water and poured into a 20 cm-long osmotic tube for dialysis (MWCO = 3.5

kDa; CelluSep®, MFPI). The sealed tube was put into 1 L of 0.1 M CH_3COOH solution under stirring in order to dissolve the skeletal parts. The decalcification proceeded for 72 h. At the end, the tube containing the dissolved organic matrix (OM) was dialysed against milli-Q water until the final pH was about 6. The obtained aqueous solution containing the OM was centrifuged at 6000 rpm for 3 min to separate the soluble (SOM) and the insoluble (IOM) organic matrix fractions. These analyses were carried out as previously reported (Reggi et al., 2014).

2.9. OM lipid content and fatty acid analysis

The fatty acid (FA) components of the lipOM were analysed by gas chromatography–mass spectrometry (GC–MS) according to reported procedures (Samorì et al., 2017). The analyses were performed on at least 2 replicates of each skeleton on a number of 5 samples of *B. europaea*, 5 of *B. regia* and 4 of *B. elegans*. Details on the procedure are extensively reported in Appendix A Supplementary data.

2.10. OM amino acid composition analysis

Amino acid analysis was conducted by Ultra High Performance Liquid Chromatography (UHPLC Agilent Technologies) equipped with a diode array detector (Agilent Technologies). Macromolecules were hydrolyzed using 6 m HCl for 24 h at 100 °C. During hydrolysis, complete or partial destruction of several amino acids occurs: tryptophan is destroyed, and serine and threonine are partially destroyed. Sulphur amino acids are altered. Then samples were dried and used for derivatization with 6-Aminoquinolyl-N-hydroxysuccinimidyl carbamate (AQC). Detection occurred at a wavelength of 260 nm.

2.11. Characterization of the organic matrix

Five ml of the volume of the soluble part of the organic matrix (SOM) was previously lyophilized, weighed and then analysed using Fourier Transform InfraRed (FTIR) spectroscopy.

The remaining part of the SOM volume was used to separate the proteins by polyacrylamide gel electrophoresis (SDS-PAGE). An extensive description of the procedure is provided in Appendix A Supplementary data.

2.12. Statistical analyses

Data were checked for normality using a Kolmogorov-Smirnov test ($N > 50$) and Shapiro-Wilk test ($N < 50$) and for homogeneity using Levene's Test. One-way analysis of variance (ANOVA) and the non-parametric Kruskal–Wallis equality-of-populations rank were used to assess differences in biometric parameters, skeletal parameters, intra-skeletal organic matrix and water content, and skeletal mineralogy among size classes for each species. ANOVA was used to compare porosity, bulk density and the % composition of the main fatty acids among species. When assumptions for parametric statistics were not fulfilled, the non-parametric Kruskal–Wallis test was used, in particular for micro-density, length, width, height, surface, skeletal mass, volume, *S*/*V* ratio, intra-skeletal organic matrix and water content, mineral phase content and the relative zone absorption intensities of SOMs. Where significant, pairwise comparisons between species were performed via Tukey's HSD or Mann Whitney post hoc tests. To obtain information about the proportion of the skeletal growth (allometric or isometric growth), a linear regression was performed to test the relation between individual width-length and height-length for each species. We assumed that when the confidence interval (CI) of the exponent of the non-linear regression did not contain 1 it indicates an allometric growth (with a biometric parameter increasing more rapidly than another) while, when the exponent of the nonlinear regression contains 1 it indicates an isometric growth. The significance of the correlation was verified using Pearson's correlation coefficient. The statistical differences in regression slopes between the three species were examined comparing the confidence intervals of regression coefficients. All analyses were computed using SPSS Statistics 20. Finally, principal component analysis (PCA) was used to explore coral biometric parameters (length, width,

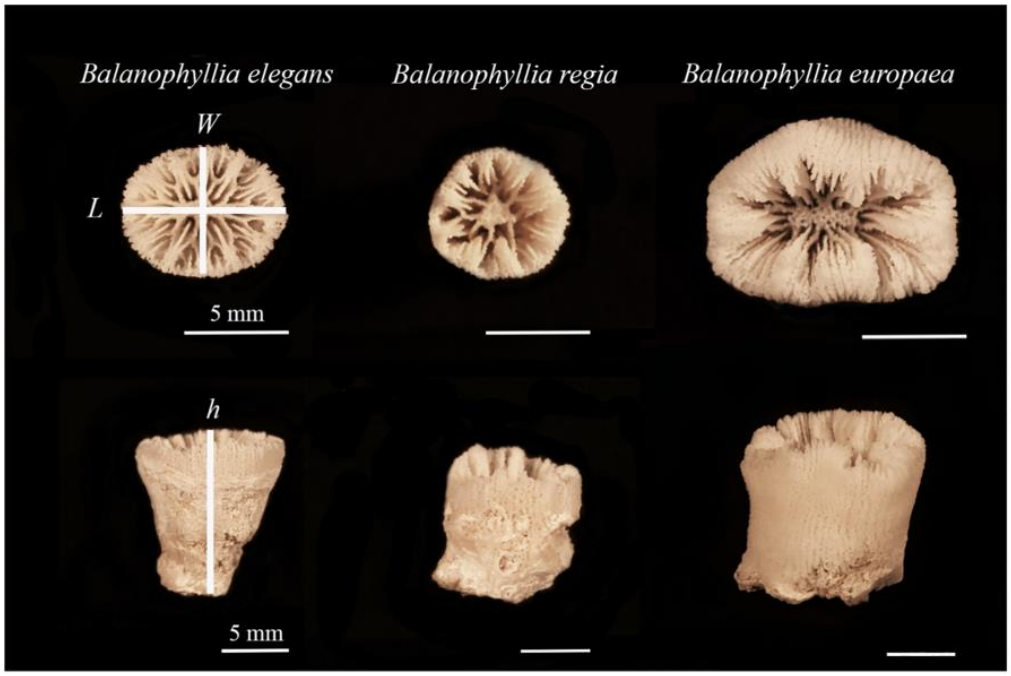

Fig. 1. *Balanophyllia elegans*, *B. regia*, *B. europaea* corallites. Lines indicate polyp length (*L*: maximum axis of the oral disc), polyp width (*W*: minimum axis of the oral disc), and polyp height (*h*: oral-aboral axis). Scale bar is set to 5 mm.

height), skeletal mass, volume, surface/volume ratio, skeletal parameters (micro-density, porosity, bulk density), structural variables (content of intraskeletal water, the organic matrix and the total weight loss), and the skeletal mineralogy (percentage of each mineral phases found in the skeletons), that drive the difference among the three species using PAST 3 software.

3. Results

Combined results of biometry, buoyant weight, SEM, XRD, FTIR, TGA, GC–MS, HPLC, SDS-PAGE revealed the detailed, multi-scale structural organization of the skeletons of three coral species of the genus *Balanophyllia*. For each species, all investigated parameters were compared among size classes and resulted homogeneous, thus the different sets of data were pooled together for comparison among the three species.

3.1. Biometric parameters

Polyp length, height, width, skeletal mass, and volume were significantly different among the three species (Kruskal–Wallis: $p < 0.001$; Fig. 1, Table 1, Fig. S3) and higher in *B. europaea* compared to *B. elegans* and *B. regia* (Mann–Whitney U: $p < 0.001$; Fig. 1, Table 1, Fig. S3). Length and height of *B. elegans* were significantly higher compared to *B. regia* (Mann–Whitney U: length $p < 0.05$; height $p < 0.01$). The surface/volume ratio (S/V) was significantly higher in both azooxanthellate corals compared to *B. europaea* (Mann–Whitney U: $p < 0.001$), while no difference was found between *B. regia* and *B. elegans* (Mann–Whitney U: $p > 0.05$; Table 1, Fig. S3). In all species, the increase of polyp width with respect to polyp length exhibited an allometric growth, with length increasing more rapidly than did width, which resulted in an oval oral disc as polyp size increased. The confidence interval CI of the regression equation exponent was <1 for all species: 0.603–0.757, 95% CI in *B. europaea*; 0.681–0.868, 95% CI in *B. regia*; 0.645–0.837, 95% CI in *B. elegans* (Table S1). The confidence interval of the exponent of the non-linear regression between polyp length and height contained 1 for both the azooxanthellate species (0.768–1.409, 95% CI in *B. regia*; 0.803–1.392, 95% CI in *B. elegans;* Table S1), indicating that coral polyp height and length have isometric growth. For the zooxanthellate *B. europaea*, the confidence interval of the exponent was >1, showing an allometric growth, with polyp height increasing more quickly than polyp length (Table S1).

3.2. Skeletal parameters

Mean skeletal parameters were significantly different among the three species (ANOVA, bulk density and porosity: $p < 0.001$; Kruskal-Wallis, micro-density: $p < 0.001$; Fig. S4). The mean micro-density was homogeneous between *B. europaea* and *B. elegans* and higher compared to *B. regia* (Mann Whitney *U* test, $p > 0.05$ and $p < 0.001$, respectively; Table 1, Fig. S4). The mean bulk density was homogeneous between *B. regia* and *B. elegans* and lower compared to *B. europaea* (Tukey's HSD post-hoc test, $p > 0.05$ and $p < 0.001$, respectively; Table 1, Fig. S4). The mean porosity was homogeneous between *B. regia* and *B. elegans* and higher compared to *B. europaea* (Tukey's HSD post-hoc test, $p > 0.05$ and $p < 0.001$, respectively; Table 1, Fig. S4).

3.3. Mineral skeletal texture

Fig. 2 reports SEM images of the coral skeletons and of mechanically fractured septa at increasing magnifications. The images of the entire skeleton clearly show the different septa organization in the three coral species. The images of cross sections of a septum were acquired for each species. These show the presence of fibrous structures and calcification centers, as previously defined in coral skeleton (Tambutté et al., 2011). The distribution of the calcification centers, as well as the size of the fibers, are difficult to quantify. A qualitative view does not show important differences in the mineralogical texture of the three species.

Table 1
Biometric parameters, skeletal parameters (micro-density, bulk density, and porosity), mineral phases and intra-skeletal organic matrix, water content, and fatty acid concentration. Data are presented as mean ± Standard Deviation (SD). Pairwise comparisons between species were performed with Mann-Whitney *U* test. Significant *p*-values are in bold. BEL = *B. elegans*, BRE = *B. regia*, BEU = *B. europaea*. * $p < 0.05$, ** $p < 0.01$, *** $p < 0.001$.

	Species			Pairwise comparison	
	BEL	BRE	BEU	Species	*p*-value
	mean (SD)	mean (SD)	mean (SD)	compared	
Length	8.61 ± 1.33	8.14 ± 1.30	12.37 ± 2.80	BEU BRE	***
(mm)	N = 65	N = 67	N = 116	BEU BEL	***
				BRE BEL	*
Width	7.07 ± 0.91	7.14 ± 0.99	9.59 ± 1.71	BEU BRE	***
(mm)	N = 65	N = 67	N = 116	BEU BEL	***
				BRE BEL	NS
Height	8.46 ± 1.96	7.69 ± 2.15	11.3 ± 3.70	BEU BRE	***
(mm)	N = 65	N = 67	N = 116	BEU BEL	***
				BRE BEL	**
Skeletal mass	0.29 ± 0.15	0.27 ± 0.18	1.25 ± 0.93	BEU BRE	***
(g)	N = 65	N = 67	N = 116	BEU BEL	***
				BRE BEL	NS
Volume	200 ± 101	194 ± 123	723 ± 537	BEU BRE	***
(mm^3)	N = 65	N = 67	N = 116	BEU BEL	***
				BRE BEL	NS
S/V ratio	1.41 ± 0.27	1.39 ± 0.37	0.82 ± 0.21	BEU BRE	***
(mm^{-1})	N = 65	N = 67	N = 116	BEU BEL	***
				BRE BEL	NS
Micro-density	2.72 ± 0.04	2.64 ± 0.07	2.71 ± 0.05	BEU BRE	***
(g/cm^3)	N = 65	N = 67	N = 116	BEU BEL	NS
				BRE BEL	***
Bulk density	1.48 ± 0.17	1.41 ± 0.18	1.72 ± 0.14	BEU BRE	***
(g/cm^3)	N = 65	N = 67	N = 116	BEU BEL	***
				BRE BEL	NS
Porosity	45.8 ± 6.26	46.3 ± 7.03	36.3 ± 5.47	BEU BRE	***
(%)	N = 65	N = 67	N = 116	BEU BEL	***
				BRE BEL	NS
Aragonite	97 ± 2.40	93 ± 4.65	98 ± 1.37	BEU BRE	**
(%)	N = 20	N = 20	*N* = 19	BEU BEL	NS
				BRE BEL	**
Magnesium-calcite	1.33 ± 1.17	3.77 ± 4.92	2.22 ± 1.28	BEU BRE	NS
(%)	N = 20	*N* = 20	N = 19	BEU BEL	*
				BRE BEL	**
Calcite	0.55 ± 0.95	2.31 ± 1.98	0.12 ± 0.38	BEU BRE	***
(%)	N = 20	N = 20	N = 19	BEU BEL	NS
				BRE BEL	**
Quartz	1.08 ± 1.48	0.9 ± 0.99	0	BEU BRE	***
(%)	N = 20	N = 20	N = 19	BEU BEL	**
				BRE BEL	NS
Water	0.67 ± 0.08	0.78 ± 0.11	0.81 ± 0.34	BEU BRE	NS
(wt%)	N = 20	N = 20	N = 19	BEU BEL	NS
				BRE BEL	**
OM	1.99 ± 0.27	2.04 ± 0.37	2.30 ± 0.44	BEU BRE	*
(wt%)	N = 20	N = 20	N = 19	BEU BEL	*
				BRE BEL	NS
Total weight loss	2.66 ± 0.32	2.82 ± 0.43	3.12 ± 0.76	BEU BRE	NS
(wt%)	N = 20	N = 20	N = 19	BEU BEL	*
				BRE BEL	NS
Fatty acid content	0.29 ± 0.05	0.17 ± 0.12	0.12 ± 0.06	BEU BRE	
(wt%)	*N* = 4	*N* = 5	N = 5	BEU BEL	NS
				BRE BEL	

3.4. Skeletal mineralogy

Other calcium carbonate mineral phases (calcite and magnesium calcite) were found in addition to aragonite in all species (Fig. 3; Figs. S5 and S6). Calcite was found in addition to aragonite in 10% of the skeletons of *B. europaea*, 80% of the skeleton of *B. regia* and 38% of

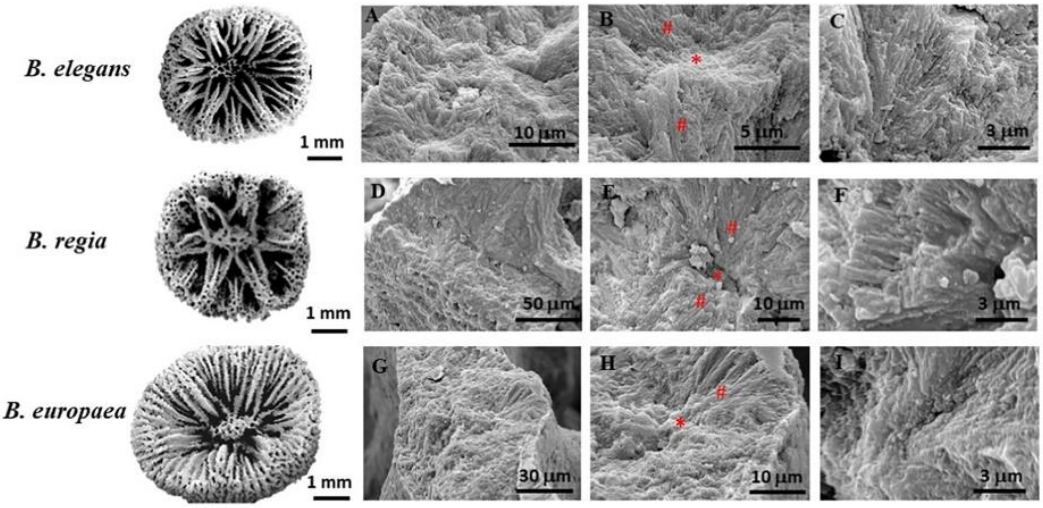

Fig. 2. Scanning electron microscopy images from coral skeleton samples of *B. elegans*, *B. regia*, and *B. europaea*. In (A-C) images at increasing magnifications of a cross section of a septum of *B. elegans* are shown. In (D—F) images at increasing magnifications of a cross section of a septum of *B. regia* are shown. In (G-I) images at increasing magnifications of a cross section of a septum of *B. europaea* are shown. * indicates the center of calcification. # indicates the fibrous region.

the *B. elegans* samples. In the remaining samples calcite content was not detectable by X-ray diffraction. Magnesium calcite was found in all the samples of the three species. In *B. regia* and *B. elegans* quartz was also detected and it was found in 70% of *B. regia* skeletons and in 48% *B. elegans* skeletons. The content in skeletal mineral phases was significantly different among the three species (Kruskal-Wallis, aragonite, calcite, quartz: $p < 0.001$, magnesium calcite, $p < 0.01$; Table 1, Fig. S5). The mean aragonite content was significantly lower in *B. regia* compared to *B. europaea* and *B. elegans* and homogeneous between *B. europaea* and *B. elegans* (Mann Whitney *U* test, $p < 0.001$ and $p > 0.05$, respectively; Table 1, Fig. 3). The content of the magnesium calcite was significantly higher in *B. regia* and in *B. europaea* compared to *B. elegans* (Mann Whitney U test, $p < 0.01$ and $p < 0.05$, respectively; Table 1, Fig. S5) and homogeneous between *B. europaea* and *B. regia* (Mann Whitney U test, $p > 0.05$; Table 1, Fig. S5). The mean calcite content was significantly higher in *B. regia* compared to *B. elegans* and *B. europaea* (Mann Whitney U test,

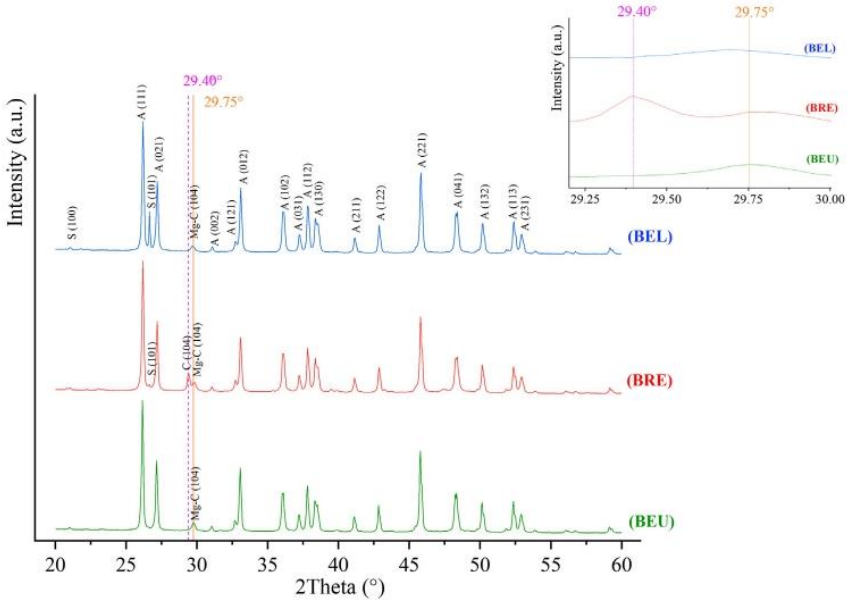

Fig. 3. X-ray powder diffraction patterns from coral skeleton samples of *B. elegans* (BEL), *B. regia* (BRE), and *B. europaea* (BEU). The characteristic diffraction peaks from aragonite (A) are observable together with weak ones from calcite (C) at 29.4°, magnesium calcite (Mg—C) at 29.75° and an additional one due to silica (S (101)) in BEL and BRE. The inserted graph is a zoom of 27.5°-32.0° diffractograms region for BEU and BRE. Notice that the max calcite peak (at 29.4°) is slightly shifted at higher 2Theta (29.75°) in corresponding of magnesium calcite. This peak asymmetry is ascribable to the isomorphic substitution of magnesium ions to calcium ions, which leads to a reduction in the calcite lattice constants thus resulting in a shift in diffraction peaks to higher 2Theta angles. The main diffraction peaks of the Miller index are indicated according to the following reference patterns: aragonite PDF 01–075–2230; calcite PDF 01–086-2336; magnesium calcium carbonate PDF 01-086-336; quartz PDF 01-085-0795.

$p < 0.01$, respectively; Table 1, Fig. 3) while no difference was found between the latter two (Mann Whitney U test, $p < 0.05$; Table 1, Fig. S5). The content of quartz did not show significant differences between the two azooxanthellate species (Mann Whitney U test, $p < 0.05$; Table 1, Fig. S5). Quartz was not found in *B. europaea*. High-resolution X-ray powder diffraction results for the planes (111) and (021) showed no variation in both crystallite size (ANOVA, $p > 0.05$) and micro-strain fluctuation (ANOVA, $p > 0.05$) among species (Tables S3 and S4).

3.5. Intra-skeletal organic matrix content

The mean intra-skeletal organic matrix (OM) and water content (% water, % OM and total weight % loss) measured by thermogravimetric analysis (TGA) were significantly different among the three species (Kruskal-Wallis: $p < 0.05$; Table 1; Figs. S7 and S8). The intra-skeletal OM content (% mass loss) was significantly higher in *B. europaea* compared to *B. regia* and *B. elegans* (Mann Whitney U test, $p < 0.05$, respectively; Table 1), while no difference was detected between the two azooxanthellate species (Mann Whitney U test, $p > 0.05$; Table 1). The intra-skeletal OM content (% mass loss) represented 1.99 ± 0.27% (mean ± SD), 2.04 ± 0.37%, and 2.30 ± 0.44% of the total weight in *B. elegans*, *B. regia*, and *B. europaea*, respectively. The intra-skeletal water content was significantly higher in *B. regia* compared to *B. elegans* (Mann Whitney U test, $p < 0.001$; Table 1), while no differences were found between *B. europaea* and the latter two (Mann Whitney U test, $p > 0.05$; Table 1). The total weight % loss (water + OM; see (Cuif et al., 2004)) was significantly higher in *B. europaea* compared to *B. elegans* (Mann Whitney U test, $p < 0.05$; Table 1), while no differences were detected compared to *B. regia* and between *B. regia* and *B. elegans* (Mann Whitney U test, $p > 0.05$, respectively; Table 1). Correlation analysis between intra-skeletal organic matrix components (water, OM and total weight % loss) and polyp length and skeletal mass revealed that the OM components do not vary with polyp length and skeletal mass in any of the species (Pearson's correlation $p > 0.05$; Table S4).

3.6. Characterization of Soluble Organic Matrix (SOM)

The chemical-physical characterization of the Soluble Organic Matrix (SOM) fractions was performed by FTIR spectroscopy and SDS-PAGE. Table S5 summarizes the observation from the FTIR spectra of SOM obtained from two extraction processes for each species (the average of the absorption peaks from two organic matrix extractions for each species are reported). In Fig. 4 the most representative spectra are shown. In general, SOM showed the same absorption bands, regardless of the coral species; however, differences were observed in their relative intensities (Table S5). In all the fractions, a weaker absorption was observed at 1734/36 cm^{-1} and a marked band at about 2924/25 cm^{-1} (which are consistent with ν C—H stretching vibration) and 28,535/4 cm^{-1}, which can be indicative of fatty acids or molecules bearing alkyl chain regions, due to the methylene and methyl groups' vibration modes. The bands at 2924 cm^{-1} and 2854 cm^{-1} were stronger in *B. regia* than *B. europaea* and *B. elegans*. Characteristic absorption bands corresponding to the protein backbone bonds were shown at 1644/55 cm^{-1} (amide I, νC=O; α-helix, random coil), at 1639 cm^{-1} (amide I; β-sheet) and at 1541/1544 cm^{-1} (amide II, νC-N). In detail, the band around 1637 cm^{-1} were observed only in the SOM from *B. europaea*, suggesting that the types of secondary structure of polypeptides are β-sheet; whereas, in the *B. regia* and *B. elegans* spectra, the band corresponding to secondary protein structure were shown only around 1644/55 cm^{-1}, which usually related to the presence of α-helix. In each SOMs the amide I was strong with respect to the amide II band. The absorption bands located in the range of 1100–950 cm^{-1} were due to glycosidic bond vibration and C—C single bond vibration modes, mainly associable to polysaccharidic moieties.

Three zones (1–3) were defined in order to estimate the relative amounts of the main functional groups of the SOMs from the FTIR spectra

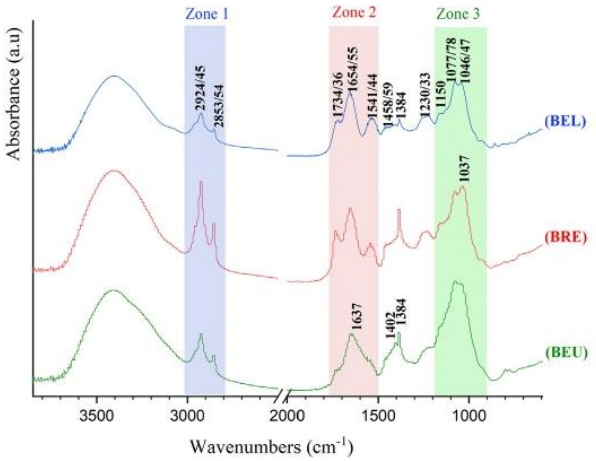

Fig. 4. FTIR spectra of intra-skeletal soluble organic matrix (SOM) extracted from the skeletons of *B. elegans* (BEL), *B. regia* (BRE), and *B. europaea* (BEU). The maximum of the absorption bands are indicated with the possible ranges of shift of absorption toward lower or upper wavenumbers. The three zones define diagnostic regions of functional groups which could be mainly associated to the presence of lipids (zone 1: 3000–2800 cm^{-1}), protein and polysaccharides (zone 2: 1750–1500 cm^{-1}) and polysaccharides (zone 3: 1100–950 cm^{-1}).

(Fig. 4, Table S6). Thus, typical absorption bands of lipids were indicated in the zone 1 (3000–2800 cm^{-1}); characteristic absorption bands corresponding to protein molecules (and to some sugar) have been framed in the zone 2 (1750–1500 cm^{-1}); typical absorption bands representing the polysaccharides pattern were located in the zone 3 (1100–950 cm^{-1}). The integrated intensities of the absorption zones 1 and 3 were normalized to that of zone 2 (Table S6). Regarding *B. europaea*, the SOM spectra showed a stronger integrated intensity absorption due to the polysaccharidic regions respect *B. regia* and *B. elegans* (Table S6), whereas in *B. regia*, the normalized intensity of the lipids region was the strongest among the species. Then a Mann–Whitney statistical test was carried out to verify if the differences in the relative zone absorption intensities between SOMs of the different species were significant. The statistical analysis didn't show differences in the relative intensity of the three zones between the species. The FTIR spectra of intraskeletal components of SOMs extracted from each species showed weak bands at around 1230/33 cm^{-1} that can be associated with the S=O stretching, suggesting the presence of sulphate groups (acid polysaccharides).

Several attempts were conducted to analyze protein components of the soluble organic matrix extracted from the exoskeletons of the three coral species. The most consistent electrophoresis pattern of SOMs are shown as gel lanes in Fig. 5A-B, alongside with the standard proteins of known molecular weights. The concentration values of proteins in the SOMs separated by SDS-PAGE were: 6.08 mg/ml ± 0.04 for *B. elegans*, 3.26 ± 0.23 mg/ml for *B. regia*, and 1.02 ± 0.02 mg/ml for *B. europaea*. The gel revealed several macromolecular species with molecular masses ranging from ca. 12 to 110 kDa. In *B. elegans*, the SDS-PAGE (Fig. 5A) analysis of the decalcified samples revealed many diffuse bands distributed from ~12 kDa to 50 kDa, with the presence of lower molecular weight molecules (ca. 12 kDa, 15 kDa, 20 kDa, 22 kDa) compared to *B. europaea* and *B. regia*. The SOM fraction of *B. regia* was characterized by the presence of two protein smears (diffused bands) of similar macromolecular species also revealed in *B. europaea*, one around 50 kDa and another from ca. 80–110 kDa (Fig. 5B). In *B. europaea*, macromolecular species, gathered around three main molecular weight distributions, having molecular masses from about 30 to 45 kDa (three discrete weak bands), from about 60 to 75 kDa (three discrete bands most strongly stained) and from ca. 80 to 100 kDa (three discrete weak bands) (Fig. 5B).

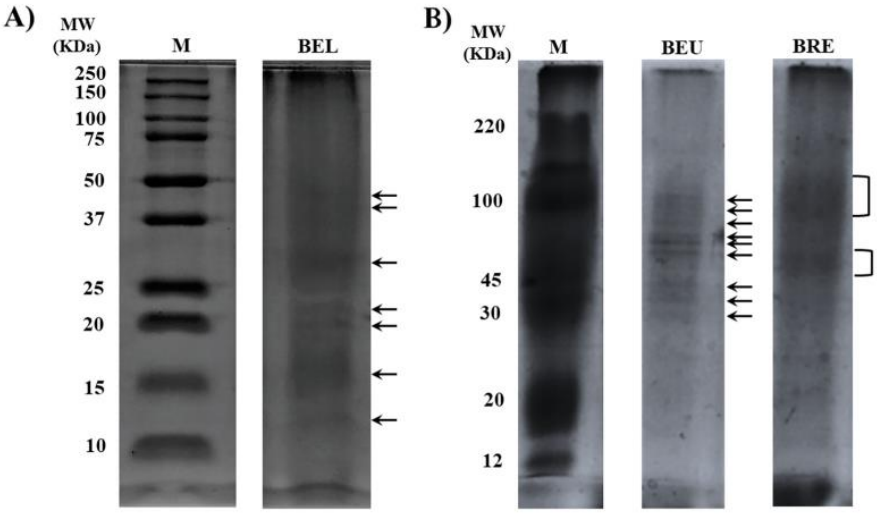

Fig. 5. SDS-PAGE of intra-skeletal SOM extracted from skeletons of *B. elegans* (BEL), *B. regia* (BRE), and *B. europaea* (BEU). The side numbers indicate the molecular weight (MW kDa) of the protein marker (M). A) Protein Marker: BIORAD Precision Plus Protein Dual Color Standard. The protein concentration value was 6.08 ± 0.04 mg/ml for BEL. The volume loaded in the gel lane was 12.3 μl. The arrows indicate the major protein bands. B) Protein Marker: SIGMA ColorBurst Electrophoresis Marker. The protein concentration values, measured by BCA analysis, were 1.02 ± 0.02 mg/ml for BEU and 3.26 ± 0.23 mg/ml for BRE. The volumes applied in the gel lane were 12.0 μl for each species. The arrows indicate the major protein bands and the brackets show the smear band regions.

3.7. OM lipid content and fatty acid analysis

The intra-skeletal FAs concentration (as mass %) were homogeneous among the three species (Kruskal Wallis test, $p > 0.05$; Table 1). *Balanophyllia elegans* showed a skeletal FA content of 0.035 ± 0.013 wt% (mean ± SD), *B. regia* 0.127 ± 0.104 wt%, and *B. europaea* of 0.133 ± 0.122 wt%. Table S7 lists the FA composition (relative distribution %) of the extracts. The detected chain length ranged from C14:0 to C20:0; C16:1, C18:1 and C20:1 were also observed. Missing FA composition data is probably due to values below detection limit (μg). Differences among species were shown in the relative distributions % of C14:0, C15:0, C16:0, C18:0. The FA composition of C14:0 was significantly higher in *B. elegans* (4.5 ± 0.1%) compared to *B. regia* (3.1 ± 0.6%) and *B. europaea* (1.4 ± 0.7%), which showed a lower relative distribution among species (Mann Whitney *U* test $p < 0.05$ Table S7). C15:0 was detected in *B. regia* (2.5 ± 0.4%) and *B. europaea* (0.4 ± 0.1%), but not in *B. elegans*, and showed statistically significant difference between *B. europaea* and the azooxanthellate species (Mann Whitney U test $p < 0.05$ Table S7). C16:0 was the most abundant FA in all the species and showed difference in its relative distribution among species: it was higher in *B. europaea* (51.4 ± 11.3%) compared to *B. regia* (35.4 ± 6.8%) (Mann Whitney U test $p < 0.01$ Table S7), while no statistically significant differences were found in the comparison *B. europaea-B. elegans* and between the azooxanthellate species (Mann Whitney U test $p > 0.05$ Table S7). C18:0 was the second most abundant FA in all the species. Its relative distribution showed differences between *B. elegans* (42.5 ± 5.0%), *B. regia* (25.0 ± 14.3%) and *B. europaea* (21.1 ± 7.0%) with a higher amount in the former compared to the latter (Mann Whitney U test $p < 0.001$ Table S7), a statistically significant difference between the azooxanthellate species (Mann Whitney U test $p < 0.01$ Table S7), and no differences between *B. regia* and *B. europaea* (Mann Whitney U test $p > 0.05$ Table S7). The third most abundant FA detected in all the species was C18:1, ranging from 11.6 ± 5.5% in *B. elegans* to 19.4 ± 8.0% in *B. regia*, but no differences were found among species. C16:1, C17:0, C20:0 and C20:1 were observed in *B. regia* and in *B. europaea*, while they were missing in *B. elegans*.

3.8. OM amino acid composition

The amino acid composition of the protein regions of *B. regia* and *B. elegans* SOM is reported in Table S8, where also the amino acid composition data of *B. europaea*, previously investigated in another study, are shown (Goffredo et al., 2011). The SOMs of *B. regia* and *B. elegans* were characterized by a lower content of acidic residues compared to *B. europaea*. The content of acidic residues in *B. elegans* was 44.0 mol% (Asp 35.7 mol%, and Glu 8.3 mol%), in *B. regia* was 49.1 mol% (Asp 41.7 mol%, and Glu 7.5 mol%) and above 56 mol% in *B. europaea*: Asx (aspartate or asparagine residues) 50.0 mol%, and Glx (glutamate or glutamine residues) about 6 mol%. The content of hydrophobic residues was higher in both azooxanthellate species than *B. europaea*. In fact, Gly, Ala, Val, Ile, Leu, Phe and Pro represented about 38.1 mol% and about 35.4 mol% in *B. elegans* and *B. regia*, respectively; while the SOM of *B. europaea* showed a lower amount of hydrophobic residues (30.0 mol%) (Goffredo et al., 2011). In both SOMs of *B. elegans* and *B. regia*, also arginine and lysine, were present, which were absent in *B. europaea*. In all the species, also serine and threonine were detected and showed differences among SOMs species. In fact, Serine was higher in *B. europaea* and represented the 12.2 mol%, while in *B. elegans* was 6.6 mol% and 7.8 mol% in *B. regia*. The threonine amount was lower in *B. europaea* (1.7 mol%) than in *B. elegans* (4.7 mol%) and *B. regia* (3.5 mol%).

4. Discussion

The heterogeneity of the skeletal architecture and composition of Scleractinian corals is an outcome of many factors related to coral performance, habitat characteristics and evolutionary history (Quattrini et al., 2020). This study provides the first multi-scale analysis of the skeletal features of three related species of the genus *Balanophyllia* and characterized by an earlier heterotrophic feeding mode and a more recent mixotrophic one, aiming to assess possible changes in skeletal phenotype related to the onset of mixotrophy.

At the macroscale (relating to feature sizes >10 μm), an allometric relationship was found between polyp width and length with a progressive ovalization of the oral disc with increasing polyp size in all species,

regardless of their trophic strategy or habitat. A previous study conducted along a Mediterranean latitudinal gradient showed the same trend with increasing polyp age in *B. europaea* (Goffredo et al., 2007). The morphology of the oral discs has been put in relation to sediment disturbances in habitat with high levels of sedimentation (PLA et al., 2012). In fact, the progressive ovalization of the oral disc with increasing length has been considered a strategy to reduce the surface available for sediment accumulation, to increase runoff of sediment and to prevent damage from this stressor, which might occur as polyps become larger (Goffredo et al., 2004; Goffredo et al., 2007; PLA et al., 2012). A different relationship between polyp length and height was found between the zooxanthellate species and the two azooxanthellate counterparts. *B. europaea* showed a positive allometric growth, with polyp height increasing more quickly than polyp length, while both *B. regia* and *B. elegans* presented an isometric growth, with polyp height and length increasing with the same ratio. The allometric behavior shown in *B. europaea* may be another adaptation to sedimentation stress, as this species lives attached to rocky substrata in the shallow waters of the Ligurian Sea, exposed to strong hydrodynamism. Thus, having a higher corallite may help contrast the deposition of sediments on the polyp oral disc.

Here we show that the zooxanthellate *B. europaea* forms larger, denser and less porous skeletons compared to its azooxanthellate sister species. A possible explanation could be that symbiotic corals tend to show higher growth rates compared to non-symbiotic ones (Samorì et al., 2017). In fact, symbiotic algae (zooxanthellae) play an important role in the calcification process of their coral hosts (Iwasaki et al., 2016) through a process known as light enhanced calcification, with calcification being on average three times higher in light than in darkness (Gattuso et al., 1999), thus affecting the size and skeletal density of organisms (Iwasaki et al., 2016).

At the micro-scale the SEM observation (Fig. 2) did not showed a clear pattern in the distribution of the center of calcification in the coral skeleton that can suggest differences among the three species. However, the texture of the fibrous region was quite similar among the three species. This is in line with the model of coral growth reported in the literature that indicated the same mineral building block are used to build up the coral skeleton (Sun et al., 2020).

At the nano-scale, (relating to feature sizes <1 μm) the mean value of micro-density of *B. regia* was significantly lower compared to the other two species as a result of a higher content of extra-mineral phases (e.g. calcite, magnesium-calcite) having lower density (2.94 g cm^{-3} for aragonite, 2.71 g cm^{-3} for calcite, (Marszalek, 1982)) in the coral skeletons. The higher percentage of extra-mineral calcium carbonate polymorphs founded in *B. regia* may be due to the presence of boring organisms (e.g., sponges, polychaetes, bivalves, cyanobacteria, microalgae and fungi), which produce calcite and magnesium-calcite (Brahmi et al., 2010), thus adding exogenous mineral phases in the coral skeleton, while digging galleries (small holes) inside the coral skeletons (Goffredo et al., 2012). Furthermore, the more porous and potentially fragile skeletal phenotype of *B. regia* and its shallow depth compared to *B. elegans* could favour the establishment of boring organisms within its skeleton (Maher et al., 2018). Calcite and magnesium-calcite were found in addition to aragonite in all species, in agreement with previous studies conducted on scleractinian corals (Goffredo et al., 2012; Stolarski et al., 2021). In *B. regia* and *B. elegans* quartz was also detected. The puzzling presence of these additional mineral phases in the skeleton can be hypothesized due to diverse causes. Indeed, previous studies suggest that the distribution of the different $CaCO_3$ forms inside skeletons of scleractinian corals may result from different mechanisms: 1) Corals may biologically precipitate calcite crystals at their early stages in order to ensure their settlement on the substrate of fixation; (2) Mg-calcite presence may come out from skeletons of other calcifying organisms such as crustose coralline algae; in fact, crustose coralline algae are almost exclusively (98–100%) made of high Mg-calcite; and/or (3) calcite may be interpreted as diagenetic infilling of microborer cavities, which are known to colonize coral skeletons (Goffredo et al., 2012; Stolarski et al., 2021). The presence of quartz may be due to boring organism such as sponges composed of silica spicules which may enter in the skeleton of corals (Rützler, 2012), or/and due to sediment particles (containing quartz) that may be trapped in the growing skeleton. It is likely that more than one of the above mentioned processes contribute to explaining the higher content of external mineral phases in the skeletons of *B. regia* and *B. elegans* compared to *B. europaea*. However, crystallite size and microstrain fluctuation resulted homogeneous among species, suggesting that the basic building blocks of aragonite crystals remained a conserved trait in these three related species. Thermograms showed a first weight loss in a range around 125–250 °C (related to the loss of structured water) followed by one between about 250 °C and 450 °C (generally associated with organic matrix pyrolysis) (Reggi et al., 2014). The results of the thermogravimetric OM investigations of the corals *B. europaea*, *B. regia* and *B. elegans* showed a possible relationship between trophic strategy and the intra-skeletal OM content. In fact, a higher OM content was reported in *B. europaea* (*w/w* 2.30 ± 0.44%) compared to *B. regia* (*w/w* 2.04 ± 0.37%) and *B. elegans* (*w/w* 1.99 ± 0.27%). This could be the result of the additional phototrophic supplies provided by the symbiotic dinoflagellates to the coral host in terms of macromolecules and energy (Muscatine et al., 1989). The higher content in intra-skeletal OM, which contains proteins, polysaccharides and lipids that promote the precipitation of $CaCO_3$ (Falini et al., 2015), could also explain the higher growth rates and therefore higher bulk density reported in this study for the zooxanthellate species. The intra-skeletal organic matrix (OM) content was not related to polyp length and skeletal mass in either species, suggesting that the ontogenesis of the investigated species does not affect the OM.

The quantitative differences between the zooxanthellate and the two azooxanthellate species highlighted by the coral skeletal features agree with the PCA analysis (Fig. S9) which shows two main clusters, one for *B. elegans* and *B. regia* and one for *B. europaea* (Fig. S9).

The SDS-PAGE observations of the SOM revealed several proteins with molecular masses ranging from ca. 30 to 100 kDa in *B. europaea*, from about 50 kDa to 110 kDa in *B. regia* and from ca. 12 to 50 kDa in *B. elegans*. The discrete bands identified in *B. europaea* matched with previously observations (Goffredo et al., 2011), showing bands clustered in three groups having molecular masses from about 30 to 45 kDa, from ca. 60 to 75 kDa and around 80–100 kDa. On the other hand, the SOMs of *B. regia* and *B. elegans* resulted in a smear of polydisperse macromolecules (diffuse color). A possible explanation for the smeary pattern in the azooxanthellate species could be due to post-translational modifications which may lead to polydisperse macromolecules and glycosylated proteins in their SOMs that mask the identification of discrete protein bands and create blurry and thick bands (Marin et al., 2016). Indeed, the amino acid composition revealed only in the azooxanthellate species the presence of arginine and lysine, which can interact with negatively charged ions (bicarbonate) or acidic matrix proteins (Mass et al., 2016). In particular, the lysine residues act as glycosylation sites and arginine as phosphorylatation ones and allow for protein post-translational modifications (Alvares, 2014). Therefore, the presence of these residues suggests the presence of glycosylated/phosphorylated proteins in the SOMs of *B. regia* and *B. elegans* that may have the capacity to bind calcium ions creating the observed smeary pattern (Mass et al., 2013). Previous studies have highlighted differences in biochemical composition of organic matrices of symbiotic and non-symbiotic corals, suggesting an involvement of zooxanthellae in the organic matrix composition, probably indirectly, through the synthesis of precursors which are assembled by calicoblastic cells to form organic matrix which is then secreted (Puverel et al., 2005). Nevertheless, also the food source might act directly by providing external amino acids necessary for organic matrix or by supplying additional energy for protein synthesis (Houlbreque, 2004). The

intra-skeletal fatty acids concentration (as mass %) were homogeneous among the species and, differently as previously reported data (Samorì et al., 2017), we didn't find any trend of higher FA concentration in zooxanthellate than in azooxanthellate corals, probably due to different environmental conditions which may influence the FA contents and compositions (Radice et al., 2019). Whereas, the OM fatty acid composition revealed differences likely linked to the different energy intake strategies. The analysis obtained by gas chromatography–mass spectrometry (GC–MS) revealed that, for all the species, palmitic acid (C16:0) was the most abundant fatty acid, followed by stearic (C18:0) and oleic acid (C18:1) in order of concentration. The first two fatty acids indicate omnivorous or carnivorous feeding modes (Sargent and McIntosh, 1974), whereas the last fatty acid (C18:1) was previously found only in the skeleton of symbiotic coral (Samorì et al., 2017) since it is likely a photosynthesis-derived product (Matthews et al., 2018). The fact that we detected oleic acid in the skeleton of azooxanthellate corals, that exclusively rely on heterotrophic feeding, indicates that phytoplankton is the most probable source of this fatty acid, assumed directly by the coral or indirectly by feeding on zooplankton whose diet is based on phytoplankton (Fox et al., 2018).

5. Conclusions

In conclusion, the comparative analysis reported in this study suggests that the onset of mixotrophy might have left a fingerprint on the skeletal structural features of these three related species of the genus *Balanophyllia*. However, further studies under controlled conditions of lighting and nutrient supply in aquaria are needed to confirm this conclusion. The current study adds to the growing body of literature highlighting the remarkable plasticity of coral skeletons which repeatedly allowed this coral group to adapt to a range of changing environments throughout its geological history.

CRediT authorship contribution statement

Quinzia Palazzo: Investigation, Formal analysis, Writing – original draft, Visualization. **Fiorella Prada:** Investigation, Formal analysis, Writing – original draft. **Tim Steffens:** Investigation. **Simona Fermani:** Investigation. **Chiara Samorì:** Investigation. **Giacomo Bernardi:** Resources, Writing – review & editing. **Alexis Terrón-Sigler:** Resources, Writing – review & editing. **Francesca Sparla:** Investigation, Resources, Writing – review & editing, Supervision. **Giuseppe Falini:** Conceptualization, Resources, Writing – review & editing, Supervision, Project administration. **Stefano Goffredo:** Conceptualization, Resources, Writing – review & editing, Supervision, Project administration.

Declaration of competing interest

The authors declare that they have no known competing financial interests or personal relationships that could have appeared to influence the work reported in this paper.

Acknowledgments

The research leading to these results has received funding from the European Research Council under the European Union's Seventh Framework Program (FP7/2007-2013)/ERC grant agreement no. 249930 (CoralWarm: Corals and global warming: the Mediterranean versus the Red Sea). The diving center Bubble Lounge Diving provided logistic assistance in the underwater activities at Genova. The research leading to these results has been conceived under the International PhD Program "Innovative Technologies and Sustainable Use of Mediterranean Sea Fishery and Biological Resources" (www.FishMed-PhD.org). This study represents partial fulfilment of the requirements for the Ph.D. thesis of Quinzia Palazzo.

Supplementary data

Supplementary data to this article can be found online at https://doi.org/10.1016/j.scitotenv.2021.148778.

References

Alvares, K., 2014. The role of acidic phosphoproteins in biomineralization. Connect. Tissue Res. 55, 34–40. https://doi.org/10.3109/03008207.2013.867336.

Arrigoni, R., Kitano, Y.F., Stolarski, J., Hoeksema, B.W., Fukami, H., Stefani, F., et al., 2014. A phylogeny reconstruction of the Dendrophylliidae (Cnidaria, Scleractinia) based on molecular and micromorphological criteria, and its ecological implications. Zool. Scr. 43, 661–688. https://doi.org/10.1111/zsc.12072.

Bosellini, F.R., Perrin, C., 2008. Estimating Mediterranean Oligocene–Miocene sea-surface temperatures: an approach based on coral taxonomic richness. Palaeogeogr. Palaeoclimatol. Palaeoecol. 258, 71–88. https://doi.org/10.1016/j.palaeo.2007.10.028.

Brahmi, C., Meibom, A., Smith, D.C., Stolarski, J., Auzoux-Bordenave, S., Nouet, J., et al., 2010. Skeletal growth, ultrastructure and composition of the azooxanthellate scleractinian coral Balanophyllia regia. Coral Reefs 29, 175–189. https://doi.org/10.1007/s00338-009-0557-x.

Cairns, S.D., 2001. A generic revision and phylogenetic analysis of the Dendrophylliidae (Cnidaria: Scleractinia). Smithson Contrib to Zool, pp. 1–75 https://doi.org/10.5479/si.00810282.615.

Campoy, A.N., Addamo, A.M., Machordom, A., Meade, A., Rivadeneira, M.M., Hernández, C.E., et al., 2020. The origin and correlated evolution of symbiosis and coloniality in scleractinian corals. Front. Mar. Sci. 7. https://doi.org/10.3389/fmars.2020.00461.

Caroselli, E., Prada, F., Pasquini, L., Marzano, F.N., Zaccanti, F., Falini, G., et al., 2011. Environmental implications of skeletal micro-density and porosity variation in two scleractinian corals. Zoology 114, 255–264. https://doi.org/10.1016/j.zool.2011.04.003.

Caroselli, E., Nanni, V., Levy, O., Falini, G., Dubinsky, Z., Goffredo, S., 2015. Latitudinal variations in biometry and population density of a Mediterranean solitary coral. Limnol. Oceanogr. 60, 1356–1370. https://doi.org/10.1002/lno.10100.

Coates, A.G., Obando, J.A., 1996. The geologic evolution of the Central American Isthmus. Evol. Environ. Trop. Am. 21–56.

Cuif, J.-P., Dauphin, Y., Berthet, P., Jegoudez, J., 2004. Associated water and organic compounds in coral skeletons: quantitative thermogravimetry coupled to infrared absorption spectrometry. Geochem. Geophys. Geosyst. 5. https://doi.org/10.1029/2004GC000783 n/a-n/a.

Dishon, G., Grossowicz, M., Krom, M., Guy, G., Gruber, D.F., Tchernov, D., 2020. Evolutionary traits that enable scleractinian corals to survive mass extinction events. Sci. Rep. 10, 3903. https://doi.org/10.1038/s41598-020-60605-2.

Fadlallah, Y.H., 1983a. Population dynamics and life history of a solitary coral, Balanophyllia elegans, from Central California. Oecologia 58, 200–207. https://doi.org/10.1007/BF00399217.

Fadlallah, Y.H., 1983b. Sexual reproduction, development and larval biology in scleractinian corals. Coral Reefs 2, 129–150. https://doi.org/10.1007/BF00336720.

Fadlallah, Y.H., Pearse, J.S., 1982. Sexual reproduction in solitary corals: overlapping oogenic and brooding cycles, and benthic planulas in Balanophyllia elegans. Mar. Biol. 71, 223–231. https://doi.org/10.1007/BF00397039.

Falini, G., Fermani, S., Goffredo, S., 2015. Coral biomineralization: a focus on intra-skeletal organic matrix and calcification. Semin. Cell Dev. Biol. 46, 17–26. https://doi.org/10.1016/j.semcdb.2015.09.005.

Foster, M.S., Reed, D.C., Carr, M.H., Dayton, P.K., Malone, D.P., Pearse, J.S., et al., 2013. Kelp forests in California. In research and discoveries: the revolution of science through scuba. Smithson. Contrib. Mar. Sci. 115–132.

Fox, M.D., Williams, G.J., Johnson, M.D., Radice, V.Z., Zgliczynski, B.J., Kelly, E.L.A., et al., 2018. Gradients in primary production predict trophic strategies of mixotrophic corals across spatial scales. Curr. Biol. 28, 3355–3363.e4. https://doi.org/10.1016/j.cub.2018.08.057.

Gattuso, J.-P., Allemand, D., Frankignoulle, M., 1999. Photosynthesis and calcification at cellular, organismal and community levels in coral reefs: a review on interactions and control by carbonate chemistry. Am. Zool. 39, 160–183. https://doi.org/10.1093/icb/39.1.160.

Gerrodette, T., 1981. Dispersal of the solitary coral balanophyllia elegans by demersal planular larvae. Ecology 62, 611–619. https://doi.org/10.2307/1937728.

Goffredo, S., Telò, T., Scanabissi, F., 2000. Ultrastructural observations of the spermatogenesis of the hermaphroditic solitary coral Balanophyllia europaea (Anthozoa, Scleractinia). Zoomorphology https://doi.org/10.1007/PL00008495.

Goffredo, S., Mattioli, G., Zaccanti, F., 2004. Growth and population dynamics model of the Mediterranean solitary coral Balanophyllia europaea (Scleractinia, Dendrophylliidae). Coral Reefs 23, 433–443. https://doi.org/10.1007/s00338-004-0395-9.

Goffredo, S., Caroselli, E., Pignotti, E., Mattioli, G., Zaccanti, F., 2007. Variation in biometry and population density of solitary corals with solar radiation and sea surface temperature in the Mediterranean Sea. Mar. Biol. 152, 351–361. https://doi.org/10.1007/s00227-007-0695-z.

Goffredo, S., Caroselli, E., Mattioli, G., Pignotti, E., Zaccanti, F., 2008. Relationships between growth, population structure and sea surface temperature in the temperate solitary coral Balanophyllia europaea (Scleractinia, Dendrophylliidae). Coral Reefs 27, 623–632. https://doi.org/10.1007/s00338-008-0362-y.

Goffredo, S., Caroselli, E., Mattioli, G., Pignotti, E., Dubinsky, Z., Zaccantia, F., 2009. Inferred level of calcification decreases along an increasing temperature gradient in a Mediterranean endemic coral. Limnol. Oceanogr. 54, 930–937. https://doi.org/10.4319/lo.2009.54.3.0930.

Goffredo, S., Vergni, P., Reggi, M., Caroselli, E., Sparla, F., Levy, O., et al., 2011. The skeletal organic matrix from Mediterranean coral balanophyllia europaea influences calcium carbonate precipitation. PLoS One 6, e22338. https://doi.org/10.1371/journal.pone.0022338.

Goffredo, S., Caroselli, E., Mezzo, F., Laiolo, L., Vergni, P., Pasquini, L., et al., 2012. The puzzling presence of calcite in skeletons of modern solitary corals from the Mediterranean Sea. Geochim. Cosmochim. Acta 85, 187–199. https://doi.org/10.1016/j.gca.2012.02.014.

Houlbreque, F., 2004. Interactions between zooplankton feeding, photosynthesis and skeletal growth in the scleractinian coral Stylophora pistillata. J. Exp. Biol. 207, 1461–1469. https://doi.org/10.1242/jeb.00911.

Iwasaki, S., Inoue, M., Suzuki, A., Sasaki, O., Kano, H., Iguchi, A., et al., 2016. The role of symbiotic algae in the formation of the coral polyp skeleton: 3-D morphological study based on X-ray microcomputed tomography. Geochem. Geophys. Geosyst. 17, 3629–3637. https://doi.org/10.1002/2016GC006536.

Kerr, A.M., Baird, A.H., Hughes, T.P., 2011. Correlated evolution of sex and reproductive mode in corals (Anthozoa: Scleractinia). Proc. R. Soc. B Biol. Sci. 278, 75–81. https://doi.org/10.1098/rspb.2010.1196.

Langford, J.I., Wilson, A.J.C., 1978. Scherrer after sixty years: a survey and some new results in the determination of crystallite size. J. Appl. Crystallogr. 11, 102–113. https://doi.org/10.1107/S0021889878012844.

Lyle, M., Barron, J., Bralower, T.J., Huber, M., Olivarez Lyle, A., Ravelo, A.C., et al., 2008. Pacific Ocean and Cenozoic evolution of climate. Rev. Geophys. 46, RG2002. https://doi.org/10.1029/2005RG000190.

Maher, R.L., Johnston, M.A., Brandt, M.E., Smith, T.B., Correa, A.M.S., 2018. Depth and coral cover drive the distribution of a coral macroborer across two reef systems. PLoS One 13, e0199462. https://doi.org/10.1371/journal.pone.0199462.

Marchegiani, F., Cibej, E., Vergni, P., Tosi, G., Fermani, S., Falini, G., 2009. Hydroxyapatite synthesis from biogenic calcite single crystals into phosphate solutions at ambient conditions. J. Cryst. Growth 311, 4219–4225. https://doi.org/10.1016/j.jcrysgro.2009.07.010.

Marin, F., Immel, F., Trinkler, N., Gaspard, D., 2016. Staining SDS-PAGE gels of skeletal matrices after western blot: a way to improve their sharpness. Key Eng. Mater. 672, 215–221. https://doi.org/10.4028/www.scientific.net/KEM.672.215.

Marszalek, D.S., 1982. The role of heavy skeletons in vertical movements of non-motile zooplankton. Mar. Behav. Physiol. 8, 295–303. https://doi.org/10.1080/10236248209387026.

Martín, J.M., Braga, J.C., Sánchez-Almazo, I.M., Aguirre, J., 2012. Temperate and Tropical Carbonatesedimentation Episodes in the Neogene Betic Basins (Southern Spain) Linked to cLimatic Oscillations and Changes in Atlantic-Mediterranean Connections: Constraints from Isotopic Data. Carbonate Syst. Dur. Oligocene-Miocene Clim. Transit. Wiley-Blackwell, Oxford, UK, pp. 49–69 https://doi.org/10.1002/9781118398364.ch4.

Mass, T., Drake, J.L., Haramaty, L., Kim, J.D., Zelzion, E., Bhattacharya, D., et al., 2013. Cloning and characterization of four novel coral acid-rich proteins that precipitate carbonates in vitro. Curr. Biol. 23, 1126–1131. https://doi.org/10.1016/j.cub.2013.05.007.

Mass, T., Putnam, H.M., Drake, J.L., Zelzion, E., Gates, R.D., Bhattacharya, D., et al., 2016. Temporal and spatial expression patterns of biomineralization proteins during early development in the stony coral Pocillopora damicornis. Proc. R. Soc. B Biol. Sci. 283, 20160322. https://doi.org/10.1098/rspb.2016.0322.

Matthews, J.L., Oakley, C.A., Lutz, A., Hillyer, K.E., Roessner, U., Grossman, A.R., et al., 2018. Partner switching and metabolic flux in a model cnidarian–dinoflagellate symbiosis. Proc. R. Soc. B Biol. Sci. 285, 20182336. https://doi.org/10.1098/rspb.2018.2336.

Misic, C., Castellano, M., Covazzi Harriague, A., 2011. Organic matter features, degradation and remineralisation at two coastal sites in the Ligurian Sea (NW Mediterranean) differently influenced by anthropogenic forcing. Mar. Environ. Res. 72, 67–74. https://doi.org/10.1016/j.marenvres.2011.05.006.

Muscatine, L., Falkowski, P.G., Dubinsky, Z., Cook, P.A., McCloskey, L.R., 1989. The effect of external nutrient resources on the population dynamics of zooxanthellae in a reef coral. Proc. R. Soc. Lond. B Biol. Sci. 236, 311–324. https://doi.org/10.1098/rspb.1989.0025.

Pandolfi, J.M., Jackson, J.B.C., 2001. Community structure of Pleistocene coral reefs of Curaçao, Netherlands Antilles. Ecol. Monogr. 71, 49–67. https://doi.org/10.1890/0012-9615(2001)071[0049:CSOPCR]2.0.CO;2.

PLA, Erftemeijer, Riegl, B., Hoeksema, B.W., Todd, P.A., 2012. Environmental impacts of dredging and other sediment disturbances on corals: a review. Mar. Pollut. Bull. 64, 1737–1765. https://doi.org/10.1016/j.marpolbul.2012.05.008.

Puverel, S., Tambutté, E., Zoccola, D., Domart-Coulon, I., Bouchot, A., Lotto, S., et al., 2005. Antibodies against the organic matrix in scleractinians: a new tool to study coral biomineralization. Coral Reefs 24, 149–156. https://doi.org/10.1007/s00338-004-0456-0.

Quattrini, A.M., Rodríguez, E., Faircloth, B.C., Cowman, P.F., Brugler, M.R., Farfan, G.A., et al., 2020. Palaeoclimate ocean conditions shaped the evolution of corals and their skeletons through deep time. Nat. Ecol. Evol. https://doi.org/10.1038/s41559-020-01291-1.

Radice, V.Z., Brett, M.T., Fry, B., Fox, M.D., Hoegh-Guldberg, O., Dove, S.G., 2019. Evaluating coral trophic strategies using fatty acid composition and indices. PLoS One 14, e0222327. https://doi.org/10.1371/journal.pone.0222327.

Reggi, M., Fermani, S., Landi, V., Sparla, F., Caroselli, E., Gizzi, F., et al., 2014. Biomineralization in Mediterranean corals: the role of the intraskeletal organic matrix. Cryst. Growth Des. 14, 4310–4320. https://doi.org/10.1021/cg5003572.

Rützler, K., 2012. The role of sponges in the Mesoamerican barrier-reef ecosystem, Belize. Adv. Mar. Biol., 211–271 https://doi.org/10.1016/B978-0-12-387787-1.00002-7.

Samorì, C., Caroselli, E., Prada, F., Reggi, M., Fermani, S., Dubinsky, Z., et al., 2017. Ecological relevance of skeletal fatty acid concentration and composition in Mediterranean scleractinian corals. Sci. Rep. 7, 1929. https://doi.org/10.1038/s41598-017-02034-2.

Sargent, J.R., McIntosh, R., 1974. Studies on the mechanism of biosynthesis of wax esters in Euchaeta norvegica. Mar. Biol. 25, 271–277. https://doi.org/10.1007/BF00404969.

Stanley, G.D., 2003. The evolution of modern corals and their early history. Earth Sci. Rev. 60, 195–225. https://doi.org/10.1016/S0012-8252(02)00104-6.

Stanley, G.D., van de Schootbrugge, B., 2009. The Evolution of the Coral–Algal Symbiosis. , pp. 7–19 https://doi.org/10.1007/978-3-540-69775-6_2.

Stolarski, J., Coronado, I., Murphy, J.G., Kitahara, M.V., Janiszewska, K., Mazur, M., et al., 2021. A modern scleractinian coral with a two-component calcite–aragonite skeleton. Proc. Natl. Acad. Sci. 118, e2013316117. https://doi.org/10.1073/pnas.2013316117.

Sun, C.-Y., Stifler, C.A., Chopdekar, R.V., Schmidt, C.A., Parida, G., Schoeppler, V., et al., 2020. From particle attachment to space-filling coral skeletons. Proc. Natl. Acad. Sci. 117, 30159–30170. https://doi.org/10.1073/pnas.2012025117.

Tambutté, S., Holcomb, M., Ferrier-Pagès, C., Reynaud, S., Tambutté, É., Zoccola, D., et al., 2011. Coral biomineralization: from the gene to the environment. J. Exp. Mar. Biol. Ecol. 408, 58–78. https://doi.org/10.1016/j.jembe.2011.07.026.

Terrón-Sigler, A., López-González, P.J., 2005. Cnidae variability in Balanophyllia europaea and B. regia (Scleractinia: Dendrophylliidae) in the NE Atlantic and Mediterranean Sea. Sci. Mar. 69, 75–86.

Terrón-Sigler, A., León-Muez, D., Peñalver-Duque, P., Gálvez-César, R., Espinosa Torre, F., 2016. Geographic distribution of Astroides calycularis (Scleractinia: Dendrophylliidae) as a baseline to assess future human impacts on the southern Iberian Peninsula. J. Mar. Biol. Assoc. UK https://doi.org/10.1017/S0025315415001113.

Toby, B.H., 2005. CMPR – a powder diffraction toolkit. J. Appl. Crystallogr. 38, 1040–1041. https://doi.org/10.1107/S0021889805030232.

Todd, P.A., 2008. Morphological plasticity in scleractinian corals. Biol. Rev. 83, 315–337. https://doi.org/10.1111/j.1469-185X.2008.00045.x.

Vaughan, T.W., Wells, J.W., 1943. Revision of the suborders families, and genera of the Scleractinia. Spec. Pap. Geol. Soc. Am., 1–394 https://doi.org/10.1130/SPE44-p1.

Vertino, A., Stolarski, J., Bosellini, F.R., Taviani, M., 2014. Mediterranean Corals Through Time: From Miocene to Present. Mediterr. Sea. Springer Netherlands, Dordrecht, pp. 257–274 https://doi.org/10.1007/978-94-007-6704-1_14.

Zibrowius, H., 1980. Les Scleractiniaires de la Mediterranee et de l'Atlantique nord-oriental. Mem l'Institut Oceanogr Monaco 11, 284.

Zolotoyabko, E., 2014. Basic Concepts of X-ray Diffraction.

Supplementary Material for

The skeleton of *Balanophyllia* coral species suggests adaptive traits linked to the onset of mixotrophy. Science of the Total Environment.

Palazzo, Q., F. Prada, T. Steffens, S. Fermani, C. Samorì, G. Bernardi, A. Terrón-Sigler, F. Sparla, G. Falini, S. Goffredo, 2021.

ADDITIONAL METHODS

Coral collection and treatment

Coral tissue was removed by dipping the specimens in a solution of 10% sodium hypochlorite (commercial bleach), changed every 3 days, until the tissue was completely dissolved. Subsequently, the skeletons were washed with double distilled water and dried in an oven at 50 °C for 4 days. Each specimen was then observed under a binocular microscope to remove fragments of substratum and external calcareous deposits produced by epibiont.

Preparation of the coral skeleton for destructive analysis

A subsample of skeleton specimens of each species was randomly selected and used for the destructive analyses. The skeletons were ground with a mortar to obtain small fragments. These skeletal fragments were further treated with a 10% sodium hypochlorite solution for 20 min to completely remove any trace of external skeletal organic tissue, and subsequently washed with milli-Q water (resistivity 18.2 MΩ cm at 25 °C; filtered through a 0.22 µm membrane) and dried in an oven at 37 °C for 24 h. Again, the small fragments were ground using an agate mortar and pestle to obtain a fine and homogeneous powder (grains smaller than 100 µm).

X-ray powder diffraction (XRD) analyses

A diffractogram was obtained for each sample using the following settings: tension = 40 kV; current 40 mA; Cu k-alpha radiation (k = 1.540 A˚); entry slit ½; exit slit ½; step time 150 s; step size 0.02; initial 2theta = 20°; final 2theta = 60° (Fig. 5).

High resolution X-ray powder diffraction (HR-XRD) analyses

A diffractogram was obtained for each sample using the following settings: tension = 40 kV; current 40 mA; Cu k-alpha radiation (k = 1.540 A˚); entry slit $^{1}/_{4}$; exit slit $^{1}/_{4}$; step time 180 s; step size 0.0167; scan speed 0.01181 (°/s); initial 2theta = 20°; final 2theta = 40°.

Spectroscopic measurements

Disk was obtained by mixing little amount (< 1 mg) of skeleton powder with 20 mg of potassium bromide (KBr, Sigma Aldrich, FTIR grade, P99%) and applying a pressure of 48.6 psi (670.2 MPa) to the mixture using a hydraulic press.

OM Lipid content and fatty acid analysis

Powder of coral skeleton samples (about 50mg) were extracted under reflux with chloroform/methanol mixture (2:1 v/v, 4ml) for 1.5 h; the solvent phase was then removed, and the

procedure was repeated three times. The solvent phases were collected and concentrated by evaporation. The total FA content was determined as follows: the lipid extracts were dissolved in dimethylcarbonate (0.4 ml), 2,2-dimethoxypropane (0.1ml) and 0.5M NaOH in MeOH (0.1ml), and then placed in an incubator at 90°C for 30min. After cooling for 5min to room temperature, 1.3M BF3-methanol 10% (w/w) reagent (0.7ml) was added before repeating the incubation for 30min. After cooling for 5min to room temperature, saturated NaCl aqueous solution (2ml) and hexane (1ml) containing methyl nonadecanoate (20 μg) were added and the samples were centrifuged at 4000 rpm for 1min. The upper hexane-dimethylcarbonate layer, containing FAs, was transferred to vials for GC-MS analysis.

Characterization of the organic matrix

Part of the soluble organic matrix (SOM) volume was concentrated using centrifugal filter units (Millipore; Amicon Ultra) which enables the concentration of proteins from a starting volume with a membrane having nominal molecular weight limit of 3 kDa. Filter units are putted in fixed angle rotor at 6000 x g (5°C). The spin times depends on the starting volume of sample. Protein content was determined using the bicinchoninic acid assay kit (BC Protein Assay). The standard curve was established with bovine serum albumin and the absorbance was measured spectrophotometrically (Agilent Cary 60 UV-Vis) at 562 nm. Sodium dodecyl sulfate-polyacrylamide gel electrophoresis (SDS-PAGE) of SOM was performed on 12.5% polyacrylamide gel in a vertical slab gel apparatus (Mini-PROTEAN®, Bio-Rad). Different sample volumes were applied for gel lane (10-20μl). Samples were prepared adding loading buffer 5× (300 mM Tris-HCl pH 6.8; 10% SDS; 12.5% β-mercaptoethanol; 50% glycerol; 0.125% bromophenol blue) and then boiled at 100°C for 5 minutes. The gels ran at a constant voltage of 110 V for 90 minutes at room temperature. Proteins were detected with Classical Coomassie stain for B. elegans and with colloidal Coomassie Brilliant Blue G-250 for B. europaea and B. regia. In the colloidal Coomassie stained procedure, the gel was immersed for 16-18 h under shaking in Staining Solution (0.12% Coomassie Brilliant Blue G-250, 10% ammonium sulfate, 10% phosphoric acid, and 20% methanol) then rinse in Milli-Q water until band became evident.

SUPPLEMENTARY TABLES

Table S1. Dependence of biometric parameters on individual length in *Balanophyllia elegans*, *B. regia*, and *B. europaea*. The confidence interval (CI) of the exponent of the nonlinear regression between polyp length and width was < 1 for all species, indicating allometric growth, with oral disc length increasing more rapidly than width. The confidence interval of the exponent of the non-linear regression between polyp length and height contained 1 in *B. regia* and *B. elegans*, indicating coral polyp height and length have isometric growth, while in *B. europaea*, the confidence interval of the exponent was > 1, showing a positive allometric growth, with polyp length increasing less quickly than polyp height. Length (mm) is the independent variable. Data were fitted to a power function model $y = ax^b$. The factor ‘‘a’’ and the exponent ‘‘b’’ are indicated together with their confidence interval. N number of samples.

	Dependent variable	**Species**	**N**	**Factor (CI)**	**Exponent (CI)**
Length (mm)	Width (mm)	*B. elegans*	65	1.433 (1.168-1.761)	0.741 (0.645-0.837)
		B. regia	67	1.408 (1.158-1.711)	0.775 (0.681-0.868)
		B. europaea	116	1.735 (1.432-2.104)	0.68 (0.603-0.757)
	Height (mm)	*B. elegans*	65	0.783 (0.416-0.678)	1.098 (0.803-1.392)
		B. regia	67	0.767 (0.393-1.499)	1.089 (0.768-1.409)
		B. europaea	116	0.498 (0.361-0.685)	1.235 (1.106-1.362)

Table S2. Position of the mean peaks of aragonite (2Theta), Full Width at Half Maximum (FWHM), size of crystal blocks (crystallite size) and the variance of lattice spacing (microstrain fluctuation) in aragonite estimated from peak broadening equations. BEL = *B. elegans*, BRE = *B. regia*, BEU = *B. europaea*.

	2Theta (°)		**FWHM**		**Crystallite size [µm]**		**Microstrain fluctuation (σ)**	
SAMPLE	**Value**	Standard Error	**Value**	Standard Error	**Value**	Standard Error	**Value**	Standard Error
BEL_08	26.230	0.001	0.132	0.003	0.061	0.001	0.00114	0.00002
	27.235	0.001	0.136	0.003	0.060	0.001	0.00113	0.00002
BEL_21	26.227	0.001	0.157	0.002	0.051	0.001	0.00136	0.00002
	27.230	0.001	0.165	0.002	0.049	0.001	0.00138	0.00002
BEL_27	26.230	0.001	0.143	0.003	0.057	0.001	0.00124	0.00003
	27.231	0.001	0.150	0.003	0.054	0.001	0.00125	0.00002
BRE_20	26.227	0.001	0.147	0.003	0.055	0.001	0.00128	0.00002
	27.229	0.001	0.152	0.003	0.053	0.001	0.00150	0.00002
BRE_30	26.228	0.001	0.145	0.002	0.056	0.001	0.00126	0.00002
	27.230	0.008	0.151	0.002	0.054	0.001	0.00126	0.00002
BRE_21	26.231	0.001	0.139	0.003	0.058	0.001	0.00120	0.00003
	27.233	0.001	0.143	0.003	0.057	0.001	0.00119	0.00002
BEU_GN_26	26.223	0.001	0.148	0.003	0.055	0.001	0.00128	0.00002
	27.226	0.001	0.151	0.003	0.054	0.001	0.00126	0.00002
BEU_GN_11	26.226	0.001	0.146	0.003	0.055	0.001	0.00126	0.00003
	27.229	0.001	0.145	0.003	0.056	0.001	0.00121	0.00002
BEU_GN_75	26.221	0.002	0.184	0.005	0.044	0.001	0.00159	0.00005
	27.223	0.002	0.178	0.004	0.045	0.001	0.00148	0.00003

Table S3. Crystallite size and microstrain estimation of aragonite crystals of skeletons, determined by fitting the (111) and (021) reflections, the most intense peaks of aragonite at the position 26.23° and 27.23° respectively. BEL = *B. elegans*, BRE = *B. regia*, BEU = *B. europaea*. SD = Standard Deviation.

Peak position (°)	**Species**	**Crystallite size [µm]**		**Microstrain (σ)**	
		mean	**SD**	**mean**	**SD**
26.23	BEL	0.0564	0.0049	0.0012	0.0001
	BRE	0.0562	0.0017	0.0012	0
	BEU	0.0514	0.0064	0.0014	0.0002
27.23	BEL	0.0543	0.0053	0.0013	0.0001
	BRE	0.0546	0.0019	0.0013	0.0002
	BEU	0.0516	0.0055	0.0013	0.0001

Table S4. Relationship between intra-skeletal organic matrix components (water, OM and total weight % loss) and polyp length and skeletal mass for *Balanophyllia elegans*, *B. regia* and *B. europaea*. NS Not significant ($p > 0.05$); N number of individuals; R^2 Pearson's coefficient of determination; R Pearson's correlation coefficient

Relationship	***B. elegans***				***B. regia***				***B. europaea***			
	N	**R^2**	**r**	***p*-value**	**N**	**R^2**	**r**	***p*-value**	**N**	**R^2**	**r**	***p*-value**
Length vs Water	20	0.009	0.094	NS	20	0.008	0.008	NS	19	0.093	0.305	NS
Length vs OM	20	0.137	0.370	NS	20	0.051	0.226	NS	19	0.100	0.317	NS
Length vs Total weight loss	20	0.082	0.286	NS	20	0.031	0.176	NS	19	0.101	0.318	NS
Skeletal mass vs Water	20	0.012	0.352	NS	20	0.013	0.114	NS	19	0.049	0.220	NS
Skeletal mass vs OM	20	0.036	0.191	NS	20	0.172	0.414	NS	19	0.070	0.265	NS
Skeletal mass vs Total weight loss	20	0.005	0.071	NS	20	0.154	0.392	NS	19	0.063	0.251	NS

Table S5. Main absorption bands in the FTIR spectra of soluble OM fractions (SOM) extracted from the skeletons of *Balanophyllia elegans*, *B. regia* and *B. europaea*. Standard absorption peaks (cm^{-1}) for the considered chemical groups is also reported. Some bands are slightly shifted toward lower or upper wave numbers. Where dash line is present, no peaks were observed for the relative standard absorption peak.

Functional groups	**Standard absorption peaks (cm^{-1})**	**SOM**		
		B. elegans	***B. regia***	***B. europaea***
CH stretching	2923	2924	2925	2925
CH stretching	2852	2853	2854	2854
Carboxylic stretching	1735	1734	1736	1735
Amide I (α-helix, r.c.)	1653	1655	1655	1654
Amide I (β-sheet)	1637	1648	1644	1639
Amide II	1541	1541	1543	1544
CH_2 bending	1456	1459	1458	1458
Carboxylate stretching	1420	1420	1420	1420
//	1402	1400	1413	1401
S=O stretching (sulfate groups)	1230	1230	1231	1233
SH groups	1222	-	-	1222
CH_3 bending	1385	1384	1384	1384
Sugar groups	1080	1077	1078	1077
//	1030	1047	1037	1046

Table S6. Average relative intensities of zone 1 (3000-2800 cm^{-1}) and zone 3 (1100-950 cm^{-1}) normalized to that of zone 2 (1750-1500 cm^{-1}) of the SOM fractions of OM from *B. elegans*, *B. regia*, and *B. europaea*. The intensity of zones 1-3 can be considered a rough approximation of the content of lipids (blue), proteins (red) and polysaccharides (green), respectively. Data are presented as mean ± Standard Deviation.

Species	Zone 1/Zone 2	Zone 3/Zone 2
B. elegans	0.402 ± 0.087	1.146 ± 0.069
B. regia	1.047 ± 0.271	1.049 ± 0.004
B. europaea	0.909 ± 0.232	1.886 ± 0.095

Table S7. Pairwise comparisons between the composition of the main fatty acids (FAs, % of the total content) of *B. elegans* (BEL) BRE *B. regia* (BRE), and *B. europaea* (BEU). Data are presented as mean ± Standard Deviation (SD). Pairwise comparisons were performed with Mann-Whitney U test. * $p < 0.05$, ** $p < 0.01$, *** $p < 0.001$.

Composition of the main fatty acids (wt. %)	**Species**			**Pairwise comparison**	
	BEL (mean ± SD)	**BRE (mean ± SD)**	**BEU (mean ± SD)**	**Species compared**	***p*- value**
C14:0	4.47 ± 0.14	3.10 ± 0.56	1.42 ± 0.74	BEU BRE BEU BEL BRE BEL	** *** *
C15:0	–	2.47 ± 0.35	0.38 ± 0.07	BEU BRE BEU BEL BRE BEL	* - -
C16:0	46.04 ± 9.02	35.45 ± 6.81	51.39 ± 11.27	BEU BRE BEU BEL BRE BEL	** NS NS
C16:1	–	6.42 ± 5.42	5.29 ± 4.42	BEU BRE BEU BEL BRE BEL	NS - -
C17:0	–	2.06 ± 0.58	1.14 ± 0.75	BEU BRE BEU BEL BRE BEL	NS - -
C18:0	42.48 ± 5.03	24.97 ± 14.29	21.06 ± 6.95	BEU BRE BEU BEL BRE BEL	NS *** **
C18:1	11.56 ± 5.45	19.43 ± 8.01	18.06 ± 6.96	BEU BRE BEU BEL BRE BEL	NS NS NS
C20:0	–	1.93 ± 1.29	1.52 ± 0.28	BEU BRE BEU BEL BRE BEL	NS - -

C20:1	–	3.72 ± 1.71	3.35 ± 0.38	BEU	BRE	NS
				BEU	BEL	-
				BRE	BEL	-

Table S8. Amino acid compositions (relative mol %) of proteins extracted from the soluble fractions of the intra-skeletal organic matrix (SOM) of *Balanophyllia elegans* (BEL), *B. regia* (BRE), and *B. europaea* (BEU). The data concerning *B. europaea* reported here comes from a previously published paper by part of the authors involved in the present study (Goffredo et al. 2011). Empty space indicates a not detectable amount. * indicates Asx (aspartate or asparagine residues) and Glx (glutamate or glutamine residues).

	SOM		
	BEL	BRE	BEU
Ala	6.4	5.5	4.1
Arg	1.9	1.7	
*Asx	35.7	41.7	50.0
Cit			
Cys			
Cys-Cys			
Eta			
*Glx	8.3	7.5	6.1
Gly	15.3	15.2	18.6
His	1.6		
HyPro			
Ile	2.5	2.3	1.5
Leu	3.6	2.7	2.0
Lys	3.1	2.5	
Met			
Orn			
Phe	1.5	1.3	1.2
Pro	3.7	3.3	
Ser	6.6	7.8	12.2
Tau			
Thr	4.7	3.5	1.7
Trp			
Tyr			
Val	5.0	5.2	2.6

SUPPLEMENTARY FIGURES

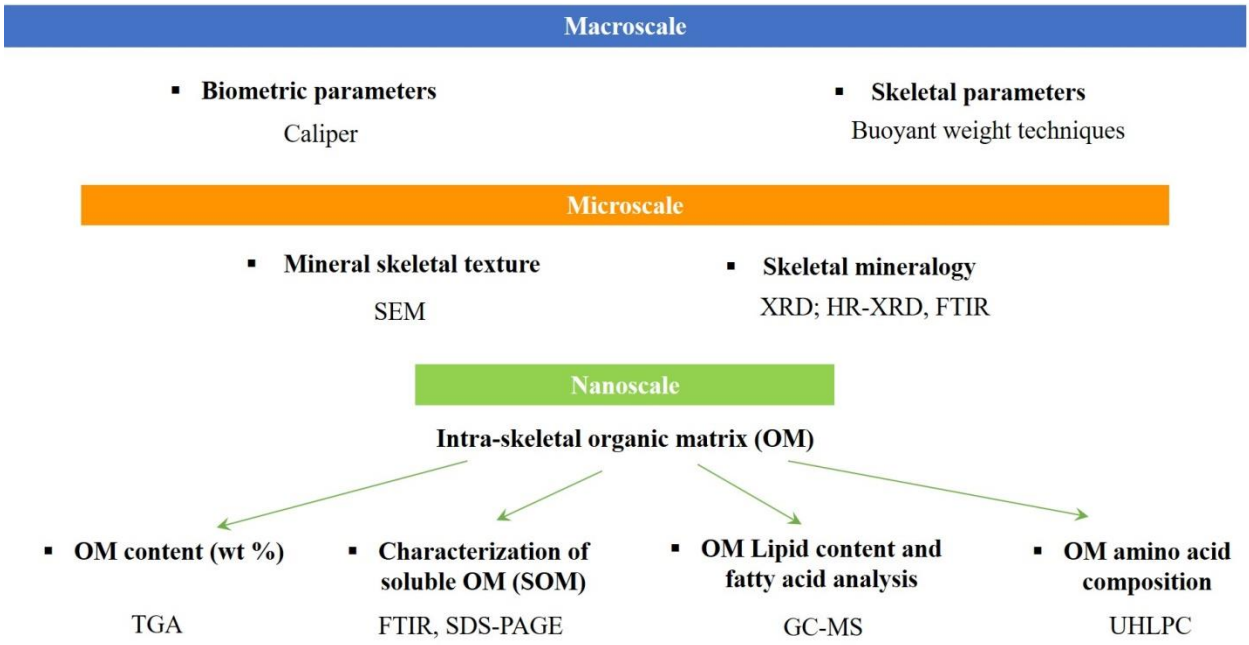

Fig. S1. Overview of the multi-scale analysis performed on coral skeletons of the three *Balanophyllia* species investigated. SEM = scanning electron microscopy; XRD = X-ray powder diffraction; HR-XRD = High resolution X-ray powder diffraction; FTIR = Fourier transform infrared spectroscopic; TGA = Thermogravimetric analysis; SDS-PAGE = Sodium dodecyl sulfate-polyacrylamide gel electrophoresis (SDS-PAGE); GC-MS = gas chromatography-mass spectrometry; UHLPC = Ultra High-Performance Liquid Chromatography.

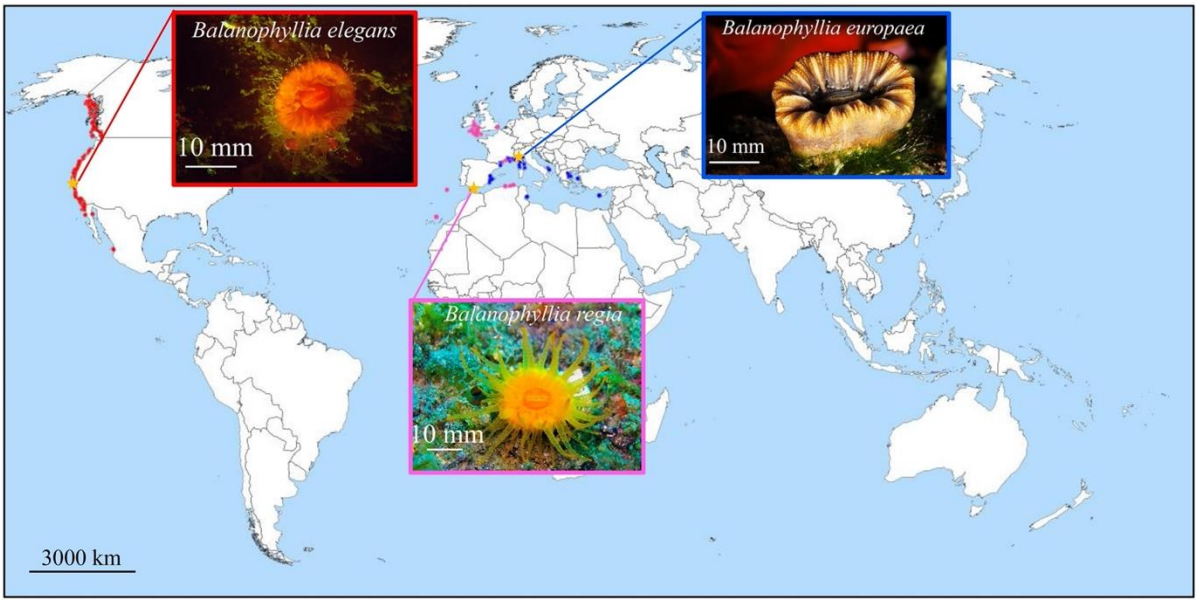

Fig. S2. Map of global distribution of the three species: red spots represent the distribution of *Balanophyllia elegans* (Eastern Pacific: USA, Mexico and Canada), pink spots represent the *B. regia* distribution (Atlantic and the Mediterranean) and the blue ones represent the geographic distribution of *B. europaea* (Mediterranean Sea). Yellow stars indicate the localities where the three investigated species were collected: *Balanophyllia europaea* at Genoa, Italy (44° 21' 44.54" N, 9° 07' 49.17" E; Ligurian Sea, North-Western Mediterranean Sea), *B. regia* at Punta de la Mona, Spain (36° 43' 08" N, 3° 43' 38" W; Alboran Sea, North-Western Mediterranean Sea) and *B. elegans* at Santa Cruz, California, USA (36° 37′ 18″ N 121° 53′ 53″ W; North Pacific Ocean). Photo credit: Giacomo Bernardi for *B. elegans*, Alexis Terrón Sigler for *B. regia*, and Francesco Sesso for *B. europaea*.

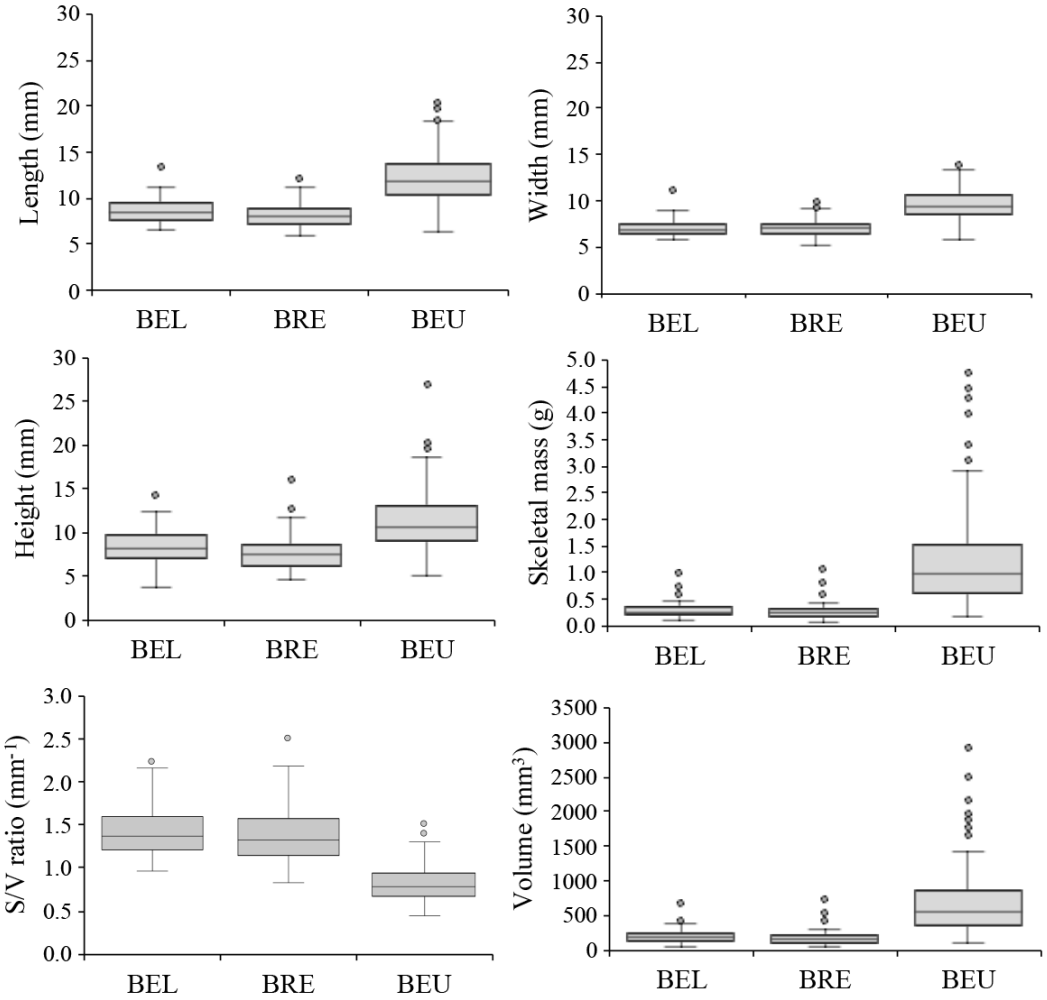

Fig. S3. Boxplots of biometric parameters per each coral species (BEL *B. elegans*; BRE *B. regia*; BEU *B. europaea*). The box indicates the 25th and 75th percentiles and the line within the box marks the median. Whisker length is equal to 1.5 × interquartile range (IQR). Circles represent outliers. N = 116 for BEU; N = 67 for BRE; N = 65 for BEL.

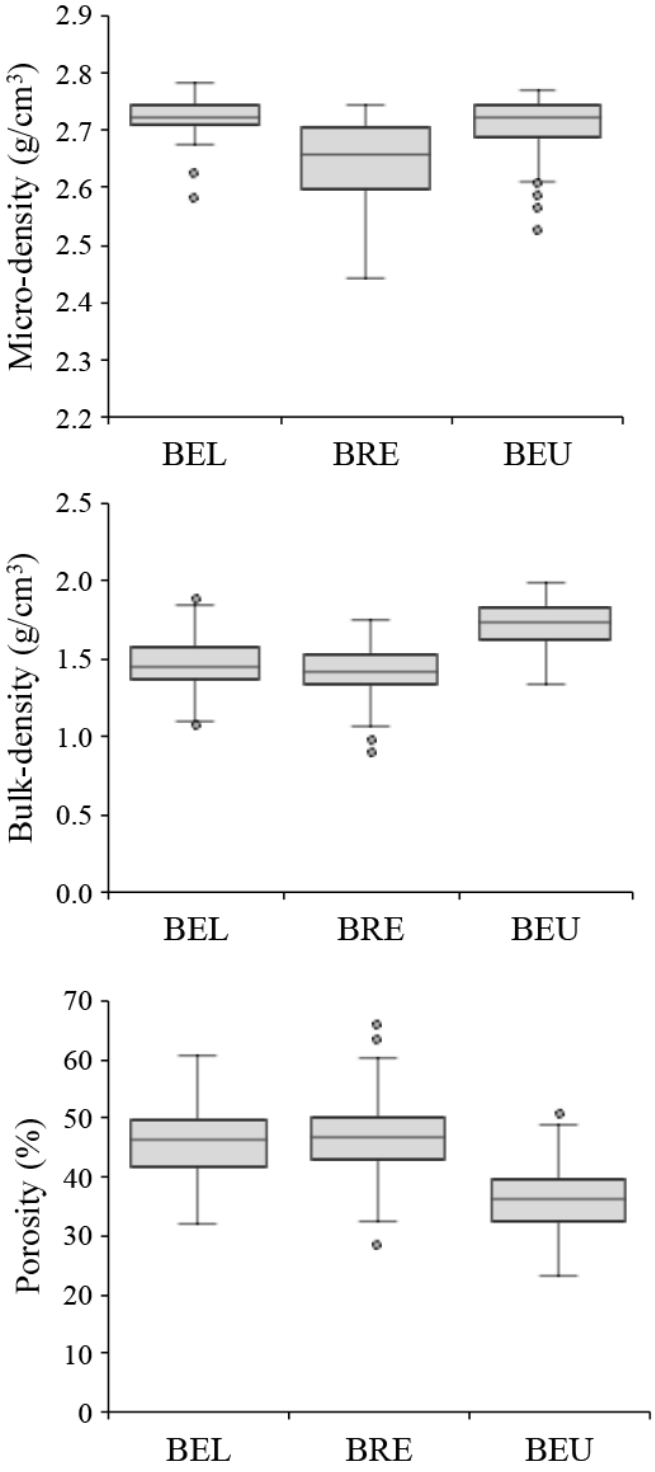

Fig. S4. Boxplots of the skeletal parameters in the three species (BEL *B. elegans*; BRE *B. regia*; BEU *B. europaea*). The box indicates the 25th and 75th percentiles and the line within the box marks the median. Whisker length is equal to 1.5 × interquartile range (IQR). Circles represent outliers. N = 116 for BEU; N = 67 for BRE; N = 65 for BEL.

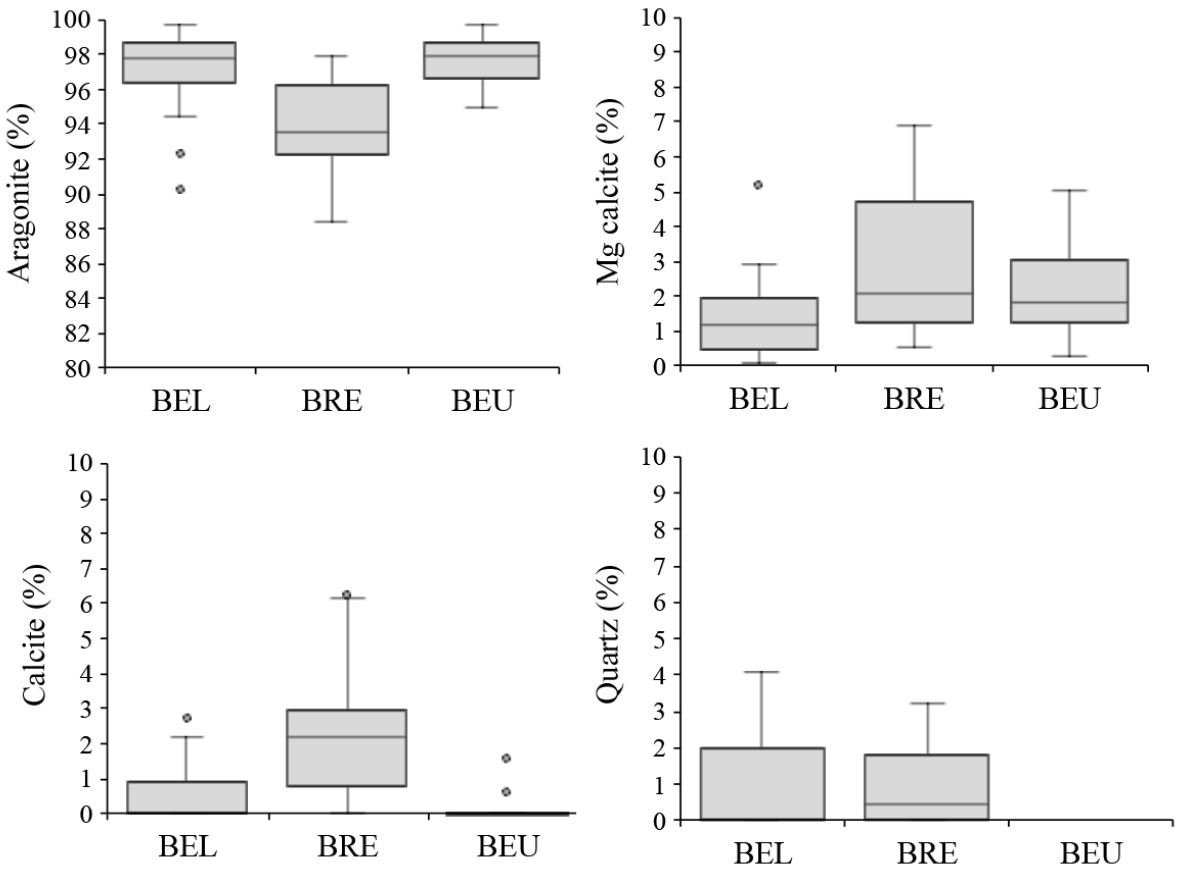

Fig. S5. Boxplots of the mineral phases detected in the three species (BEL *B. elegans*; BRE *B. regia*; BEU *B. europaea*). The box indicates the 25th and 75th percentiles and the line within the box marks the median. Whisker length is equal to 1.5 × interquartile range (IQR). Circles represent outliers. N = 19 for BEU; N = 20 for BRE; N = 20 for BEL.

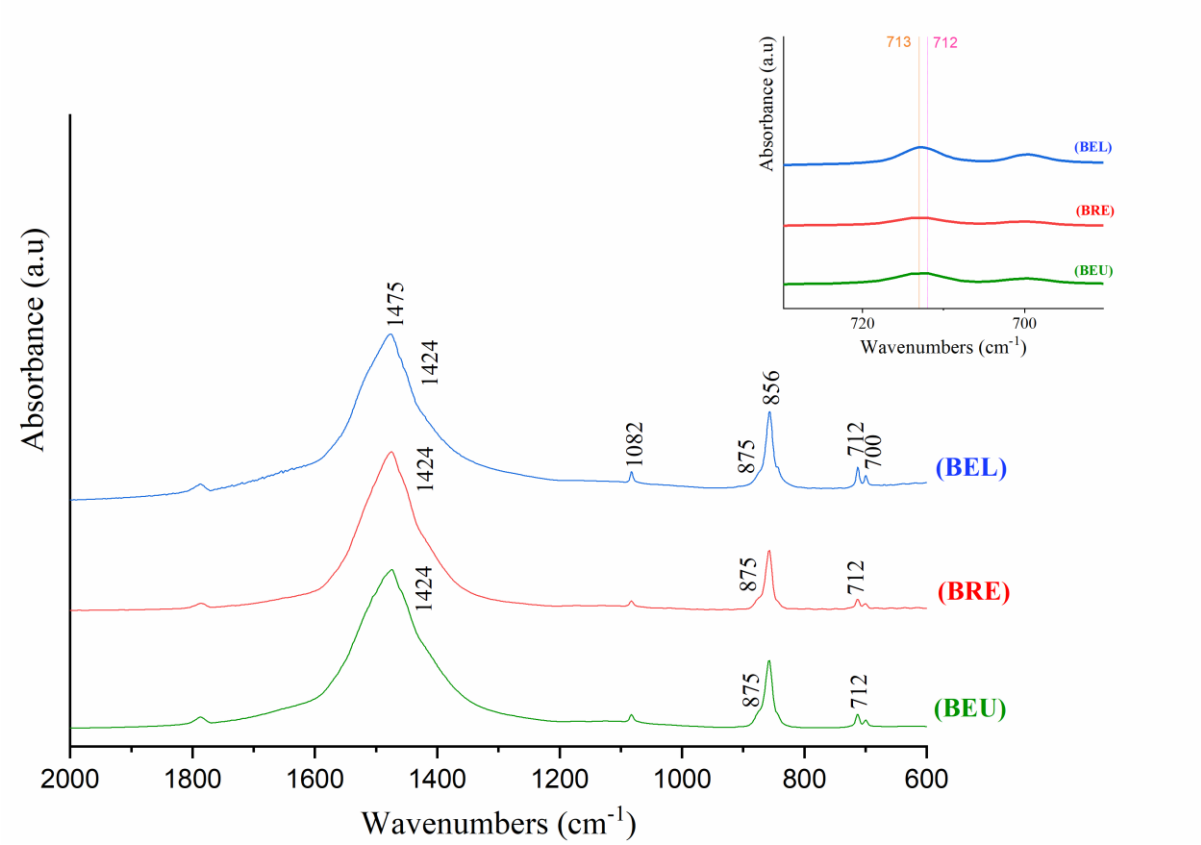

Fig. S6. Representative FTIR spectra of coral skeletons of *Balanophyllia elegans* (BEL), *B. regia* (BRE), and *B. europaea* (BEU). The FTIR spectra showed the characteristic absorption bands of aragonite: ν3=1475 cm−1; ν1=1082 cm−1; ν2=856 cm−1; ν4=712 cm−1; ν4=700 cm−1; and calcite/magnesium calcite: ν3=1424 cm-1; ν2=875/876 cm-1; ν4=712/713 cm-1). The inserted graph is a zoom in the range 700-720 cm^{-1}. In presence of magnesium calcite, the calcite peak at 712 cm-1 slightly shifts at higher wavenumbers 713 cm-1.

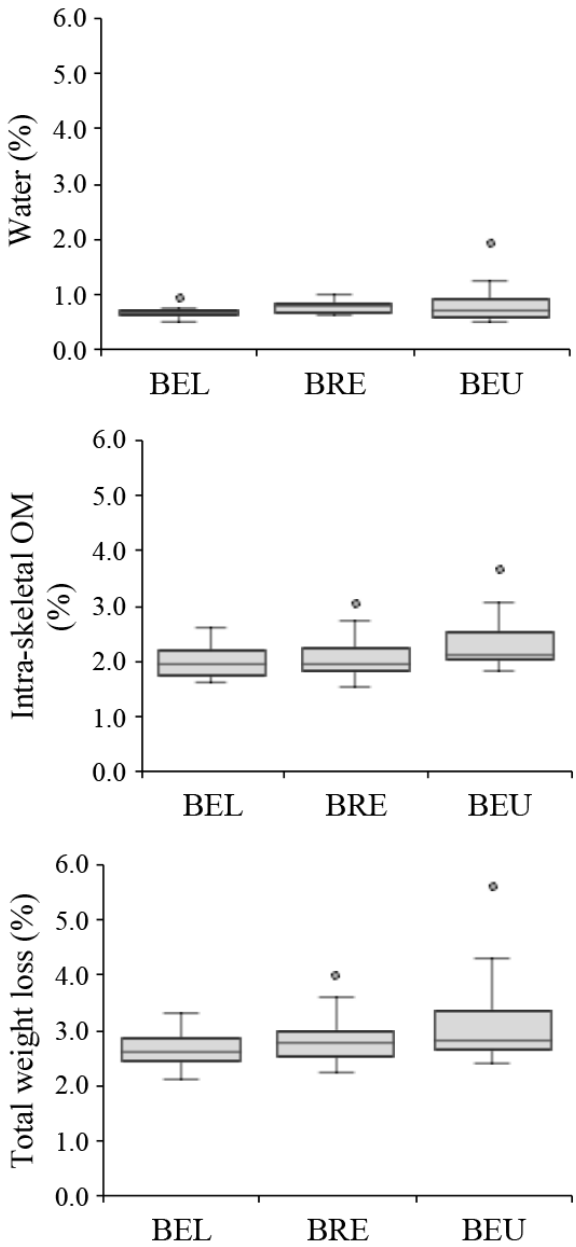

Fig. S7. Boxplots representing the content of intra-skeletal OM, as weight percentage, measured by thermogravimetric analysis (TGA). In detail, the boxplots represent the percentage amount of structured water (water), organic matrix (OM), and total weight loss (water + OM) in the three coral species skeletons (BEL *B. elegans*; BRE *B. regia*; BEU *B. europaea*). The box indicates the 25th and 75th percentiles and the line within the box marks the median. Whisker length is equal to 1.5 × interquartile range (IQR). Circles represent outliers. N = 19 for BEU; N = 20 for BRE; N = 20 for BEL.

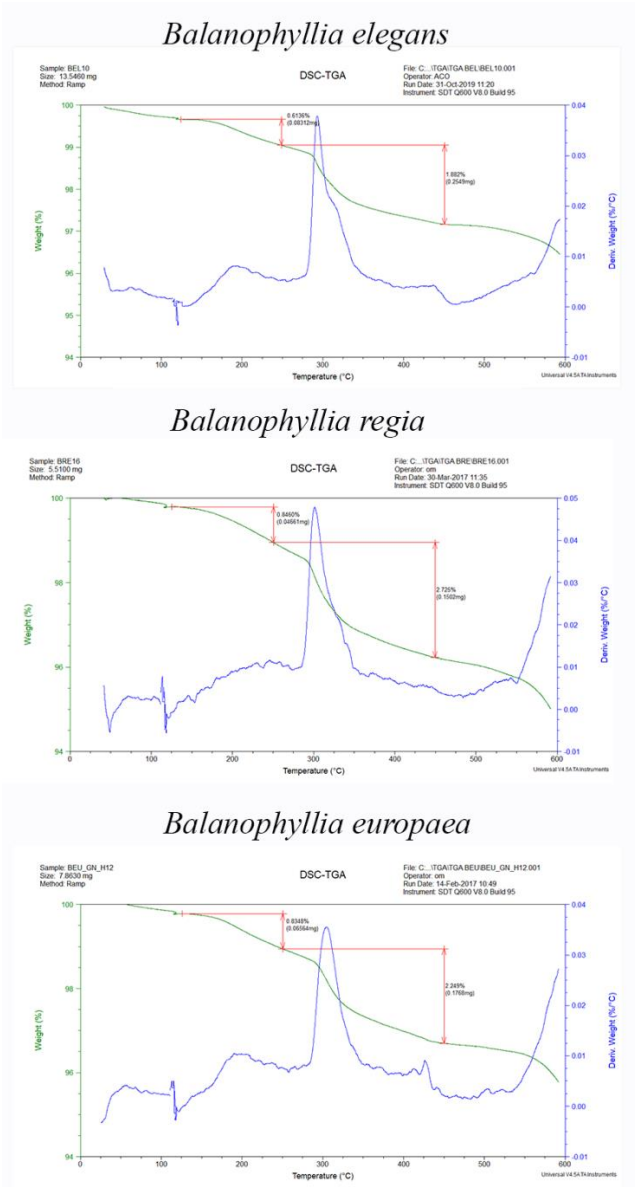

Fig. S8. Representative Thermo-Gravimetric (TGA) profiles of powdered coral skeletons of *Balanophyllia elegans* (BEL), *B. regia* (BRE), and *B. europaea* (BEU). The two lines show the percentage weight loss of the samples with increasing temperature (thermo-gravimetric profiles, green curves) and the first derivate of change weight (blue curves). The weight loss profiles of each species show two significant mass loss events: one occurs between 125-250°C, which is associated with the structured water loss, and the other (the most prominent one) occurring between 250 – 450°C, which is related to the pyrolysis of the organic matrix.

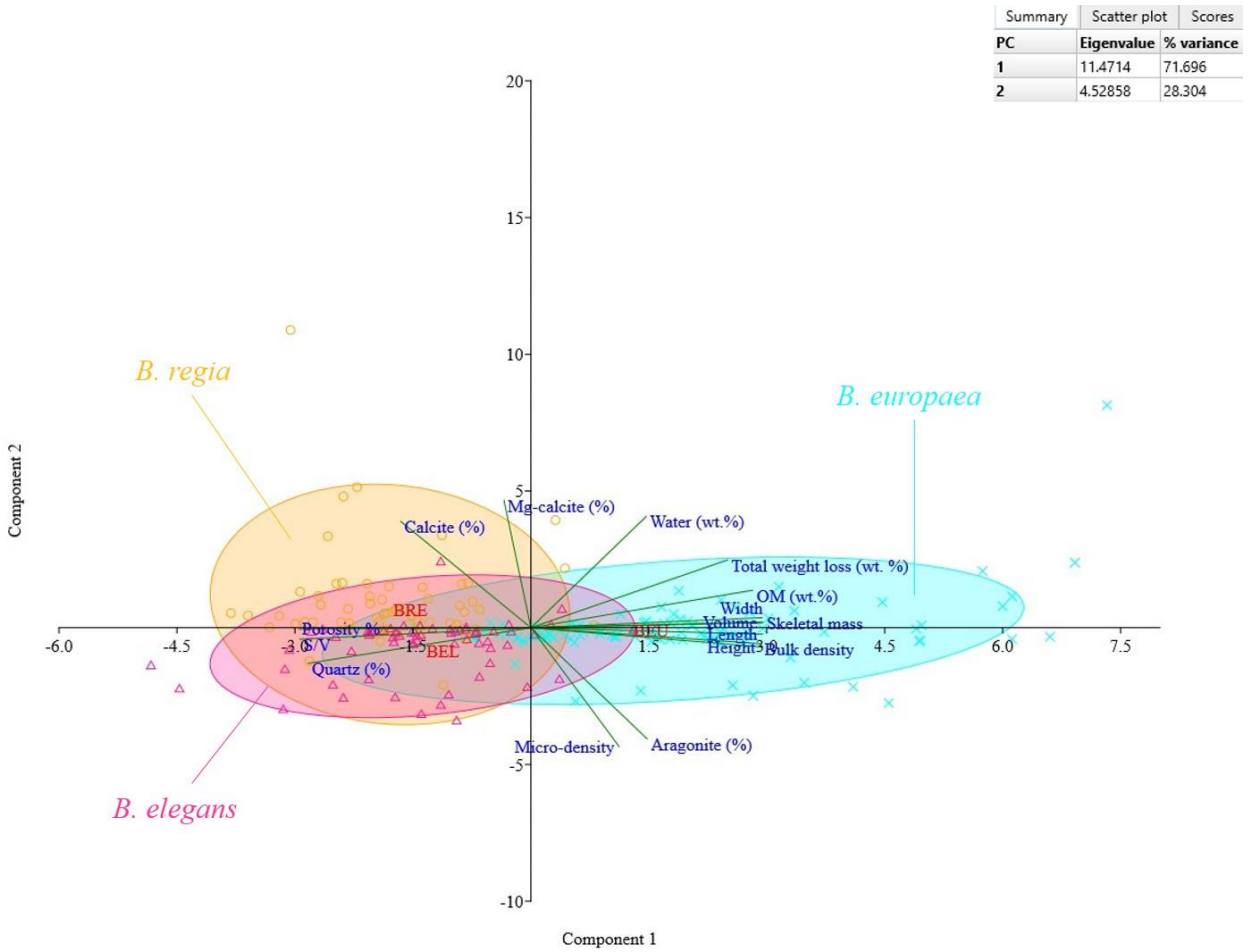

Fig. S9. Principal component analysis (PCA) on the correlation matrix between the three groups representing the coral species investigated. PCA plot of the distribution of the values in the space related to the bi-dimensional coral skeleton biometric, skeletal, and structural parameters, interpreted by PC1 and PC2. Each symbol represents one coral sample. BEL (*Balanophyllia elegans*) in pink triangles; BRE (*B. regia*) in yellow cercles; BEU (*B. europaea*) in blue crosses. Green arrows indicate the correlation of the different parameters with PC1 and PC2. Eigenvalue's plot shows the percentage of explained variance for the two components (PC1=71.7 %, PC2=28.3%). Length, width, height, skeletal mass, volume, S/V ratio, bulk density, porosity %, quartz (%), OM (wt. %), total weight loss (wt. %) related to PC1. Micro-density, aragonite (%), Mg-calcite (%), calcite (%), intraskeletal water (wt. %) were related to PC2.

Chapter 5. Life-long coral skeletal acclimatization at CO_2 vents in Papua New Guinea reveals species- and environment-specific effects

(Published in Scientific Reports)

www.nature.com/scientificreports

scientific reports

OPEN

Coral micro- and macro-morphological skeletal properties in response to life-long acclimatization at CO_2 vents in Papua New Guinea

Fiorella Prada[1,12], Leonardo Brizi[2], Silvia Franzellitti[3,12], Stefano Mengoli[4], Simona Fermani[5], Iryna Polishchuk[6], Nicola Baraldi[1], Francesco Ricci[7], Quinzia Palazzo[5,12], Erik Caroselli[1,12], Boaz Pokroy[6], Loris Giorgini[8,9], Zvy Dubinsky[10], Paola Fantazzini[2]✉, Giuseppe Falini[5,12,13]✉, Stefano Goffredo[1,12]✉ & Katharina E. Fabricius[11]

This study investigates the effects of long-term exposure to OA on skeletal parameters of four tropical zooxanthellate corals naturally living at CO_2 seeps and adjacent control sites from two locations (Dobu and Upa Upasina) in the Papua New Guinea underwater volcanic vent system. The seeps are characterized by seawater pH values ranging from 8.0 to about 7.7. The skeletal porosity of *Galaxea fascicularis*, *Acropora millepora*, massive *Porites*, and *Pocillopora damicornis* was higher (up to ~ 40%, depending on the species) at the seep sites compared to the control sites. *Pocillopora damicornis* also showed a decrease of micro-density (up to ~ 7%). Thus, further investigations conducted on this species showed an increase of the volume fraction of the larger pores (up to ~ 7%), a decrease of the intraskeletal organic matrix content (up to ~ 15%), and an increase of the intraskeletal water content (up to ~ 59%) at the seep sites. The organic matrix related strain and crystallite size did not vary between seep and control sites. This multi-species study showed a common phenotypic response among different zooxanthellate corals subjected to the same environmental pressures, leading to the development of a more porous skeletal phenotype under OA.

Tropical coral reefs support the livelihoods of hundreds of millions of people around the world, harbor 25% of all marine species, and protect thousands of kilometers of shoreline from waves and storms[1]. However, coral reefs face an intensifying array of threats deriving from pollution and overexploitation which is leading to a decline in their health[2]. In addition, global climate change compounds these threats in multiple ways. Increases in seawater CO_2 and associated decreases in carbonate ion concentration, known as ocean acidification (OA), are projected

[1]Marine Science Group, Department of Biological, Geological and Environmental Sciences, University of Bologna, Via F. Selmi 3, 40126 Bologna, Italy. [2]Department of Physics and Astronomy, University of Bologna, Viale Berti Pichat 6/2, 40127 Bologna, Italy. [3]Animal and Environmental Physiology Laboratory, Department of Biological, Geological and Environmental Sciences, University of Bologna, via S. Alberto 163, 48123 Ravenna, Italy. [4]Department of Management, University of Bologna, Via Capo di Lucca 34, 40126 Bologna, Italy. [5]Department of Chemistry 'Giacomo Ciamician', University of Bologna, Via F. Selmi 2, 40126 Bologna, Italy. [6]Department of Material Sciences and Engineering and the Russell Berrie Nanotechnology Institute, Technion – Israel Institute of Technology, Haifa, Israel. [7]School of BioSciences, University of Melbourne, Parkville 3010, Australia. [8]Department of Industrial Chemistry "Toso Montanari", University of Bologna, Viale Risorgimento 4, 40136 Bologna, Italy. [9]Interdepartmental Center for Industrial Research on Advanced Applications in Mechanical Engineering and Materials Technology, CIRI-MAM, University of Bologna, Viale Risorgimento 2, 40136 Bologna, Italy. [10]The Mina and Everard Goodman Faculty of Life Sciences, Bar-Ilan University, 52900 Ramat-Gan, Israel. [11]Australian Institute of Marine Science, PMB 3, Townsville, QLD 4810, Australia. [12]Fano Marine Center, The Inter-Institute Center for Research on Marine Biodiversity, Resources and Biotechnologies, Viale Adriatico 1/N, 61032 Fano, Italy. [13]Consiglio Nazionale delle Ricerche, Istituto per lo Studio dei Materiali Nanostrutturati (CNR-ISMN), Via P. Gobetti 101, 40129 Bologna, Italy. ✉email: paola.fantazzini@unibo.it; giuseppe.falini@unibo.it; s.goffredo@unibo.it

to have profound implications for marine calcifiers, as carbonate ions are essential for biotic calcification[3]. Coral responses to OA may be affected by several factors including colony morphology, size, skeletal mineralogy and structure, tissue thickness, symbiont types, and/or the mechanisms of nutrient acquisition[4]. Moreover, the discrepancy among responses could derive from different experimental designs and analytical methods (e.g., addition of acid vs CO_2 bubbling to mimic OA), co-limiting environmental conditions (e.g., temperature, light intensity, flow, feeding, etc.), and exposure times (days to months or even life times)[5].

To date, most studies both under controlled conditions and under natural conditions in the field (e.g., CO_2 vents), support predictions of decreased rates of calcification and increased rates of dissolution and bioerosion as seawater pH decreases[6]. However, studies conducted using skeletal cores have shown that coral calcification rates have not declined at a constant rate as ocean pH decreased and temperatures warmed throughout the twentieth century. On the contrary, at some locations, calcification rates have remained stable and in others they have even increased over this time period[7–9]. Even where declines in calcification have occurred, many other factors such as ocean warming, sea level rise, changes in surface ocean productivity, as well as many localized anthropogenic disturbances co-occur with OA. These additional factors also influence coral growth and could obscure our ability to attribute changes in coral calcification solely to OA[10].

Most of the available knowledge about OA effects on marine organisms derives from short-term laboratory or mesocosm experiments on isolated organisms[11], which can substantially underestimate full organism acclimatization[12]. In fact, taxa that appear unaffected by high CO_2 under controlled conditions may be: (1) vulnerable in the long-term[13], (2) affected during life stages that were not considered during the experiment[14], or (3) be indirectly affected by OA-driven ecological changes (e.g., food webs, competition, diseases and/or community structures, habitat properties such as microbial surface biofilms)[15]. Likewise, other taxa that respond negatively to OA under controlled conditions may be capable of acclimatizing in the longer term. Thus, field experiments, where organisms are naturally exposed to OA for their entire life, as found around submarine CO_2 vents, could provide important new insights. However, vent systems are not perfect predictors of future ocean ecology owing to temporal variability in pH, spatial proximity of populations unaffected by acidification, and the unknown effects of other changing parameters (e.g., temperature, currents)[16]. Nonetheless, vents acidify sea water on sufficiently large spatial and temporal scales to integrate ecosystem processes such as reproduction, competition and predation[17]. Field-based studies conducted at volcanic CO_2 seeps in Italy[17–19], Japan[20], Mexico[21], and Papua New Guinea (PNG)[15] provide a unique opportunity to investigate long-term effects of OA on marine ecosystems that have been naturally exposed to chronic low pH and concomitant altered carbonate chemistry parameters for years/decades. These studies have already demonstrated substantial changes in community structure and functional biodiversity[22] of benthic species, as well as an array of responses to OA spanning from sharp decrease to no effect on calcification rate[23].

Studies conducted on corals at volcanic CO_2 vents in Papua New Guinea (PNG) have supported the mixed effects observed in laboratory experiments[15,24]. Hard coral cover is similar at acidified and control sites (33% versus 31%). However, the cover of massive *Porites* is doubled under OA, whereas the cover of more structurally complex corals is reduced by one third[24]. Some species are significantly less common or even absent under OA. For instance, while the coverage of *Pocillopora damicornis* decreases by 43% in acidified sites, in situ growth measurements have found small differences in linear extension rate[15], but large differences in recruitment success[25]. Population reductions in situ, combined with observations of negative physiological impacts, including declines in calcification under OA, strongly suggest that low pH imposes selection pressure on less resilient taxa within the PNG system[23].

The aim of this study was to assess the effects of long-term exposure to OA on the skeletal parameters (micro-density, porosity, bulk density) of four tropical zooxanthellate coral species *Galaxea fascicularis* (Linnaeus, 1767), *Acropora millepora* (Ehrenberg, 1834), massive *Porites* Link, 1807, and *P. damicornis* (Linnaeus, 1758), living at CO_2 vents and adjacent control sites in Milne Bay Province, PNG[15]. Additional macroscale and microscale skeletal analyses, namely Time-Domain Nuclear Magnetic Resonance (TD-NMR), Thermogravimetric Analysis (TGA), and synchrotron high-resolution powder X-ray diffraction (HRPXRD) analyses were performed on *P. damicornis*, the only species displaying differences in micro-density at the seep sites compared to control.

Materials and methods

Study sites and coral sampling. The study was conducted at two shallow-water (1–5 m) volcanic CO_2 seeps at ambient temperature and adjacent control sites at Milne Bay Province, PNG, namely Dobu and Upa Upasina (Fig. 1). Almost pure CO_2 (~99%) has been streaming from the seabed for an unknown period of time (confirmed for approximately 70 years, but likely much longer)[15], resulting in localized acidified conditions. Environmental parameters (measured: pH, dissolved inorganic carbon, total alkalinity, salinity, and temperature; calculated with CO2SYS software: pCO_2 and aragonite saturation state) were obtained across a 4-year period (2010–2013) at 1–5 m depth in both control and seep sites[15,24]. Two-cm coral fragments, which corresponds to approximately a 1.5-year growth increment in all the investigated species[15,26,27], were collected at 1–5 m depth from adult colonies of *P. damicornis*, *G. fascicularis*, *A. millepora*, and massive *Porites* at control and seep sites in August 2010 (N = 6–15 fragments per site, each fragment from a different colony)[28]. Tissue from the coral fragments was totally removed using established protocols applied in previous studies on corals which include immersing the samples in a solution of 10% commercial bleach for 3 days and drying them for 24 h at a maximum temperature of 40°C[29–32]. Dried fragments were kept in codified Eppendorf tubes prior to skeletal measurements.

Skeletal porosity, bulk density, and micro-density determination. The skeletal porosity, bulk density, and micro-density of the 192 fragments from the control and seep sites at Dobu and at Upa Upasina were

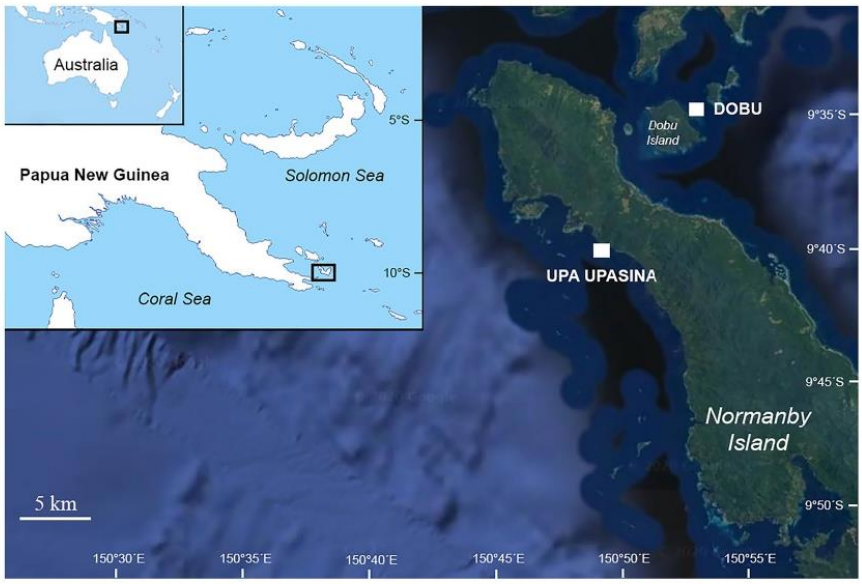

Figure 1. Maps of Papua New Guinea and the two study locations (Dobu and Upa Upasina) on Normanby and Dobu Islands, Milne Bay Province. This Figure was created using Adobe Photoshop CC 2018 (https://www.adobe.com/products/photoshop.html) with imagery from Google Earth (V 9.140.0.4. Eye alt 45 km. SIO, NOAA, U.S. Navy, NGA, GEBCO. TerraMetrix 2020, Digital Globe 2020. https://earth.google.com. 10 December 2020). The inset map was made modifying an image freely available at the following website: https://d-maps.com/carte.php?num_car=3336&lang=en.

obtained as follows. After determining the dry mass, the fragments were placed inside a drying chamber connected to a vacuum pump to evacuate air and water from the pores, a necessary step in order to allow effective saturation of the samples in the followig phase. After 3 h, distilled water was gently introduced to fully saturate the samples which were then weighed in air to determine the saturated weight. Buoyant weight was then measured with a hydrostatic balance (Ohaus Explorer Pro balance ± 0.0001 g) equipped with a density determination kit and used to calculate porosity, bulk density, and micro-density by means of standard calculations (details in Supplementary Methods)[29].

Time-domain nuclear magnetic resonance for pore size distribution determination. To investigate the distribution of pore-size classes, through the analysis of the NMR transverse relaxation time T_2 distributions from control and seep site (details in Supplementary Methods), coral fragments still fully saturated with water, were placed on a wet paper to dry the excess of water on their surface. Then, every fragment was put inside a glass tube, sealed and immediately inserted into the magnetic field to be subjected to TD-NMR measurement. A home-built relaxometer based on an electromagnet JEOL C-60 (magnetic field $B_0 = 0.5$ Tesla) with a radiofrequency coil ≈ 8 mm in diameter, and equipped with a Spinmaster portable console (Stelar, Mede, Pavia, Italy) was used. The Carr- Purcell-Meiboom-Gill (CPMG) sequence with 200 μs echo time was used to acquire for each specimen the transverse relaxation curve. The measured multi-exponential relaxation curves, affected by unavoidable measurement noise, were transformed into distributions of the transverse relaxation time T_2 by the algorithm UPEN (Uniform-Penalty inversion algorithm)[33], implemented in the UpenWin software[34]. The ratio between the signal under a particular portion of the T_2 distribution and the total acquired signal will correspond to the ratio of the volume of the pores with a particular pore size to the total pore volume. TD-NMR measurements were performed on 2 fragments per site per species for *A. millepora*, massive *Porites*, and *G. fascicularis* and on all available fragments of *P. damicornis* (a total of 60 fragments). The T_2 distributions showed a cut-off at 3 ms allowing to divide the pores containing water into two classes, distinguishing the smaller pores (smaller volumes, estimated pore sizes < 1 μm) from the remaining larger ones (larger volumes, estimated pore sizes > 1 μm). For the sake of simplicity, the two classes were named micro-scale and macro-scale pores[13,35].

Thermogravimetric analysis for organic matrix content determination. To determine the intraskeletal organic matrix and water content, thermal gravimetric measurements were performed using a TA Instruments thermobalance model SDT-Q600 with 0.1 μg of balance sensitivity. Powdered subsamples (5 to 10 mg), held in alumina pans, were heated under a linear gradient from ambient (ca. 20 °C) up to 600 °C with an isotherm at 120 °C for 5 min to remove the adsorbed water; heating rate: 10 °C/min under an N_2 atmosphere,

with flux fixed to 100 ml/min. Two main weight loss regimes were identified: a first one in a range around 125–250° C (related to the loss of structured water molecules) followed by another thermal region between 250 and 470 °C (generally associated with organic matrix pyrolysis)[36]. A total of 32 fragments from the control and seep sites at Dobu (10 for each site) and at Upa Upasina (6 for each site) were analyzed.

Synchrotron high-resolution X-ray powder diffraction. To determine crystallite parameters, coral fragments were measured at the ID22 beamline of the European Synchrotron Radiation Facility (Grenoble, France) using a wavelength of 0.4 Å (details in Supplementary Methods). Subsamples of the fine powder were loaded into borosilicate glass capillaries of 0.7–1 mm in diameter and measured at room temperature, and again after ex-situ heating at 300 °C for 2 h, to remove the organic matrix effects on the strain[37]. Rietveld refinement was used to calculate the unit-cell parameters from the diffraction pattern profiles. The line profile analysis was applied to a specific diffraction peak to obtain the coherence length (nm) along various crystallographic directions, which was achieved by fitting the profile to a Voigt function and deconvoluting the Lorentzian and Gaussian widths. Analyses were conducted on fragments of *P. damicornis* from Upa Upasina in the control (N = 3) and seep (N = 3) site.

Statistical analyses. Permutation multivariate analysis of variance (PERMANOVA) was perfomed using PRIMER v6[38] and based on Euclidean distances (999 permutation) to test for (1) variations of environmental parameters amongst locations and sites; (2) variations of skeletal parameters amongst locations, sites, and species. When the main tests revealed statistical differences ($P < 0.05$), PERMANOVA pairwise comparisons were carried out. The BEST routine in PRIMER v6 (999 permutations) was carried out to check for auto-correlated environmental variables, thus obtaining the minimum subset of variables that may explain differences in environmental conditions amongst locations, sites and seasons (i.e., Spring included data collected in April and May; Winter included data collected in January and December). Organic matrix related strain and crystallite size in *P. damicornis* were compared between control and seep sites using the non-parametric Mann–Whitney U-test, due to deviations from parametric t-test assumption (Normality: Shapiro–Wilk's test; equal variance: Levene's test). This statistical analysis was performed using SPSS 20.0. Data visualization and graphics were obtained with the ggplot2 package in R[39]. Statistical differences were accepted when $P < 0.05$.

Results

Environmental parameters. The values of the environmental parameters collected at control and seep sites in Dobu and Upa Upasina over a 3-year period are summarized in Fig. S1. Briefly, pH and pCO_2 across both seep sites averaged 7.72 ± 0.23 (SD) and 1133 ± 1161 µatm, while at the control sites it averaged 7.93 ± 0.10 and 518 ± 250 µatm, respectively. The complete dataset of environmental parameters (Fig. S1) was analyzed to test for differences between sampling locations, and between control *vs* seep sites within each location. Effects of seasonality were also considered. PERMANOVA analyses showed that environmental conditions were different between locations and sites and that seasons did not differ significantly (Supplementary Table S1 and Fig. S1). PERMANOVA pair-wise comparisons showed that within each of the two locations control and seep sites were significantly different (Dobu: t = 3.127, $P = 0.001$; Upa Upasina: t = 2.547, $P = 0.001$). The two control sites also differed between the two locations (t = 2.112, $P = 0.002$), while seep sites were similar (t = 1.244, $P = 0.154$). The BEST routine revealed that pCO_2 and Ω_{AR} were strongly autocorrelated with the other environmental parameters (Rho = 0.995, $P = 0.001$) and were therefore excluded from the following PERMANOVA analysis. PERMANOVA analyses on single environmental parameters showed that pH and total alkalinity were significantly different between control and seep sites, while temperature was significantly different between locations (Table 1 and Supplementary Table S1). DIC was significantly different between controls of Upa Upasina and Dobu (t = 6.137, $P = 0.001$) while at the seep sites DIC was homogeneous (t = 0.061, $P = 0.962$). Salinity was unchanged between either locations or sites (Table 1 and Supplementary Table S1).

Skeletal parameters in corals sampled at the control and seep sites of Dobu and Upa Upasina. Results for bulk density, micro-density, and porosity are reported in Fig. 2 and in Supplementary Table S2. PERMANOVA analyses indicated significant differences among species in micro-density, porosity, and bulk density (Table 2). Porosity and bulk density were also significantly different between sites (Table 2). For all species, porosity and bulk density were significantly different between control and seep sites at Upa Upasina (t = 4.752, $P = 0.001$ and t = 5.864, $P = 0.001$, respectively), with higher porosity and lower bulk density at the seep site compared to the control (Fig. 2). Bulk density was significantly lower at the seep site compared to the control also at Dobu (t = 2.675, $P = 0.010$; Fig. 2). Micro-density showed a significant interaction between the factor Site and Species (Table 2); indeed micro-density values assessed in *P. damicornis* were significantly lower at the seep site compared to the control at both locations (Fig. 2; Table 3).

Micro-density changes in *P. damicornis* were further explored both statistically and through additional macroscale and microscale skeletal analyses. Specifically, Time-Domain Nuclear Magnetic Resonance (TD-NMR), Thermogravimetric Analysis (TGA), and synchrotron high-resolution powder X-ray diffraction (HRPXRD) analyses were performed. TD-NMR measurements were performed on two fragments for all species to have a general overview of the T_2 distributions (Supplementary Fig. S2). Further analyses were conducted on all available fragments of *P. damicornis* to quantify macro-scale pore volume fraction. PERMANOVA analyses showed that macro-scale pore volume fraction was significantly higher at the seep site compared to the control in both locations (Upa Upasina: t = 2.126, $P = 0.041$; Dobu: t = 2.549, $P = 0.028$; Fig. 3 and Supplementary Table S3). The intraskeletal organic matrix (OM; t = 4.856, $P = 0.004$) and water content (t = 4.891, $P = 0.001$) were significantly different between Sites only at Upa Upasina (Table 4; Fig. 3; Supplementary Table S4). In particular, the former

Location	Dobu		Upa Upasina	
Site	Control	Seep	Control	Seep
pH	7.96 (0.04)	7.66 (0.27)	7.91 (0.13)	7.75 (0.19)
	N = 46	N = 130	N = 67	N = 222
	a	b	a	b
DIC	1946 (15)	2106 (90.0)	2082 (38)	2060 (30.0)
	N = 32	N = 30	N = 71	N = 254
	a	b	c	b
TA	2235 (9)	2275 (1)	2252 (21)	2285 (18)
	N = 47	N = 207	N = 71	N = 254
	a	b	a	b
Salinity	34.9 (0.8)	34.7 (0.7)	35.2 (0.8)	34.8 (0.7)
	N = 59	N = 207	N = 71	N = 254
	a	a	a	a
T (°C)	29.1 (1.4)	29.0 (0.7)	30.1 (1.3)	30.2 (0.9)
	N = 59	N = 207	N = 71	N = 242
	a	a	b	b

Table 1. Means and standard deviation (in parenthesis) of the investigated environmental parameters in seep and control sites in Dobu and Upa Upasina. Lettering indicates significantly different groups (PERMANOVA on single parameters). pH_{TS} pH in total scale, pCO_2 carbon dioxide partial pressure, Ω_{AR} aragonite saturation, *DIC* dissolved inorganic carbon, *TA* total alkalinity, *T* seawater temperature, *N* number of measurements.

showed lower values at the seep site compared to control, while the latter showed the opposite trend (Fig. 3).The intraskeletal OM content was significantly different also among locations (Table 4).

Three *P. damicornis* skeletal fragments from the control and from the seep sites in Upa Upasina were analysed by HRPXRD. All HRPXRD patterns were well indexed as aragonite and no additional diffraction peaks were detected. Then, the peaks were refined using the Rietveld method[40] and lattice parameters and strain (Supplementary Table S5), and microstructural data[41], crystallite size, and microstrain (Supplementary Table S6), were calculated. No significant differences were found between the control and seep site. To test the influence of the OM on the mineral strain, ex-situ heat treatments prior the HRPXRD measurements, which remove the effect of the OM on the strain[37], were performed. The data showed that OM induced a positive strain on *a*- and *c*-axis and a negative one on the *b*-axis, but no significant differences were found between the control and seep site (Supplementary Table S5). We also measured crystallite size after the thermal annealing together with the transition to calcite (Supplementary Tables S5 and S6). These latter parameters did not show any significant difference between the control and seep sites.

Discussion

In the past decades, significant efforts have been made to quantify the ecological effects of ongoing ocean acidification (OA) in tropical regions. However, assessing the effects of OA on reef-building corals poses major challenges because multiple environmental changes, including ocean warming, are co-occurring with OA, impacting coral growth[42,43]. This study investigated the effects of long-term exposure to elevated CO_2 on skeletal properties in tropical zooxanthellate corals naturally living at CO_2 vents.

Similar to Mediterranean[13] and other tropical coral species[44], increased porosity and decreased bulk density was observed at the seep sites compared to the control sites, with some species showing more marked trends than others, in agreement with a general decreasing trend of net calcification rates at relatively low pH conditions resembling IPCC projections[15,45]. A 2-year field transplant experiment conducted on *Porites astreoides*, *Siderastrea siderea* and *Porites porites* at low pH submarine springs in the Yucatán peninsula (Mexico) showed species-specific OA-related vulnerability in calcification rates which may be linked to differential growth rates, with fast-growing corals being likely more sensitive to low carbonate ion availability[46]. Species-specific sensitivities to OA also depend on its impacts on chemistry within the calcifying fluid[47,48] and/or in the diverse use of metabolic reserves[49]. Moreover, different populations of the same species might display variable responses to OA, as highlighted for instance by the intra-specific variability displayed by calcification rates of *Acropora digitifera* from two distinct locations after exposure to acidified conditions in aquaria[50]. All these aspects could contribute to explain the variability observed by the different species in the two locations considered in the current study.

Micro-density showed lower values at the seep sites compared to the control sites of both locations only in *P. damicornis*. Micro-density, which represents the mass per unit volume of the biogenic calcium carbonate composing the skeleton[51], depends on the mineral composition of the skeleton and on intraskeletal organic matrix (OM) and water content[29]. The evaluation of additional macro- and micro- scale parameters performed in this species also revealed an increase in macro-scale pore volume fraction and intraskeletal water content and a decrease in OM, and eventually strong linked water[36]. In particular, the observed increase of intraskeletal water content at the seep site can partially justify the observed decrease in skeletal micro-density. According to literature, the observed decrease of skeletal micro-density could also stem from a variation in chemistry and micro-architecture

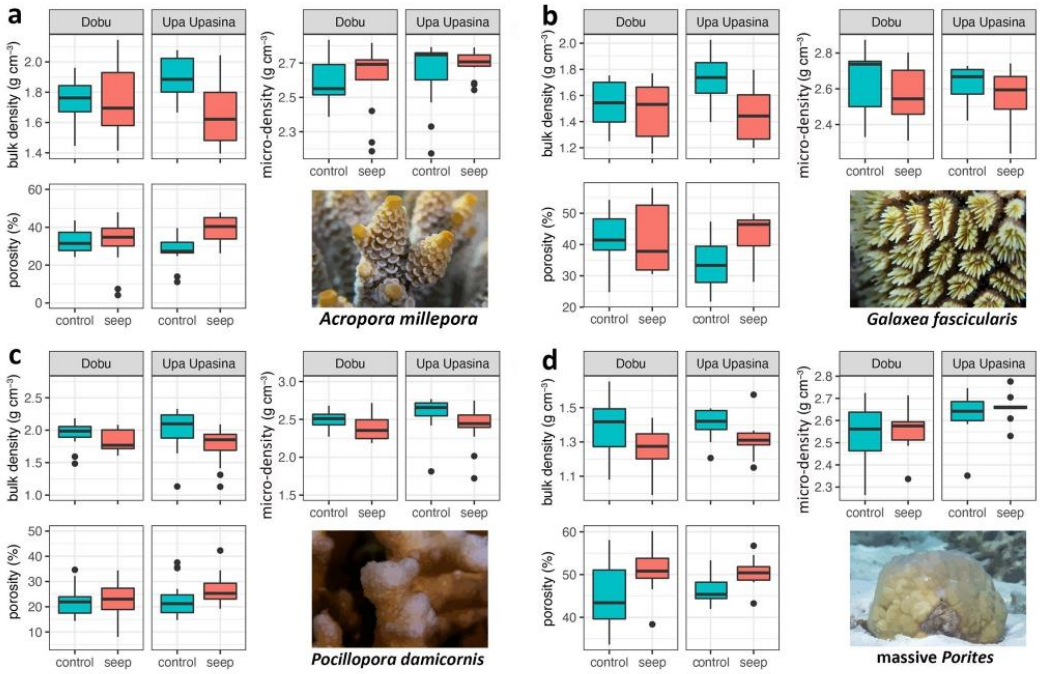

Figure 2. Skeletal parameters micro-density, porosity and bulk density at control (green box plots) and seep sites (pink box plots) in Dobu and Upa Upasina (UPA) for (**a**) *Acropora millepora*, (**b**) *Galaxea fascularis*, (**c**) *Pocillopora damicornis*, and (**d**) massive *Porites*. The boxes indicate the 25th and 75th percentiles and the line within the boxes mark the medians. Whisker length is equal to 1.5 × interquartile range (IQR). Circles represent outliers. Statistical analyses for these data are reported in Tables 2 and 3. Plots were created with the R package ggplot2[62]. Plots were created with the R package ggplot2[62]. (photographs by co-author FR).

		Porosity		Bulk density		Micro-density	
	df	Pseudo-F	*P*	Pseudo-F	*P*	Pseudo-F	*P*
Sp	3	61.541	**0.001**	78.244	**0.001**	10.096	**0.001**
Lo	1	0.034	0.853	3.791	0.054	8.732	**0.007**
Si(Lo)	2	10.374	**0.001**	20.775	**0.001**	2.645	0.073
SpxLo	3	0.276	0.841	0.174	0.922	1.487	0.223
SpxSi(Lo)	6	0.850	0.546	1.211	0.327	3.535	**0.006**

Table 2. Results of the PERMANOVA analysis for porosity, bulk density, and micro-density in the control and seep sites at Dobu and Upa Upasina for *Acropora millepora*, *Galaxea fascularis*, *Pocillopora damicornis*, and massive *Porites*. Significant values are reported in bold. *Sp* species, *Lo* location, *Si* site.

	Upa Upasina		Dobu	
	t	*P*	t	*P*
Acropora milepora	1.002	0.375	0.815	0.440
Galxea fascicularis	1.092	0.291	0.802	0.424
massive *Porites*	0.813	0.488	0.476	0.650
Pocillopora damicornis	4.787	**0.002**	3.615	**0.003**

Table 3. PERMANOVA pairwise comparisons for micro-density based between Control and Seep sites within locations (Dobu and Upa Upasina) for the four investigated species. The pairwise test was conducted only for micro-density based on the significant interaction between Site and Species (Table 2). Significant values are reported in bold.

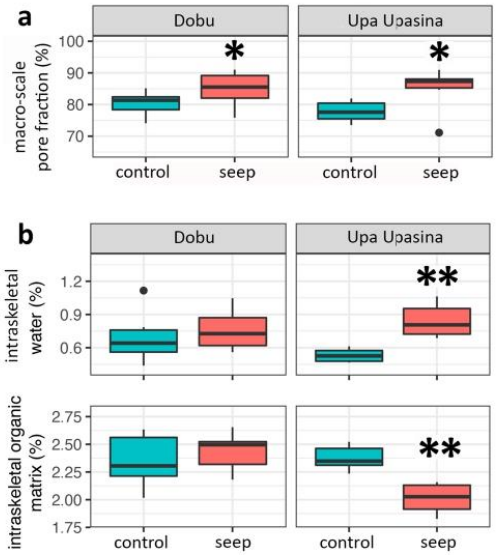

Figure 3. Macro-scale pore volume fraction (in the figure simply macro pore fraction) and intraskeletal OM and water content for *P. damicornis* from control and seep sites at Dobu and Upa Upasina. (**a**) Time Domain-Nuclear Magnetic Resonance measurement of macro-scale pore volume fraction. (**b**) Thermogravimetric Analysis of microscale parameters, namely intraskeletal organic matrix (OM), intraskeletal water content, and total (the sum of OM and water). The box indicates the 25th and 75th percentiles and the line within the box marks the median. Whisker length is equal to 1.5 × interquartile range (IQR). Circles represent outliers. Significant differences between control and seep sites are represented by asterisks, $^{**}P<0.01$, $^{*}P<0.05$. Plots were created with the R package ggplot2[62].

Factor	df	Pseudo-F	*P*
Intraskeletal water content			
Lo	1	0.279	0.608
Si(Lo)	2	6.831	**0.005**
Intraskeletal organic matrix content			
Lo	1	12.318	**0.001**
Si(Lo)	2	7.164	**0.002**
Macro-scale pore volume fraction			
Lo	1	0.775	0.380
Si(Lo)	2	5.715	**0.012**

Table 4. Results of the PERMANOVA analysis for intraskeletal water and organic matrix (OM) content and macro-scale pore fraction volume in *Pocillopora damicornis* in control and seep sites at Dobu and Upa Upasina. *Lo* location, *Si* site.

of the skeleton[52], the presence of occluded nano-porosity[13], and the presence of amorphous calcium carbonate[53]. Changes in OM and water content with pH reduction have been previously reported, showing either an increase in the tropical *Stylophora pistillata* kept in aquaria at pH 7.2 for approximately 1 year[36,44], or no variation in the temperate *Balanophyllia europaea* naturally living along a CO_2 vent at average seawater pH 7.7[32]. Moreover, *P. damicornis* exposed to pH 7.8, 7.4 and 7.2 in aquaria for 3 weeks showed a 4 to 70-fold up-regulation of genes encoding skeleton organic matrix proteins at all pH treatments[54]. In these studies, the observed up-regulation of genes linked to OM proteins and the increase in OM content was hypothesized to promote calcification under less favorable acidified conditions. Thus, the observed decline in OM in *P. damicornis* in the current study suggests a possible decline in net calcification rates at the seep site, which is in agreement with the observed increase in skeletal porosity. However, considering the natural setting in which the study was performed, we cannot exclude

the influence of other covarying environmental factors in determining the observed responses (e.g., turbidity, light availability, organic/inorganic nutrient availability, feeding)[55–58].

The decrease of intra-skeletal OM content in samples from seep sites was not associated with a significant change in strain, micro-strain, or crystallite size. These observations may indicate that the amount of intra-crystallite OM does not change since the crystallite sizes after the thermal annealing are the same for samples from the control and the seep sites. Thus, the observed decrease in OM is likely associated with a decrease in the inter-crystallite OM. In addition, the stability of aragonite through the transition to calcite and the lattice parameters of the calcite formed after thermal annealing did not show a significant difference between control and seep samples. The crystallographic features of aragonite from coral skeletons have been previously investigated[59]. The reef building coral *Stylophora pistillata* grown in aquaria under different experimental seawater acidification (pH 8.2, 7.6, and 7.3) showed anisotropic distortions of aragonite lattice parameters and a reduction of the crystallite sizes under acidified conditions[36]. In the presented study, these parameters were unaffected by decreasing pH, suggesting that biological control over calcification does not change at the nanoscale, as reported for *B. europaea*[13]. The fact that different species were used, but most of all that *S. pistillata* was exposed for 1 year (short-term acclimation) while in the current study species were exposed to acidified conditions for generations (life-long acclimatization) likely accounts for these discrepancies. The calcite phase obtained by annealing of coral samples has similar lattice parameters in samples from the control and seep sites. These parameters, when compared with those of synthetic calcite[60], did not show differences. A different behavior was observed for calcite obtained from *Desmophyllum* and *Favia* aragonitic skeletons, which showed different strain compared with geological or synthetic calcite[59].

Conclusions

This multi-species study showed a common phenotypic response among four zooxanthellate corals which displayed a more porous skeletal phenotype under OA. Additionally, these skeletal macromorphological adjustments led to decreased micro-density in *P. damicornis* but did not affect the measured crystallite features, suggesting that the fundamental structural components produced by the biomineralization process might be substantially unaffected by increased acidification[13,61]. Nonetheless, the porous phenotype here described may render structurally complex and massive corals more vulnerable to damage and bio-erosion under climate change, which in the future may lead to a weakening of the reef framework and subsequent degradation of the complex coral reef ecosystem.

Data availability

The datasets generated during and/or analysed during the current study are available from the corresponding author on reasonable request.

Received: 30 December 2020; Accepted: 6 September 2021
Published online: 07 October 2021

References

1. Hoegh-Guldberg, O. *et al.* Coral reefs under rapid climate change and ocean acidification. *Science (80-.)* **318**, 1737–1742 (2007).
2. Roberts, M., Hanley, N., Williams, S. & Cresswell, W. Terrestrial degradation impacts on coral reef health: Evidence from the Caribbean. *Ocean Coast. Manag.* **149**, 52–68 (2017).
3. Mollica, N. R. *et al.* Ocean acidification affects coral growth by reducing skeletal density. *Proc. Natl. Acad. Sci.* **115**, 1754–1759 (2018).
4. Ries, J. B. Skeletal mineralogy in a high-CO_2 world. *J. Exp. Mar. Biol. Ecol.* **403**, 54–64 (2011).
5. Erez, J., Reynaud, S., Silverman, J., Schneider, K. & Allemand, D. Coral calcification under ocean acidification and global change. In *Coral Reefs: An Ecosystem in Transition* (2011). https://doi.org/10.1007/978-94-007-0114-4_10.
6. Dove, S. G. *et al.* Future reef decalcification under a business-as-usual CO_2 emission scenario. *Proc. Natl. Acad. Sci.* **110**, 15342–15347 (2013).
7. Cooper, T. F., De'ath, G., Fabricius, K. E. & Lough, J. M. Declining coral calcification in massive *Porites* in two nearshore regions of the northern Great Barrier Reef. *Glob. Chang. Biol.* **14**, 529–538 (2008).
8. Cooper, T. F., O'Leary, R. A. & Lough, J. M. Growth of Western Australian corals in the Anthropocene. *Science (80-.)* **335**, 593–596 (2012).
9. Teixidó, N. *et al.* Ocean acidification causes variable trait-shifts in a coral species. *Glob. Chang. Biol.* https://doi.org/10.1111/gcb.15372 (2020).
10. Pandolfi, J. M. Incorporating uncertainty in predicting the future response of coral reefs to climate change. *Annu. Rev. Ecol. Evol. Syst.* **46**, 281–303 (2015).
11. Kroeker, K. J., Kordas, R. L., Crim, R. N. & Singh, G. G. Meta-analysis reveals negative yet variable effects of ocean acidification on marine organisms. *Ecol. Lett.* **13**, 1419–1434 (2010).
12. Jokiel, P. L. *et al.* Ocean acidification and calcifying reef organisms: A mesocosm investigation. *Coral Reefs* **27**, 473–483 (2008).
13. Fantazzini, P. *et al.* Gains and losses of coral skeletal porosity changes with ocean acidification acclimation. *Nat. Commun.* **6**, 7785 (2015).
14. Wittmann, A. C. & Pörtner, H.-O. Sensitivities of extant animal taxa to ocean acidification. *Nat. Clim. Chang.* **3**, 995–1001 (2013).
15. Fabricius, K. E. *et al.* Losers and winners in coral reefs acclimatized to elevated carbon dioxide concentrations. *Nat. Clim. Chang.* **1**, 165–169 (2011).
16. Riebesell, U. Acid test for marine biodiversity. *Nature* **454**, 46–47 (2008).
17. Hall-Spencer, J. M. *et al.* Volcanic carbon dioxide vents show ecosystem effects of ocean acidification. *Nature* **454**, 96–99 (2008).
18. Johnson, V. R., Russell, B. D., Fabricius, K. E., Brownlee, C. & Hall-Spencer, J. M. Temperate and tropical brown macroalgae thrive, despite decalcification, along natural CO_2 gradients. *Glob. Chang. Biol.* https://doi.org/10.1111/j.1365-2486.2012.02716.x (2012).
19. Prada, F. *et al.* Ocean warming and acidification synergistically increase coral mortality. *Sci. Rep.* **7**, 1–10 (2017).
20. Inoue, S., Kayanne, H., Yamamoto, S. & Kurihara, H. Spatial community shift from hard to soft corals in acidified water. *Nat. Clim. Chang.* **3**, 683–687 (2013).

21. Crook, E. D., Cohen, A. L., Rebolledo-Vieyra, M., Hernandez, L. & Paytan, A. Reduced calcification and lack of acclimatization by coral colonies growing in areas of persistent natural acidification. *Proc. Natl. Acad. Sci.* **110**, 11044–11049 (2013).
22. Teixidó, N. *et al.* Functional biodiversity loss along natural CO_2 gradients. *Nat. Commun.* **9**, 5149 (2018).
23. Strahl, J. *et al.* Physiological and ecological performance differs in four coral taxa at a volcanic carbon dioxide seep. *Comp. Biochem. Physiol. Part A Mol. Integr. Physiol.* **184**, 179–186 (2015).
24. Fabricius, K. E., De'ath, G., Noonan, S. & Uthicke, S. Ecological effects of ocean acidification and habitat complexity on reef-associated macroinvertebrate communities. *Proc. R. Soc. B Biol. Sci.* **281**, 20132479 (2014).
25. Fabricius, K. E., Noonan, S. H. C., Abrego, D., Harrington, L. & De'ath, G. Low recruitment due to altered settlement substrata as primary constraint for coral communities under ocean acidification. *Proc. R. Soc. B Biol. Sci.* **284**, 20171536 (2017).
26. Siahainenia, L., Tuhumury, S. F., Uneputty, P. A. & Tuhumury, N. C. Survival and growth of transplanted coral reef in lagoon ecosystem of Ihamahu, Central Maluku, Indonesia. *IOP Conf. Ser. Earth Environ. Sci.* **339**, 012003 (2019).
27. Horwitz, R., Hoogenboom, M. O. & Fine, M. Spatial competition dynamics between reef corals under ocean acidification. *Sci. Rep.* **7**, 40288 (2017).
28. Noonan, S. H. C., Fabricius, K. E. & Humphrey, C. *Symbiodinium* community composition in scleractinian corals is not affected by life-long exposure to elevated carbon dioxide. *PLoS ONE* **8**, e63985 (2013).
29. Caroselli, E. *et al.* Environmental implications of skeletal micro-density and porosity variation in two scleractinian corals. *Zoology* **114**, 255–264 (2011).
30. Reggi, M. *et al.* Biomineralization in Mediterranean corals: The role of the intraskeletal organic matrix. *Cryst. Growth Des.* **14**, 4310–4320 (2014).
31. Goffredo, S. *et al.* The skeletal organic matrix from Mediterranean coral Balanophyllia Europaea influences calcium carbonate precipitation. *PLoS ONE* **6**, e22338 (2011).
32. Goffredo, S. *et al.* Biomineralization control related to population density under ocean acidification. *Nat. Clim. Chang.* **4**, 593–597 (2014).
33. Borgia, G. C., Brown, R. J. S. & Fantazzini, P. Uniform-penalty inversion of multiexponential decay data. *J. Magn. Reson.* **132**, 65–77 (1998).
34. Bortolotti, F., Brown, R. & Fantazzini, P. *UpenWin: A Software for Inversion of Multiexponential Decay Data* (Windows System Alma Mater Studiorum—Università di Bologna, 2012).
35. Fantazzini, P. *et al.* A time-domain nuclear magnetic resonance study of Mediterranean scleractinian corals reveals skeletal-porosity sensitivity to environmental changes. *Environ. Sci. Technol.* **47**, 12679–12686 (2013).
36. Coronado, I., Fine, M., Bosellini, F. R. & Stolarski, J. Impact of ocean acidification on crystallographic vital effect of the coral skeleton. *Nat. Commun.* **10**, 2896 (2019).
37. Pokroy, B., Fitch, A. & Zolotoyabko, E. The microstructure of biogenic calcite: A view by high-resolution synchrotron powder diffraction. *Adv. Mater.* **18**, 2363–2368 (2006).
38. Anderson, M. J., Gorley, R. N. & Clarke, K. R. PERMANOVA+ for PRIMER: Guide to software and statistical methods. In *Plymouth* (2008).
39. R Development Core Team. *R: A Language and Environment for Statistical Computing* (R Foundation for Statistical Computing, 2018). ISBN 3-900051-07-0. http://www.R-project.org.
40. Toby, B. H. & Von Dreele, R. B. GSAS-II: The genesis of a modern open-source all purpose crystallography software package. *J. Appl. Crystallogr.* **46**, 544–549 (2013).
41. Jiang, H. G., Rühle, M. & Lavernia, E. J. On the applicability of the x-ray diffraction line profile analysis in extracting grain size and microstrain in nanocrystalline materials. *J. Mater. Res.* **14**, 549–559 (1999).
42. Vercelloni, J. *et al.* Forecasting intensifying disturbance effects on coral reefs. *Glob. Chang. Biol.* **26**, 2785–2797 (2020).
43. Guo, W. *et al.* Ocean acidification has impacted coral growth on the Great Barrier Reef. *Geophys. Res. Lett.* **47**, 1–9 (2020).
44. Tambutté, E. *et al.* Morphological plasticity of the coral skeleton under CO_2-driven seawater acidification. *Nat. Commun.* **6**, 7368 (2015).
45. Schneider, K. & Erez, J. The effect of carbonate chemistry on calcification and photosynthesis in the hermatypic coral *Acropora eurystoma*. *Limnol. Oceanogr.* **51**, 1284–1293 (2006).
46. Martinez, A. *et al.* Species-specific calcification response of Caribbean corals after 2-year transplantation to a low aragonite saturation submarine spring. *Proc. Biol. Sci.* **286**, 20190572 (2019).
47. Comeau, S. *et al.* Resistance to ocean acidification in coral reef taxa is not gained by acclimatization. *Nat. Clim. Chang.* **9**, 477–483 (2019).
48. McCulloch, M. *et al.* Resilience of cold-water scleractinian corals to ocean acidification: Boron isotopic systematics of pH and saturation state up-regulation. *Geochim. Cosmochim. Acta* **87**, 21–34 (2012).
49. Movilla, J. *et al.* Differential response of two Mediterranean cold-water coral species to ocean acidification. *Coral Reefs* **33**, 675–686 (2014).
50. Kurihara, H., Takahashi, A., Reyes-Bermudez, A. & Hidaka, M. Intraspecific variation in the response of the scleractinian coral Acropora digitifera to ocean acidification. *Mar. Biol.* **165**, 38 (2018).
51. Barnes, D. J. & Devereux, M. J. Variations in skeletal architecture associated with density banding in the hard coral *Porites*. *J. Exp. Mar. Biol. Ecol.* **121**, 37–54 (1988).
52. Bucher, D. J., Harriott, V. J. & Roberts, L. G. Skeletal micro-density, porosity and bulk density of acroporid corals. *J. Exp. Mar. Biol. Ecol.* **228**, 117–136 (1998).
53. Mass, T. *et al.* Amorphous calcium carbonate particles form coral skeletons. *Proc. Natl. Acad. Sci.* **114**, E7670–E7678 (2017).
54. Vidal-Dupiol, J. *et al.* Genes related to ion-transport and energy production are upregulated in response to CO_2-driven pH decrease in corals: New insights from transcriptome analysis. *PLoS ONE* **8**, e58652 (2013).
55. Suggett, D. J. *et al.* Light availability determines susceptibility of reef building corals to ocean acidification. *Coral Reefs* **32**, 327–337 (2013).
56. Vogel, N., Meyer, F., Wild, C. & Uthicke, S. Decreased light availability can amplify negative impacts of ocean acidification on calcifying coral reef organisms. *Mar. Ecol. Prog. Ser.* **521**, 49–61 (2015).
57. Tanaka, Y. *et al.* Nutrient availability affects the response of juvenile corals and the endosymbionts to ocean acidification. *Limnol. Oceanogr.* **59**, 1468–1476 (2014).
58. Towle, E. K., Enochs, I. C. & Langdon, C. Threatened Caribbean coral is able to mitigate the adverse effects of ocean acidification on calcification by increasing feeding rate. *PLoS ONE* **10**, e0123394 (2015).
59. Stolarski, J., Przeniosło, R., Mazur, M. & Brunelli, M. High-resolution synchrotron radiation studies on natural and thermally annealed scleractinian coral biominerals. *J. Appl. Crystallogr.* **40**, 2–9 (2007).
60. Maslen, E. N., Streltsov, V. A., Streltsova, N. R. & Ishizawa, N. Electron density and optical anisotropy in rhombohedral carbonates. III. Synchrotron X-ray studies of $CaCO_3$, $MgCO_3$ and $MnCO_3$. *Acta Crystallogr. Sect. B Struct. Sci.* **51**, 929–939 (1995).
61. Wall, M. *et al.* Linking internal carbonate chemistry regulation and calcification in corals growing at a Mediterranean CO_2 vent. *Front. Mar. Sci.* **6**, 699 (2019).
62. Wickham, H. *ggplot2* (Springer International Publishing, 2016). https://doi.org/10.1007/978-3-319-24277-4.

Acknowledgements
We would like to thank the communities at Upa Upasina and at Dobu to allow us to work at their unique reefs. Many thanks also to Craig Humphrey and Sam Noonan for collecting the samples. The field research was funded by the Australian Institute of Marine Science.

Author contributions
K.E.F. designed the experimental setting, initiated the collection of the specimens, and provided the background environmental data. F.P., L.B., S.Fe., I.P., N.B., F.R., Q.P., B.P., and L.G. analyzed the samples. FP, SFr, and EC performed the statistical analyses. F.P., L.B., S.Fr., S.M., and P.F. contributed to the initial draft. F.P., L.B., S.Fr., S.M., N.B., E.C., Z.D., P.F., G.F., S.G., and K.E.F. contributed to the scientific discussion and interpretation of the data. All authors contributed to writing the manuscript and gave final approval for publication.

Competing interests
The authors declare no competing interests.

Additional information
Supplementary Information The online version contains supplementary material available at https://doi.org/10.1038/s41598-021-98976-9.

Correspondence and requests for materials should be addressed to P.F., G.F. or S.G.

Reprints and permissions information is available at www.nature.com/reprints.

Publisher's note Springer Nature remains neutral with regard to jurisdictional claims in published maps and institutional affiliations.

Open Access This article is licensed under a Creative Commons Attribution 4.0 International License, which permits use, sharing, adaptation, distribution and reproduction in any medium or format, as long as you give appropriate credit to the original author(s) and the source, provide a link to the Creative Commons licence, and indicate if changes were made. The images or other third party material in this article are included in the article's Creative Commons licence, unless indicated otherwise in a credit line to the material. If material is not included in the article's Creative Commons licence and your intended use is not permitted by statutory regulation or exceeds the permitted use, you will need to obtain permission directly from the copyright holder. To view a copy of this licence, visit http://creativecommons.org/licenses/by/4.0/.

© The Author(s) 2021

Supplementary Material for

Coral micro- and macro-morphological skeletal properties in response to life-long acclimatization at CO_2 vents in Papua New Guinea. Scientific Reports

Fiorella Prada, Leonardo Brizi, Silvia Franzellitti, Stefano Mengoli, Simona Fermani, Iryna Polishchuk, Nicola Baraldi, Francesco Ricci, Quinzia Palazzo, Erik Caroselli, Boaz Pokroy, Loris Giorgini, Zvy Dubinsky, Paola Fantazzini, Giuseppe Falini, Stefano Goffredo, Katharina E. Fabricius

SUPPLEMENTARY METHODS

Skeletal Parameters determination

Skeletal parameters were obtained by applying the buoyant weight technique from the following measurements: density of the fluid medium (ρ); dry mass of the fragment (DW); buoyant weight of the fragment (BW = weight of the fragment minus weight of the water displaced by it); and SW (saturated weight of the fragment = weight of the fragment plus weight of the water enclosed in its volume). These measurements were used to calculate: V_{MATRIX} (matrix volume = volume of the fragment, not including the volume of its pores); V_{PORES} (pore volume = volume of the pores in the fragment); and V_{TOT} (bulk volume = total volume of the fragment including its pores). The skeletal parameters of the samples were calculated as follows: the micro-density (ratio of DW to V_{MATRIX}); the bulk density (ratio DW to V_{TOT}); and the porosity (ratio V_{PORES} to V_{TOT}).

Definitions:

Micro-density = intended as mass per unit volume of the mineral and intraskeletal organic matrix and water content composing the skeleton, which cannot exceed 2.94 mg/mm^{-3} which is the density of pure aragonite [169].

Bulk density = defined as the skeletal dry mass divided by total skeletal volume which includes the skeletal voids

Porosity = defined as the percentage of enclosed volume occupied by pores connected with the external surface compared to the total skeletal volume. Pores inside the biomineral that are not connected to the external surface (occluded pores) are not measured.

Time-Domain Nuclear Magnetic Resonance for pore size distribution determination

TD-NMR, and in particular magnetic resonance relaxometry of water ^{1}H nuclei, has been validated as a useful tool for analyzing internally connected skeletal porosity in Mediterranean scleractinian corals [89]. It provides several advantages compared to other methods used for the estimation of pore sizes distribution as it is a non-destructive and non-invasive technique which allows preserving intact specimens for further analyses. TD-NMR has been theoretically established for different porous materials, from silica glass, porcelain samples and sedimentary rocks to biological cells [170] and bone tissue [171]. In this study, the samples, saturated with distilled water, were placed in a static magnetic field that polarized the ^{1}H nuclear spins, inducing a nuclear magnetization along the field direction. The process that involves the return of the magnetization vector to equilibrium, after a

radio-frequency perturbation, is called NMR relaxation. The evolution of the magnetization vector components has a multi-exponential trend characterized by time constants named T_1 (relaxation time of the longitudinal component) and T_2 (relaxation time of the transverse component). In this study, only the relaxation of the transverse magnetization component was investigated.

In porous media saturated by water, under the assumptions that diffusion of water molecules is fast enough to maintain the nuclear magnetization constant over the pore volume (V_{PORES}) before relaxing, including at the surfaces (S), the measured relaxation rate $(1/T_2)_{observed}$ is increased compared to the bulk rate by the amount $\rho\ S/V_{PORES}$ (where ρ is the surface relaxivity, with the physical dimensions of a velocity, is a constant that depends on the material) following the equation:

$$(1/\ T_2)_{observed} = \rho\ S/V_{PORES} + 1/T_{2bulk}$$

where T_{2bulk} is the relaxation time of the unconfined fluid. Water confined in real porous media shows a distribution of relaxation times that can cover several orders of magnitude, reflecting a wide distribution of local S/V_{PORES} values.

The total NMR signal (SNMR), represented by the area below each T_2 distribution, is proportional to the volume of water saturating the pore-space volume V_{PORES}. The distribution can be divided in different classes, depending on the shape of the distribution, with shorter relaxation times corresponding to smaller pores.

Synchrotron high-resolution X-ray powder diffraction

The measurements were performed at beamline ID22 of the European Synchrotron Radiation Facility (ESRF, Grenoble, France) using a radiation with wavelength of 0.4 Å. This beam line uses a highly collimated and monochromatic beam to perform powder diffraction in the Laue setting. The beam passes through the sample and diffracts, to be collected on the opposite side by a set of 9 synchronized detectors, mounted 2.2° apart. The intensity of the diffractions is integrated over all detectors to produce high-resolution diffraction patterns. Instrument calibration and wavelength refinement have been performed with silicon standard NIST 640c.

References

1. Bucher, D. J., Harriott, V. J. & Roberts, L. G. Skeletal micro-density, porosity and bulk density of acroporid corals. J. Exp. Mar. Bio. Ecol. 228, 117–136 (1998).

2. Fantazzini, P. et al. Gains and losses of coral skeletal porosity changes with ocean acidification acclimation. Nat. Commun. 6, 7785 (2015).

3. Brizi, L. et al. Water compartmentalization, cell viability and morphology changes monitored under stress by 1 H-NMR relaxometry and phase contrast optical microscopy. J. Phys. D. Appl. Phys. 48, 415401 (2015).

4. Brizi, L. et al. Bone volume-to-total volume ratio measured in trabecular bone by single-sided NMR devices. Magn. Reson. Med. 79, 501–510 (2018).

5. Wickham, H. ggplot2. (Springer International Publishing, 2016). doi:10.1007/978-3-319-24277-4

6. Bortolotti, F., Brown, R. & Fantazzini, P. UpenWin: a software for inversion of multiexponential decay data. Windows system Alma Mater Studiorum—Università di Bologna. (2012).

7. Anderson, M. J. PERMANOVA: a FORTRAN computer program for permutational multivariate analysis of variance. Department of Statisitics. Dep. Stat. (2005).

SUPPLEMENTARY FIGURES

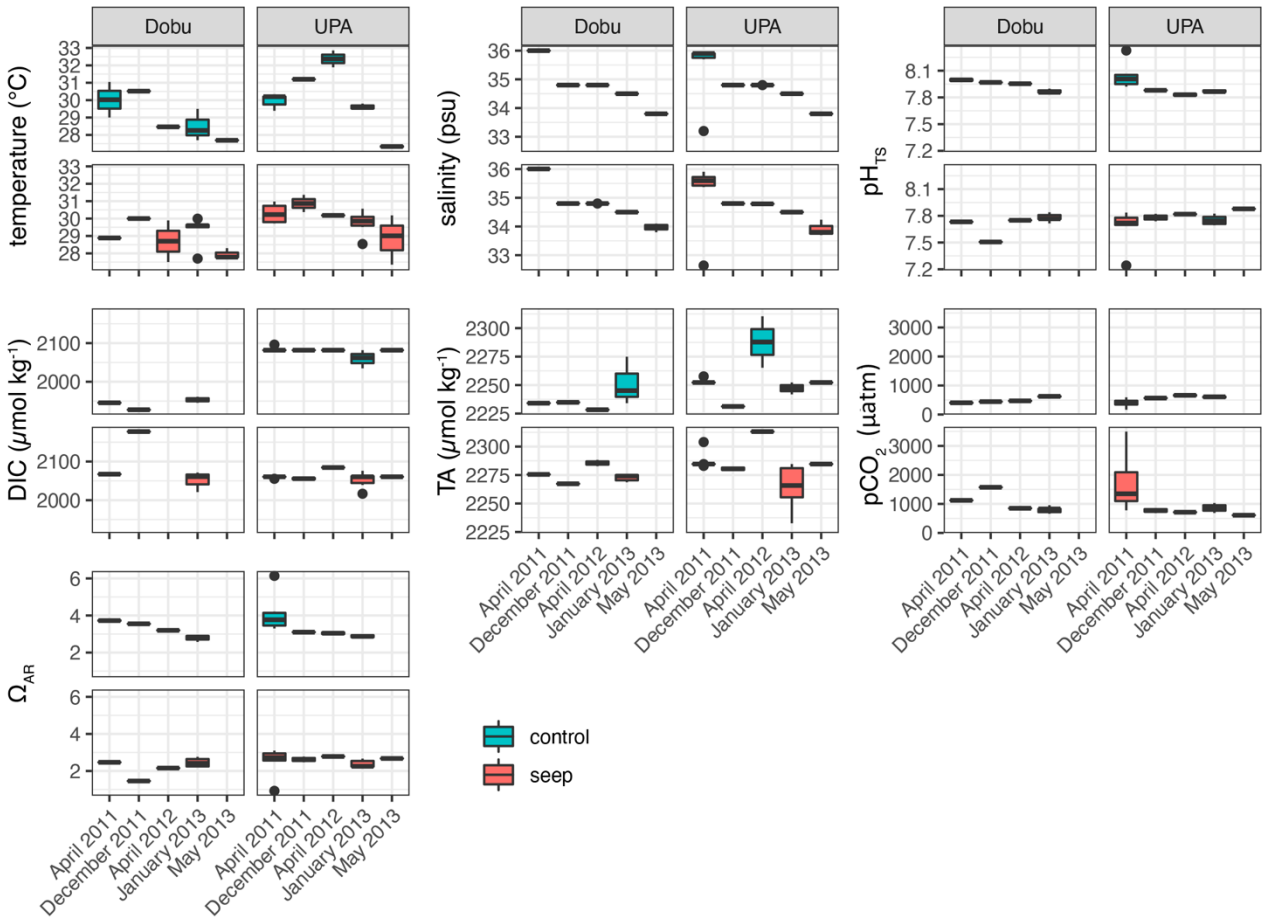

Figure S1. Environmental parameters at control (green box plots) and seep sites (pink box plots) in Dobu and Upa Upasina (UPA) over a 4-year period (2010-2013). The box indicates the 25th and 75th percentiles and the line within the box marks the median. Whisker length is equal to 1.5 × interquartile range (IQR). Dots represent outliers. Statistical analyses for these data are reported in Supplementary Table 1. Plots were created with the R package ggplot2[172].

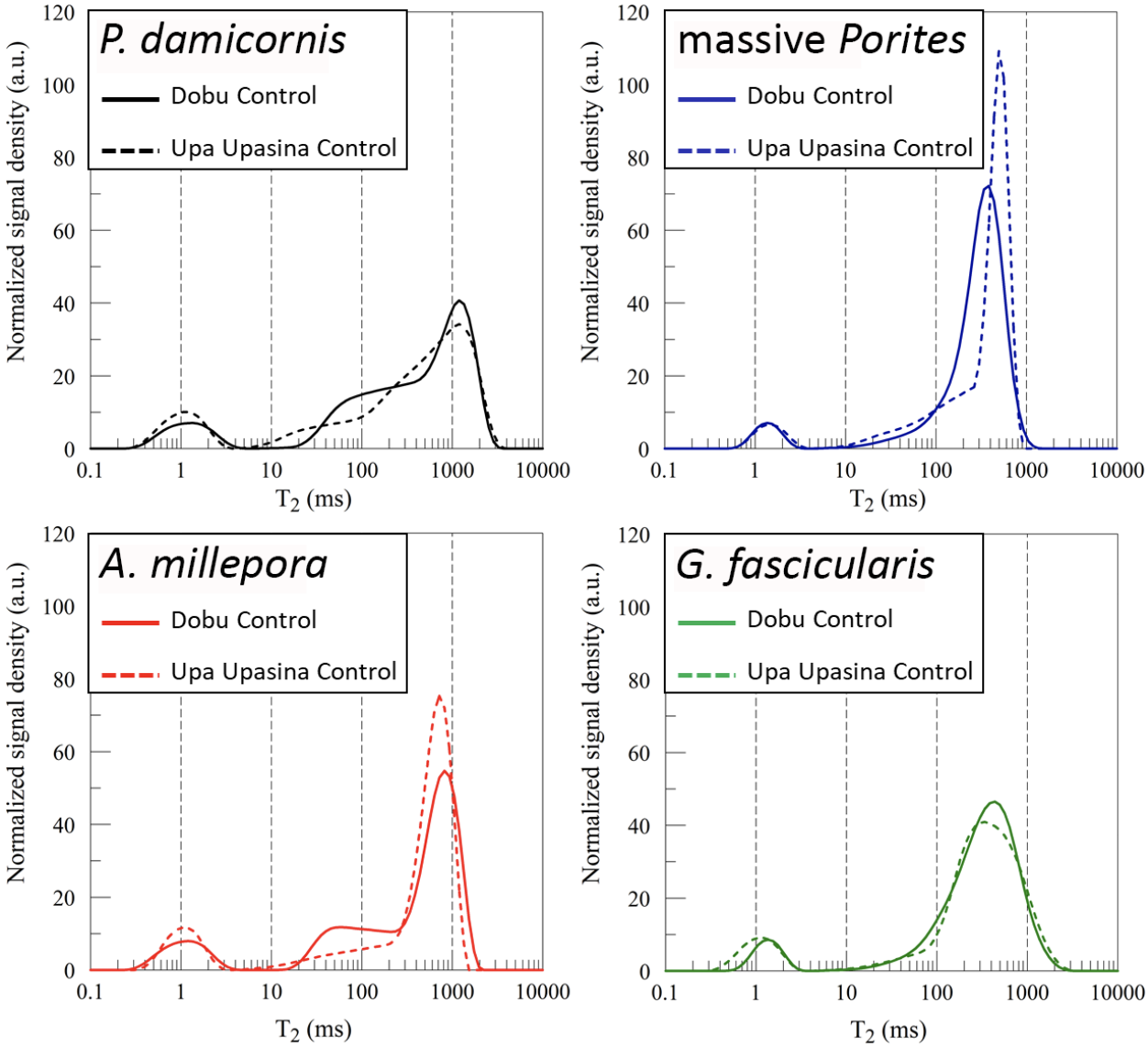

Figure S2. Representative T_2 distributions for *P. damicornis*, massive *Porites*, *A. millepora*, and *G. fascicularis* at Dobu and Upa Upasina in control sites. The area below each T_2 distribution is proportional to the amount of water saturating the pore space and consequently to the volume of the connected pore space. All the distributions show two classes of pores separated by the cut-off at ~3 ms, called for the sake of simplicity micro-scale and macro-scale pores. Plots were created with the UpenWin software[173].

SUPPLEMENTARY TABLES

Table S1. Results of the PERMANOVA analysis for the environmental dataset (see Fig. S1) and for pH, DIC, Total Alkalinity, salinity, and temperature (based on the BEST analysis) in control and seep sites at Dobu and Upa Upasina. Significant values are reported in bold. df: degrees of freedom; Pseudo-F: F value by permutation [174]; P: significance of pseudo-F

		Whole dataset		pH		DIC		Total Alkalinity		Salinity		Temperature	
Factor	df	Pseudo-F	P	Pseudo-F	P	Pseudo-F	P	Pseudo-F	P	Pseudo-F	P	Pseudo-F	P
Season (Se)	1	1.898	0.114	1.525	0.255	0.743	0.409	3.438	0.079	1.538	0.243	0.806	0.392
Location (Lc)	1	4.443	**0.005**	0.106	0.747	27.645	**0.001**	2.814	0.107	0.000	0.994	8.129	**0.011**
Site (Si)	1	11.970	**0.001**	19.335	**0.001**	12.029	**0.001**	43.038	**0.001**	0.770	0.386	0.065	0.803
SexLc	1	0.896	0.459	0.142	0.715	0.489	0.499	6.412	**0.012**	0.002	0.959	0.271	0.600
SexSi	1	0.851	0.476	0.339	0.553	2.625	0.115	0.540	0.460	0.680	0.411	0.745	0.395
LcxSi	1	2.770	**0.028**	0.061	0.817	28.388	**0.001**	0.027	0.874	0.140	0.702	0.023	0.870
SexLcxSi	1	0.571	0.686	0.723	0.384	1.210	0.289	0.067	0.797	0.103	0.761	0.507	0.485

Table S2. Means and standard deviations (SD) of the skeletal parameters micro-density, porosity and bulk density in seep and control sites for the investigated species.

		Micro-density ($g\ cm^{-3}$)			Porosity (%)			Bulk density ($g\ cm^{-3}$)		
species		N	mean	SD	N	mean	SD	N	mean	SD
					Dobu					
Acropora	Seep	14	2.62	0.19	14	32.27	12.61	14	1.75	0.22
millepora	Control	14	2.59	0.14	14	32.13	6.44	14	1.76	0.14
Galaxea	Seep	10	2.56	0.17	10	41.60	10.95	10	1.49	0.23
fascicularis	Control	6	2.64	0.21	6	41.58	10.32	6	1.53	0.20
massive	Seep	10	2.55	0.10	10	51.06	6.04	10	1.25	0.14
Porites	Control	10	2.53	0.15	10	44.77	7.73	10	1.39	0.17
Pocillopora	Seep	15	2.39	0.17	15	22.42	7.14	15	1.85	0.16
damicornis	Control	15	2.49	0.11	15	22.17	6.32	15	1.94	0.19
					Upa Upasina					
Acropora	Seep	15	2.70	0.07	15	38.71	7.18	15	1.65	0.19
millepora	Control	15	2.65	0.19	15	27.98	7.65	15	1.90	0.14
Galaxea	Seep	8	2.56	0.16	8	42.88	7.87	8	1.46	0.22
fascicularis	Control	11	2.64	0.10	10	34.35	8.46	10	1.72	0.22
massive	Seep	9	2.66	0.07	9	50.57	3.86	9	1.31	0.12
Porites	Control	10	2.62	0.11	10	46.41	3.51	10	1.41	0.09
Pocillopora	Seep	15	2.41	0.26	15	27.01	6.06	15	1.77	0.28
damicornis	Control	15	2.59	0.23	15	22.99	7.47	15	2.00	0.32

Table S3. Macro-scale pore volume fraction for *P. damicornis* obtained by TD-NMR analysis in control and seep sites in the two locations. The mean, standard deviations, number of corals examined and p value by the non-parametric test are reported. N is the number of corals examined.

Location	Site	Mean (%)	SD (%)	N
Dobu	control	81.3	3.9	15
	seep	83.7	5.0	15
Upa Upasina	control	78.9	4.9	15
	seep	84.4	6.7	15

Table S4. Results of thermo-gravimetric analysis on *P. damicornis* samples from Dobu and Upa Upasina.

Variable	site	N	Mean % mass loss	SD % mass loss
Dobu				
H_2O	control	10	0.675	0.193
	seep	10	0.755	0.168
OM	control	10	2.364	0.213
	seep	10	2.528	0.250
Upa Upasina				
H_2O	control	6	0.531	0.061
	seep	6	0.844	0.155
OM	control	6	2.376	0.113
	seep	6	2.014	0.140

Table S5. Aragonite crystallographic axes, macrostrain associated to the organic matrix (removed by thermal annealing) and aragonite to calcite transition after thermal annealing (300 °C for 2 hours) of skeletal fragments of *P. damicornis* sampled in control and seep sites at Upa Upasina (N = 3 for control and for seep sites). The statistical significance between control and seep sites by the non-parametric Kruskal-Wallis test is reported in the last row. Values are indicated as means with standard deviation in parenthesis.

	aragonite						calcite after thermal annealing		
Site	crystallographic axis			macrostrain			%	crystallographic axis	
	a (Å)	b (Å)	c (Å)	Δa	Δb	Δc		a	c
control	4.96E+00 (2.71E-05)	7.97E+00 (9.78E-04)	5.75E+00 (2.82E-04)	5.53E-04 (5.01E-05)	-2.15E-04 (2.27E-04)	4.94E-04 (1.21E-04)	3.73E+01 (6.03E+00)	4.9842 (5)	17.06 (1)
seep	4.96E+00 (9.19E)	7.97E+00 (3.86E-04)	5.75E+00 (3.88E-04)	5.10E-04 (5.70E-05)	-2.09E-04 (6.24E-05)	4.35E-04 (1.40E-04)	3.70E+01 (2.65E+00)	4.9842 (1)	17.064 (4)
Statistical significance	NS	NS	NS	NS	NS	NS	NS	NS	NS

Table S6. Crystallite size and microstrain estimation for the planes (111), (021) and (221) of aragonite using peak broadening equations and Rietveld parameters skeletal fragments of *P. damicornis* sampled in control and seep sites at Upa Upasina (N = 3 for control and for seep sites). The statistical significance between control and seep sites by the non-parametric Kruskal-Wallis test is reported in the last column to the right. Values are indicated as means with standard deviation in parenthesis.

Site		(111)		(021)		(221)		Statistical significance
		crystallite size (um)	microstrain (%)	crystallite size (um)	microstrain (%)	crystallite size (um)	microstrain (%)	
control	pristine	2.77E-01 (8.31E-02)	2.27E-01 (1.23E-02)	2.48E-01 (9.44E-02)	1.98E-01 (1.12E-01)	2.06E-01 (5.23E-02)	1.652E-01 (2.03E-02)	NS
seep		2.74E-01 (4.84E-02)	2.276E-01 (1.33E-02)	2.35E-01 (5.66E-02)	1.71E-01 (8.68E-02)	2.00E-01 (3.44E-02)	1.50E-01 (1.95E-02)	
control	after thermal annealing	1.13E-01 (1.03E-02)	8.75E-01 (1.86E-02)	1.08E-01 (3.14E-03)	8.55E-01 (7.45E-02)	7.06E-02 (9.94E-03)	6.08E-01 (2.41E-01)	NS
seep		1.04E-01 (7.46E-03)	5.70E-01 (1.54E-01)	1.08E-01 (1.29E-02)	8.21E-01 (1.40E-01)	7.07E-02 (2.56E-03)	3.30E-01 (2.27E-02)	

Section 3. Bioaccumulation of organic pollutants in corals

− One must be a sea, to receive a polluted stream without becoming impure.−

This session evaluates the sources, the accumulation and potentially effects of organic pollutants in scleractinian corals.

Chapter 6. Accumulation of PAHs in the tissues and algal symbionts of a common Mediterranean coral: Skeletal storage relates to population age structure

(Published in Science of the Total Environment)

Science of the Total Environment 743 (2020) 140781

Contents lists available at ScienceDirect

Science of the Total Environment

journal homepage: www.elsevier.com/locate/scitotenv

Accumulation of PAHs in the tissues and algal symbionts of a common Mediterranean coral: Skeletal storage relates to population age structure

Erik Caroselli [a,e,1], Emanuela Frapiccini [b,e,1], Silvia Franzellitti [c,e], Quinzia Palazzo [d,e], Fiorella Prada [a,e], Mattia Betti [b,e], Stefano Goffredo [a,e,*], Mauro Marini [b,e,*]

[a] Marine Science Group, Department of Biological, Geological and Environmental Sciences, University of Bologna, via Selmi 3, 40126 Bologna, Italy
[b] Institute of Biological Resources and Marine Biotechnology (IRBIM), National Research Council (CNR), Largo Fiera della Pesca 2, 60125 Ancona, Italy
[c] Animal and Environmental Physiology Laboratory, Department of Biological, Geological and Environmental Sciences, University of Bologna, via S. Alberto 163, 48123 Ravenna, Italy
[d] Department of Chemistry "Giacomo Ciamician", University of Bologna, Via Selmi 2, 40126 Bologna, Italy
[e] Fano Marine Center, The Inter-Institute Center for Research on Marine Biodiversity, Resources and Biotechnologies, Viale Adriatico 1/N, 61032 Fano, Italy

HIGHLIGHTS

- PAHs were quantified by QuEChERS and were of petrogenic origin.
- In all biological samples, low molecular weight PAHs prevailed.
- Concentration of 4 PAHs was higher in zooxanthellae than in coral tissue and skeleton.
- PAH concentration was unrelated to coral skeletal age.
- PAH long-term skeletal storage in a coral population was quantified.

GRAPHICAL ABSTRACT

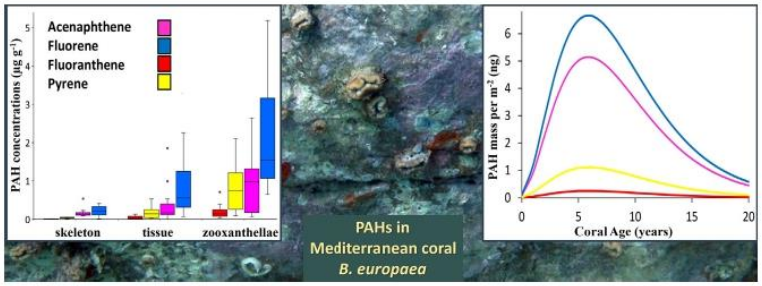

ARTICLE INFO

Article history:
Received 16 May 2020
Received in revised form 1 July 2020
Accepted 4 July 2020
Available online 08 July 2020

Editor: Damia Barcelo

Keywords:
PAH
Bioaccumulation
Scleractinian coral
Balanophyllia europaea
QuEChERS
Mediterranean Sea

ABSTRACT

Polycyclic aromatic hydrocarbons (PAHs) are widespread and harmful environmental pollutants that threaten marine ecosystems. Assessing their level and source is crucial to estimate the potential risks for marine organisms, as PAHs represent an additional threat to organism resilience under ongoing climatic change. Here we applied the QuEChERS extraction method to quantify four PAHs (i.e. acenaphthene, fluorene, fluoranthene, and pyrene) in three biological compartments (i.e. skeleton, tissue, and zooxanthellae symbiotic algae) of adult and old specimens of a scleractinian coral species (*Balanophyllia europaea*) that is widespread throughout the Mediterranean Sea. A higher concentration of all four investigated PAHs was observed in the zooxanthellae, followed by the coral tissue, with lowest concentration in the skeleton, consistently with previous studies on tropical species. In all the three biological compartments, the concentration of low molecular weight PAHs was higher with respect to high-molecular weight PAHs, in agreement with their bioaccumulation capabilities. PAH concentration was unrelated to skeletal age. Observed PAHs were of petrogenic origin, reflecting the pollution sources of the sampling area. By coupling PAH data with population age structure data measured in the field, the amount of PAHs stored in the long term (i.e. up to 20 years) in coral skeletons was quantified and resulted in 53.6 ng m^{-2} of acenaphthene, 69.4 ng m^{-2} of fluorene, 2.7 ng m^{-2} of fluoranthene, and 11.7 ng m^{-2} of pyrene. This estimate provides the basis for further assessments of long-term sequestration of PAHs from the marine environment in the whole Mediterranean, given the widespread distribution of the investigated coral species.
© 2020 Elsevier B.V. All rights reserved.

* Corresponding authors at: Fano Marine Center, The Inter-Institute Center for Research on Marine Biodiversity, Resources and Biotechnologies, Viale Adriatico 1/N, 61032 Fano, Italy.
E-mail addresses: erik.caroselli@unibo.it (E. Caroselli), emanuela.frapiccini@cnr.it (E. Frapiccini), silvia.franzellitti@unibo.it (S. Franzellitti), quinzia.palazzo2@unibo.it (Q. Palazzo), fiorella.prada2@unibo.it (F. Prada), mattia.betti@cnr.it (M. Betti), s.goffredo@unibo.it (S. Goffredo), mauro.marini@cnr.it (M. Marini).
[1]Equally contributing authors.

https://doi.org/10.1016/j.scitotenv.2020.140781
0048-9697/© 2020 Elsevier B.V. All rights reserved.

1. Introduction

Coastal marine areas host the most productive, yet threatened, ecosystems in the world (Lazzari et al., 2019). Many interacting natural and anthropogenic stressors, including suspended sediments, nutrients, hypoxia, turbidity, temperature, and pollutants can impair the health and fitness of resident biota (Adams, 2005; Schulte, 2007). Polycyclic aromatic hydrocarbons (PAHs) are a large group of hydrophobic organic compounds whose chemical structure is based on two or more fused benzene rings (Combi et al., 2020). PAHs are among the most hazardous constituents of fuels and oils that threaten marine ecosystems (Rocha and Palma, 2019). Natural sources of PAHs include forest fires, oil seeps, and diagenesis of organic matter and biological processes (Santana et al., 2018; Sun et al., 2018; Thompson et al., 2017). Nevertheless, the main sources of PAHs in the marine environment are related to anthropogenic activities. The main artificial contributors of PAH pollution in aquatic ecosystems result from the incomplete combustion of fossil fuels and organic matter (pyrogenic PAHs) or from ships, industrial discharges, sewage sludge, spills of crude oil and petroleum products (petrogenic PAHs) (Abdel-Shafy and Mansour, 2016; Lawal, 2017; Yang et al., 2019; Combi et al., 2020). PAHs from different sources can enter the marine environment through effluent discharges, surface runoff, marine transport, petroleum spills, and atmospheric deposition (Lin et al., 2013; Santana et al., 2018; Sun et al., 2018; Zhang et al., 2020). Due to their hydrophobic nature, PAHs in the water column are easily adsorbed onto suspended particulate matter and partitioned into sediments (Kim et al., 1999; Neff et al., 2005; Wang et al., 2007; Sun et al., 2018), but can be further remobilized and become bioavailable, thus making benthic organisms (e.g. sessile invertebrates) particularly subjected to PAH bioaccumulation (Frapiccini et al., 2020). Their environmental occurrence raises major ecological concerns, given their high persistency and the serious toxic effects that some PAHs exert on organisms, including teratogenicity, carcinogenicity, and mutagenicity (Frapiccini and Marini, 2015; Wang et al., 2017; Li et al., 2019; Zhang et al., 2020). Based on these features, the United States Environmental Protection Agency has identified 16 PAHs as priority pollutants worldwide (Ko et al., 2014; Nácher-Mestre et al., 2014; Abdel-Shafy and Mansour, 2016; IARC, 2018; Han et al., 2020).

The concentration of PAHs in marine organisms varies in relation to biological aspects (e.g. sex, lipid content, reproduction status), ecological factors (e.g. feeding behavior, trophic levels, habitats), and physicochemical characteristics of the contaminants (El Deeb et al., 2007; Leonards et al., 2008; Rahmanpour et al., 2014; Mashroofeh et al., 2015; Frapiccini et al., 2020). PAH accumulation is also affected by organism biotransformation capacities and by the bioavailability of these compounds, such as PAH concentration in the preys on which organisms feed on (Baumard et al., 1998).

In the Mediterranean Sea, although many studies focus on PAH contamination in benthic organisms such as mollusks (Cocchieri et al., 1990; Ausili et al., 1996; Minier et al., 2006; Perugini et al., 2007; Galgani et al., 2011; León et al., 2013; Mercogliano et al., 2016), crustaceans (Porte and Albaige's, 1993; Perugini et al., 2007; Costa et al., 2016), and fishes (Baumard et al., 1998; Perugini et al., 2007; Solé et al., 2013; Guerranti et al., 2016; Ferrante et al., 2018; Frapiccini et al., 2018, 2020), no study has yet been performed on corals. Corals are benthic organisms in close association with sediments. Therefore, they can be directly exposed to PAHs present in seawater and in resuspended sediments (Yang et al., 2019). Recent investigations report a wide occurrence of chemical pollutants in corals, suggesting that some characteristics such as growth stage, lipid content, and feeding strategy may play an important role in contaminant accumulation (Yang et al., 2019; Han et al., 2020). Studies on PAH accumulation in corals report the highest concentration in symbiotic algae (i.e. zooxanthellae), followed by the coral tissue, and the lowest one in the skeleton (Ko et al., 2014; Ranjbar Jafarabadi et al., 2018). In general, the amount and types of accumulated PAHs reflect the bioavailable fraction (Thomas and Li, 2000). Nevertheless, coral ability to metabolize these compounds remains unclear (Ranjbar Jafarabadi et al., 2018). This issue is further complicated by the intricated (and only partially disclosed) relationships across all members of the holobiont and the possible roles of microbiota in contaminant accumulation and toxicity towards the coral host (Fragoso Ados Santos et al., 2015). Evidence of the adverse effects of PAHs on both coral host and the endosymbiotic zooxanthellae is increasing, with physiological outcomes such as altered gene expression (Woo et al., 2014), metabolic changes (reduced growth rate, increased protein-to-lipid ratios, and shifts from metabolic homeostasis; Guzmán et al., 1991; Downs et al., 2006; Guzmán Martínez et al., 2007), decreased photosynthetic yield, tissue damage and bleaching (Guzmán Martínez et al., 2007), impaired larval development, and settlement inhibition (Overmans et al., 2018; Nordborg et al., 2018).

Corals in the Mediterranean Sea are likely to face the combined effects of climate change and environmental pollution more than in other areas. In fact, the Mediterranean Sea is warming two to three times faster than the global ocean (Vargas-Yáñez et al., 2008), with an increased occurrence of hot extremes (Diffenbaugh et al., 2007). Concomitantly, due to its hydro-geomorphological features (semi-enclosed nature, restricted water exchanges with the Atlantic Ocean), intense coastal urbanization, industrial activity, and heavy shipping, the Mediterranean is influenced by widespread sources of PAHs (Castro-Jiménez et al., 2012). This study focused on *Balanophyllia europaea* (Risso, 1826), a simultaneously hermaphrodite (Goffredo et al., 2002), solitary, and zooxanthellate scleractinian coral living on rocky substratum and endemic to the Mediterranean Sea, where it is widespread (reaching abundances of >100 individuals m^{-2}; Goffredo et al., 2004) both in the Western and the Eastern basin (Ozalp et al., 2018), at depths from 0 to 50 m (Zibrowius, 1980). This species has been deeply investigated for its vulnerability towards ocean warming and acidification in terms of population dynamics (Goffredo et al., 2007, 2008, 2014; Caroselli et al., 2019), mortality rate (Prada et al., 2017), photosynthetic efficiency (Caroselli et al., 2015), reproductive efficiency (Airi et al., 2014), skeletal parameters (Caroselli et al., 2011; Fantazzini et al., 2015; Goffredo et al., 2015), and net calcification rate (Goffredo et al., 2009; Fantazzini et al., 2015). In light of this, PAH contamination of Mediterranean shallow water environments should be considered as an additional threat for coral resilience under ongoing climatic changes.

Acenaphthene, fluorene, fluoranthene and pyrene were chosen among PAH priority pollutants for this study due to their environmental relevance and physicochemical features. Acenaphthene and fluorene have a high bioaccumulation capacity in marine organisms given their propensity for partition in seawater, while fluoranthene and pyrene are more abundant in marine sediments due to their high hydrophobicity (Marini and Frapiccini, 2013). Although these PAHs are not classified as carcinogenic (IARC, 2018), they can induce toxic reactions in marine organisms (Nácher-Mestre et al., 2014). Mechanisms of toxicity response shown in fishes include trigger of downstream molecular cascades that are involved in the activation of detoxifying enzymes (Cousin and Cachot, 2014). If the toxicants are maintained over a long period, they may saturate the detoxifying enzymes and alter neurochemical/metabolic processes (Little and Finger, 1990), resulting in severe aberrations of the locomotory behavior (e.g. lethargy) (Gonçalves et al., 2008). The aims of this study were to: 1) apply the QuEChERS extraction method to provide a methodological advancement towards a suitable protocol for quantifying PAHs in corals; 2) investigate PAH concentration and origin in three biological compartments (i.e. skeleton, tissue, and zooxanthellae) of *B. europaea*; 3) investigate coral age effects on PAH concentration in *B. europaea* specimens; and 4) quantify the skeletal storage of PAHs in relation to the age structure in a population of *B. europaea*.

2. Materials and methods

2.1. Coral sampling and study area

On May 31st 2019, thirteen specimens of *B. europaea* were haphazardly collected by scuba divers with a hammer and chisel at a depth of 6 m in Calafuria (43°27′ N, 10°21′ E, Italy, Ligurian Sea; Fig. 1). The Ligurian Sea is characterized by a narrow continental shelf bordering a deep bottom (~2000 m depth), under the influence of open sea conditions and upwelling currents providing considerable input of nutrients in shallow waters (Cattaneo-Vietti et al., 2010; Casella et al., 2011). Several rivers discharge into the Ligurian Sea, leading to frequent occurrence of seawater high turbidity and nutrient enrichment (Bassano et al., 2000; Attolini and Coppo, 2005). The sampling site of Calafuria is southeast of the port of Livorno, which is one of the largest seaports in the Mediterranean Sea and one of the most polluted sites in Italy (Iannelli et al., 2012). Longshore currents govern a local eastward oriented water circulation, which transports sediments along the coast (Bertolotto et al., 2003). Consequently, polluting agents (i.e. mainly petroleum hydrocarbons and heavy metals resulting from commercial and industrial activities) are dispersed from the Livorno urban and port area to adjacent sites (Bertolotto et al., 2003; Iannelli et al., 2012). The sampling was performed at depths known to have high population densities and where the reproduction, growth rate, and population dynamics of the species are documented (Goffredo et al., 2002, 2004). Upon collection, samples were stored in ice and transferred to the laboratory of the Department of Biological, Geological and Environmental Sciences (Bologna, Italy), where they were stored at −20 °C.

2.2. Sample preparation

The length (*L*: maximum axis of the oral disc) of each specimen was measured with calipers (Goffredo et al., 2004, 2007, 2008). The age of each specimen was estimated by applying the length-age relationship previously obtained for this species at the same site and depth (Goffredo et al., 2004). Based on estimated age, samples were categorized in two age classes: Adult (6 < age (years) ≤ 10; $N = 6$) and Old (10 < age (years) ≤ 14; $N = 7$). Coral tissue was removed from the skeleton using an airbrush with filtered artificial seawater (FSW). The extracted tissue was mechanically disrupted using an electrical homogenizer (IKA) for 3 × 10 s. The homogenate was centrifuged at 5000*g* for 5 min at 4 °C to separate the zooxanthellae symbiont cells from the coral host tissue. The resulting zooxanthellae pellet was separated from the supernatant and resuspended in 2 ml FSW, centrifuged and resuspended two more times, thus obtaining all the zooxanthellae of the coral suspended in 2 ml (Caroselli et al., 2015). After three centrifugation rounds, the supernatant fractions (host tissue) were pooled. Homogenates containing the coral host tissue or symbiont cells were independently lyophilized. The skeleton of each specimen was treated in a solution of 10% sodium hypochlorite (commercial bleach) for 3 days to completely remove any residue of soft tissue. The skeletons were then washed several times with double distilled water and dried in an oven at 50 °C for 3 days. Each skeleton was then observed under a binocular microscope to remove fragments of substratum and external calcareous deposits produced by epibionts (Caroselli et al., 2011). After these treatments, each skeleton was ground using an agate mortar to obtain a fine and homogeneous powder (Goffredo et al., 2012). The powdered skeleton was weighed with an Ohaus Explorer Pro analytical balance (±0.0001 g). Lyophilized coral compartments (i.e. tissue and zooxanthellae) and the powdered skeleton were then weighed with a precision balance (±0.0001 g, Scaltec). The mass of intra-skeletal organic matrix (OM), was estimated as the 2.9% of total skeletal mass, as previously reported for this species sampled at the same site and depth (Reggi et al., 2014). Pollutant concentration in the skeleton compartment (see Section 2.3 PAH analysis) was calculated over the mass of OM.

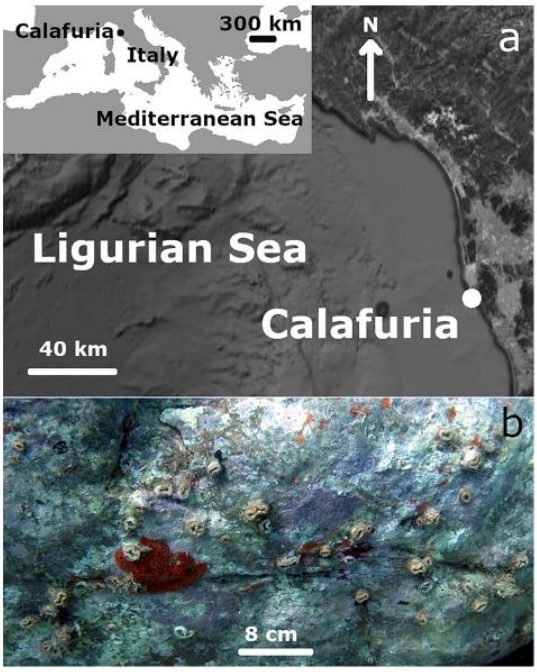

Fig. 1. Location where corals were collected. (a) Map of Calafuria (43°27′ N, 10°21′ E, Italy, Ligurian Sea). (b) Specimens of the common and abundant coral *B. europaea* on a rock at 6 m in Calafuria.

2.3. PAH analysis

The Quick Easy Cheap Effective Rugged and Safe (QuEChERS) method was applied for extraction and purification of selected PAHs (i.e. acenaphthene, fluorene, fluoranthene and pyrene) from skeleton, tissue and zooxanthellae samples of *B. europaea* (Frapiccini et al., 2018). The QuEChERS method is a simple, fast, and valid alternative to conventional extraction methods for multi-residue analysis, as it involves few steps (extraction and clean up), it is low time-consuming and it requires a low amount of solvent (Grimalt and Dehouck, 2016). Originally, it was applied to investigate multiresidue pesticides in agricultural products (Kim et al., 2019). Then, the QuEChERS method was modified and applied to other persistent organic pollutants, including PAHs, from other matrices like fish and seafood (Ramalhosa et al., 2009), but not in non-edible tissue. A comparison between this new method of extraction and a traditional method (accelerated solvent extraction, ASE) was performed by analyzing standard reference material (SRM NIST 1974c). Examined PAHs were extracted with the QuEChERS kit using acetonitrile as the reagent partitioned from the aqueous matrix using anhydrous $MgSO_4$ and NaCl. Samples were purified by a dispersive solid-phase extraction (dSPE) clean up with $MgSO_4$ and primary secondary amine (PSA). The purified extracts were concentrated and recovered with acetonitrile for chemical analysis in UHPLC (Ultimate 3000, Thermo Scientific, Waltham, MA, USA) equipped with a fluorescence (RF2000) detector (Thermo Scientific). A Hypersil Green PAH column (2.1 × 150 mm, 1.8 μm, 120 Å) in a reversed-phase LC with a mobile phase (water:acetonitrile, *v*/v) gradient elution was used. The flow rate was 0.3 ml min^{-1} at the temperature of 40 °C. Identified PAHs were qualified by their retention time. Analysis of the procedural blanks ($N = 6$) and the external standard multipoint calibration technique were used to assess quality control. All laboratory blank extract concentrations were below the limits of quantification (LOQ) for investigated PAHs. Calibration curves were obtained through serial dilutions

Table 1
HPLC-FLD determination of selected PAHs: slope of the calibration curve, coefficient of determination, limits of detection (LODs), limits of quantification (LOQs), and recovery (%).

PAH	Slope	Coefficient of determination (%)	LOD (ng ml^{-1})	LOQ (ng ml^{-1})	Recovery (%) (mean ± std. dev.)
Acenaphthene	1.131	99.945	0.007	0.023	81.71 ± 12.80
Fluorene	1.994	99.997	0.004	0.013	85.14 ± 17.61
Fluoranthene	0.842	99.943	0.010	0.030	77.52 ± 3.77
Pyrene	3.541	99.966	0.002	0.007	74.10 ± 11.74

(from 1:1000 to 1:8000 v/v) from a standard PAH solution (EPA 610 PAH Mix), purchased from Supelco, Bellafonte, PA, USA.

The percentage of recovery was calculated as reported in Table 1. Concentration of PAH compounds was not corrected for surrogate recoveries. Limits of detection (LOD) and LOQ were calculated according to ICH Q2B (ICH, 2005), using the following equations:

$$\mathrm{LOD} = 3.3\, Sa/b$$

$$\mathrm{LOQ} = 10\, Sa/b$$

where Sa is the standard deviation of the intercept of the regression line and b is the slope of the calibration curve (Table 1).

2.4. Population life table with PAHs skeletal content

The population age structure ($N_{(t)}$, number of individuals per each age class t from 0 to 20 years, i.e. up to the maximum estimated lifespan), polyp length ($L_{(t)}$), and skeletal mass ($M_{(t)}$) at each age class of *B. europaea* at 6 m depth in Calafuria was derived by Goffredo et al., 2004. The cumulative amount of OM in each age class was calculated by multiplying $N_{(t)}$ by the OM mass in the skeleton for that age class $M_{OM(t)}$. The cumulative amount of each PAH in each age class was calculated by multiplying the mean content of that PAH in all collected skeletal samples (PAH_{SK}) by the cumulative amount of OM in that age class. The total amount of each PAH stored in the skeletons of 1 m^2 of *B. europaea* population at 6 m in Calafuria was obtained by summing up the cumulative content of that PAH in all age classes (Eq. (1)).

$$\textit{Total PAH amount} = \sum_{t=0}^{t=20} \left(N_{(t)} \times M_{OM(t)} \times PAH_{SK}\right) \quad (1)$$

2.5. Statistics

Due to the heteroskedastic dataset, PAH concentration was compared among PAHs, coral biological compartments and age classes with a permutation multivariate analysis of variance (PERMANOVA; Anderson, 2005) based on Euclidean distances using a crossed design with three fixed factors (factor "PAH" with four levels: acenaphthene, fluorene, fluoranthene, pyrene; factor "Compartment" with 3 levels: Skeleton, Tissue, Zooxanthellae; factor "Age class" with 2 levels: Adult, Old) and 999 permutations included the Monte Carlo correction for small sample size. A further PERMANOVA analysis based on Euclidean distances was performed separately for each PAH using a crossed design with two fixed factors (factor "Compartment" with 3 levels: Skeleton, Tissue, Zooxanthellae; factor "Age class" with 2 levels: Adult, Old) and 999 permutations included the Monte Carlo correction for small sample size. PERMANOVA analyses were performed with software Primer 6 (Primer-e Ltd).

3. Results

Acenaphthene, fluorene, fluoranthene, and pyrene concentration was quantified in the skeleton, tissue, and zooxanthellae of adult (N = 6) and old ($N = 7$) individuals of *B. europaea* collected in the Ligurian Sea (NW Mediterranean Sea; Table 2; Supplementary Table 1, Supplementary Fig. 1). In all biological compartments, both in adult and old individuals, the dominant compound was fluorene, followed by acenaphthene, pyrene and fluoranthene. In addition, fluoranthene had a significantly lower concentration than fluorene, while pyrene generally had an intermediate concentration (Fig. 2; Table 3; Supplementary Table 2). Acenaphthene concentration was clustered with that of fluorene in the skeleton and tissue, while it was clustered with that of pyrene in the tissue and zooxanthellae (Fig. 2; Supplementary Table 2). For all the four PAHs, the concentration in the skeleton was lower than the concentration in the zooxanthellae, while tissue had an intermediate concentration (Fig. 2; Supplementary Table 3). No significant effect of age was observed (Table 3).

For each individual PAH (i.e. analyzed separately from the others), the concentration in the skeleton was significantly lower than the concentration in the zooxanthellae, while the tissue generally had an intermediate concentration (i.e. for fluorene, fluoranthene in old individuals, and pyrene) or the same concentration of the skeleton (i.e. for fluoranthene in adult individuals and acenaphthene; Fig. 3; Table 4; Supplementary Tables 4 and 5). Age did not show significant effects, with the only exceptions of the concentration of fluoranthene in the tissue and zooxanthellae, that was higher in old individuals than in adults (Fig. 3; Table 4; Supplementary Table 5).

Diagnostic ratio was applied to identify the source of PAHs in the three biological compartments of *B. europaea* samples. The ratio *fluoranthene/(fluoranthene + pyrene)* was used to distinguish between combustion and petroleum sources (Yunker et al., 2002). Most of the samples (95%) exhibited low values of *fluoranthene/(fluoranthene + pyrene)* (<0.4) indicating that PAH contamination originated mainly from petroleum sources (unburned petroleum; Table 5). Only the tissue of two old individuals reflected a combination of petrogenic and pyrolytic contaminations (*fluoranthene/(fluoranthene + pyrene)* > 0.4).

Since no age effect was observed for the concentration of PAHs in the skeleton (Tables 3 and 4; Supplementary Table 5), the amount of each

Table 2
Concentration (μg g^{-1} dry weight, d.w.) of the four PAHs in the three biological compartments and in the two age classes of *B. europaea* specimens. Values are indicated as means with 95% Confidence Intervals in parentheses. N: Number of samples.

		N	acenaphtene (μg g^{-1} d.w.)	fluorene (μg g^{-1} d.w.)	fluoranthene (μg g^{-1} d.w.)	pyrene (μg g^{-1} d.w.)
Skeleton	Adult	6	0.21 (0.08–0.35)	0.24 (0.12–0.36)	0.009 (0.006–0.012)	0.042 (0.029–0.054)
	Old	7	0.13 (0.10–0.16)	0.20 (0.11–0.29)	0.008 (0.006–0.010)	0.032 (0.024–0.041)
	Total	13	0.17 (0.15–0.23)	0.22 (0.15–0.29)	0.008 (0.007–0.010)	0.037 (0.029–0.044)
Tissue	Adult	6	0.17 (0.12–0.22)	0.51 (0.34–0.69)	0.012 (0.002–0.022)	0.074 (0.032–0.116)
	Old	7	0.55 (0.05–1.04)	1.21 (0.38–2.05)	0.078 (0.053–0.103)	0.282 (0.146–0.418)
	Total	13	0.37 (0.09–0.65)	0.89 (0.41–1.37)	0.048 (0.025–0.071)	0.186 (0.092–0.280)
Zooxanthellae	Adult	6	1.06 (0.39–1.74)	2.13 (1.04–3.22)	0.086 (0.049–0.122)	0.570 (0.000–1.147)
	Old	7	0.77 (0.20–1.34)	2.05 (0.89–3.22)	0.289 (0.133–0.445)	1.025 (0.596–1.453)
	Total	13	0.91 (0.48–1.33)	2.09 (1.32–2.86)	0.195 (0.095–0.296)	0.815 (0.455–1.175)

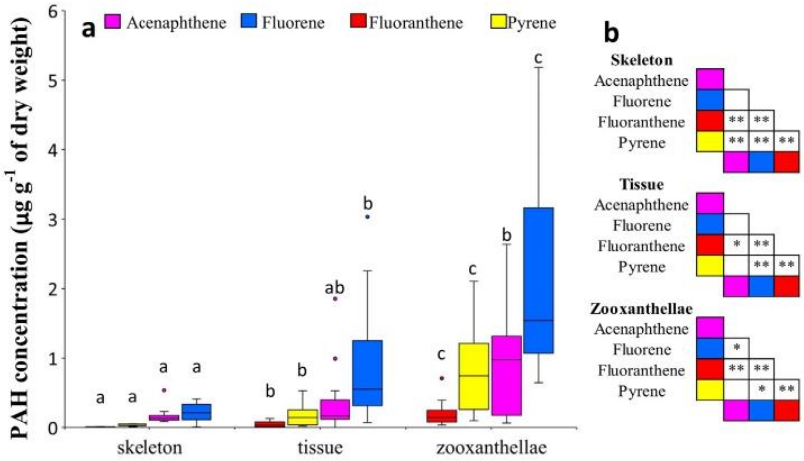

Fig. 2. Concentration (µg g^{-1} of dry weight) of PAHs in the three biological compartments of *B. europaea*. (a) Boxplots represent median, upper and lower quartiles ($N = 13$) of PAH concentration in coral skeleton, tissue, and zooxanthellae. Different letters indicate significant differences in the concentration of each PAH between biological compartments ($P < 0.05$; PERMANOVA pairwise comparisons *t*-tests; 999 permutations). (b) Within each biological compartment, triangular matrices report differences between pairs of PAHs (**$P < 0.01$, *$P < 0.05$; PERMANOVA pairwise comparisons t-tests; 999 permutations).

PAH stored in the skeletons of 1 m^2 of *B. europaea* population at 6 m depth in Calafuria was estimated by multiplying the total concentration of each PAH (Table 2) by the amount of OM in the skeleton (Eq. (1)), which resulted in 53.6 ng of acenaphthene, 69.4 ng of fluorene, 2.7 ng of fluoranthene, and 11.7 ng of pyrene (Fig. 4; Supplementary Table 6).

4. Discussion

To our knowledge, this is the first study investigating PAHs in a Mediterranean coral species. This is also the first application of the QuEChERS extraction method to quantify PAHs in a coral species. The comparison between this method and the traditional ASE method is shown in Supplementary Table 7. *Balanophyllia europaea* specimens from the Ligurian Sea retained acenaphthene, fluorene, fluoranthene, and pyrene up to about 1 µg g^{-1} dry weight (d.w.), with consistent accumulation pathways between coral skeleton, tissue, and symbiotic zooxanthellae algae. In all three biological compartments, a preferential accumulation of the low molecular weight PAH compounds fluorene and acenaphthene was observed, in agreement with studies on tropical coral species from the China Sea (Ko et al., 2014; Han et al., 2020) and the Persian Gulf (Ranjbar Jafarabadi et al., 2018). In general, PAHs with 2–3 aromatic rings are more soluble in seawater than PAHs with 4 or more aromatic rings, thus they are more effectively accumulated by organisms (Sverdrup et al., 2002).

PAH concentration in the tissue of *B. europaea* (Table 2) was comparable to that reported for the tissue of the tropical scleractinian *Acropora hyacinthus* from the South China Sea (0.03–0.34 µg g^{-1} dry weight; Yang et al., 2019) and to those recorded in several scleractinian corals from the Persian Gulf (0.16–0.18 µg g^{-1} dry weight; Ranjbar Jafarabadi et al., 2018). Skeletal PAH concentrations reported in this study are expressed in relation to the skeletal fraction of intra-skeletal organic matrix (OM), since this is the lipid storage component and PAH accumulation site in the skeleton. When expressed over the skeletal dry weight, the concentrations of PAHs in *B. europaea* range between 0.0002 and 0.006 µg g^{-1}, which is two orders of magnitude lower than those assessed in skeletons of *Acropora* sp. corals from the Red Sea (0.03–0.3 µg g^{-1} dry weight; El-Sikaily et al., 2003). This may depend on: 1) a lower environmental burden of PAHs in the Ligurian Sea in 2019 than in the Egyptian Red Sea in 1999 (El-Sikaily et al., 2003), 2) a higher skeletal storage capacity of *Acropora* sp. with respect to *B. europaea*, likely related to a species-specific difference in OM and/or lipid content in the skeleton; 3) different metabolic capacities of the two species towards PAHs, or 4) a combination of these factors. The literature lacks studies on species-specific or location-specific differences in coral skeletal PAH concentration, highlighting the need to increase the basic research effort on PAH contamination in corals and the related physiological outcomes.

The accumulation pattern of all investigated PAHs in *B. europaea* was: zooxanthellae > coral tissue > coral skeleton, in agreement with studies on other coral species from different locations (Ko et al., 2014; Ranjbar Jafarabadi et al., 2018), suggesting that this could be a common pattern. The distinct organic pollutant accumulation capacity in corals tissues (soft and skeleton) and zooxanthellae may be related to the lipid content, since the bioaccumulation of hydrophobic compounds is affected by the amount and relative composition of lipids within biological compartments (Kennedy et al., 1992; Readman et al., 1996; Samorì et al., 2017). In this light, performing similar investigations on non-zooxanthellate corals, where symbiotic algae-associated lipids are not present, may give relevant insights on the effect of symbiosis in PAH accumulation and metabolic pathways in corals.

The petrogenic origin of detected PAHs reflects the impact of petroleum contamination at the sampling site (Bertolotto et al., 2003; Iannelli et al., 2012). Since all biological compartments had a similar PAH origin, the following pathway of accumulation may be hypothesized: PAHs are first absorbed by zooxanthellae and translocated through lipid storage to the coral soft tissue (Krueger et al., 2018; Hambleton et al., 2019; Radice et al., 2019) and then to the OM (Reggi et al., 2016; Samorì et al., 2017), where lipids are present as free fatty acids, phospholipids, sterols, ceramids, and sterol esters (Farre et al., 2010), likely serving as $CaCO_3$ nucleation sites (Isa and Okazaki, 1987). Furthermore, corals use lipid vesicles for ion transport to the sites of mineralization, after which lipids are incorporated into the growing skeleton (e.g. Samorì

Table 3
Results of the comparative PERMANOVA analysis for PAH concentration.

Factor	df	Pseudo-F	P
PAH	3	18.541	0.001
Age class	1	1.708	0.198
Compartment	2	30.318	0.001
PAH × Age class	3	0.268	0.863
PAH × Compartment	6	4.667	0.001
Age class × Compartment	2	1.330	0.294
PAH × Age class × Compartment	6	0.688	0.649

df: degrees of freedom; Pseudo-F: F value by permutation (Anderson, 2005); P: significance of pseudo-F with Monte Carlo correction.

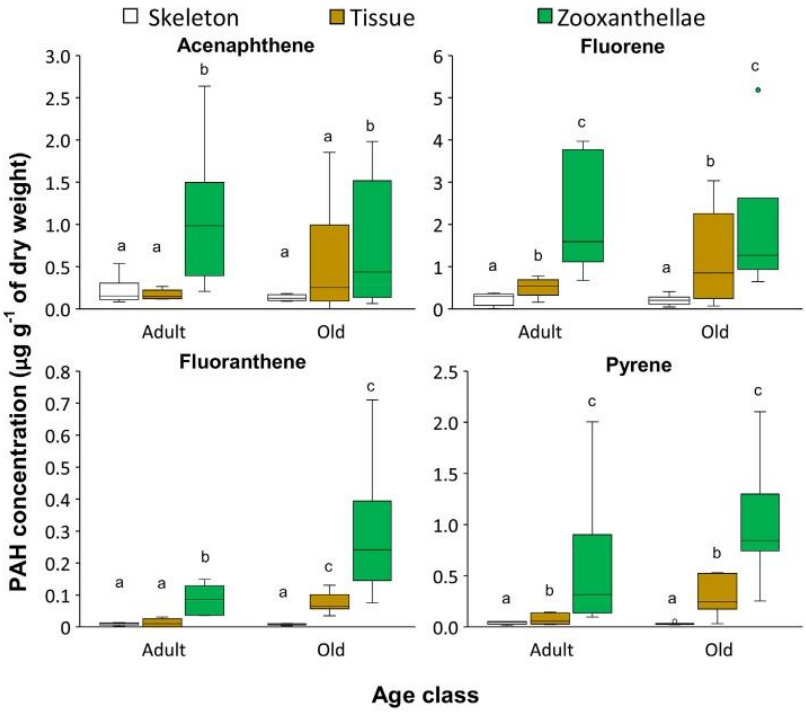

Fig. 3. Concentration (µg g^{-1} of dry weight) of individual PAHs (acenaphthene, fluorene, fluoranthene and pyrene) according to age classes in the three biological compartments of *B. europaea*. Boxplots represent median, upper and lower quartiles of PAH concentrations in coral skeleton, tissue and zooxanthellae in adult ($N = 6$) and old individuals ($N = 7$). Different letters indicate significant differences in the concentration of each PAH between biological compartments and/or age classes ($P < 0.05$; PERMANOVA pairwise comparisons t-tests; 999 permutations).

et al., 2017). A further source of PAH contamination in corals may be predation on zooplankton, a feeding strategy that is present in all coral species, with different degrees of importance depending on the heterotrophic/autotrophic ratio shown by zooxanthellate species. Zooplankton accumulate PAHs (Almeda et al., 2013; Ziyaadini et al., 2016; Hsieh et al., 2019) and is a relevant source of organic pollutants in low trophic level feeding organisms (Wan et al., 2007; Alekseenko et al., 2018). Given their high solubility, PAHs may enter coral tissues also through coral mucus (Wild et al., 2004). Furthermore, contaminants adsorbed onto the particulate matter trapped on the surface of coral mucus may enter the coral (Zhang et al., 2019; Han et al., 2020). PAHs accumulated by the zooxanthellae, zooplankton, and coral mucus may further circulate between biological compartments depending on physiological processes (e.g. skeletal biomineralization). Biotransformation of organic pollutants may also play a determinant role in PAH bioaccumulation. In this regard, it is worth noting that data on detoxification/biotransformation mechanisms in corals are very scarce. Considering the general assumption of relatively slow coral growth rate (Goffredo et al., 2004), PAH levels assessed in *B. europaea* in this study may result from the effective uptake routes depicted above, and from a low biotransformation efficiency for PAHs in live tissues, which are further affected by algae contribution to uptake and/or degradative processes (Gust et al., 2014). The skeleton may be the final repository of both parental and metabolic compounds.

Coupling PAH concentration data with population structure of *B. europaea* at Calafuria (Goffredo et al., 2004) allowed to estimate the amount of PAHs stored in the OM, and thus to evaluate the capacity of natural coral populations to sequester and immobilize PAHs for a relatively long time (20 years = maximum estimated longevity of corals in the investigated population; 4 years = turnover time; i.e. average age of individuals in the population; see Goffredo et al., 2004 for parameter estimation). The content of PAHs in the population reached a maximum in individuals of 6 years of age. Younger individuals are more represented in the population, but their PAH content is low, given their small size and skeletal mass. Individuals older than 6 years are so rare that their contribution to the overall population PAH content is lower. PAHs trapped in the skeleton become unavailable for animal metabolic mechanisms and thus are stored in a non-biologically active form until coral death and skeletal dissolution occurs. Under the scenarios of projected ocean acidification trends (IPCC, 2019), which is expected to speed-up the dissolution of shallow water carbonates, including coral skeletons, this process is particularly relevant, and its fine-scale investigation is urgent. In this context, since physiological traits related to growth and biomineralization vary widely among

Table 4
Results of the PERMANOVA analysis for the concentration of each of the four PAHs.

Factor	df	Acenaphthene		Fluorene		Fluoranthene		Pyrene	
		Pseudo-F	P	Pseudo-F	P	Pseudo-F	P	Pseudo-F	P
Compartment	2	6.436	0.004	11.987	0.001	13.418	0.001	14.483	0.001
Age class	1	$1.21E^{-04}$	0.993	0.374	0.549	8.955	0.008	3.138	0.091
Compartment × Age class	2	1.269	0.290	0.639	0.535	4.101	0.027	1.192	0.311

df: degrees of freedom; Pseudo-F: F value by permutation (Anderson, 2005); P: significance of pseudo-F with Monte Carlo correction. Significant differences are indicated in bold.

Table 5
Diagnostic ratio *fluoranthene/(fluoranthene + pyrene)* for source identification of PAHs.

Sample code	Age class	skeleton	tissue	zooxanthellae
BEU_10	Adult	<0.4	n.d.	<0.4
BEU_15	Adult	<0.4	<0.4	<0.4
BEU_16	Adult	<0.4	n.d.	<0.4
BEU_18	Adult	<0.4	<0.4	<0.4
BEU_20	Adult	<0.4	<0.4	<0.4
BEU_22	Adult	<0.4	<0.4	<0.4
BEU_08	Old	<0.4	0.4–0.5	<0.4
BEU_09	Old	<0.4	<0.4	<0.4
BEU_11	Old	<0.4	<0.4	<0.4
BEU_12	Old	<0.4	<0.4	<0.4
BEU_14	Old	<0.4	<0.4	<0.4
BEU_17	Old	<0.4	>0.5	<0.4
BEU_19	Old	<0.4	<0.4	<0.4

Petroleum, *fluoranthene/(fluoranthene + pyrene)* < 0.4; Petroleum combustion, *fluoranthene/(fluoranthene + pyrene)* = 0.4–0.5; Grass, wood or coal combustion, *fluoranthene/(fluoranthene + pyrene)* > 0.5 (Yunker et al., 2002). n.d.: not detected.

populations of *B. europaea* located throughout the latitudinal extension of Italian coasts (>1000 km; Goffredo et al., 2008), applying the experimental setup employed in this study across this gradient (currently underway) will likely provide an accurate and wide range estimation of how coral biomineralization buffers PAH contamination in coastal environments. To improve the detection of possible age effects on PAH concentration that were not identified in the present study, the sampling range should be expanded to include younger individuals (<6 years), which are sexually inactive (<3–4 years: Goffredo et al., 2004) and whose different physiology may alter the concentration of PAHs in their biological compartments.

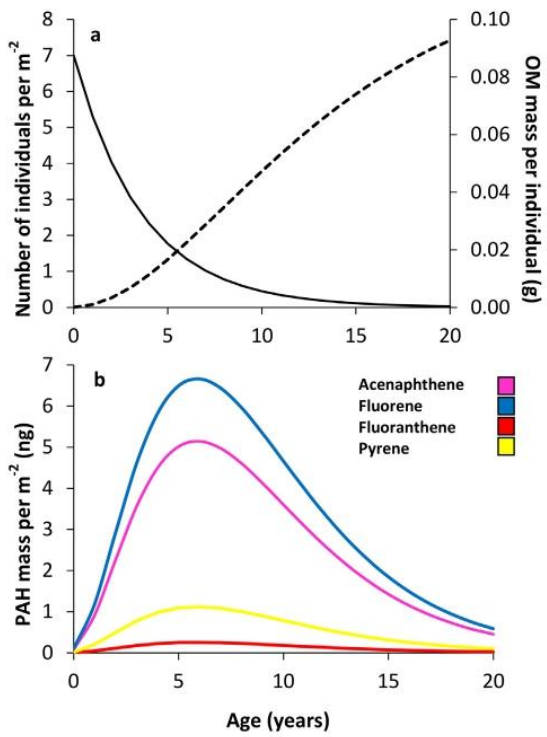

Fig. 4. PAH storage in the skeletons of *B. europaea* in 1 m^2 of population at 6 m depth in Calafuria (Italy, Ligurian Sea), according to population age structure. (a) Distribution of the number of individuals (solid line), and OM mass (dotted line) with coral age. (b) PAH mass stored in the skeleton (blue = fluorene, pink = acenaphthene, yellow = pyrene, red = fluoranthene) over the age of *B. europaea* specimens.

In conclusion, this study showed that the Mediterranean coral *B. europaea* accumulates acenaphthene, fluorene, fluoranthene and pyrene likely as a result of its mixotrophic strategy, comprising both zooplankton predation and macromolecules (in particular lipids) acquisition from the symbiotic partnership with the zooxanthellae algae. Low molecular weight PAHs were preferentially accumulated compared to high molecular weight PAHs, with higher concentrations in the symbiotic algae, followed by the host tissue, and finally in the skeleton. This trend is common to other coral species analyzed outside the Mediterranean Sea. Detected PAHs were of petrogenic origin, reflecting pollution sources of the sampling area. PAHs were effectively stored in the skeletons of *B. europaea*, likely due to their hydrophobicity and interaction with lipids. Skeletal lipids contribute to the formation and function of the OM, the non-mineral fraction composed of a framework of macromolecules (besides lipids, it includes proteins, glycoproteins, and polysaccharides) that regulates biomineral deposition and skeletal developmental patterns (Goffredo et al., 2012). Therefore, the possible PAH partitioning in and interaction with OM macromolecules may represent a threat for coral biomineralization, as already reported for vertebrate bone mineralization (Duan et al., 2014; Zanaty et al., 2020). Besides evaluating potential detrimental effects, the quantification of PAHs stored in coral skeleton reported in this study provides the basis for further assessments of long-term sequestration of PAHs from the environment in the whole Mediterranean, given the widespread distribution of the target coral species.

CRediT authorship contribution statement

Erik Caroselli: Investigation, Formal analysis, Resources, Writing - original draft, Visualization. **Emanuela Frapiccini:** Investigation, Formal analysis, Resources, Writing - original draft, Visualization. **Silvia Franzellitti:** Investigation, Resources, Writing - review & editing. **Quinzia Palazzo:** Investigation, Resources, Writing - review & editing. **Fiorella Prada:** Investigation, Writing - review & editing. **Mattia Betti:** Investigation. **Stefano Goffredo:** Conceptualization, Resources, Writing - review & editing, Supervision, Project administration. **Mauro Marini:** Conceptualization, Resources, Writing - review & editing, Supervision, Project administration.

Declaration of competing interest

The authors declare that they have no known competing financial interests or personal relationships that could have appeared to influence the work reported in this paper.

Acknowledgements

The research leading to these results has been conceived under the collaboration between the University of Bologna and the National Research Council for the implementation of the International PhD Program "Innovative Technologies and Sustainable Use of Mediterranean Sea Fishery and Biological Resources" (www.FishMed-PhD.org). EC was supported by the ALMA IDEA grant of the University of Bologna for the project "STRAMICRO". The Scientific Diving School supplied technical and logistical support. The experiments comply with current Italian law.

Appendix A. Supplementary data

Supplementary data to this article can be found online at https://doi.org/10.1016/j.scitotenv.2020.140781.

References

Abdel-Shafy, H.I., Mansour, M.S., 2016. A review on polycyclic aromatic hydrocarbons: source, environmental impact, effect on human health and remediation. Egypt. J. Pet. 25, 107–123. https://doi.org/10.1016/j.ejpe.2015.03.011.

Adams, S.M., 2005. Assessing cause and effect of multiple stressors on marine systems. Mar. Pollut. Bull. 51, 649–657. https://doi.org/10.1016/j.marpolbul.2004.11.040.

Airi, V., Gizzi, F., Falini, G., Levy, O., Dubinsky, Z., Goffredo, S., 2014. Reproductive efficiency of a Mediterranean endemic zooxanthellate coral decreases with increasing temperature along a wide latitudinal gradient. PLoS One 9, e91792. https://doi.org/10.1371/journal.pone.0091792.

Alekseenko, E., Thouvenin, B., Tronczyński, J., Carlotti, F., Garreau, P., Tixier, C., Baklouti, M., 2018. Modeling of PCB trophic transfer in the Gulf of Lions; 3D coupled model application. Mar. Pollut. Bull. 128, 140–155. https://doi.org/10.1016/j.marpolbul.2018.01.008.

Almeda, R., Wambaugh, Z., Wang, Z., Hyatt, C., Liu, Z., Buskey, E.J., 2013. Interactions between zooplankton and crude oil: toxic effects and bioaccumulation of polycyclic aromatic hydrocarbons. PLoS One 8, e67212. https://doi.org/10.1371/journal.pone.0067212.

Anderson, M.J., 2005. PERMANOVA: A FORTRAN Computer Program for Permutational Multivariate Analysis of Variance. Department of Statistics, Univ. of Auckland.

Attolini, A., Coppo, S., 2005. Misure di trasparenza nelle acque costiere liguri. Genova: Regione Liguria, Settore Opere Marittime ed Ecosistema Costiero (In Italian).

Ausili, A., Vacchi, M., Ciuffa, G., 1996. Bioaccumulation of PAHs in *Venus verrucosa* from Ligurian coast. Polycycl Aromat Comp 11, 99–106. https://doi.org/10.1080/10406639608544654.

Bassano, E., Boniforti, R., Pezzani, A., 2000. Parametri meteorologici e idrologici. In: Peroni, C. (Ed.), Sistema informativo e di monitoraggio marino costiero della provincia della Spezia. ENEA, Rapp Tec, pp. 17–55 (In Italian).

Baumard, P., Budzinski, H., Garrigues, P., Sorbe, J.C., Burgeot, T., Bellocq, J., 1998. Concentrations of PAHs (polycyclic aromatic hydrocarbons) in various marine organisms in relation to those in sediments and to trophic level. Mar. Pollut. Bull. 36, 951–960. https://doi.org/10.1016/S0025-326X(98)00088-5.

Bertolotto, R.M., Ghioni, F., Frignani, M., Alvarado-Aguilar, D., Bellucci, L.G., Cuneo, C., Picca, M.R., Gollo, E., 2003. Polycyclic aromatic hydrocarbons in surficial coastal sediments of the Ligurian Sea. Mar. Pollut. Bull. 46, 907–913. https://doi.org/10.1016/S0025-326X(03)00114-0.

Caroselli, E., Prada, F., Pasquini, L., Nonnis Marzano, F., Zaccanti, F., Falini, G., Levy, O., Dubinsky, Z., Goffredo, S., 2011. Environmental implications of skeletal microdensity and porosity variation in two scleractinian corals. Zoology 114, 255–264. https://doi.org/10.1016/j.zool.2011.04.003.

Caroselli, E., Falini, G., Goffredo, S., Dubinsky, Z., Levy, O., 2015. Negative response of photosynthesis to natural and projected high seawater temperatures estimated by pulse amplitude modulation fluorometry in a temperate coral. Front. Physiol. 6, 317. https://doi.org/10.3389/fphys.2015.00317.

Caroselli, E., Gizzi, F., Prada, F., Marchini, C., Airi, V., Kaandorp, J., Falini, G., Dubinsky, Z., Goffredo, S., 2019. Low and variable pH decreases recruitment efficiency in populations of a temperate coral naturally present at a CO_2 vent. Limnol. Oceanogr. 64, 1059–1069. https://doi.org/10.1002/lno.11097.

Casella, E., Molcard, A., Provenzale, A., 2011. Mesoscale vortices in the Ligurian Sea and their effect on coastal upwelling processes. J Mar Sys 88, 12–19. https://doi.org/10.1016/j.jmarsys.2011.02.019.

Castro-Jiménez, J., Berrojalbiz, N., Wollgast, J., Dachs, J., 2012. Polycyclic aromatic hydrocarbons (PAHs) in the Mediterranean Sea: atmospheric occurrence, deposition and decoupling with settling fluxes in the water column. Environ. Pollut. 166, 40–47. https://doi.org/10.1016/j.envpol.2012.03.003.

Cattaneo-Vietti, R., Albertelli, G., Aliani, S., Bava, S., Bavestrello, G., Benedetti Cecchi, L., Bianchi, C.N., Bozzo, E., Capello, M., Castellano, M., Cerrano, C., Chiantore, M., Corradi, N., Cocito, S., Cutroneo, L., Diviacco, G., Fabiano, M., Faimali, M., Ferrari, M., Gasparini, G.P., Locritani, M., Mangialajo, L., Marin, V., Moreno, M., Morri, C., Relini Orsi, L., Pane, L., Paoli, C., Petrillo, M., Povero, P., Pronzato, R., Relini, G., Santangelo, G., Tucci, S., Tunesi, L., Vacchi, M., Vassallo, P., Vezzulli, L., Wurtz, M., 2010. The Ligurian Sea: present status, problems and perspectives. Chem. Ecol. 26, 319–334. https://doi.org/10.1080/02757541003689845.

Cocchieri, R.A., Arnese, A., Minicucci, A.M., 1990. Polycyclic aromatic hydrocarbons in marine organisms from Italian Central Mediterranean coasts. Mar. Pollut. Bull. 21, 15–18. https://doi.org/10.1016/0025-326X(90)90146-Y.

Combi, T., Pintado-Herrera, M.G., Lara-Martín, P.A., Lopes-Rocha, M., Miserocchi, S., Langone, L., Guerra, R., 2020. Historical sedimentary deposition and flux of PAHs, PCBs and DDTs in sediment cores from the western Adriatic Sea. Chemosphere 241, 125029. https://doi.org/10.1016/j.chemosphere.2019.125029.

Costa, E., Piazza, V., Gambardella, C., Moresco, R., Prato, E., Biandolino, F., Cassin, D., Botter, M., Maurizio, D., D'Adamo, R., Fabbrocini, A., Faimali, M., Garaventa, F., 2016. Ecotoxicological effects of sediments from Mar Piccolo, South Italy: toxicity testing with organisms from different trophic levels. Environ. Sci. Pollut. Res. 23, 12755–12769. https://doi.org/10.1007/s11356-015-5471-x.

Cousin, X., Cachot, J., 2014. PAHs and fish—exposure monitoring and adverse effects—from molecular to individual level. Environ. Sci. Pollut. Res. 21, 13685–13688. https://doi.org/10.1007/s11356-014-3161-8.

Diffenbaugh, N.S., Pal, J.S., Giorgi, F., Gao, X., 2007. Heat stress intensification in the Mediterranean climate change hotspot. Geophys. Res. Lett. 34, L11706. https://doi.org/10.1029/2007GL030000.

Downs, C.A., Richmond, R.H., Mendiola, W.J., Rougee, L., Ostrander, G.K., 2006. Cellular physiological effects of the MV Kyowa Violet fuel-oil spill on the hard coral, *Porites lobata*. Environ. Toxicol. Chem. 25, 3171–3180. https://doi.org/10.1897/05-509R1.1.

Duan, W., Meng, X., Sun, Y., Jia, C., 2014. Association between polycyclic aromatic hydrocarbons and osteoporosis: data from NHANES, 2005–2014. Arch. Osteoporos. 13, 112. https://doi.org/10.1007/s11657-018-0527-4.

El Deeb, K.Z., Said, T.O., Naggar, M.H.E., Shreadah, M.A., 2007. Distribution and sources of aliphatic and polycyclic aromatic hydrocarbons in surface sediments, fish and bivalves of Abu Qir Bay (Egyptian Mediterranean Sea). Bull. Environ. Contam. Toxicol. 78, 373–379. https://doi.org/10.1007/s00128-007-9173-z.

El-Sikaily, A., Khaled, A., El Nemr, A., Said, T.O., Abd-Alla, A.M.A., 2003. Polycyclic aromatic hydrocarbons and aliphatics in the coral reef skeleton of the Egyptian Red Sea Coast. Bull Environ Con Tox 71, 1252–1259. https://doi.org/10.1007/s00128-003-8736-x.

Fantazzini, P., Mengoli, S., Pasquini, L., Bortolotti, V., Brizi, L., Mariani, M., Di Giosia, M., Fermani, S., Capaccioni, B., Caroselli, E., Prada, F., Zaccanti, F., Levy, O., Dubinsky, Z., Kaandorp, J.A., Konglerd, P., Hammel, J.U., Dauphin, Y., Cuif, J.-P., Weaver, J.C., Fabricius, K.E., Wagermaier, W., Fratzl, P., Falini, G., Goffredo, S., 2015. Gains and losses of coral skeletal porosity changes with ocean acidification acclimation. Nat. Commun. 6, 7785. https://doi.org/10.1038/ncomms8785.

Farre, B., Cuif, J.P., Dauphin, Y., 2010. Occurrence and diversity of lipids in modern coral skeletons. Zoology 113, 250–257. https://doi.org/10.1016/j.zool.2009.11.004.

Ferrante, M., Zanghì, G., Cristaldi, A., Copat, C., Grasso, A., Fiore, M., Signorelli, S.S., Zuccarello, P., Oliveri Conti, G., 2018. PAHs in seafood from the Mediterranean Sea: an exposure risk assessment. Food Chem. Toxicol. 115, 385–390. https://doi.org/10.1016/j.fct.2018.03.024.

Fragoso Ados Santos, H., Duarte, G.A.S., Rachid, C.T.D.C., Chaloub, R.M., Calderon, E.N., Marangoni, L.F.D.B., Bianchini, A., Nudi, A.H., Do Carmo, F.L., Van Elsas, J.D., Rosado, A.S., Castro, C.B.E., Peixoto, R.S., 2015. Impact of oil spills on coral reefs can be reduced by bioremediation using probiotic microbiota. Sci. Rep. 5, 18268. https://doi.org/10.1038/srep18268.

Frapiccini, E., Marini, M., 2015. Polycyclic aromatic hydrocarbon degradation and sorption parameters in coastal and open-sea sediment. Water Air Soil Pollut. 226, 246. https://doi.org/10.1007/s11270-015-2510-7.

Frapiccini, E., Annibaldi, A., Betti, M., Polidori, P., Truzzi, C., Marini, M., 2018. Polycyclic aromatic hydrocarbon (PAH) accumulation in different common sole (*Solea solea*) tissues from the North Adriatic Sea peculiar impacted area. Mar Poll Bull 137, 61–68. https://doi.org/10.1016/j.marpolbul.2018.10.002.

Frapiccini, E., Panfili, M., Guicciardi, S., Santojanni, A., Marini, M., Truzzi, C., Annibaldi, A., 2020. Effects of biological factors and seasonality on the level of polycyclic aromatic hydrocarbons in red mullet (*Mullus barbatus*). Environ. Pollut. 258, 113742. https://doi.org/10.1016/j.envpol.2019.113742.

Galgani, F., Martínez-Gómez, C., Giovanardi, F., Romanelli, G., Caixach, J., Cento, A., Scarpato, A., Benbrahim, S., Messaoudi, S., Deudero, S., Boulahdid, M., Benedicto, J., Andral, B., 2011. Assessment of polycyclic aromatic hydrocarbon concentrations in mussels (*Mytilus galloprovincialis*) from the Western basin of the Mediterranean Sea. Environ. Monit. Assess. 172, 301–317. https://doi.org/10.1007/s10661-010-1335-5.

Goffredo, S., Arnone, S., Zaccanti, F., 2002. Sexual reproduction in the Mediterranean solitary coral *Balanophyllia europaea* (Scleractinia, Dendrophylliidae). Mar. Ecol. Prog. Ser. 229, 83–94 83-94. https://doi.org/10.3354/meps229083.

Goffredo, S., Mattioli, G., Zaccanti, F., 2004. Growth and population dynamics model of the Mediterranean solitary coral *Balanophyllia europaea* (Scleractinia, Dendrophylliidae). Coral Reefs 23, 433–443. https://doi.org/10.1007/s00338-004-0395-9.

Goffredo, S., Caroselli, E., Pignotti, E., Mattioli, G., Zaccanti, F., 2007. Variation in biometry and population density of solitary corals with environmental factors in the Mediterranean Sea. Mar. Biol. 152, 351–361. https://doi.org/10.1007/s00227-007-0695-z.

Goffredo, S., Caroselli, E., Mattioli, G., Pignotti, E., Zaccanti, F., 2008. Relationships between growth, population structure and sea surface temperature in the temperate solitary coral *Balanophyllia europaea* (Scleractinia, Dendrophylliidae). Coral Reefs 27, 623–632. https://doi.org/10.1007/s00338-008-0362-y.

Goffredo, S., Caroselli, E., Mattioli, G., Pignotti, E., Dubinsky, Z., Zaccanti, F., 2009. Inferred level of calcification decreases along an increasing temperature gradient in a Mediterranean endemic coral. Limnol. Oceanogr. 54, 930–937. https://doi.org/10.4319/lo.2009.54.3.0930.

Goffredo, S., Caroselli, E., Mezzo, F., Laiolo, L., Vergni, P., Pasquini, L., Levy, O., Zaccanti, F., Tribollet, A., Dubinsky, Z., Falini, G., 2012. The puzzling presence of calcite in skeletons of modern solitary corals from the Mediterranean Sea. Geochim. Cosmochim. Acta 85, 187–199. https://doi.org/10.1016/j.gca.2012.02.014.

Goffredo, S., Prada, F., Caroselli, E., Capaccioni, B., Zaccanti, F., Pasquini, L., Fantazzini, P., Fermani, S., Reggi, M., Levy, O., Fabricius, K.E., Dubinsky, Z., Falini, G., 2014. Biomineralization control related to population density under ocean acidification. Nat. Clim. Chang. 4, 593–597. https://doi.org/10.1038/nclimate2241.

Goffredo, S., Mancuso, A., Caroselli, E., Prada, F., Dubinsky, Z., Falini, G., Levy, O., Fantazzini, P., Pasquini, L., 2015. Skeletal mechanical properties of Mediterranean corals along a wide latitudinal gradient. Coral Reefs 34, 121–132. https://doi.org/10.1007/s00338-014-1222-6.

Gonçalves, R., Scholze, M., Ferreira, A.M., Martins, M., Correia, A.D., 2008. The joint effect of polycyclic aromatic hydrocarbons on fish behavior. Environ. Res. 108, 205–213. https://doi.org/10.1016/j.envres.2008.07.008.

Grimalt, S., Dehouck, P., 2016. Review of analytical methods for the determination of pesticide residues in grapes. J. Chromatogr. A 1433, 1–23. https://doi.org/10.1016/j.chroma.2015.12.076.

Guerranti, C., Grazioli, E., Focardi, S., Renzi, M., Perra, G., 2016. Levels of chemicals in two fish species from four Italian fishing areas. Mar. Pollut. Bull. 111, 449–452. https://doi.org/10.1016/j.marpolbul.2016.07.002.

Gust, K.A., Najar, F.Z., Habib, T., Lotufo, G.R., Piggot, A.M., Fouke, B.W., Laird, J.G., Wilbanks, M.S., Rawat, A., Indest, K.J., Roe, B.A., Perkins, E.J., 2014. Coral-zooxanthellae metatranscriptomics reveals integrated response to pollutant stress. BMC Genomics 15, 591. https://doi.org/10.1186/1471-2164-15-591.

Guzmán Martínez, M.D.C., Ramírez Romero, P., Banaszak, A.T., 2007. Photoinduced toxicity of the polycyclic aromatic hydrocarbon, fluoranthene, on the coral, *Porites*

divaricata. J Environ Sci Health Part A 42, 1495–1502. https://doi.org/10.1080/10934520701480946.

Guzmán, H.M., Jackson, J.B., Weil, E., 1991. Short-term ecological consequences of a major oil-spill on Panamanian subtidal reef corals. Coral Reefs 10, 1–12. https://doi.org/10.1007/BF00301900.

Hambleton, E.A., Jones, V.A.S., Maegele, I., Kvaskoff, D., Sachsenheimer, T., Guse, A., 2019. Sterol transfer by atypical cholesterol-binding NPC2 proteins in coral-algal symbiosis. Elife 8, e43923. https://doi.org/10.7554/eLife.43923.

Han, M., Zhang, R., Yu, K., Li, A., Wang, Y., Huang, X., 2020. Polycyclic aromatic hydrocarbons (PAHs) in corals of the South China Sea: occurrence, distribution, bioaccumulation, and considerable role of coral mucus. J. Hazard. Mater. 384, 121299. https://doi.org/10.1016/j.jhazmat.2019.121299.

Hsieh, H.-Y., Huang, K.-C., Cheng, J.-O., Lo, W.-T., Meng, P.-J., Ko, F.-C., 2019. Environmental effects on the bioaccumulation of PAHs in marine zooplankton in Gaoping coastal waters, Taiwan: concentration, distribution, profile, and sources. Mar. Pollut. Bull. 144, 68–78. https://doi.org/10.1016/j.marpolbul.2019.04.048.

Iannelli, R., Bianchi, V., Macci, C., Peruzzi, E., Chiellini, C., Petroni, G., Masciandaro, G., 2012. Assessment of pollution impact on biological activity and structure of seabed bacterial communities in the Port of Livorno (Italy). Sci. Total Environ. 426, 56–64. https://doi.org/10.1016/j.scitotenv.2012.03.033.

IARC, 2018. List of Classifications. vols. volumes 1–123. https://monographs.iarc.fr/list-of-classifications-volumes/. (Accessed 5 November 2018).

ICH 5 AD, 2005. Harmonized Tripartite Guideline, Validation of Analytical Procedure: Text and Methodologies, Q2(R1), Current Step 4 Version. Parent Guidelines on Methodology Dated November 6 1996, Incorporated in November 2005.

IPCC (2019) IPCC Special Report on the Ocean and Cryosphere in a Changing Climate. Pörtner H-O, Roberts DC, Masson-Delmotte V, Zhai P, Tignor M, Poloczanska E, Mintenbeck K, Alegría A, Nicolai M, Okem A, Petzold J, Rama B, Weyer NM (eds.). (In press).

Isa, Y., Okazaki, M., 1987. Some observations on the Ca^{2+}-binding phospholipids from scleractinian coral skeletons. Comp Biochem Phys B 87, 507–512.

Kennedy, C., Gassman, N., Walsh, P., 1992. The fate of benzo [a] pyrene in the scleractinian corals *Favia fragum* and *Montastrea annularis*. Mar. Biol. 113, 313–318. https://doi.org/10.1007/BF00347286.

Kim, G.B., Maruya, K.A., Lee, R.F., Lee, J.-H., Koh, C.-H., Tanabe, S., 1999. Distribution and sources of polycyclic aromatic hydrocarbons in sediments from Kyeonggi Bay, Korea. Mar Poll Bull 38, 7–15. https://doi.org/10.1016/S0025-326X(99)80006-X.

Kim, L., Lee, D., Cho, H.K., Choi, S.D., 2019. Review of the QuEChERS method for the analysis of organic pollutants: persistent organic pollutants, polycyclic aromatic hydrocarbons, and pharmaceuticals. Trends Environ Anal Chem 22, e00063. https://doi.org/10.1016/j.teac.2019.e00063.

Ko, F.-C., Chang, C.-W., Cheng, J.-O., 2014. Comparative study of polycyclic aromatic hydrocarbons in coral tissues and the ambient sediments from Kenting National Park, Taiwan. Environ. Pollut. 185, 35–43. https://doi.org/10.1016/j.envpol.2013.10.025.

Krueger, T., Bodin, J., Horwitz, N., Loussert-Fonta, C., Sakr, A., Escrig, S., Fine, M., Meibom, A., 2018. Temperature and feeding induce tissue level changes in autotrophic and heterotrophic nutrient allocation in the coral symbiosis - a NanoSIMS study. Sci. Rep. 8, 12710. https://doi.org/10.1038/s41598-018-31094-1.

Lawal, A.T., 2017. Polycyclic aromatic hydrocarbons. A review. Cogent Environ Sci 71, 1–89. https://doi.org/10.1080/23311843.2017.1339841.

Lazzari, N., Becerro, M.A., Sanabria-Fernandez, J.A., Martín-López, B., 2019. Spatial characterization of coastal marine social-ecological systems: insights for integrated management. Environ. Sci. Pol. 92, 56–65. https://doi.org/10.1016/j.envsci.2018.11.003.

León, V.M., Moreno-González, R., González, E., Martinez, F., García, V., Campillo, J.A., 2013. Interspecific comparison of polycyclic aromatic hydrocarbons and persistent organochlorines bioaccumulation in bivalves from a Mediterranean coastal lagoon. Sci. Total Environ. 463-464, 975–987. https://doi.org/10.1016/j.scitotenv.2013.06.075.

Leonards, P.E., van Hattum, B., Leslie, H., 2008. Assessing the risks of persistent organic pollutants to top predators: a review of approaches. Integr Environ Asses 4, 386–398. https://doi.org/10.1897/IEAM_2008-008.1.

Li, Y.L., Wang, C.L., Zou, X.Q., Feng, Z.Y., Yao, Y.L., Wang, T., Zhang, C.C., 2019. Occurrence of polycyclic aromatic hydrocarbons (PAHs) in coral reef fish from the South China Sea. Mar. Pollut. Bull. 139, 339–345. https://doi.org/10.1016/j.marpolbul.2019.01.001.

Lin, T., Hu, L., Guo, Z., Zhang, G., Yang, Z., 2013. Deposition fluxes and fate of polycyclic aromatic hydrocarbons in the Yangtze River estuarine-inner shelf in the East China Sea. Global Biogeochem Cy 27, 77–87. https://doi.org/10.1029/2012GB004317.

Little, E.E., Finger, S.E., 1990. Swimming behavior as an indicator of sublethal toxicity in fish. Environ. Toxicol. Chem. 9, 13–19. https://doi.org/10.1002/etc.5620090103.

Marini, M., Frapiccini, E., 2013. Persistence of polycyclic aromatic hydrocarbons in sediments in the deeper area of the Northern Adriatic Sea (Mediterranean Sea). Chemosphere 90, 1839–1846. https://doi.org/10.1016/j.chemosphere.2012.09.080.

Mashroofeh, A., Bakhtiari, A.R., Pourkazemi, M., 2015. Distribution and composition pattern of polycyclic aromatic hydrocarbons in different tissues of sturgeons collected from Iranian coastline of the Caspian Sea. Chemosphere 120, 575–583. https://doi.org/10.1016/j.chemosphere.2014.09.071.

Mercogliano, R., Santonicola, S., De Felice, A., Anastasio, A., Murru, N., Ferrante, M.C., Cortesi, M.L., 2016. Occurrence and distribution of polycyclic aromatic hydrocarbons in mussels from the gulf of Naples, Tyrrhenian Sea, Italy. Mar. Pollut. Bull. 104, 386–390. https://doi.org/10.1016/j.marpolbul.2016.01.015.

Minier, C., Moore, M.N., Galgani, F., Claisse, D., 2006. Multixenobiotic resistance protein expression in *Mytilus edulis*, *M. galloprovincialis* and *Crassostrea gigas* from the French coasts. Mar. Ecol. Prog. Ser. 322, 143–154. https://doi.org/10.3354/meps322143.

Nácher-Mestre, J., Serrano, R., Portolés, T., Berntssen, M.H.G., Pérez-Sánchez, J., Hernández, F., 2014. Screening of pesticides and polycyclic aromatic hydrocarbons in feeds and fish tissues by gas chromatography coupled to high- resolution mass spectrometry using atmospheric pressure chemical ionization. J. Agric. Food Chem. 62, 2165–2174. https://doi.org/10.1021/jf405366n.

Neff, J.M., Stout, S.A., Gunster, D.G., 2005. Ecological risk assessment of polycyclic aromatic hydrocarbons in sediments: identifying sources and ecological hazard. Integr Environ Asses 1, 22–23. https://doi.org/10.1897/IEAM_2004a-016.1.

Nordborg, F.M., Flores, F., Brinkman, D.L., Agustí, S., Negri, A.P., 2018. Phototoxic effects of two common marine fuels on the settlement success of the coral *Acropora tenuis*. Sci. Rep. 8, 8635. https://doi.org/10.1038/s41598-018-26972-7.

Overmans, S., Nordborg, M., Díaz-Rúa, R., Brinkman, D.L., Negri, A.P., Agustí, S., 2018. Phototoxic effects of PAH and UVA exposure on molecular responses and developmental success in coral larvae. Aquat. Toxicol. 198, 165–174. https://doi.org/10.1016/j.aquatox.2018.03.008.

Ozalp, B., Caroselli, E., Raimondi, F., Goffredo, S., 2018. Skeletal growth, morphology and skeletal parameters of a temperate, solitary and zooxanthellate coral along a depth gradient in the Dardanelles (Turkey). Coral Reefs 37, 633–646. https://doi.org/10.1007/s00338-018-1687-9.

Perugini, M., Visciano, P., Giammarino, A., Manera, M., di Nardo, W., Amorena, M., 2007. Polycyclic aromatic hydrocarbons in marine organisms from the Adriatic Sea, Italy. Chemosphere 66, 1904–1910. https://doi.org/10.1016/j.chemosphere.2006.07.079.

Porte, C., Albaige's, J., 1993. Bioaccumulation patterns of hydrocarbons and polychlorinated biphenyls in bivalves, crustaceans and fishes. Arch Environ Con Tox 26, 273–281. https://doi.org/10.1007/BF00203552.

Prada, F., Caroselli, E., Mengoli, S., Brizi, L., Fantazzini, P., Capaccioni, B., Pasquini, L., Fabricius, K.E., Dubinsky, Z., Falini, G., Goffredo, S., 2017. Ocean warming and acidification synergistically increase coral mortality. Sci. Rep. 7, 40842. https://doi.org/10.1038/srep40842.

Radice, V.Z., Brett, M.T., Fry, B., Fox, M.D., Hoegh-Guldberg, O., Dove, S.G., 2019. Evaluating coral trophic strategies using fatty acid composition and indices. PLoS One 14, e0222327. https://doi.org/10.1371/journal.pone.0222327.

Rahmanpour, S., Farzaneh Ghorghani, N., Lotfi Ashtiyani, S.M., 2014. Polycyclic aromatic hydrocarbon (PAH) in four fish species from different trophic levels in the Persian Gulf. Environ. Monit. Assess. 186, 7047–7053. https://doi.org/10.1007/s10661-014-3909-0.

Ramalhosa, M.J., Paíga, P., Morais, S., Delerue-Matos, C., Oliveira, M.B.P.P., 2009. Analysis of polycyclic aromatic hydrocarbons in fish: evaluation of a quick, easy, cheap, effective, rugged, and safe extraction method. J. Sep. Sci. 32, 3529–3538. https://doi.org/10.1002/jssc.200900351.

Ranjbar Jafarabadi, A., Riyahi Bakhtiari, A., Aliabadian, M., Laetitia, H., Shadmehri Toosi, A., Yap, C.K., 2018. First report of bioaccumulation and bioconcentration of aliphatic hydrocarbons (AHs) and persistent organic pollutants (PAHs, PCBs and PCNs) and their effects on alcyonacea and scleractinian corals and their endosymbiotic algae from the Persian Gulf, Iran: inter and intra-species differences. Sci. Total Environ. 627, 141–157. https://doi.org/10.1016/j.scitotenv.2018.01.185.

Readman, J., Tolosa, I., Law, A., Bartocci, J., Azemard, S., Hamilton, T., Mee, L., Wagener, A., Le Tissier, M., Roberts, C., 1996. Discrete bands of petroleum hydrocarbons and molecular organic markers identified within massive coral skeletons. Mar. Pollut. Bull. 32, 437–443. https://doi.org/10.1016/0025-326X(96)83974-9.

Reggi, M., Fermani, S., Landi, V., Sparla, F., Caroselli, E., Gizzi, F., Dubinsky, Z., Levi, O., Cuif, J.P., Dauphin, Y., Goffredo, S., Falini, G., 2014. Biomineralization in Mediterranean corals: the role of the intra-skeletal organic matrix. Cryst. Growth Des. 14, 4310–4320. https://doi.org/10.1021/cg5003572.

Reggi, M., Samori, C., Fermani, S., Gizzi, F., Prada, F., Dubinsky, Z., Goffredo, S., Falini, G., 2016. Influence of intra-skeletal coral lipids on calcium carbonate precipitation. CrystEngComm 18, 8829–8833. https://doi.org/10.1039/C6CE01939K.

Rocha, A.C., Palma, C., 2019. Source identification of polycyclic aromatic hydrocarbons in soil sediments: application of different methods. Sci. Total Environ. 652, 1077–1089. https://doi.org/10.1016/j.scitotenv.2018.10.014.

Samorì, C., Caroselli, E., Prada, F., Reggi, M., Fermani, S., Dubinsky, Z., Goffredo, S., Falini, G., 2017. Ecological relevance of skeletal fatty acid concentration and composition in Mediterranean scleractinian corals. Sci. Rep. 7, 1929. https://doi.org/10.1038/s41598-017-02034-2.

Santana, M.S., Sandrini-Neto, L., Filipak Neto, F., Oliveira Ribeiro, C.A., Di Domenico, M., 2018. Biomarker responses in fish exposed to polycyclic aromatic hydrocarbons (PAHs): systematic review and meta-analysis. Environ. Pollut. 242, 449–461. https://doi.org/10.1016/j.envpol.2018.07.004.

Schulte, P.M., 2007. Responses to environmental stressors in an estuarine fish: interacting stressors and the impacts of local adaptation. J. Therm. Biol. 32, 152–161. https://doi.org/10.1016/j.jtherbio.2007.01.012.

Solé, M., Manzanera, M., Bartolomé, A., Tort, LI, Caixach, J., 2013. Persistent organic pollutants (POPs) in sediments from fishing grounds in the NW Mediterranean: ecotoxicological implications for the benthic fish *Solea* sp. Mar. Pollut. Bull. 67, 158–165. https://doi.org/10.1016/j.marpolbul.2012.11.018.

Sun, R.X., Sun, Y., Li, Q.X., Zheng, X., Luo, X., Mai, B., 2018. Polycyclic aromatic hydrocarbons in sediments and marine organisms: implications of anthropogenic effects on the coastal environment. Sci. Total Environ. 640-641, 264–272. https://doi.org/10.1016/j.scitotenv.2018.05.320.

Sverdrup, L.E., Nielsen, T., Krogh, P.H., 2002. Soil ecotoxicity of polycyclic aromatic hydrocarbons in relation to soil sorption, lipophilicity and water solubility. Environ Sci Technol 36, 2429–2435. https://doi.org/10.1021/es010180s.

Thomas, S.D., Li, Q.X., 2000. Immunoaffinity chromatography for analysis of polycyclic aromatic hydrocarbons in corals. Environ Sci Technol 34, 2649–2654. https://doi.org/10.1021/es991069d.

Thompson, K.L., Picard, C.R., Chan, H.M., 2017. Polycyclic aromatic hydrocarbons (PAHs) in traditionally harvested bivalves in northern British Columbia, Canada. Mar. Pollut. Bull. 121, 390–399. https://doi.org/10.1016/j.marpolbul.2017.06.018.

Vargas-Yáñez, M., Jesús García, M., Salat, J., García-Martínez, M.C., Pascual, J., Moya, F., 2008. Warming trends and decadal variability in the Western Mediterranean shelf. Glob. Planet. Chang. 63, 177–184. https://doi.org/10.1016/j.gloplacha.2007.09.001.

Wan, Y., Jin, X., Hu, J., Jin, F., 2007. Trophic dilution of polycyclic aromatic hydrocarbons (PAHs) in a marine food web from Bohai Bay, north China. Environ Sci Technol 41, 3109–3114. https://doi.org/10.1021/es062594x.

Wang, J.Z., Guan, Y.F., Ni, H.G., Luo, X.L., Zeng, E.Y., 2007. Polycyclic aromatic hydrocarbons in riverine runoff of the Pearl River Delta (China): concentrations, fluxes, and fate. Environ Sci Technol 41, 5614–5619. https://doi.org/10.1021/es070964r.

Wang, C.L., Zou, X.Q., Li, Y.L., Zhao, Y.F., Song, Q.C., Yu, W.W., 2017. Pollution levels and risks of polycyclic aromatic hydrocarbons in surface sediments from two typical estuaries in China. Mar. Pollut. Bull. 114, 917–925. https://doi.org/10.1016/j.marpolbul.2016.11.027.

Wild, C., Rasheed, M., Werner, U., Franke, U., Johnstone, R., Huettel, M., 2004. Degradation and mineralization of coral mucus in reef environments. Mar. Ecol. Prog. Ser. 267, 159–171. https://doi.org/10.3354/meps267159.

Woo, S., Lee, A., Denis, V., Chen, C.A., Yum, S., 2014. Transcript response of soft coral (*Scleronephthya gracillimum*) on exposure to polycyclic aromatic hydrocarbons. Environ. Sci. Pollut. Res. 21, 901–910. https://doi.org/10.1007/s11356-013-1958-5.

Yang, T., Cheng, H., Wang, H., Drews, M., Li, S., Huang, W., Zhou, H., Chen, C.M., Diao, X., 2019. Comparative study of polycyclic aromatic hydrocarbons (PAHs) and heavy metals (HMs) in corals, surrounding sediments and surface water at the Dazhou Island, China. Chemosphere 218, 157–168. https://doi.org/10.1016/j.chemosphere.2018.11.063.

Yunker, M.B., Macdonald, R.W., Vingarzan, R., Mitchell, R.H., Goyette, D., Sylvestre, S., 2002. PAHs in the Fraser River basin: a critical appraisal of PAH ratios as indicators of PAH source and composition. Org. Geochem. 33, 489–515. https://doi.org/10.1016/S0146-6380(02)00002-5.

Zanaty, M.I., Sawada, N., Kitani, Y., Nassar, H.F., Mahmoud, H.M., Hayakawa, K., Sekiguchi, T., Ogiso, S., Tabuchi, Y., Urata, M., Matsubara, H., Takeuchi, Y., Hattori, A., Srivastav, A.K., Amornsakun, T., Suzuki, N., 2020. Influence of benz[a]anthracene on bone metabolism and on liver metabolism in nibbler fish, *Girella punctata*. Int. J. Environ. Res. Public Health 17, E1391. https://doi.org/10.3390/ijerph17041391.

Zhang, R., Yu, K., Li, A., Wang, Y., Huang, X., 2019. Antibiotics in corals of the South China Sea: occurrence, distribution, bioaccumulation, and considerable role of coral mucus. Environ. Pollut. 250, 503–510. https://doi.org/10.1016/j.envpol.2019.04.036.

Zhang, C., Li, Y., Wang, C., Feng, Z., Hao, Z., Yu, W., Wang, T., Zou, X., 2020. Polycyclic aromatic hydrocarbons (PAHs) in marine organisms from two fishing grounds, South Yellow Sea, China: bioaccumulation and human health risk assessment. Mar. Pollut. Bull. 153, 110995. https://doi.org/10.1016/j.marpolbul.2020.110995.

Zibrowius, H., 1980. Les scleractiniaires de la Mediterraee et de l'Atlantique nord-oriental. Mem Inst Oceanogr Monaco 11, 1–284.

Ziyaadini, M., Mehdinia, A., Khaleghi, L., Nasiri, M., 2016. Assessment of concentration, bioaccumulation and sources of polycyclic aromatic hydrocarbons in zooplankton of Chabahar Bay. Mar. Pollut. Bull. 107, 408–412. https://doi.org/10.1016/j.marpolbul.2016.02.045.

Supplementary Material for

Accumulation of PAHs in the tissues and algal symbionts of a common Mediterranean coral: Skeletal storage relates to population age structure. Science of The Total Environment

Erik Caroselli, Emanuela Frapiccini, Silvia Franzellitti ,QuinziaPalazzo, Fiorella Prada, Mattia Betti, Stefano Goffredo, Mauro Marini

SUPPLEMENTARY TABLES

Supplementary Table 1 Age and PAH concentration (µg g^{-1} dry weight, d.w.) data in the three biological compartments of each sample of *B. europaea.* Samples are arranged in increasing age order.

Sample code	Age	Biological compartment	acenaphtene (µg g^{-1} d.w.)	fluorene (µg g^{-1} d.w.)	fluoranthene (µg g^{-1} d.w.)	pyrene (µg g^{-1} d.w.)
		skeleton	0.160	0.275	0.011	0.034
BEU_22	6.3	tissue	0.123	0.382	0.011	0.063
		zooxanthellae	0.992	1.265	0.037	0.098
		skeleton	0.119	0.380	0.012	0.054
BEU_20	8.0	tissue	0.125	0.538	0.024	0.134
		zooxanthellae	0.456	3.967	0.036	0.151
		skeleton	0.086	0.329	0.007	0.014
BEU_10	8.4	tissue	0.169	0.665	<LOQ	0.030
		zooxanthellae	0.208	0.677	0.122	0.535
		skeleton	0.150	0.008	0.002	0.051
BEU_18	9.2	tissue	0.209	0.158	0.009	0.049
		zooxanthellae	1.117	1.642	0.088	0.365
		skeleton	0.230	0.108	0.010	0.044
BEU_15	9.4	tissue	0.117	0.554	0.031	0.146
		zooxanthellae	2.636	3.700	0.149	2.005
		skeleton	0.537	0.339	0.013	0.054
BEU_16	9.6	tissue	0.267	0.781	<LOQ	0.023
		zooxanthellae	0.974	1.541	0.083	0.268
		skeleton	0.182	0.280	0.006	0.021
BEU_17	10.2	tissue	0.252	0.856	0.101	0.031
		zooxanthellae	1.983	5.183	0.710	2.105
		skeleton	0.098	0.046	0.004	0.026
BEU_09	10.2	tissue	0.093	0.248	0.064	0.531
		zooxanthellae	0.438	1.202	0.257	1.127
		skeleton	0.134	0.114	0.011	0.056
BEU_08	10.3	tissue	<LOQ	0.072	0.131	0.175
		zooxanthellae	0.065	1.271	0.075	0.254
		skeleton	0.114	0.119	0.007	0.035
BEU_14	10.6	tissue	0.123	0.388	0.101	0.523
		zooxanthellae	1.518	2.622	0.242	0.846
		skeleton	0.127	0.214	0.010	0.034
BEU_12	10.8	tissue	0.992	2.255	0.057	0.247
		zooxanthellae	0.138	0.936	0.394	1.300
		skeleton	0.089	0.411	0.006	0.024
BEU_19	11.2	tissue	0.530	1.647	0.035	0.202
		zooxanthellae	1.116	2.525	0.200	0.797
		skeleton	0.170	0.204	0.009	0.030
BEU_11	13.8	tissue	1.853	3.035	0.057	0.263
		zooxanthellae	0.144	0.646	0.145	0.745

LOQ: limit of quantification

Supplementary Table 2 Results of the comparative PERMANOVA pairwise tests between PAHs within each biological compartment of *B. europaea* (999 permutations).

PAHs	Skeleton		Tissue		Zooxanthellae	
	t	P	t	P	t	P
acenaphthene *vs* fluorene	0.957	0.342	1.852	0.078	2.504	**0.023**
acenaphthene *vs* fluoranthene	5.141	**0.001**	2.273	**0.025**	3.198	**0.006**
acenaphthene *vs* pyrene	4.217	**0.001**	1.263	0.230	0.418	0.666
fluorene *vs* fluoranthene	5.629	**0.001**	3.476	**0.002**	4.595	**0.002**
fluorene *vs* pyrene	4.844	**0.001**	2.875	**0.008**	2.879	**0.014**
fluoranthene *vs* pyrene	7.355	**0.001**	3.340	**0.001**	3.294	**0.005**

t: t-Statistics; P: significance of t with Monte Carlo correction. Statistically significant values are in bold ($P < 0.05$).

Supplementary Table 3 Results of the comparative PERMANOVA pairwise tests between biological compartments within each PAH of *B. europaea* (999 permutations).

Biological compartments	acenaphthene		fluorene		fluoranthene		pyrene	
	t	P	t	P	t	P	t	P
Skeleton *vs* Tissue	1.320	0.193	2.704	**0.015**	5.008	**0.001**	3.592	**0.002**
Skeleton *vs* Zooxanthellae	3.295	**0.004**	4.525	**0.001**	4.059	**0.001**	4.226	**0.002**
Tissue *vs* Zooxanthellae	2.126	0.053	2.590	**0.013**	3.182	**0.004**	3.366	**0.004**

t: t-Statistics; P: significance of t with Monte Carlo correction. Significant differences are indicated in bold.

Supplementary Table 4 Results of the PERMANOVA pairwise tests for acenaphthene, fluorene and pyrene between biological compartments of *B. europaea* (999 permutations).

Biological compartments	acenaphthene		fluorene		pyrene	
	t	P	t	P	t	P
Skeleton *vs* Tissue	1.320	0.192	2.704	**0.017**	3.592	**0.005**
Skeleton *vs* Zooxanthellae	3.295	**0.004**	4.525	**0.001**	4.226	**0.002**
Tissue *vs* Zooxanthellae	2.126	**0.033**	2.590	**0.025**	3.366	**0.005**

t: t-Statistics; P: significance of t with Monte Carlo correction. Significant differences are indicated in bold.

Supplementary Table 5 Results of the PERMANOVA pairwise tests for fluoranthene between age classes within biological compartments and between biological compartments within age classes of *B. europaea* (999 permutations).

Age classes	Skeleton		Tissue		Zooxanthellae	
	t	P	t	P	t	P
Adult *vs* Old	0.839	0.415	4.493	**0.001**	2.308	**0.045**

Biological compartments	Adults		Olds	
	t	P	t	P
Skeleton *vs* Tissue	0.611	0.549	5.522	**0.001**
Skeleton *vs* Zooxanthellae	4.126	**0.004**	3.537	**0.006**
Tissue *vs* Zooxanthellae	3.821	**0.008**	2.620	0.023

t: t-Statistics; P: significance of t with Monte Carlo correction. Significant differences are indicated in bold.

Supplementary Table 6 Life table estimating the mass of each of the four pollutants stored in the skeletons of *B. europaea* in 1 m^2 of the Calafuria population at 6 m depth.

Coral age (yr), *t*	**Coral mean length (mm), L_t**	**Coral skeletal mass (g), M_t**	**Coral skeletal OM mass (g), $M_{OM(t)}$**	**Number of corals per m^{-2}, N_t**	**Cumulative OM mass per m^{-2} (g)**	**acenaphthene per m^{-2} (ng)**	**fluorene per m^{-2} (ng)**	**fluoranthene per m^{-2} (ng)**	**pyrene per m^{-2} (ng)**
0	1.1	0.002	0.00007	6.994	0.0005	0.08	0.11	0.004	0.02
1	3.2	0.036	0.00103	5.313	0.0055	0.93	1.20	0.046	0.20
2	5.1	0.114	0.00332	4.035	0.0134	2.28	2.94	0.113	0.50
3	6.8	0.236	0.00684	3.065	0.0210	3.57	4.62	0.177	0.78
4	8.4	0.393	0.01139	2.328	0.0265	4.51	5.83	0.223	0.98
5	9.7	0.576	0.01670	1.768	0.0295	5.02	6.50	0.249	1.09
6	10.9	0.777	0.02253	1.343	0.0303	5.15	6.66	0.255	1.12
7	12.0	0.989	0.02867	1.020	0.0293	4.97	6.44	0.246	1.08
8	13.0	1.205	0.03495	0.775	0.0271	4.60	5.96	0.228	1.00
9	13.9	1.421	0.04121	0.589	0.0243	4.12	5.34	0.204	0.90
10	14.6	1.633	0.04735	0.447	0.0212	3.60	4.66	0.178	0.78
11	15.3	1.838	0.05329	0.340	0.0181	3.08	3.98	0.152	0.67
12	16.0	2.034	0.05898	0.258	0.0152	2.59	3.35	0.128	0.56
13	16.5	2.219	0.06436	0.196	0.0126	2.14	2.77	0.106	0.47
14	17.0	2.394	0.06942	0.149	0.0103	1.76	2.27	0.087	0.38
15	17.5	2.557	0.07415	0.113	0.0084	1.43	1.84	0.071	0.31
16	17.9	2.708	0.07854	0.086	0.0067	1.15	1.48	0.057	0.25
17	18.2	2.848	0.08261	0.065	0.0054	0.92	1.19	0.045	0.20
18	18.6	2.977	0.08635	0.050	0.0043	0.73	0.94	0.036	0.16
19	18.9	3.096	0.08978	0.038	0.0034	0.57	0.74	0.028	0.13
20	19.1	3.201	0.09282	0.029	0.0027	0.45	0.58	0.022	0.10
					Total PAH amount	**53.6**	**69.4**	**2.7**	**11.7**

Supplementary Table 7 Comparison of determined PAH concentration (wet weight basis) between QuEChERS and accelerated solvent extraction (ASE) methods for SRM NIST 1974c[a].

PAH	Certified/reference NIST 1974c	QuEChERS method		ASE method	
	value, ng g^{-1} ± SD	Measured value, ng g^{-1} ± SD, n = 4	% Accuracy (RSD, %) n = 4	Measured value, ng g^{-1} ± SD, n = 4	% Accuracy (RSD, %) n = 4
acenaphthene	0.343 ± 0.019	0.319 ± 0.068	93 (21)	0.311 ± 0.072	91 (23)
fluorene	2.31 ± 0.04	2.27 ± 0.28	98 (12)	2.17 ± 0.33	94 (15)
fluoranthene	45.3 ± 0.8	45.5 ± 2.7	100 (6)	45.9 ± 0.9	101 (2)
pyrene	23.9 ± 1.6	22.6 ± 2.0	94 (9)	23.0 ± 1.4	96 (6)

[a]https://www-s.nist.gov/m-srmors/certificates/1974C.pdf

SUPPLEMENTARY FIGURE

Supplementary Figure 1 Chromatograms of a blank, skeleton, tissue, and zooxanthellae sample, obtained by UHPLC-FLD at 325 mn. 1: acenaphthene; 2: fluorene; 3: fluoranthene; 4: pyrene)

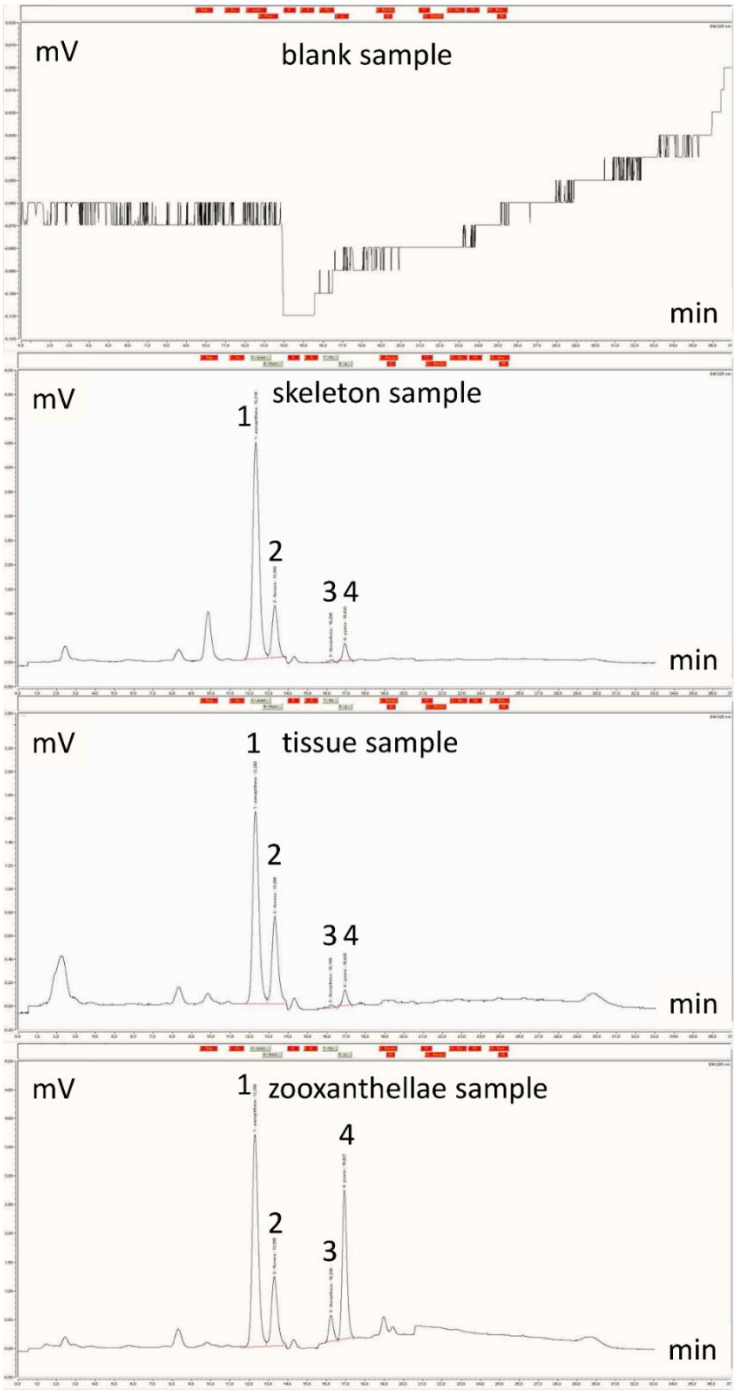

Chapter 7. Conclusion and future perspective

The overall view of my thesis highlights the myriad of valuable contribution that calcium carbonate organism can provide at multidisciplinary and multiscale levels. Therefore, an integrated approach, that aims to study the connection among functionalities of biomineralized materials, their properties, and the influence of the environment in modelling and altering their characteristics, may advance in understanding the physical, chemical, and biological properties of marine organisms, their ecology, and the ecosystems. Furthermore, looking to the future of marine biotechnologies, a detailed understanding of the organic–mineral relationships, of the biominerals properties and their structure–function relations will provide new insights in the development of new and promising approaches in engineering, fisheries research, biology, and medicine.

Concerning the first session of this thesis "Structure-function relationship in otolith", the preliminary results of the investigations performed during my PhD have revealed interesting differences in otoliths from individuals of different sizes and genders that can have an adaptive and functional role in the perception of sounds. In particular, the analysis of micro-CT scans highlighted morphological differences between sexually undifferentiated samples and individuals of different sex. Based on the outcomes of the previous investigation, future perspective will aim to explore the acoustical implication of otolith variability and to establish the shape/structure–function relationships in otoliths during fish ontogenesis and between genders. In detail, through a programmatic approach, the goal of the next research is to unravel the following challenging issue: What is the effect of otolith shape and density on its displacement? How do otolith structural features influence its response to sound stimuli? To this end, virtual experiments of vibroacoustic will be conduct in the Structural Engineering Department at the University of California, San Diego, a centre with expertise in virtual experiments in marine bioacoustics. The hosting research group has been long interested in bioacoustics simulations in fishes. Indeed, through the development of a methodology that combines X-ray CT scans with tissue elasticity measurements and finite-element modelling software (VATk) developed, they have provided significant insights and discoveries in the last decade. Additional software tools have since been developed. And so, in order to determine the effect that otolith shape might have on otolith motion, two sets of simulations will be run using a suite of software tools. In the first simulations (Extracted Otoliths Simulations), we will extract the shapes of the otoliths from high-resolution micro-CT scans of the *Merluccius merluccius*. These otoliths would be assigned uniform calcareous material properties, immersed in a simulated shear-soft jelly, and exposed to planar harmonic waves of different stimulus frequencies and directions. In the second set of simulations (Simplified Otolith Simulations), we will compare the responses of "simplified otolith shapes" with the results of the Extracted Otoliths Simulations. In this second simulation, we will use two simple shapes, a "spherical otolith" and a "hemispherical otolith." Another point that will be considered in using the finite element model is the

validation process to tests the veracity of the model by comparing virtual simulations to actual experimental results. The result expected from the future research are the following: 1) to formulate a three-dimensional description of the motion patterns from otolith micro-CT scans by applying a "virtual sound tomography" and 2) investigate whether there are any differences in the otolith response to sound waves which could bring a significance in a certain habitat or improve fish communication in specific contexts. In conclusion, the implementation of a vibroacoustic model to otoliths previously investigated in their structural and morphological characteristics will allow us to shed light on the functional and ecological significance of the juvenile/adults and females/males otolith differences highlighted in my PhD research so far. Furthermore, another implementation to this research which could be applied in future studies concerns the sampling collection. In fact, little is known about the genetic structuring of *Merluccius merluccius* in the center western Adriatic Sea. Therefore, further spatial, and temporal studies are needed to better elucidate the otolith intra-population variability in the genus *Merluccius merluccius* in this area. Future sampling could be carried out in different regions and/or during different periods to check whether there are some modifications in the otolith structures due to variations in the distribution of energy dedicated to the growth of otolith and/or water chemistry which may affect the shape and composition of the otolith, or whether the otolith is homogeneous between European hake stocks of different regions or periods.

Concerning the second session "Adaptation and acclimatation in coral skeletons", interesting results revealed that in corals, the onset of new trophic strategies and a shift in the metabolism triggered by changes in environment conditions, might have left a fingerprint on the skeletal structural features. Indeed, significant changes in skeletal phenotype have been found in the skeletal features of azooxanthellate vs zooxanthellate species of the genus Balanophyllia. However, further studies under controlled conditions of lighting and nutrient supply in aquaria are needed to confirm this conclusion. In this section, a multi-species study has been presented too. Here the results showed that the combination of different environmental conditions can have a stronger effect on macro-scale skeletal parameters than average low pH values alone. These findings revealed a common phenotypic response among three zooxanthellate corals which all displayed a more porous skeletal phenotype under ocean acidification (OA) but also highlighted that OA is not always the main driver and that other local environmental conditions likely interacted with OA to determine the observed responses. More generally, these findings remarked the importance of using a multi-parameter and multispecies analysis when investigating the vulnerability of coral species to OA, to understand what induces corals in a certain environment to acclimatize, and whether other species under the same conditions have the same capacity to adjust to future changes.

In the last section “Bioaccumulation of organic pollutants in corals” has been evaluated the sources, the accumulation and potentially effects of organic pollutants in a Mediterranean widespread Scleractinia corals species, providing the basis for further assessments of long-term sequestration of PAHs from the marine environment in the whole Mediterranean. Future research will aim to investigate the sources of the different accumulations in coral biological compartments and whether different physiology (younger *vs* adult individuals) or metabolism (mixotrophic *vs* heterotroph) may alter the concentration of PAHs.

In conclusion, the research of this thesis focused on two different biomineralization systems: fish otoliths and coral skeletons. While these two mineralized tissues are fundamentally different, their ontogenesis are determined and affected by external/environmental factors. The outputs of this work can be significant in advancing the understanding of how environmental factors, beyond the classical biological machinery directly involved in biomineralization, affects the formation and structure of mineralized tissues.

Appendix

Appendix 1

BioMet 2021 - XX Workshop on Pharmacobiometallics April 15 – 16, 2021

Multi-scale analysis of fish otolith ontogenesis reveals sexual dimorphism

Quinzia Palazzo[1,6], Marco Stagioni[2], Steven Raaijmakers[3], Robert G. Belleman[3], Fiorella Prada[4,6], Jörg U. Hammel[5], Jaap Kaandorp[3*], Stefano Goffredo[4,6*], Giuseppe Falini[1,6]*

[1] *Department of Chemistry <<Giacomo Ciamician>>, University of Bologna, Via Selmi 2, 40126 Bologna, Italy*
[2] *Laboratory of Fisheries and Marine Biology at Fano, Department of Biological, Geological and Environmental Sciences, University of Bologna, Viale Adriatico 1/N, 61032, Fano, Italy*
[3] *Computational Science Lab, University of Amsterdam, Science Park 904, 1098XH, Amsterdam, the Netherlands*
[4] *Marine Science Group, Department of Biological, Geological and Environmental Sciences, University of Bologna, Via Selmi 3, 40126 Bologna, Italy*
[5] *Institute of Materials Physics, Helmholtz-Zentrum Geesthacht, Max-Planck-Straße 1, Geesthacht, D-21502, Germany*
[6] *Fano Marine Center, The Inter-Institute Center for Research on Marine Biodiversity, Resources and Biotechnologies, Viale Adriatico 1/N 61032 Fano, Italy*

Corresponding authors: Jaap Kaandorp, J.A.Kaandorp@uva.nl;
Stefano Goffredo, s.goffredo@unibo.it;
Giuseppe Falini, giuseppe.falini@unibo.it

Otolith biomineralization results from biochemical processes regulated by the interaction of internal (physiological) and external (environmental) factors which leads to morphological and ultrastructural variability at intra- and inter-specific levels. Here we describe, for the first time, the relationship between multi-scale otolith parameters and fish somatic growth (i.e., total fish length), in juveniles, females, and males of *Merluccius merluccius* (European hake) from the western Adriatic Sea. We show that juvenile's otoliths had faster growth in length, width, area, perimeter, volume, weight and a higher amount of organic matter and trace element concentration compared to adult's otoliths. Secondly, with increasing fish length, female saccular otoliths contained a higher amount of protuberances compared to male specimens which showed more uniform mean curvature density. The differences between females and males highlighted in this study could be associated with the sexual dimorphism of sound-generating muscles (drumming muscles) previously observed in this species. Another possible explanation may be related to the detection of natural soundscapes to orient and navigate during migration towards spawning grounds. This discovery is of primary importance in the eco-zoological field suggesting that otolith shape can be used to explore the relationship between otolith features and fish ecological and behavioral patterns.

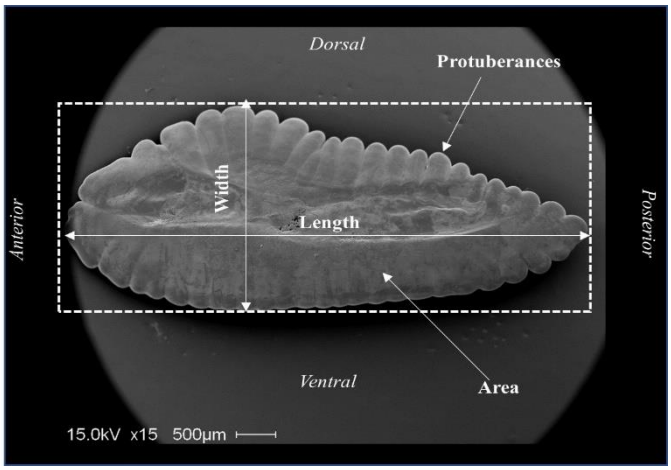

Figure. Otolith morphometrics viewed on a micrograph of proximal (inner) face of sagittal otolith of *Merluccius merluccius*.

Appendix 2

IUCr 2021 - XXV General Assembly and Congress of the International Union of Crystallography - August 14-22, 2021

Ecomorphological, behavioural and physiological patterns in otoliths

Q. Palazzo[1,6], M. Stagioni[2], S. Raaijmakers[3], R.G. Belleman[3], F. Prada[4,6], S. Fermani[1], J.U. Hammel[5], J. Kaandorp[3], S. Goffredo[4,6], G. Falini[1,6]

[1]Department of Chemistry "Giacomo Ciamician", University of Bologna, Via Selmi 2, 40126 Bologna, Italy, [2]Laboratory of Fisheries and Marine Biology at Fano, Department of Biological, Geological and Environmental Sciences, University of Bologna, Viale Adriatico 1/N, 61032, Fano, Italy, [3]Computational Science Lab, University of Amsterdam, Science Park 904, 1098XH, Amsterdam, the Netherlands, [4]Marine Science Group, Department of Biological, Geological and Environmental Sciences, University of Bologna, Via Selmi 3, 40126 Bologna, Italy, [5]Institute of Materials Physics, Helmholtz-Zentrum Geesthacht, Max-Planck-Straße 1, Geesthacht, D-21502, Germany, [6]Fano Marine Center, The Inter-Institute Center for Research on Marine Biodiversity, Resources and Biotechnologies, Viale Adriatico 1/N 61032 Fano, Italy

giuseppe.falini@unibo.it

Otolith biomineralization results from biochemical processes regulated by the interaction of internal (physiological) and external (environmental) factors which leads to morphological and ultrastructural variability at intra- and inter-specific levels [1]. Here, for the first time, we: 1) describe the relationship between multi-scale otolith parameters and fish somatic growth (i.e., total fish length) in juveniles, females, and males of Merluccius merluccius (European hake) from the western Adriatic Sea; 2) characterize the sulcus acusticus and its subregions (ostial colliculum, caudal colliculum and collum) and measured the corresponding area and volume; 3) reveal a sexual dimorphism in the morphology of otolith during ontogenesis. We show that juvenile's otoliths had faster growth in length, width, area, perimeter, volume, weight, a higher amount of organic matter and trace element concentration, a lower density (both micro-density and bulk-density), a higher porosity and a higher value of sulcus volume: otolith volume ratio (SV:OV) compared to adult's otoliths. Furthermore, the sexual dimorphism in the morphology of otolith during ontogenesis has been revealed for the first time through a novel 3D shape analysis approach based on micro-CT scans.

We found that, with increasing fish length, female saccular otoliths contained a higher amount of protuberances compared to male specimens which showed more uniform mean curvature density. The changes observed in the otolith features and sulcus acusticus regions during the growth could be linked to an eco-morphological adaptation to different biological, behavioral and environmental characteristics between juveniles and adults, which could have a functional meaning in terms of otolith response to sound waves (shape/structure–function relationships). In addition, the differences between females and males discovered in this study could be associated with fish hearing adaptation to reproductive behavioral strategies during the spawning season. Based on the outcomes of this first investigation, the use of innovative approaches is promising in highlighting differences in otoliths that could bring functional significance in specific ecological and behavioral contexts. Furthermore, the results obtained from this study can also provide inputs for further investigations aiming to understand otolith growth process according to fish size and gender and to explore the sources of otolith morphological variability during ontogenesis.

Future virtual experiments of vibroacoustic will be addressed in order to establish the shape/structure–function relationships in otoliths during fish ontogenesis and between sex and, consequently, investigate if there are any differences in the otolith response to sound waves which could enhance auditory abilities in a certain habitat or improve fish communication in specific contexts.

[1] Campana, S.E. (1992) Measurement and interpretation of the microstructure of fish otoliths. Canadian Special Publication of Fisheries and Aquatic Sciences, 117, 59-71.

Keywords: otolith; shape; morphology; physiological patterns; micro-CT

IUCr 2021 - XXV General Assembly and Congress of the International Union of Crystallography - August 14-22, 2021

ALMA MATER STUDIORUM UNIVERSITY OF BOLOGNA

Ecomorphological, behavioural and physiological patterns in otoliths

FishMed-PhD

Quinzia Palazzo[1] ,Marco Stagioni[2], Steven Raaijmakers[3], Robert G. Belleman[3], Fiorella Prada[4], Jörg U. Hammel[5], Jaap Kaandorp[3*], Stefano Goffredo[4*], Giuseppe Falini[1*]

[1]Univ. of Bologna, Dept of Chemistry & Fano Marine Center, Bologna, Italy, [2]Univ. of Bologna, BiGeA, Laboratory of Fisheries and Marine Biology at Fano, Italy, [3]Univ. of Amsterdam, Computational Science Lab, Amsterdam, Netherlands, [4]Univ. of Bologna, BiGeA, Mar Sci Group & Fano Marine Center, Fano, Italy, [5]Institute of Materials Physics, Helmholtz-Zentrum Geesthacht, Germany

OVERVIEW

Otolith biomineralization results from biochemical processes regulated by the interaction of internal (physiological) and external (environmental) factors which leads to morphological and ultrastructural variability at intra- and inter-specific levels. Here, for the first time, we: 1) describe the relationship between multi-scale sagittal otolith parameters and fish somatic growth (i.e., total fish length) in juveniles, females, and males of *Merluccius merluccius* (European hake) from the western Adriatic Sea; 2) present a method to characterize the 3D anatomical information of the otolith and sulcus acusticus from scans obtained by micro-CT imaging; 3) characterize the sulcus acusticus and its subregions (ostial colliculum, caudal colliculum and collum) and measure the corresponding area and volume;) reveal a sexual dimorphism in the morphology of otolith during ontogenesis.

HIGHLIGHTS

- Otolith 3D curvature, bulk density and crystallite size increased with fish length
- Faster growth in juveniles' otoliths
- Higher amount of organic matrix found in juveniles respect adults
- Ontogenetic variation in otolith microchemistry
- Sexual differences in otolith shape detected by a new 3D analysis based on micro-CT scans
- The ratio between the sulcus acusticus and otolith area (SA:OA) decreases during the ontogenesis, while no difference in the ratio between the sulcus and otolith volume (SV:OV) is revealed
- The relative area and volume of the sulcus acusticus subregions (ostial, collum and caudal) change during the ontogenesis.

MATERIALS AND METHODS

Juveniles (J) and adults (A) individuals of European hake (*Merluccius merluccius*) were collected in the western Adriatic Sea by local fishermen through commercial benthic trawlers, longlines and gillnets. The juvenile size class included individuals which do not have yet reached sexual maturity and have a total body length <15 cm, while the adult size class included (M) and (F) having a total body length 15-50 cm. The species object of this study is known to show a different spatial (bathymetric) distribution, induced by a change in trophic requirements during the ontogenesis, while no differences were highlighted in the spatial distribution between females and males [1-2]. (Fig. 1).

Data acquired and the methods used:

-Otolith biometry, morphology, and structural parameters (micro-density, bulk density and porosity): *Leica MZ6 light microscope, Buoyant weight technique by hydrostatic balance;*

-Otolith composition: *X-ray powder diffraction (XRD), Fourier transform infrared spectroscopic analysis (FTIR), Thermogravimetric analysis (TGA);*

-Otolith microchemistry: *Induced Coupling Plasma-Optical Emission Spectroscopy (ICP-OES);*

-Ultrastructure of otolith proximal surface: *Scanning Electron Microscopy (SEM) observations;*

- 3D morphological analysis of otoliths and sulcus acusticus based on microcomputed tomography: *High resolution microcomputed tomography (Micro-CT) scans.*

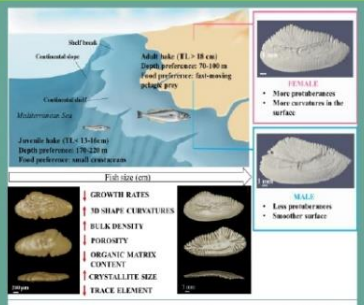

Figure 1 – Summary of the otolith's changes observed during the ontogenesis and between females and males in the Mediterranean *Merluccius merluccius*.

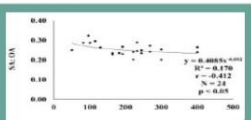

Figure 3 – Relationship between the ratios of computed surface area of sulcus (SA) and otolith area (OV) with fish length.

RESULTS

Juvenale's otoliths have faster growth in length, width, area, perimeter, volume, weight and a higher amount of organic matter and trace element concentration compared to adult's otoliths. With increasing fish length, female saccular otoliths contained a higher number of protuberances compared to male specimens which show more uniform mean curvature density (Fig. 1).

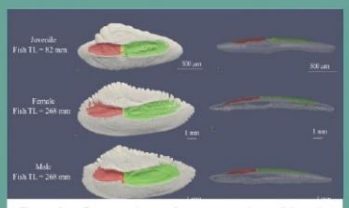

Figure 2 – Representative surface reconstructions of juvenile, female and male otolith and sulcus acusticus parts in xz-plane alignment (left) and yz-plane one (right) visualized with ParaView. The red part represents the ostial colliculum, the yellow region represents the collum (the central narrowing of the sulcus) and the green one is the caudal colliculum.

A stronger three-dimensional curvature of both otolith and sulcus acusticus is observed in adults respect juveniles (Fig. 2). Furthermore, during the ontogenesis there is a change in the relative ratio of area and volume of the sulcus acusticus sub-regions (Fig. 2).

The ratio between the sulcus acusticus and otolith area (SA:OA) decreases during the ontogenesis, while no difference in the ratio between the sulcus and otolith volume (SV:OV) is revealed (Fig. 3).

DISCUSSION AND CONCLUSIONS

The otolith's changes observed during the growth could be related to a mixture of effects reflecting endogenous processes such as development, and external conditions associated with changes in habitat, behaviour and diet. The sexual dimorphism in the morphology of otolith during ontogenesis discovered in this study could be associated with fish hearing adaptation to reproductive behavioral strategies during the spawning season. Furthermore, our study provides a new 3D approach to investigate the otolith and the sulcus acusticus that emphasizes features not revealed with the canonical methods based on 2D descriptors.

In conclusion, the results obtained from this study can provide inputs for further investigations aiming to understand otolith growth processes according to fish size and gender and to explore the sources of otolith morphological variability during ontogenesis.

REFERENCES

[1] Bartolino V, Ottavi A, Colloca F, Ardizzone GD, Stefánsson G. 2008 Bathymetric preferences of juvenile European hake (Merluccius merluccius). *ICES J. Mar. Sci.* **65**, 963–969.

[2] Stagioni M, Montanini S, Vallisneri M. 2011 Feeding Habits of European Hake, Merluccius Merluccius (Actinopterygii: Gadiformes: Merlucciidae), from the Northeastern Mediterranean Sea. *Acta Ichthyol. Piscat.* **41**, 277–284.

Appendix 3

14th International Coral Reef Symposium (ICRS) 2021 Virtual July 19 – 23, 2021

The skeleton of *Balanophyllia* coral species suggests adaptive traits linked to the onset of mixotrophy

Quinzia Palazzo[1,7,#], Fiorella Prada[2,7,#], Tim Steffens[3], Simona Fermani[1,8], Chiara Samorì[1], Giacomo Bernardi[4], Alexis Terrón-Sigler[5,9], Francesca Sparla[6,*], Giuseppe Falini[1,7,10,*], Stefano Goffredo[2,7,*]

[1] *Department of Chemistry <<Giacomo Ciamician>>, University of Bologna, Via Selmi 2, 40126 Bologna, Italy*
[2] *Marine Science Group, Department of Biological, Geological and Environmental Sciences, University of Bologna, Via Selmi 3, 40126 Bologna, Italy*
[3] *Xell AG, Waldweg 21, 33758 Schloss Holte-Stukenbrock, Germany*
[4] *Department of Ecology and Evolutionary Biology, University of California Santa Cruz, 115 McAllister Way, Santa Cruz, CA 95060, USA*
[5] *Departamento de Zoologıa, Facultad de Biologıa, Universidad de Sevilla, Avda. Reina Mercedes 6, 41012-Sevilla, Spain*
[6] *Department of Pharmacy and Biotechnology, University of Bologna, Via Irnerio 42, 40126 Bologna, Italy*
[7] *Fano Marine Center, The Inter-Institute Center for Research on Marine Biodiversity, Resources and Biotechnologies, Viale Adriatico 1/N 61032 Fano, Italy*
[8] *CIRI Health Sciences & Technologies (HST), University of Bologna, I-40064 Bologna, Italy*
[9] *Asociacion Hombre y Territorio, C/Betania no. 13. CP. 41007 Sevilla, Espana*
[10] *Consiglio Nazionale delle Ricerche, Istituto per lo Studio dei Materiali Nanostrutturati (CNR-ISMN), Via P. Gobetti 101, 40129 Bologna, Italy*

[#] Equally contributing authors
* corresponding authors: Francesca Sparla, francesca.sparla@unibo.it; Giuseppe Falini, giuseppe.falini@unibo.it; Stefano Goffredo, s.goffredo@unibo.it

ABSTRACT

The diversity in the skeletal features of coral species is an outcome of their evolution, distribution and habitat. Here, we explored, from macro- to nano-scale, the skeletal structural and compositional characteristics of three coral species belonging to the genus *Balanophyllia* having different trophic strategies. The goal is to address whether the onset of mixotrophy influenced the skeletal features of *B. elegans*, *B. regia*, and *B. europaea*. The macroscale data suggest that the presence of symbiotic algae in *B. europaea* can lead to a surplus of energy input that increases its growth rate and skeletal bulk density, leading to larger and denser corals compared to the azooxanthellate ones, *B. regia* and *B. elegans*. The symbiosis would also explain the higher intra-skeletal organic matrix (OM) content, which is constituted by macromolecules promoting the calcification, in *B. europaea* compared to the azooxanthellate species. The characterization of the soluble OM also revealed differences between *B. europaea* and the azooxanthellate species, which may be linked to diverse macromolecular machineries responsible for skeletal biosynthesis and final morphology. Differently, the crystallographic features were homogenous among species, suggesting that the basic building blocks of skeletons remained a conserved trait in these related species, regardless of the trophic strategy. These results show changes in skeletal phenotype that could be triggered by the onset of mixotrophy, as a consequence of the symbiotic association, displaying remarkable plasticity of coral skeletons which repeatedly allowed this coral group to adapt to a range of changing environments throughout its geological history.

14th ICRS 2021 – Poster n° 0455

The skeleton of Balanophyllia coral species suggests adaptive traits linked to the onset of mixotrophy

Q. PALAZZO[1], F. PRADA[2], T. STEFFENS[3], S. FERMANI [1], C. SAMORÌ[1], G. BERNARDI[4], A. TERRÓN SIGLER[5], F. SPARLA[6], G. FALINI[1], S. GOFFREDO[2]

[1]Univ. of Bologna, Dept of Chemistry & Fano Marine Center, Bologna, Italy, [2]Univ. of Bologna, BiGeA, Mar Sci Group & Fano Marine Center, Fano, Italy, [3]Xell AG, Waldweg, Germany, [4]UC Santa Cruz (USA), Ecology and Evolutionary Biology, Santa Cruz, United States, [5]Univ. of Seville (ES), Departament of Zoology, Seville, Spain, [6]Univ. of Bologna (IT), FaBiT, Bologna, Italy

Quinzia Palazzo: PhD Student in "Innovative technologies and sustainable use of Mediterranean fisheries and biological resources (FISHMED-PHD)" at Department of Chemistry, University of Bologna. E-mail: quinzia.palazzo2@unibo.it

OVERVIEW

Coral species descriptions were traditionally based solely on skeletal morphology. However, skeletal features are known to exhibit variations unrelated to evolutionary divergence, which may explain why coral species are notoriously difficult to identify, hindering our ability to understand their ecology, evolution, and biodiversity.
This study provides the first multi-scale comparative analysis of the skeletal structural and compositional features of three coral species belonging to the genus *Balanophyllia*, collected on the Western Mediterranean Sea and North-East Pacific Ocean and characterized by different trophic strategies.
According to some indirect evidences [1,2], the zooxanthellate and hermaphrodite *europaea* it is supposed to have a recent history compared to the azooxanthellate *B. elegans* and *B. regia*. In fact, the *B. europaea*, could have evolved from the azooxanthellate and gonochoric *B. regia*, which survived the Messinian salinity crisis in the Late Miocene (~ 7.2 to 5.3 Mya), acquiring the symbiosis and hermaphroditism which would have been advantageous traits in evolutionary terms during the environmental changes of Mediterranean Late Miocene scenario.

GOAL

The study aimed to answer the following question: **were the skeletal features of *B. elegans*, *B. regia*, and *B. europaea* influenced by the trophic strategies (heterotrophic vs mixotrophic)?**

MATERIALS AND METHODS

Coral skeletons features were investigated at micro (biometry, skeletal parameters), micro (mineralogy, texture) and nanoscale (organic matrix composition) levels on three different *Balanophyllia* species. In particular, *B. elegans* specimens (n = 65) were randomly collected by SCUBA diving off the California coast at Pacific Grove (36° 37' 18" N 121° 53' 53" W). *B. regia* specimens (n = 67) were randomly collected along the Granada coast, southern Iberian Peninsula, on Marina del Este beach (36° 43' 08" N 3° 43' 38" W). *B. europaea* specimens (n = 116) were randomly collected at Punta Chiappa, east of Genoa, Italy (44° 21' 44.54" N, 9° 07' 49.17" E, Ligurian Sea, North-Western Mediterranean Sea. (Fig. 1).

Data acquired with the methods used:
- Biometric parameters: skeletal length,width, height, dry corallite mass, surface/volume ratio (**Caliper, analytical balance**);
- Skeletal parameters: micro-density, bulk density and porosity(**Buoyant weight technique using a hydrostatic balance**);
- Mineral skeletal texture (**Scanning electron microscopy (SEM) observations**);
- Skeletal mineralogy (**X-ray and High-resolution powder diffraction (XRD, HR-XRD), Fourier transform infrared spectroscopic analysis (FTIR)**);
- Intra-skeletal organic matrix (OM) content (**Thermogravimetric analysis (TGA)**);
- Characterization of Soluble Organic Matrix (SOM) (**FTIR, Sodium dodecyl sulfate-polyacrylamide gel electrophoresis (SDS-PAGE)**);
- OM Lipid content and fatty acid analysis (**Gas chromatography-mass spectrometry (GC-MS)**);
- OM amino acid composition (**Ultra High-Performance Liquid Chromatography (UHPLC Agilent Technologies)**).

HIGHLIGHTS

- Preserved skeletal structural features in *Balanophyllia* azooxanthellate species
- The onset of mixotrophy led to larger, denser and less porous coral skeletons
- Higher amount of intra-skeletal organic matrix found in zooxanthellate species
- Skeletal protein migration differs between azooxanthellate and zooxanthellate species
- Crystallographic features preserved regardless trophic strategy

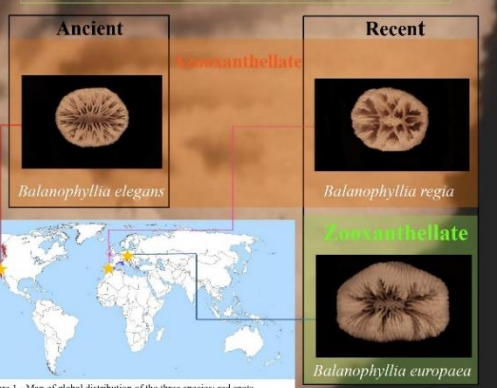

Figure 1 - Map of global distribution of the three species: red spots represent the distribution of *Balanophyllia elegans* (Eastern Pacific: USA, Mexico and Canada), pink spots represent the *B. regia* distribution (Atlantic and the Mediterranean) and the blue ones represent the geographic distribution of *B. europaea* (Mediterranean Sea). Yellow stars indicate the localities where the three investigated species were collected.

RESULTS

Biometric measurements and assessment of skeletal density and porosity revealed that the zooxanthellate *B. europaea* forms larger, denser and less porous skeletons compared to the azooxanthellate *B. regia* and *B. elegans* (Fig. 2).
The investigation of the intra-skeletal organic matrix (OM), which drives the biomineralization process, showed a higher content in the zooxanthellate species compared to the azooxanthellate species (Fig. 2).

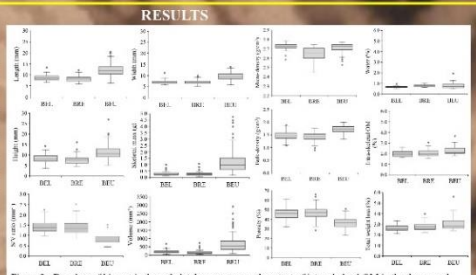

Figure 2 - Boxplots of biometric data, skeletal parameters and content of intra-skeletal OM in the three coral species (BFE: *B. elegans*; BRE: *B. regia*; BEU: *B. europaea*).

The characterization of the soluble OM revealed differences between *B. europaea* and the two azooxanthellate species (Fig. 3, Tab.1). Indeed, the SDS-page observations revealed discrete bands for *B. europaea*, while the SOMs of *B. regia* and *B. elegans* resulted in a smear of polydisperse macromolecules (diffuse color, Fig. 3). The amino acid composition revealed only in the azooxanthellate species the presence of arginine and lysine (Tab. 1).

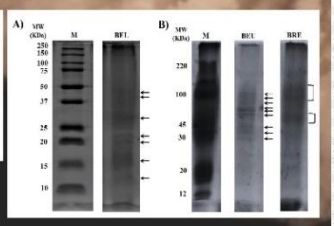

Figure 3 - SDS-PAGE of intra-skeletal SOM extracted from the skeletons of *B. elegans* (BFE), *B. regia* (BRE), and *B. europaea* (BEU). The arrows indicate the major protein bands, and the brackets show the smear band regions.

	SOM		
	BEE	BRE	BEU
Ala	4.4	5.5	4.1
Arg	1.9	1.7	
*Asx	35.7	42.7	50.0
Cys			
Cys-Cys			
Glu			
*Glx	8.3	7.5	6.1
Gly	15.3	15.2	18.6
His	1.6		
Hypro			
Ile	2.5	2.3	1.5
Leu	3.6	2.7	2.0
Lys	3.1	2.5	
Met			
Orn			
Phe	1.3	1.3	1.2
Pro	3.7	3.3	
Ser	4.6	7.8	12.2
Thr			
Val	4.7	3.5	1.7
Trp			
Tyr			
Total	5.6	5.2	2.6

Table 1 - Amino acid compositions (relative mol %) of proteins extracted from the soluble fractions of the intra-skeletal organic matrix (SOM).

Nevertheless, the crystallographic feature were homogenous among species (Tab. 2, Fig. 4). Indeed, the HR-XRD analysis revealed that the crystallite size and microstrain fluctuation results homogeneous among species (Tab. 2).

Peak position (°)	Species	Crystallite size [µm]		Microstrain (ε)	
		mean	SD	mean	SD
26.23	BEE	0.0564	0.0049	0.0012	0.0001
	BRE	0.0562	0.0017	0.0012	0
	BEU	0.0514	0.0064	0.0014	0.0002
27.23	BEE	0.0543	0.0053	0.0013	0.0001
	BRE	0.0546	0.0019	0.0013	0.0002
	BEU	0.0516	0.0055	0.0013	0.0001

Table 2 - Crystallite size and microstrain estimation of aragonitic crystals of skeletons, determined by fitting the (111) and (021) reflections, the most intense peaks of aragonite at the position 26.23° and 27.23°. SD Standard Deviation

Furthermore, SEM observation (Fig. 4) did not show a clear pattern in the distribution of the center of calcification in the coral skeleton that can suggest differences among the three species. However, the texture of the fibrous region was quite similar among the three species. This is in line with the model of coral growth reported in the literature that indicated the same mineral building block are used to build up the coral skeleton [3].

Figure 4 - Scanning electron microscopy images from coral skeleton samples of *B. elegans*, *B. regia*, and *B. europaea*. In (A-C) images at increasing magnifications of a cross section of a septum of *B. elegans* are shown. In (D-F) images at increasing magnifications of a cross section of a septum of *B. regia* are shown. In (G-I) images at increasing magnifications of a cross section of a septum of *B. europaea* are shown. * indicates the center of calcification. # indicates the fibrous region.

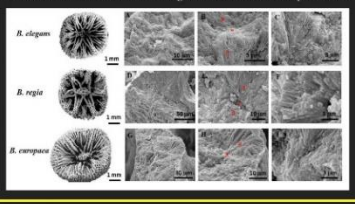

DISCUSSION AND CONCLUSION

The macroscale data suggest that the presence of symbiotic algae in *B. europaea* can lead to a surplus of energy input that increases its growth rate and skeletal bulk density, leading to larger and denser corals compared to the azooxanthellate ones, *B. regia* and *B. elegans*. Indeed, it was hypothesized that the symbiotic zooxanthellae, which provide their hosts with orders of magnitude more energy than normally available to heterotrophic organisms, could ultimately enhance host's calcification rates compared to the azooxanthellate species. At micro- and nano-scale, the symbiosis would also explain the higher intra-skeletal organic matrix (OM) content, which is constituted by macromolecules promoting the calcification, in *B. europaea* compared to the azooxanthellate species. The characterization of the soluble OM also revealed differences between *B. europaea* and the azooxanthellate species, which may be linked to diverse macromolecular machineries responsible for skeletal biosynthesis and final morphology. In detail, a smeary patterns of protein migration were observed only in the azooxanthellate species, and they could be due to post-translational modifications which may lead to polydisperse macromolecules and glycosylated proteins in their SOMs that mask the identification of discrete protein bands (instead showed for *B. europaea*). Indeed, the amino acid composition revealed only in the azooxanthellate species the presence of arginine and lysine, which can interact with negatively charged ions (bicarbonate) or acidic matrix proteins [4]. In particular, the lysine residues act as glycosylation sites and arginine as phosphorylatation ones and allow for protein post-translational modifications [3]. Therefore, the observation of these residues suggests the presence of glycosylated/phosphorylated proteins in the SOMs of *B. regia* and *B. elegans* that may have the capacity to bind calcium ions creating the observed smeary patterns. On the other hand, the crystallographic features were homogenous among species, suggesting that the basic building blocks of skeletons remained a conserved trait in these related species, regardless of the trophic strategy.

These results highlight significant changes in skeletal phenotype triggered by the onset of mixotrophy, as a consequence of the symbiotic association, displaying remarkable plasticity of coral skeletons which repeatedly allowed this coral group to adapt to a range of changing environments throughout its geological history. Moreover, the use of a multiscale approach to compare a variety of coral skeleton parameters may advance biologist community in assessing the evolutionary and adaptive driving forces in an integrated and wider perspective.

REFERENCES

[1] Campoy et al. The Origin and Correlated Evolution of Symbiosis and Coloniality in Scleractinian Corals. Front Mar Sci 2020:7.
[2] Kerr et al. Correlated evolution of sex and reproductive mode in corals (Anthozoa: Scleractinia). Proc R Soc B Biol Sci 2011;278:75–81.
[3] Sun et al. From particle attachment to space-filling coral skeletons. Proc Natl Acad Sci 2020;117:30159–70.
[4] Mass et al. et al. Temporal and spatial expression patterns of biomineralization proteins during early development in the stony coral *Pocillopora damicornis*. Proc R Soc B Biol Sci 2016;283:20160322.

ACKNOWLEDGMENTS

The research leading to these results has been conceived under the International PhD Program "Innovative Technologies and Sustainable Use of Mediterranean Sea Fishery and Biological Resources" (www.FishMed-PhD.org). This study represents partial fulfilment of the requirements for the Ph.D. thesis of Quinzia Palazzo.

Appendix 4

Horizon 2020

Call: H2020-MSCA-RISE-2017 (Marie Skłodowska-Curie Research and Innovation Staff Exchange)

Topic: MSCA-RISE-2017

Type of action: MSCA-RISE (RISE)

Number: 777822

Project Title: Geometric and Harmonic Analysis with Interdisciplinary Applications Acronym: GHAIA

Status: Granter

PROPOSAL TITLE: Shape-function relation in otolith: vibroacoustic virtual experiments of the movement patterns of fish otoliths of different size and gender
NAME AND AFFILIATION OF THE APPLICANT: Quinzia Palazzo, FishMed PhD Student Department of Chemistry "Giacomo Ciamician" University of Bologna, Italy, Via Selmi 2, 40126 Bologna
PROPOSED HOST INSTITUTE: Structural Engineering Department, University of California, San Diego
PROPOSED DURATION AND DATES OF THE RESEARCH STAY: From February 2022 to June 2022
NAME AND AFFILIATION OF THE SCIENTIST IN CHARGE OF SUPERVISING THE RESEARCH IN THE HOST INSTITUTE: Prof. Petr Krysl Structural Engineering Department at the University of California, San Diego (USA).
SCIENTIFIC PROPOSAL: **Shape-function relation in otolith: vibroacoustic virtual experiments of the movement patterns of fish otoliths of different size and gender** Sound is a major sensory channel for fishes and plays a key role in their ecology and life-history strategies, since it is used for communication between conspecifics or heterospecifics, navigation, feeding, detection of predators, reproductive

interactions, and habitat selection [43]. For its importance, fishes have evolved various physiological adaptations for sound reception and production [45]. The size and shape of otoliths likely influence the frequencies that can be detected and the sensitivity (auditory threshold) to those frequencies [47]. Thus, the wide morphological and ultrastructural variability in otoliths is likely linked to the diversity in hearing capabilities at intra- and inter-specific levels [48], but the mechanism that allows fish to analyse sound frequency and direction remains elusive. One obstacle to understanding the processes for these abilities is our lack of knowledge about the movements of the otoliths themselves. For example, do otoliths show simple translation back and forth along the axis of sound wave propagation or, are the motions more complex?

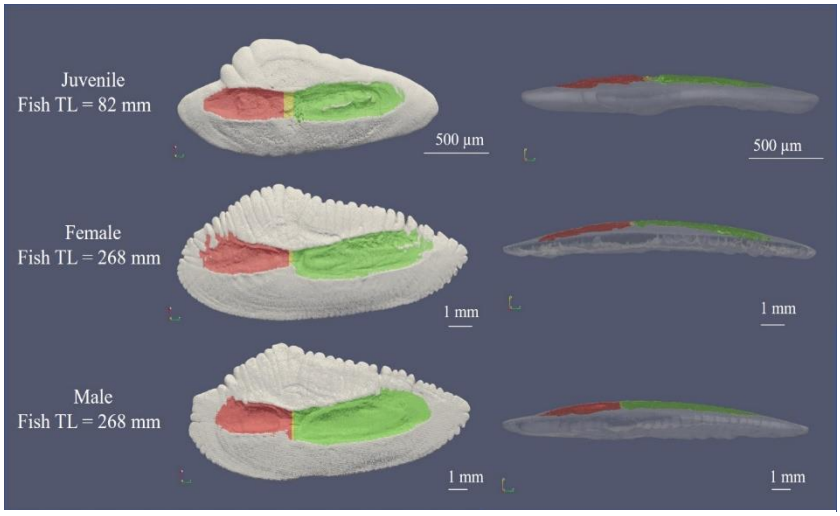

Figure 1 – Representative surface reconstructions of juvenile, female and male otolith and sulcus acusticus parts in *xz*-plane alignment (left) and *yz*-plane one (right) visualized with ParaView. The red part represents the ostial colliculum, the yellow region represents the collum (the central narrowing of the sulcus) and the green one is the caudal colliculum. TL= total length of fish individuals.

The preliminary results of the investigations performed during my PhD have shown interesting differences in otoliths from individuals of different sizes and genders that can have an adaptive and functional role in the perception of sounds (Figure 1). In particular, the analysis of micro-CT scans highlighted morphological differences between juveniles and adults of different sex. Based on the outcomes of the previous investigation, this research proposal aims to explore the acoustical implication of otolith variability and to establish the shape/structure–function relationships in otoliths during fish ontogenesis and between genders.

In detail, through a programmatic approach, the research proposal aims to unravel the following challenging issue: What is the effect of otolith shape and density on its displacement? How do otolith structural features influence its response to sound

stimuli? To this end, virtual experiments of vibroacoustic will be conduct in the Structural Engineering Department at the University of California, San Diego under the guidance of Prof. Petr Krysl, a centre with expertise in virtual experiments in marine bioacoustics.

The hosting research group has been long interested in bioacoustics simulations in fishes. Indeed, through the development of a methodology that combines X-ray CT scans with tissue elasticity measurements and finite-element modelling software (VATk) developed by Krysl et al. [175] and Cranford et al. [176,177], they have provided significant insights and discoveries in the last decade. Additional software tools have since been developed. And so, in order to determine the effect that otolith shape might have on otolith motion, two sets of simulations will be run using a suite of software tools. In the first simulations (Extracted Otoliths Simulations), we will extract the shapes of the otoliths from high-resolution micro-CT scans of the *Merluccius merluccius*. These otoliths would be assigned uniform calcareous material properties, immersed in a simulated shear-soft jelly, and exposed to planar harmonic waves of different stimulus frequencies and directions. In the second set of simulations (Simplified Otolith Simulations), we will compare the responses of "simplified otolith shapes" with the results of the Extracted Otoliths Simulations. In this second simulation, we use two simple shapes, a "spherical otolith" and a "hemispherical otolith." Another point that will be taken into account in using the finite element model is the validation process to tests the veracity of the model by comparing virtual simulations to actual experimental results.

The result expected from the research period in the host institute is 1) to formulate a three-dimensional description of the motion patterns from otolith micro-CT scans by applying a "virtual sound tomography" and 2) investigate whether there are any differences in the otolith response to sound waves which could bring a significance in a certain habitat or improve fish communication in specific contexts. In conclusion, the implementation of a vibroacoustic model to otoliths previously investigated in their structural and morphological characteristics will allow us to shed light on the functional and ecological significance of the juvenile/adults and females/males otolith differences highlighted in my PhD research so far.

References

1. Popper AN, Hawkins AD. 2019 An overview of fish bioacoustics and the impacts of anthropogenic sounds on fishes. J. Fish Biol. 94, 692–713. (doi:10.1111/jfb.13948)

2. Putland RL, Montgomery JC, Radford CA. 2019 Ecology of fish hearing. J. Fish Biol. (doi:10.1111/jfb.13867)

3. Hawkins AD, Rasmussen KJ. 1978 The calls of gadoid fish. J. Mar. Biol. Assoc. United Kingdom (doi:10.1017/S0025315400056848)

4. Brawn VM. 1961 Sound Production By the Cod (Gadus Callarias L.). Behaviour (doi:10.1163/156853961X00150)

5. Krysl P, Cranford TW, Hildebrand JA. 2008 Lagrangian finite element treatment of transient vibration/acoustics of biosolids immersed in fluids. Int. J. Numer. Methods Eng. (doi:10.1002/nme.2192)

6. Cranford TW, Krysl P, Hildebrand JA. 2008 Acoustic pathways revealed: Simulated sound transmission and reception in Cuvier's beaked whale (Ziphius cavirostris). Bioinspiration and Biomimetics (doi:10.1088/1748- 3182/3/1/016001)

7. Cranford TW, Krysl P, Hildebrand JA. 2008 Sound pathways revealed: Simulated sound transmission and reception in cuvier's beaked whale ziphius cavirostris using the vibro-acoustic toolkit. Bioacoustics (doi:10.1080/09524622.2008.9753767)

Acknowledgments

First, I would like to greatly acknowledge my supervisor Prof. Giuseppe Falini and my co-supervisors Prof. Stefano Goffredo and Prof. Jaap Kaandorp, for their invaluable support throughout my PhD. In particular, my supervisor Giuseppe, your inestimable support, your intuitions and precious suggestions always gave me new insights on the problems we were facing and showed me new ways to tackle them. I would like to express my sincere gratitude also to Stefano, for the opportunity to work within the Marine Science Group Lab of University of Bologna. Ever since we had our first meeting (in the far 2012), you have given me useful feedback and ideas on how to approach my studies and your love for research always motivated me in these years. Another special thank you goes to Jaap, for giving me the great opportunity to work at the Computational Science Lab of University of Amsterdam, for your constant readiness in answering my questions, for being supportive, encouraging, and understanding, and for all the talks we had (and the fun we had during them!). I also thanks Prof. Rob Belleman and Steven Raaijmakers for your inestimable help, which have made working on a completely new topic much more manageable. I particularly appreciate your willingness to support me and your patience in getting to grips with a new, complex field such as computational sciences.

I would like to thank the Dr. Jörg U. Hammel, for giving me the opportunity to visit the DESY synchrotron of Hamburg, to acquire the micro-CT scans (without whom a large part of otolith experiments would not has been possible), and to let me feel as a beamline scientist!

Out of all the people with whom I have spent these important challenging years, Dr. Fiorella Prada deserves a special mention. Many thank for always being there to help me out, for your immense support, for all the loopy weekends and late-night sessions. Working with you has been a privilege. You are such a great scientist and human being.

I am thankful to all the colleagues over these years at both the University of Bologna, the Lab in Fano and the National Research Council of Ancona (ISMAR-CNR). A special thank you to Dr. Mauro Marini, for sharing your expert knowledge, but also for your friendliness which made me feel sincerely comfortable to work in such synergic and stimulating research environment.

A very special thank you goes to my family and to friends that were as close as a family, for always being by my side, for let me keep my integrity safe and for reminding me what really matters.

A thank you goes to Michele. The night conversations and wondering chats I had with you have been the most engaging I had during these years, and in you I have found a friend with who to share my nerd ideas without regrets.

Last, but not least, I would like to thank all the scientists that inspired me along this path, all of them that shared their research, and to all of them who keep as a fundamental aspect of their life the love for nature and knowledge. Life can feel heavy sometimes, but nature has a way of making those things feel smaller in the best ways.

To all those who I did not mention but hold a place dear in my hearth: you know who you are. Thanks for being there for me throughout these years.